



# Università degli Studi di Ferrara

DOTTORATO DI RICERCA IN  
FISICA  
CICLO XXIV

COORDINATORE Prof. Filippo Frontera

## Measurement of Collins asymmetries in inclusive production of pion pairs at *BABAR*

Settore Scientifico Disciplinare FIS/04

**Dottorando**

*Dott.* ISABELLA GARZIA

.....

**Tutore**

*Prof.* DIEGO BETTONI

.....

**co-Tutore**

*Dott.* FABIO ANULLI

.....

---

ANNI 2008/2011



*“Theory is when we know everything but nothing works.  
Praxis is when everything works but we do not know why.  
We always end up by combining theory with praxis:  
nothing works... and we do not know why.”*

*“La teoria è quando si sa tutto e niente funziona.  
La pratica è quando tutto funziona e nessuno sa il perchè.  
Noi abbiamo messo insieme la teoria e la pratica:  
non c'è niente che funzioni... e nessuno sa il perchè.”*

A. Einstein



# Contents

<b>List of Figures</b>	<b>V</b>
<b>List of Tables</b>	<b>XI</b>
<b>Introduction</b>	<b>1</b>
<b>1 Theoretical motivations</b>	<b>5</b>
1.1 TMDs . . . . .	6
1.1.1 Partonic interpretation and proprieties of the TMDs . . . . .	7
1.2 Semi Inclusive Deep Inelastic Scattering . . . . .	9
1.3 Transversity distribution . . . . .	10
1.3.1 The Collins effects . . . . .	11
1.3.2 Phenomenological extraction of transversity function . . . . .	13
1.3.3 Dihadron fragmentation function . . . . .	15
1.4 Summary . . . . .	16
<b>2 Fragmentation Functions in <math>e^+e^-</math> annihilation</b>	<b>19</b>
2.1 Introduction . . . . .	19
2.2 Fragmentation models . . . . .	21
2.2.1 Independent fragmentation . . . . .	21
2.2.2 String fragmentation . . . . .	22
2.2.3 Cluster fragmentation . . . . .	24
2.3 Theoretical aspects of Collins Fragmentation Function in $e^+e^-$ annihilation . . . . .	24
2.3.1 General angular dependence . . . . .	24
2.3.2 Two-particle inclusive cross section . . . . .	25
2.3.3 Hadron tensor . . . . .	29
2.3.4 Cross section . . . . .	30
2.3.5 Universality of the Collins effect . . . . .	34
2.3.6 Higher twist . . . . .	35
2.3.7 Jet frame asymmetry . . . . .	36

<b>3</b>	<b>The <i>BABAR</i> Experiment</b>	<b>39</b>
3.1	The PEP-II <i>B</i> Factory . . . . .	39
3.1.1	PEP-II Layout . . . . .	40
3.1.2	PEP-II performances . . . . .	42
3.1.3	PEP-II background . . . . .	44
3.2	Overview of the <i>BABAR</i> detector . . . . .	45
3.3	The Silicon Vertex Tracker (SVT) . . . . .	48
3.3.1	Detector layout . . . . .	48
3.3.2	Detector performance . . . . .	50
3.4	The Drift CHamber (DCH) . . . . .	51
3.4.1	Detector layout . . . . .	52
3.4.2	Detector performance . . . . .	54
3.5	The Čerenkov light detector . . . . .	56
3.5.1	Detector layout . . . . .	57
3.5.2	Detector performance . . . . .	58
3.6	The Electromagnetic Calorimeter . . . . .	62
3.6.1	Detector layout . . . . .	62
3.6.2	Detector performance . . . . .	64
3.7	The Instrumented Flux Return . . . . .	65
3.7.1	Detector layout . . . . .	66
3.7.2	Detector performance . . . . .	69
3.8	The <i>BABAR</i> Trigger . . . . .	72
<b>4</b>	<b>Collins Asymmetry: analysis strategy</b>	<b>75</b>
4.1	Thrust Reference Frame: RF12 . . . . .	76
4.2	Second-hadron momentum Reference Frame: RF0 . . . . .	77
4.3	Analysis strategy and selection criteria . . . . .	78
4.3.1	Charged particle reconstruction . . . . .	79
4.3.2	Particle identification . . . . .	80
4.3.3	Analysis strategy . . . . .	82
4.4	Raw Asymmetries . . . . .	91
4.5	Double Ratios . . . . .	94
<b>5</b>	<b>Study of systematic effects</b>	<b>101</b>
5.1	Asymmetries in the <i>uds</i> Monte Carlo . . . . .	101
5.2	Background study: $c\bar{c}$ , $B\bar{B}$ , and $\tau^+\tau^-$ . . . . .	111
5.3	Monte Carlo Re-weighted sample . . . . .	133
5.4	Particle Identification . . . . .	139
5.5	Bin size . . . . .	140
5.6	Higher harmonic contributions . . . . .	141

5.7	$\pi^+\pi^+/\pi^-\pi^-$ Double Ratio test . . . . .	142
5.8	Subtraction and Double Ratio methods . . . . .	142
5.9	Beam Polarization studies . . . . .	143
5.10	Toy MC . . . . .	145
5.11	Asymmetries versus thrust . . . . .	146
5.12	Asymmetries measured in different data taking periods . . . . .	149
5.13	Handling of systematic errors . . . . .	149
<b>6</b>	<b>Results</b>	<b>155</b>
6.1	Collins asymmetries <i>vs</i> $(\mathbf{z}_1, \mathbf{z}_2)$ , $(\mathbf{p}_{t1}, \mathbf{p}_{t2})$ , and $\mathbf{p}_{t0}$ bins . . . . .	155
6.2	Collins asymmetries <i>vs</i> polar angle $\sin^2 \theta / (1 + \cos^2 \theta)$ . . . . .	159
	<b>Conclusion</b>	<b>165</b>
<b>A</b>	<b>Light-Cone Quantization</b>	<b>167</b>
<b>B</b>	<b>Transverse momenta in (semi-)inclusive reactions</b>	<b>171</b>
B.1	The concept of Parton Distribution Function (PDF) and Parton Fragmentation Function (PFF) . . . . .	171
B.2	PFFs . . . . .	175
<b>C</b>	<b>Dirac matrices in chiral (Weyl) representation</b>	<b>181</b>



# List of Figures

1.1	Leading-twist TMD functions . . . . .	6
1.2	SIDIS diagram and kinematics . . . . .	9
1.3	Hermers and Compass results on Collins amplitude. . . . .	12
1.4	Collins asymmetries measured by the Belle Colladoration . . . . .	13
1.5	Transversity distribution and Collins fragmentation function results from global fit analysis (HERMES, COMPASS, and BELLE data). . . . .	14
1.6	Kinematic of the production of two hadrons in SIDIS processes. . . . .	15
1.7	Kinematic for the $e^+e^- \rightarrow (h_1h_2)_{jet1}(\bar{h}_1\bar{h}_2)_{jet2}X$ . . . . .	16
2.1	Fragmentation function in $e^+e^-$ annihilation for charged particles . . . . .	21
2.2	Scaling violations of the FF for charged particles . . . . .	21
2.3	Schematic view of the independent fragmentation process into mesons for a jet originated by the quark $q_0$ . . . . .	22
2.4	String fragmentation and meson production in $t - x$ space. . . . .	23
2.5	Gottfried-Jackson frame . . . . .	27
2.6	Collins-Soper frame . . . . .	27
2.7	Factorized diagram contributing to $e^+e^-$ annihilation at leading order . . . . .	30
2.8	Schematic view of the Collins effect . . . . .	33
2.9	Diagrams contributing to $e^+e^-$ annihilation at order $1/Q$ , involving one gluon which connects one of the two soft part. . . . .	35
3.1	The first four S-wave $\Upsilon$ resonances shown with the hadronic cross section versus center-of-mass energy/ $c^2$ in the $\Upsilon$ mass region . . . . .	40
3.2	The PEP-II asymmetric storage ring and the SLAC linear accelerator . . . . .	41
3.3	Total luminosity delivered by PEP-II . . . . .	43
3.4	Trickle injection: comparison of three different mode of PEP-II operation . . . . .	44
3.5	Layout of the <i>BABAR</i> detector . . . . .	46
3.6	Longitudinal section of the SVT detector. . . . .	49
3.7	Transverse section of the SVT detector. . . . .	49
3.8	SVT hit resolution in the $z$ (a) and $\phi$ (b) coordinate . . . . .	51

3.9	Energy loss per unit length ( $dE/dx$ ) as measured in the SVT as a function of momentum . . . . .	51
3.10	Drift chamber: longitudinal section . . . . .	52
3.11	<i>BABAR</i> DCH cell configuration . . . . .	54
3.12	Track reconstruction efficiency in the DCH for different voltages, and $p_t$ resolution . . . . .	55
3.13	DCH: $dE/dx$ . . . . .	56
3.14	Schematics of the DIRC mechanical support structure. . . . .	57
3.15	Schematics of the DIRC fused silica radiator bar and imaging region. . . . .	57
3.16	DIRC: Čerenkov angle and photon arrival time . . . . .	59
3.17	Number of detected photons versus track polar angle for reconstructed tracks in di-muon events compared to the Monte Carlo simulation. . . . .	60
3.18	Measured Čerenkov angle for pions and kaons . . . . .	60
3.19	Display of an $e^+e^- \rightarrow \mu^+\mu^-$ event reconstructed with two different time cuts . . . . .	61
3.20	Schematic view of one EMC crystal module, and longitudinal cross section of the EMC . . . . .	63
3.21	Energy and angular resolution for the EMC . . . . .	65
3.22	Electron efficiency and pion misidentification probability as a function of a) the particle momentum and b) the polar angle, measured in the laboratory system. . . . .	66
3.23	Cross section of a planar RPC with the schematics of the HV connection. . . . .	66
3.24	Overview of the IFR detector . . . . .	67
3.25	Schematic view of a standard Limited Streamer Tube configuration. . . . .	68
3.26	Average RPC efficiency in the barrel, forward end cap, and backward end cap as a function of the time . . . . .	69
3.27	Time evolution efficiency of the LST detector . . . . .	70
3.28	Muon efficiency and pion misidentification probability . . . . .	71
3.29	Pion mis-identification vs. muon efficiency rate of neural network algorithm for different period of <i>BABAR</i> data taking. . . . .	71
4.1	Definition of the azimuthal angles $\phi_1, \phi_2$ in the thrust reference frame (RF12), and $\phi_0$ in the second hadron momentum frame (RF0). . . . .	76
4.2	$R'_2$ and visible energy distributions for multi-hadrons events . . . . .	83
4.3	Normalized distribution of the number of tracks in the data sample, MC sample, and $\tau^+\tau^-$ MC sample . . . . .	84
4.4	Comparison of the thrust distributions in the MC and data sample . . . . .	84
4.5	Total visible energy of the events as a function of the thrust value for the on-resonance data sample . . . . .	85
4.6	(a,b) $Q_t$ vs $W_{hemi}$ distribution for pion pairs with $z > 0.2$ and $z < 0.2$ , respectively. (c) Angle between pions and thrust axis. (d), (e) Opening angle between the thrust and pion . . . . .	86
4.7	Transverse momentum distribution for pions with $z > 0.1$ . . . . .	88

4.8	Transverse momentum distribution for pions with $z > 0.15$ . . . . .	89
4.9	Azimuthal angle distributions of reconstructed and generated MC sample . . . . .	90
4.10	$\phi_1 + \phi_2$ azimuthal distribution in the RF12 frame and $2\phi_0$ distribution in the RF0 frame . . . . .	91
4.11	Raw asymmetry parameters $a_{12,0}$ for like-sign pion pairs and for unlike-sign pion pairs as a function of the transverse virtual photon momentum $Q_t$ . . . . .	93
4.12	Raw asymmetries for like and unlike sign pion pairs . . . . .	94
4.13	Double ratio $R^U/R^L$ calculated in the MC and data sample . . . . .	96
4.14	Comparison of asymmetries as a function of $6 \times 6$ ( $z_1, z_2$ )-bin subdivision calculated in data and MC samples . . . . .	98
4.15	RF12: comparison of asymmetries as a function of $4 \times 4$ ( $p_{t1}, p_{t2}$ )-bin subdivision calculated in data and MC samples . . . . .	98
4.16	RF0: comparison of asymmetries as a function of four $p_{t0}$ -bin calculated in data and MC samples . . . . .	99
5.1	Double ratio asymmetries measured on MC sample in different ( $z_1, z_2$ ) bins in the RF12 and RF0 frames . . . . .	102
5.2	MC double ratio study as a function of 16 bins of ( $p_{t1}, p_{t2}$ ), and as a function of 4 $p_{t0}$ bins . . . . .	103
5.3	RF12: comparison of distribution obtained selecting pions with $p_{t1,2} < 0.5$ GeV/ $c$ and distribution for pions with $p_{t1,2} > 0.5$ GeV/ $c$ . . . . .	104
5.4	RF0: comparison of distribution obtained selecting pions with $p_{t1,2} < 0.5$ GeV/ $c$ and distribution for pions with $p_{t1,2} > 0.5$ GeV/ $c$ . . . . .	105
5.5	Distribution as a function of ( $z_1, z_2$ ) for generate associated pions (a) and (c), and distribution and for generated pions (b) and (d) . . . . .	107
5.6	Distribution as a function of ( $p_{t1}, p_{t2}$ ) for generate pions (a) and (c), and distribution for generated associated pions (b) and (d) . . . . .	108
5.7	$D^0$ mass for the decay mode $D^0 \rightarrow K\pi$ (mode 1), $D^0 \rightarrow K3\pi$ (mode 2), $D^0 \rightarrow K\pi\pi^0$ (mode 3), and $D^0 \rightarrow K_s\pi\pi$ (mode 4) . . . . .	113
5.8	Monte Carlo distributions of $\Delta M$ reconstructed in the $c\bar{c}$ (a) and $B\bar{B}$ (b) samples . . . . .	114
5.9	Distributions of (a) $M_{D^0}$ and (b) $\Delta M$ reconstructed in the off-peak data sample. . . . .	115
5.10	Event thrust distribution for the $\tau$ -enhanced data sample, and thrust distribution for pure $\tau^+\tau^-$ events obtained from the $\tau$ MC sample normalized to the data integrated luminosity . . . . .	117
5.11	U/L double ratio asymmetries for (a) RF12 and (b) RF0 calculated in the $\tau$ MC samples. . . . .	118
5.12	Comparison between the number of pion pairs in the data sample and the relative contribution due to $\tau^+\tau^-$ events, plus $B\bar{B}$ , plus $c\bar{c}$ , plus $uds$ . . . . .	119
5.13	Light quark asymmetries as a function of fractional energies, after the correction of charm, bottom and tau contributions . . . . .	121

5.14	Light quark asymmetries as a function of $p_t$ , after the correction of charm, bottom and tau contributions . . . . .	122
5.15	Charm asymmetries as a function of fractional energies . . . . .	123
5.16	Charm asymmetries as a function of $p_t$ . . . . .	124
5.17	Opening angle $\Delta(\theta)$ between the thrust axis and the real $q\bar{q}$ axis. The peak is at about 0.1 rad with an r.m.s. of about 0.05 rad. . . . .	133
5.18	Distributions of the reconstructed $\phi_1 + \phi_2$ (a) and $2\phi_0$ (b) combination, versus the corresponding values for the generated tracks . . . . .	134
5.19	Average fraction (%) of asymmetries results, in the RF12 (a) and RF0 (b) frames, as a function of $(z_1, z_2)$ subdivision for the reconstructed light quark MC events, re-weighted as described in the text . . . . .	135
5.20	Average fraction (%) of asymmetries results, in the RF12 (a) and RF0 (b) frames, as a function of $p_t$ bins subdivision for the reconstructed light quark MC events, re-weighted as described in the text . . . . .	135
5.21	Absolute values of the difference between the asymmetries calculated using tight pions selection (selection chosen in this analysis) and the asymmetries calculated using looser selection . . . . .	139
5.22	Comparison of $z$ -binned asymmetries measured with or without veto on muons and electrons . . . . .	140
5.23	Absolute values of the difference between the asymmetries calculated for 100 bins subdivision of the azimuthal angles, and 10 bins subdivision . . . . .	141
5.24	$\pi^+\pi^+/\pi^-\pi^-$ double ratio test . . . . .	142
5.25	Difference between the asymmetry measured using the DR method and the Sub method . . . . .	143
5.26	Angular distribution for $\cos(\theta)$ (a) and $\phi$ (b) for muon pairs in the center of mass frame . . . . .	145
5.27	Toy MC results for the UL averaged asymmetry measured in the RF12 frame . . . . .	146
5.28	Study of the asymmetries for different thrust bins, and for different thrust cuts . . . . .	147
5.29	Raw asymmetries for different $\cos(\theta_{th})$ bins . . . . .	148
5.30	Comparison of UL double ratio parameters as a function of $p_t$ measured for each data taking period (Run1 to Run6) . . . . .	149
6.1	Collins asymmetries for light quarks as a function of $z_2$ for 6 $z_1$ bins . . . . .	156
6.2	Comparison between <i>BABAR</i> results obtained using the full statistics, the <i>BABAR</i> preliminary off-resonance data, and the Belle results . . . . .	157
6.3	Dilution of the $A^{UL}$ asymmetry due to different cuts of the opening angle between the pion momentum and the thrust axis . . . . .	158
6.4	Light quark ( $uds$ ) Collins asymmetries as a function of $p_{t2}$ for 4 $p_{t1}$ bins, and as a function of 4 $p_{t0}$ bins . . . . .	160
6.5	Light quark asymmetry parameters as a function of $\sin^2 \theta/(1 + \cos^2 \theta)$ . . . . .	161

---

B.1	DIS: the "handbag" diagram leading to the dominant contribution to the cross section. . . . .	173
B.2	Dominant contribution to the differential cross section of $e^+e^-$ annihilation with one observed hadron in the final state. . . . .	174
B.3	Illustration of transverse momentum components quarks can have relative to their parent hadron momenta, and transverse momentum dependent PDFs and PFFs . . . . .	175
B.4	Probability interpretation of leading order integrated PFFs and Transverse Momentum Dependent PFFs . . . . .	177



# List of Tables

3.1	Cross section of the main physics processes at the $\Upsilon(4S)$ . . . . .	41
3.2	PEP-II beam parameters . . . . .	42
3.3	Overview of the coverage, segmentation, and performance of the <i>BABAR</i> detector system . . . . .	45
3.4	DCH wire specification. All wires are gold plated. . . . .	53
3.5	Proprieties of helium-isobutane gas mixture at atmospheric pressure and 20° C .	53
3.6	Proprieties of CsI(Tl). . . . .	63
3.7	Effective cross section, production rates, and trigger rates for the principal physics processes at the $\Upsilon(4S)$ for a luminosity of $\mathcal{L} = 3 \cdot 10^{33} \text{ cm}^{-2}\text{s}^{-1}$ . . . . .	73
3.8	L3 trigger efficiency (%) for various physics processes, derived from Monte Carlo simulation. . . . .	73
4.1	Data and MC samples used in this analysis . . . . .	79
4.2	Summary of the cuts used in this analysis . . . . .	92
4.3	$z$ -bin subdivision . . . . .	97
4.4	$p_t$ -bin subdivision . . . . .	97
5.1	Number of events and equivalent luminosity ( $\mathcal{L} = N/\sigma$ ) for each $uds$ MC run . .	101
5.2	Fit results of $uds$ MC asymmetries as a function of 36 $(z_1, z_2)$ . . . . .	109
5.3	Fit results of $uds$ MC asymmetries as a function of 16 $(p_{t1}, p_{t2})$ in the first part of table, and as a function of 4 $p_{t0}$ bins in the second part. . . . .	110
5.4	$M_{D^0}$ fit parameters for $c\bar{c}$ MC and for the off-peak data sample . . . . .	116
5.5	$\Delta M$ fit parameters for $c\bar{c}, b\bar{b}$ MC, and for the off-peak data sample . . . . .	116
5.6	Fraction of pion pairs in the data sample as a function of $(z_1, z_2)$ bins (36 bins) . .	125
5.7	Fraction of pion pairs in the data sample as a function of $(p_{t1}, p_{t2})$ bins (16 bins) and $p_{t0}$ bins (4 bins) . . . . .	126
5.8	Thrust reference frame (RF12): double ratio of U/L pion pairs as a function of $(z_1, z_2)$ -bins. In the second and third columns are reported the measured asymmetries in the full data sample ( $A_{meas}$ ) and in the $D^*$ enhanced sample ( $A_{D^*}$ ). In the last two columns are reported the light quark and the charm asymmetries . .	127

5.9	Second hadron momentum frame (RF0): double ratio of U/L pion pairs as a function of $(z_1, z_2)$ -bins. In the second and third columns are reported the measured asymmetries in the full data sample ( $A_{meas}$ ) and in the $D^*$ enhanced sample ( $A_{D^*}$ ). In the last two columns are reported the light quark and the charm asymmetries . . . . .	128
5.10	Thrust reference frame (RF12): double ratio of U/C pion pairs as a function of $(z_1, z_2)$ -bins. The same caption as Tab. 5.8. . . . .	129
5.11	Thrust reference frame (RF12): double ratio of U/C pion pairs as a function of $(z_1, z_2)$ -bins. The same caption as Tab. 5.9. . . . .	130
5.12	RF12 and RF0 frame: double ratio of U/L pion pairs as a function of $p_t$ -bins. are compared the asymmetries measured ( $A_{meas}$ ) in the full data, the asymmetries measured in the $D^*$ enhanced sample ( $A_{D^*}$ ), the light quark ( $A_{uds}$ ) and charm ( $A_{charm}$ ) asymmetries . . . . .	131
5.13	RF12 and RF0 frame: double ratio of U/C pion pairs as a function of $p_t$ -bins. are compared the asymmetries measured ( $A_{meas}$ ) in the full data, the asymmetries measured in the $D^*$ enhanced sample ( $A_{D^*}$ ), the light quark ( $A_{uds}$ ) and charm ( $A_{charm}$ ) asymmetries . . . . .	132
5.14	Thrust reference frame (RF12): estimated average fractions of the asymmetry measured fitting the double ratios U/L and U/C as a function of $(z_1, z_2)$ and corresponding correction factors $\zeta$ . . . . .	136
5.15	Second pion momentum frame (RF0): estimated average fractions of the asymmetry measured fitting the double ratios U/L and U/C as a function of $(z_1, z_2)$ and corresponding correction factors $\zeta$ . . . . .	137
5.16	Estimated average fractions of the asymmetry measured fitting the double ratios U/L and U/C as a function of $(p_{t1}, p_{t2})$ (RF12) in the first part of the table, and as a function of $p_{t0}$ (RF0) in the second part of the table. It is also summarized the corresponding correction factors $\zeta$ . . . . .	138
5.17	Beam polarization study: fit results for the $\cos(\theta)$ and $\phi$ distributions for the process $e^+e^- \rightarrow \mu^+\mu^-$ . . . . .	145
5.18	Asymmetry fit results for different fit function for the double ratio U/L and U/C as a function of $(z_1, z_2)$ . . . . .	151
5.19	Asymmetry fit results for different fit function for the double ratio U/L and U/C as a function of $p_t$ . . . . .	152
5.20	Absolute contribution to the systematic error on the $A_\alpha^{UL}$ and $A_\alpha^{UC}$ results for the $(z_1, z_2)$ bins, where $\alpha = 1, 2, 0$ indicates the reference frames . . . . .	153
5.21	Absolute contribution to the systematic error on the $A_\alpha^{UL}$ and $A_\alpha^{UC}$ results for the $(p_{t1}, p_{t2})$ bins, in the RF12 frame . . . . .	154
5.22	Absolute contribution to the systematic error on the $A_\alpha^{UL}$ and $A_\alpha^{UC}$ results for the 4 $p_{t0}$ bins, in the RF0 frame . . . . .	154

---

6.1	Light quark ( $uds$ ) Collins asymmetries obtained fitting the UL double ratio as a function of $(z_1, z_2)$ . . . . .	162
6.2	Light quark ( $uds$ ) Collins asymmetries obtained fitting the UC double ratio as a function of $(z_1, z_2)$ . . . . .	163
6.3	Light quark ( $uds$ ) Collins asymmetries obtained fitting the UL and UC double ratios as a function of $p_t$ . . . . .	164



# Introduction

The great improvements in the physics of particle accelerators occurred in the late 1950s have lead to the discovery of a number of new hadrons produced by experiments. In the 1964, Gell-Mann and Zweig [1, 2] independently proposed a scheme to categorized many of the observed hadrons. All the hadrons are described as combination of elementary particles, called quarks, and the hadrons quantum numbers are calculated from those of quarks. Baryons, including the protons and the neutrons, consist of three quarks, while mesons, such as pions and kaons, consist of a pair of quark and antiquark.

Since late 1960s to 1970s, the existence of structure within the proton was established by experiments of electron-proton Deep Inelastic Scattering (DIS) through  $\gamma^*$  exchange. However, the experimental results revealed that about half of momentum of the proton can be described by the charged components (quarks), and neutral particles, called gluons, have to be introduced in order to explain the other half of the momentum. In hadrons, gluons are created by dynamical processes: quarks create or absorb gluons, a gluon converts into a quark-antiquarks pair, and a quark-antiquark pair annihilates into gluons. Such dynamical quarks and gluons are called *partons* (parton model).

The theoretical framework to explain the interaction between quarks and gluons is based on Quantum Chromo Dynamics (QCD) which is a color SU(3) symmetry, a theory of strong interaction which is part of the Standard Model. In the parton model, partons are divided in three groups: “valence quarks” which carry the quantum number of the hadrons, “sea quarks” which are quark and anti-quark pairs generated by pair creation in the hadron vacuum, and “gluons” which are the mediators of the strong force.

Although some proprieties of the proton are explained by valence quarks, it was revealed by polarized DIS experiments that quarks and antiquarks in the proton carry only  $\sim 30\%$  of the proton spin [3, 4, 5]. The immediate consequence of this result is that there ought to be additional sources of spin within the nucleon besides the quarks. The most natural candidates are the spin of the gluon ( $\Delta G$ ) and the orbital angular momentum of quarks ( $L_z^q$ ) and gluons ( $L_z^g$ ):

$$S^N = \frac{1}{2} = \frac{1}{2}\Delta\Sigma + \Delta G + L^q + L^g, \quad (1)$$

where

$$\Delta\Sigma = \Delta u + \Delta d + \Delta q_s \quad (2)$$

is the contribution carried by the valence and sea quark spins, respectively. A variety of experiments have been realized to investigate the nucleon's spin structure with unprecedented precision, with the main goal to provide high precision measurements of all the various spin contributions listed in Eq. (1). In particular, the contribution due to the gluon spin  $\Delta G$ , was found to be very small [6, 7, 8], which suggests that the orbital angular momentum terms  $L^q$  and  $L^g$  are the dominant factors in Eq. (1).

Experimentally, Semi-Inclusive Deep Inelastic Scattering (SIDIS) measurements are one approach to probe the spin structure of the nucleon, and in particular they provide a separate measurement of the valence quarks and sea quarks contributions, as well as information on the orbital motion at the subatomic level. In particular, this method combines information from the nucleon target, and uses correlations in the fragmentation process between the observed final state hadrons and the flavor of its originating parton. The fragmentation process is described in terms of fragmentation functions.

One of these functions is the Collins fragmentation function [9] which measures how the orientation of the quark spin influences the direction of emission of hadrons in the fragmentation process and can thus be used as a quark spin analyzer. In other words, the Collins effect is due to the spin-orbit correlation in the fragmentation process. In addition to SIDIS experiments, it contributes to several Single Spin Asymmetries (SSA) in hard process  $pp$  collision, and  $e^+e^-$  annihilation into hadrons. We use the term *Collins asymmetries* to denote any asymmetry where the Collins function plays a role. The first experimental evidence of a non-zero Collins function for pions comes from the measurement of a Collins Asymmetry in SIDIS on a proton target by the HERMES Collaboration [10]. The same asymmetry, but on a deuteron target, was found to be consistent with zero by the COMPASS Collaboration [11]. Direct evidence of a non-zero pion Collins function has been found in  $e^+e^-$  annihilation data from DELPHI [12, 13] and Belle [14, 15]. A global fit to SIDIS and  $e^+e^-$  data allows the simultaneous extraction of the Collins fragmentation function and of the transversity parton distribution function, clearly showing the importance of the Collins function as a tool to investigate the structure of hadrons [16, 17]. The Collins fragmentation function for kaons is at the moment unknown.

Despite the primary goals of the *BABAR* experiment are the measurement of CP violation effects in the  $B$  meson system, the precise measurement of the CKM matrix element, and the measurement of rare  $B$  meson decays, a wide range of other physics may also be studied. In particular, the very clean environment and the good particle identification, make the *BABAR* detector suitable also for studies of inclusive hadrons production. In this dissertation, I report on the first *BABAR* measurement of the Collins effect in *inclusive production of two back-to-back hadrons in the reaction  $e^+e^- \rightarrow h_1 h_2 X$* .

This thesis is organized in six chapters:

- **Chapter 1:** the theoretical motivations of the measurement of the Collins asymmetry are presented, together with the physics context in which it plays a crucial role;
- **Chapter 2:** the concept of Fragmentation Function in  $e^+e^-$  annihilation, and the theoretical aspects of the Collins Fragmentation Function are introduced;
- **Chapter 3:** it contains information about the general structure of the accelerator facility and the *BABAR* detector, with details on the performances of each subsystems;
- **Chapter 4:** the data analysis is presented. The two different reference frames in which we perform the measurement of the Collins asymmetries are introduced, then the analysis strategy is summarized, followed by the description of the Double Ratio method used for measuring the azimuthal asymmetry.
- **Chapter 5:** the systematic uncertainties, the background contributions due to  $c\bar{c}$ ,  $B\bar{B}$ , and  $\tau^+\tau^-$  events, and cross check studies are discussed;
- **Chapter 6:** the final results for the light quarks Collins asymmetry are summarized and discussed. In particular, the asymmetry is shown as a function of the pions fractional energy ( $z$ ), pions transverse momentum ( $p_t$ ), and as a function of  $\sin^2\theta/(1 + \cos^2\theta)$ . The  $p_t$  dependence has never been studied before in  $e^+e^-$  annihilation.



# Chapter 1

## Theoretical motivations

The exploration of the internal structure of the nucleon in terms of quarks and gluons<sup>1</sup> has been and still is at the frontier of hadronic high energy physics research. In particular, Deep Inelastic Scattering (DIS) experiments of high energy leptons off nucleons have led to the most significant progresses in the knowledge of nucleon structure. By observing the momentum of the lepton in the final state one obtains information about the quark and the gluon content of the nucleon. This information is encoded in the Parton Distribution Function (PDF)  $f_1^a(x, Q^2)$  where  $x$  is the fraction of the nucleon momentum which is carried by the parton,  $Q$  is the energy in the center of mass frame, and  $a = q, g$  stands for quark and gluon, respectively.

However, our understanding of the nucleon structure from DIS experiments is one dimensional. From DIS we only learn about the longitudinal motion of parton in a fast moving nucleon, since the nucleon is seen as a bunch of fast-moving quarks, antiquarks, and gluons, whose transverse momenta are not resolved. A fast moving nucleon is Lorentz-contracted, but its transverse size is still about 1 fm, which is a large distance on the strong interaction scale.

Therefore, it make sense to ask question like: how are the quarks spatially distributed inside the nucleon? How do they move in the transverse plane?

To answer the above questions, we need to consider the description of a quark in the transverse plane in momentum space and in coordinate space. The theoretical tools adequate to describe the former are the Transverse Momentum Dependent PDFs (TMDs), and the theoretical object tailored to describe the spatial distributions of quarks in mixed longitudinal momentum and transverse space are the Generalized Parton Distributions (GPDs).

Despite the experimental nature of this dissertation, the first part of this chapter is focalized of the physics formalism of TMDs and Semi-Inclusive DIS, which is necessary for understanding the importance of the measurement of the Collins asymmetry in  $e^+e^-$  annihilation at *BABAR*.

---

<sup>1</sup>Quarks and gluons are the fundamental degrees of freedom of Quantum Chromo Dynamics (QCD)

## 1.1 TMDs

The “simplest” TMD is the unpolarized function  $f_1^q(x, k_\perp)$  which describes, in a fast moving nucleon, the probability to find a quark carrying a fraction  $x$  of the nucleon momentum, and a transverse momentum  $k_\perp = |\mathbf{k}_\perp|$ . It is formally related to the collinear (integrated over  $k_\perp$ ) PDF by:

$$f_1^q(x) = \int d^2\mathbf{k}_\perp f_1^q(x, k_\perp). \quad (1.1)$$

In general, the TMDs are defined in terms of the unintegrated quark-quark correlator [18, 19] in the light-cone coordinate:

$$\Phi_{ij}(x, \mathbf{k}_\perp, \mathbf{S})_\eta = \int \frac{dz^- d^2z_\perp}{(2\pi)^3} e^{ik \cdot z} \langle \mathbf{P}, \mathbf{S} | \bar{\psi}_j(0) \mathcal{W}_\eta(0, z) \psi_i(z) | \mathbf{P}, \mathbf{S} \rangle \Big|_{z^+=0}, \quad (1.2)$$

in which the path-dependent gauge link operator  $\mathcal{W}_\eta(0, z)$  ensures the color gauge invariance of the matrix element, and  $\eta$  indicates that  $\mathcal{W}_\eta(0, z)$  depends on the process. The light-cone coordinate are defined in Appendix A.

The power and the rich possibilities of the TMD approach arise from the simplest fact that  $\mathbf{k}_\perp$  is a vector which allows various correlations with the other vectors involved: the nucleon momentum  $\mathbf{P}$  and the nucleon spin  $\mathbf{S}$ . Of particular importance are *leading-twist* TMDs, i.e. TMDs which enter in observables without power suppression. In this context, a TMD or observable is said to be *twist- $t$*  if its contribution to a cross section is suppressed by the factor  $(M/Q)^{t-2}$  [20] in addition to kinematic overall factors ( $M$  is a generic hadronic scale including the transverse momentum).

		quark		
		U	L	T
n u c l e o n	U	$f_1$		$h_1^\perp$
	L		$g_1$	$h_{1L}^\perp$
	T	$f_{1T}^\perp$	$g_{1T}^\perp$	$h_{1T}^\perp$

Figure 1.1: Leading-twist TMD functions. Rows: nucleon polarization. Columns: quark polarization. U=unpolarized, L=longitudinal polarization, T=transverse polarization. TMDs for antiquarks and gluons are defined similarly in terms of correlators analogous to Eq. (1.2).

The leading-twist TMDs are associated with the large positive component of the nucleon momentum (in the frame where the nucleon moves fast). For a spin 1/2 particle like the nucleon there are 8 leading-twist TMDs, summarized in Fig. 1.1, where the common subscript 1

is used to indicate twist-2 TMDs<sup>2</sup> (see Appendix B for the complete name description).

### 1.1.1 Partonic interpretation and proprieties of the TMDs

TMDs contain information on the longitudinal and transverse motion of quarks and gluons inside a fast moving nucleon. When adding the spin degree of freedom they link the parton spin ( $s_q$ ) to the parent proton spin ( $S$ ) and to the intrinsic motion ( $\mathbf{k}_\perp$ ). We denote the most general spin dependent TMD by  $f_1^q(x, \mathbf{k}; s_q, \mathbf{S})$ , which may depend on all possible combinations of the pseudo-vector  $s_q$ ,  $\mathbf{S}$  and the vector  $\mathbf{k}_\perp$ ,  $\mathbf{P}$ .

A similar correlation between spin and transverse motion can occur in the fragmentation process of a transversely polarized quark, with spin vector  $s_q$  and three-momentum  $\mathbf{k}_\perp$ , into a hadron with longitudinal momentum fraction  $z$  and transverse momentum  $\mathbf{P}_\perp$  with respect to the quark direction. This mechanism is called Collins effect [9] and appears in the fragmentation via a  $s_q \cdot (\mathbf{k}_q \times \mathbf{P}_\perp)$  term. In particular, for a quark fragmenting into a spinless hadron there are two independent leading-twist transverse momentum dependent fragmentation function.

Below, we briefly list the eight leading-twist TMD PDFs with their partonic interpretation, and the two TMD fragmentation functions for a final spinless hadron, which are the main objects in the investigation of the nucleon momentum structure. The superscript  $a$  refers to a generic parton,  $q$  or  $g$ .

→  $f_1^a(x, k_\perp)$  is the unpolarized,  $k_\perp$  dependent distribution of parton  $a$  inside a proton. Its integrated version is the usual PDF measured in DIS  $q(x) = f_1^q(x) = \int d^2\mathbf{k}_\perp f_1^q(x, k_\perp)$  for a quark and similarly for a gluon; in the Quark Parton Model  $f_1(x) = q^+(x) + q^-(x)$ , where  $q^{+(-)}$  refers to parallel (antiparallel) orientation of the quark and nucleon spins.

Most of experimental and theoretical efforts have so far been dedicated to this PDF, which are the best known partonic distributions, and the comparison of the predicted  $Q^2$  dependence with data has been a great success of perturbative QCD.

→  $g_{1L}^a(x, k_\perp)$ , or simply  $g_1^a$ , is the unintegrated helicity distribution: the difference between the number density of partons  $a$  with the same and opposite helicity of the parent proton ( $g_1(x) = q^+(x) - q^-(x)$ ). Common notations for the integrated helicity distributions for quarks are  $\Delta q(x) = g_1^q(x) = \int d^2\mathbf{k}_\perp g_1^q(x, k_\perp)$  and similarly for gluons.

The  $g_1^q(x)$ 's are not so well known as the corresponding  $f_1(x)$ , as they require polarized DIS, but have been measured by several experiments.

→  $h_1^q(x, k_\perp)$  is the **transversity distribution**. It is the analogue of the helicity distribution, for transverse nucleon spin. The integrated version has several notations in the literature

---

<sup>2</sup>Notice that in the TMD literature is often used a different notation in which, for instance,  $\Delta^N f_{q/p\uparrow}(x, k_\perp) = -(2k_\perp/M)f_{1T}^{\perp q}(x, k_\perp)$  [21].

$\Delta_{\perp}q(x) = h_1^q(x) = \int d^2\mathbf{k}_{\perp} h_1^q(x, k_{\perp})$  for quarks of flavor  $q$ , and in a transversity basis  $h_1(x) = q^{\uparrow}(x) - q^{\downarrow}(x)$ , where the arrows indicate the transverse spin of the quarks with respect to the direction of motion. For hadrons with spin 1/2, there is no transversity gluon distribution.

The unpolarized, the helicity and the transversity distribution are the only three independent TMD PDFs which survive in the collinear limit (integration over  $\mathbf{k}_{\perp}$ ). In particular, the transversity distribution is a chiral-odd function and needs to be coupled to another chiral-odd function to be observed, that is the Collins fragmentation function. In Sec. 1.3.2 the first extraction of the transversity PDF for  $u$  and  $d$  quarks, obtained by a combined fits of SIDIS and  $e^+e^-$  data, is discussed.

→  $f_{1T}^{a\perp}(x, k_{\perp})$  is the Sivers function [22] (chiral-even and naive T-odd function<sup>3</sup>), appearing in the distribution of unpolarized partons inside a transversely polarized proton. It links the parton intrinsic motion to the proton spin via a  $\mathbf{S} \cdot (\mathbf{P} \times \mathbf{k}_{\perp})$  term.

Its observation, already confirmed, is a clear indication of parton orbital motion; the opposite values for  $u$  and  $d$  quarks is argued to be linked to the nucleons' anomalous magnetic moments.

→  $h_1^{q\perp}(x, k_{\perp})$  is the Boer-Mulders function [23], appearing in the distribution of transversely polarized quarks  $q$  inside an unpolarized proton via a  $\mathbf{s}_q \cdot (\mathbf{P} \times \mathbf{k}_{\perp})$  term.

It is considered as the counterpart of the Sivers function  $f_{1T}^{\perp}$  and, like this, it is a naive T-odd function but chiral-odd. This implies that  $h_1^{q\perp}$ , in general, is harder to measure than  $f_{1T}^{\perp}$ .

→ The remaining three TMDs,  $g_{1T}^a(x, k_{\perp})$ ,  $h_{1L}^{q\perp}(x, k_{\perp})$  (worm-gear), and  $h_{1T}^{q\perp}(x, k_{\perp})$  (pretzelocity) are related to double spin correlation in the PDFs; respectively, the amount of longitudinally polarized partons in a transversely polarized proton, of transversely polarized quarks in a longitudinally polarized proton, and of transversely polarized quarks in a transversely (but in a different direction) polarized proton.

- $D_1^a(z, P_{\perp})$  is the unpolarized,  $P_{\perp}$  dependent, parton  $a$  Fragmentation Function (FF) into hadron  $h$ , and the integrated version  $D_{1h}^a(z) = \int d^2\mathbf{P}_{\perp} D_1^a(z, P_{\perp})$  is the usual FF [24, 25, 26].

- $H_1^{\perp q}(z, P_{\perp})$  is the Collins function [9], describing the fragmentation of a polarized quark into a spinless (or unpolarized) hadron  $h$ :

$$D_1^q(z, \mathbf{P}_{\perp}; \mathbf{s}_q) = D_1^q(z, P_{\perp}) + \frac{P_{\perp}}{zM_h} H_1^{\perp q}(z, P_{\perp}) \mathbf{s}_q \cdot (\mathbf{k}_q \times \mathbf{P}_{\perp}). \quad (1.3)$$

<sup>3</sup>This term is not related to real violation of T-invariance but, roughly speaking, is associated with a nontrivial phase at the amplitude level of a process.

The Collins effect has been observed by several experiments, and it is considered as a universal property of the quark hadronization process. In addition, its chiral-odd nature makes it the ideal partner to access chiral-odd TMD PDFs.

## 1.2 Semi Inclusive Deep Inelastic Scattering

Semi Inclusive Deep Inelastic Scattering (SIDIS) experiments allow to obtain information on all the leading-twist TMDs previously described. Figure 1.2(a) shows the diagram of the SIDIS process in which a lepton collides on a nucleon and a hadron, in addition to the scattered lepton, is observed in the final state.

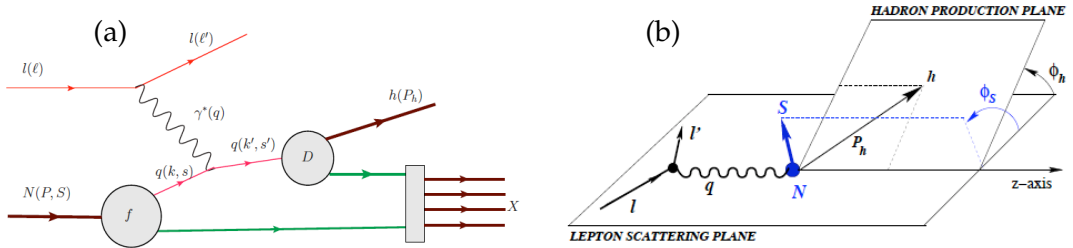


Figure 1.2: (a) SIDIS diagram. (b) Illustration of the kinematics, and definition of the azimuthal angles of SIDIS process in the target rest frame.  $\mathbf{P}_{hT}$  and  $\mathbf{S}_T$  are the transverse components of  $\mathbf{P}_h$  and  $\mathbf{S}$  with respect to the virtual photon momentum  $\mathbf{q}$

In the one-photon exchange approximation, the SIDIS cross section can be decomposed in terms of structure functions and, following the notation of [27], one has:

$$\begin{aligned} \frac{d\sigma}{dx dy dz d\phi_S d\phi_h d\mathbf{P}_{hT}^2} \propto & \left\{ F_{UU,T} + \epsilon F_{UU,L} + \sqrt{2\epsilon(1+\epsilon)} \cos\phi_h F_{UU}^{\cos\phi_h} \right. & (1.4) \\ & + \epsilon \cos(2\phi_h) F_{UU}^{\cos(2\phi_h)} + \lambda_e \sqrt{2\epsilon(1-\epsilon)} \sin\phi_h F_{LU}^{\sin\phi_h} \\ & + S_{||} \left[ \sqrt{2\epsilon(1+\epsilon)} \sin\phi_h F_{UL}^{\sin\phi_h} + \epsilon \sin(2\phi_h) F_{UL}^{\sin 2\phi_h} \right] \\ & + S_{||} \lambda_e \left[ \sqrt{1-\epsilon^2} F_{LL} + \sqrt{2\epsilon(1-\epsilon)} \cos\phi_h F_{LL}^{\cos\phi_h} \right] \\ & + |\mathbf{S}_{\perp}| \left[ \sin(\phi_h - \psi_S) (F_{UT,T}^{\sin(\phi_h - \psi_S)} + \epsilon F_{UT,L}^{\sin(\phi_h - \psi_S)}) \right. \\ & + \epsilon \sin(\phi_h + \phi_S) F_{UT}^{\sin(\phi_h + \phi_S)} + \epsilon \sin(3\phi_h - \phi_S) F_{UT}^{\sin(3\phi_h - \phi_S)} \\ & \left. + \sqrt{2\epsilon(1+\epsilon)} \sin\phi_S F_{UT}^{\sin\psi_S} + \sqrt{2\epsilon(1+\epsilon)} \sin(2\phi_h - \phi_S) F_{UT}^{\sin(2\phi_h - \phi_S)} \right] \\ & + |\mathbf{S}_{\perp}| \lambda_e \left[ \sqrt{1-\epsilon^2} \cos(\phi_h - \phi_S) F_{LT}^{\cos(\phi_h - \phi_S)} + \sqrt{2\epsilon(1-\epsilon)} \cos\psi_S F_{LT}^{\cos\phi_S} \right. \\ & \left. + \sqrt{2\epsilon(1-\epsilon)} \cos(2\phi_h - \phi_S) F_{LT}^{\cos(2\phi_h - \phi_S)} \right] \left. \right\}, \end{aligned}$$

where  $\epsilon$  is the degree of longitudinal polarization of the virtual photon,  $S_{||}$  denotes the longitudinal target polarization, and  $\lambda_e$  is the electron helicity. The structure functions  $F_{XY}$  (where

$X$  and  $Y$  refer to the electron and nucleon, respectively: U = unpolarized; L,T = longitudinally, transversely polarized) merely depend on  $x, z$ , and  $P_{hT}$ ; the third subscript  $F_{XY,T}$  specifies the polarization of the virtual photon, and the azimuthal angles are defined in Fig. 1.2(b). By choosing specific polarization states and weighting with the appropriate azimuthal dependence, one can extract every structure function in Eq. (1.4).

For TMD studies one is interested in the kinematical region defined by

$$P_{hT} \simeq \Lambda_{QCD} \ll Q,$$

for which the structure functions can be written as a convolution of TMDs. For this reason, measuring the structure functions in Eq. (1.4) allows to obtain information on all eight leading quark TMDs. In particular, for a spinless final state hadron, one has [27, 28]:

$$F_{UU} \sim \sum_q e_q^2 f_1^q \otimes D_1^q \quad F_{LT}^{\cos(\phi-\phi_S)} \sim \sum_q e_q^2 g_{1T}^q \otimes D_1^q \quad (1.5)$$

$$F_{LL} \sim \sum_q e_q^2 g_{1L}^q \otimes D_1^q \quad F_{UT}^{\sin(\phi-\phi_S)} \sim \sum_q e_q^2 f_{1T}^{\perp q} \otimes D_1^q \quad (1.6)$$

$$F_{UU}^{\cos(2\phi)} \sim \sum_q e_q^2 h_1^{\perp q} \otimes H_1^{\perp q} \quad F_{UT}^{\sin(\phi+\phi_S)} \sim \sum_q e_q^2 h_1^q \otimes H_1^{\perp q} \quad (1.7)$$

$$F_{UL}^{\sin(2\phi)} \sim \sum_q e_q^2 h_{1L}^{\perp q} \otimes H_1^{\perp q} \quad F_{UT}^{\sin(3\phi-\phi_S)} \sim \sum_q e_q^2 h_{1T}^{\perp q} \otimes H_1^{\perp q} \quad (1.8)$$

where  $e_q$  is the charge of the struck quark in units of the elementary charge (the factorized expressions for the structure functions in the above equations hold in this form in the parton model approximation). Notice that the four chiral-even TMDs couple to the well known unpolarized fragmentation function  $D_1$ , while the chiral-odd TMDs couple to the chiral-odd Collins function  $H_1^\perp$ . The accurate knowledge of the Collins function, therefore, is important in order to extract information about the chiral-odd TMDs, like the transversity distribution (or Boer-Mulders function).

In the next Section the first extraction of the transversity PDFs, made possible by the measurement of the Collins FF from  $e^+e^-$  annihilation data, is briefly described. The same procedure can be applied to all chiral-odd TMDs, taking care of the appropriate azimuthal amplitude in SIDIS.

### 1.3 Transversity distribution

At leading twist, three collinear distribution functions are needed to describe the quark distribution in the nucleon:  $f_1$ ,  $g_1$ , and  $h_1$ . An important difference between transversity  $h_1$  and  $g_1$

is that in spin-1/2 hadron there is no gluonic function analogous to transversity. The most important consequence is that  $h_1^q$  for a quark of flavor  $q$  does not mix with gluons in its evolution and it behaves as a non-singlet quantity.

In addition, a good knowledge of the transversity distributions  $h_1$  for quarks and antiquarks would allow computation of the tensor charge, given by  $\int_0^1 dx [h_1^q(x) - h_1^{\bar{q}}(x)]$ , a non perturbative quantity for which lattice and model computations exist.

For these reasons, the extraction of transversity is of fundamental interest for obtaining a complete description of the nucleon structure even for the case when the transverse momenta is integrated over.

### 1.3.1 The Collins effects

To measure transversity there are essentially two options: single or double transverse spin asymmetries in  $ep$  or  $pp$  processes.

The most promising approach is the latter from the study of double transverse spin asymmetries  $A_{TT}$  in Drell-Yan process of two colliding hadrons transversely polarized. This measurement is feasible, for instance, at RICH ( $\sqrt{s} = 200$  GeV), with  $A_{TT}$  proportional to the product of the two transversity distributions, one for the quark and one for the antiquark (sea quark). This means that the  $A_{TT}$  values are very small, of the order of few percent or less [29]. A much larger  $A_{TT}$ , around 20-40%, could be observed in Drell-Yan processes in  $p\bar{p}$  interaction at  $\sqrt{s} = 200$  GeV, as proposed by the PAX Collaboration [30]. However, this requires the availability of polarized antiprotons with high efficiency which will be a formidable challenge for the future.

Presently, the most accessible channel to measure the transversity distribution is the azimuthal asymmetry  $A_{UT}^{\sin(\phi_h + \phi_S)}$  in Semi Inclusive Deep Inelastic Scattering (SIDIS) processes<sup>4</sup> ( $lp^\uparrow \rightarrow lhX$ , see Fig. 1.2) in which one or more final state hadrons are detected together with the scattered lepton. As discussed in section 1.2, at tree level and leading-twist, the SIDIS  $F_{UT}^{\sin(\phi_h + \phi_S)}$  structure function can be described as a convolution between the transversity  $h_{1T}^q$  and the Collins fragmentation function  $H_1^\perp$ :

$$F_{UT}^{\sin(\phi_h + \phi_S)} \sim \sum_q e_q^2 h_1^q \otimes H_1^{\perp q}. \quad (1.9)$$

In order to project out  $F_{UT}^{\sin(\phi_h + \phi_S)}$ , the so called Collins amplitude  $2\langle \sin(\phi_h + \phi_S) \rangle_{UT}^h$  for a specific hadron  $h$  is extracted by measuring the asymmetry:

$$A_{UT}^{\sin(\phi_h + \phi_S)} \propto \frac{d\sigma_\uparrow(\phi_h, \phi_S) - d\sigma_\downarrow(\phi_h, \phi_S)}{d\sigma_\uparrow(\phi_h, \phi_S) + d\sigma_\downarrow(\phi_h, \phi_S)} \quad (1.10)$$

<sup>4</sup>The subscript  $U$  indicates an unpolarized lepton beam, and  $T$  a transversely polarized target nucleon.

where the up and down arrows indicate two opposite transverse spin states, and the azimuthal angles are illustrated in Fig. 1.2(b). This amplitude has so far been extracted by HERMES [10, 31] and COMPASS Collaborations [11, 32, 33], and a selection of results are shown in Fig. 1.3.

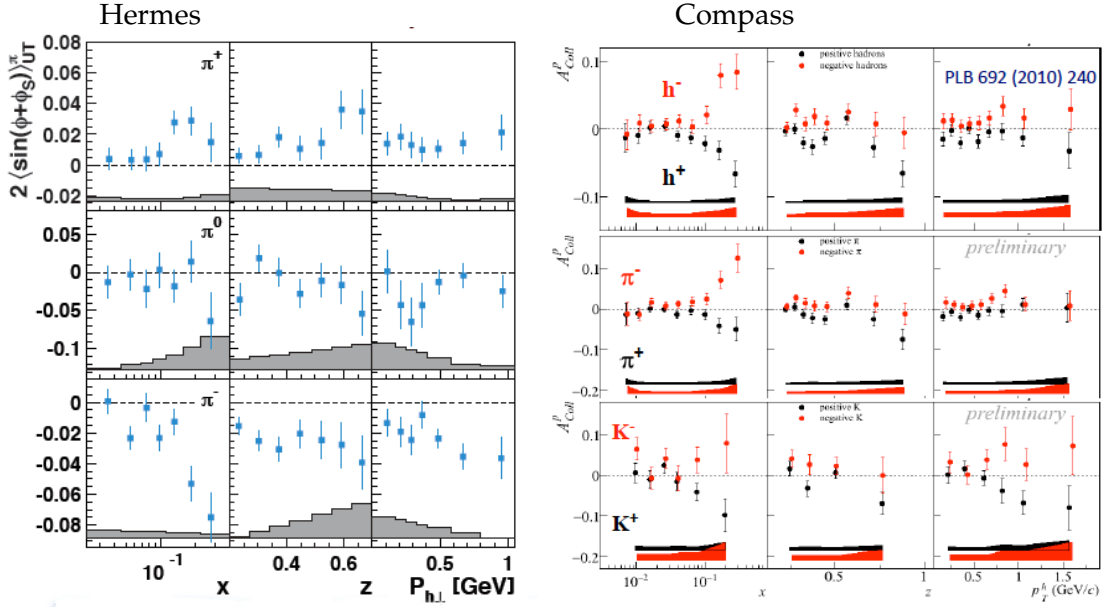


Figure 1.3: Hermers and Compass results on Collins amplitude.

For the second unknown function in Eq.1.9, the Collins FF, model calculations are available [34, 35, 36]. However, for a model independent extraction of transversity from SIDIS asymmetry amplitudes it is necessary to determine the Collins function from an independent source, like the *measurement of azimuthal asymmetries in the distribution of back-to-back pions in two jet events in  $e^+e^-$  annihilations* [37] ( $e^+e^- \rightarrow \pi^+\pi^-X$ ), which is the subject of this dissertation. The reference frame, the angles involved in  $e^+e^-$  annihilation, and the procedure for extracting the asymmetry are described in detail in Chapter 4. Here, we report the results of the first measurements of this spin-dependent fragmentation function as a function of pions fractional energies  $z$  (Fig. 1.4), which have been performed by the BELLE Collaboration [14, 15]. Experimentally, double ratios of asymmetries for like-sign (L), unlike-sign (U), and any charged (C) pion pairs are built in order to cancel contributions from experimental acceptance and radiative effects. The resulting asymmetries,  $A^{UL}$  and  $A^{UC}$ , are then sensitive to different combinations of favored and disfavored fragmentation functions as given in [15] and shown in section 4.4.

The experimental results shown in Fig. 1.3 and 1.4 are striking. First, they clearly demonstrate that the Collins effect as a manifestation of chiral-odd and naive T-odd mechanisms is different from zero and not suppressed, both in SIDIS and in  $e^+e^-$  annihilation. Second, the results for oppositely charged pions (hadrons) in Fig. 1.3 suggest a very peculiar feature of the Collins FF. As scattering off  $u$  quarks dominates these data due to the charge factor, the large

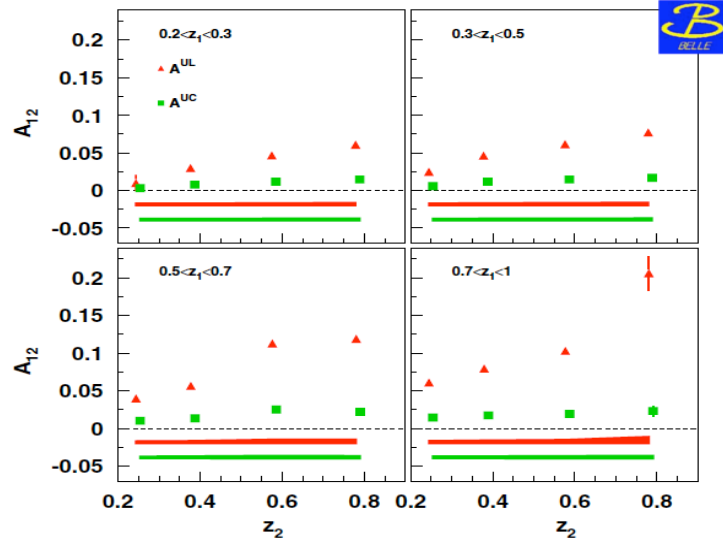


Figure 1.4: Collins asymmetry  $A_{12}$  for the double ratios for like-sign (L), unlike-sign (U), and any charged (C) pion pairs as a function of the fractional energies of the two pions,  $z_1$  and  $z_2$  [15].

magnitude of  $\pi^-$  ( $\bar{u}d$ ) amplitudes being of similar size than the  $\pi^+$  ( $u\bar{d}$ ) ones but having opposite sign, can only be understood if the *disfavored* Collins function ( $H_1^{\perp dif}$ ) is large and opposite in sign to the *favored* one. Opposite signs for favored and disfavored Collins functions are also supported by the different size of the  $A^{UL}$  and  $A^{UC}$  asymmetries from Belle, shown in Fig. 1.4, and from our results reported in chapter 6.

### 1.3.2 Phenomenological extraction of transversity function

A combined fit of SIDIS asymmetries together with  $e^+e^-$  data allows the simultaneous extraction of the transversity distribution and the Collins FF. The first global analysis has been performed by M. Anselmino and Collaborators in references [16, 17]. In order to resolve the convolution in Eq. 1.9, a Gaussian dependence on the intrinsic transverse momentum is used:

$$f_1^q(x, k_\perp^2) = f_1^q(x) \frac{1}{\pi \langle k_\perp^2 \rangle} \exp\left(-\frac{\mathbf{k}_\perp^2}{\langle k_\perp^2 \rangle}\right), \quad (1.11)$$

$$D_1^q(z, p_\perp^2) = D_1^q(z) \frac{1}{\pi \langle p_\perp^2 \rangle} \exp\left(-\frac{\mathbf{p}_\perp^2}{\langle p_\perp^2 \rangle}\right) \quad (1.12)$$

where  $f_1(x)$  and  $D_1(z)$  are the usual integrated parton distribution and fragmentation function, available in literature, and  $\mathbf{p}_\perp = \mathbf{P}_T - z\mathbf{k}_\perp$  is the transverse momentum of the observed hadron  $h$  with respect to the direction of the fragmenting quark. The transversity and Collins FF, instead, are unknown, and the following parametrizations are adopted:

$$h_1^q(x, k_\perp) = \frac{1}{2} \mathcal{N}_q^T(x) [f_1^q(x) + g_1^q(x)] \frac{1}{\pi \langle k_\perp^2 \rangle} \exp\left(-\frac{\mathbf{k}_\perp^2}{\langle k_\perp^2 \rangle}\right) \quad (1.13)$$

$$H_1^{\perp q}(z, p_{\perp}) = 2\mathcal{N}_q^C(z)D_1^q(z)h(p_{\perp})\frac{1}{\pi\langle p_{\perp}^2 \rangle}\exp\left(-\frac{\mathbf{p}_{\perp}^2}{\langle p_{\perp}^2 \rangle}\right) \quad (1.14)$$

where the functions  $\mathcal{N}_q^T(x)$ ,  $\mathcal{N}_q^C(z)$ , and  $h(p_{\perp})$  are defined in reference [16].<sup>5</sup>

The results of the global fit analysis for the transversity function and Collins FF are reported in Fig. 1.5. In particular, the transversity distribution for  $u$  and  $d$  quarks are plotted in Fig. 1.5(a), where the shaded area corresponds to the uncertainty in the parameter values. Similarly, the Collins functions (favored and disfavored) are plotted as a function of  $z$  and  $p_{\perp}$  in Fig. 1.5(b), which confirm the feature discussed in section 1.3.1

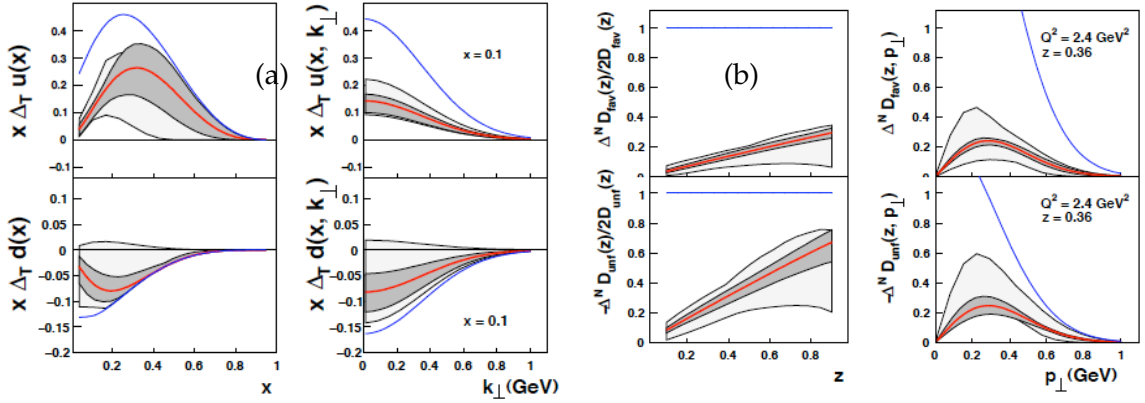


Figure 1.5: (a) Transversity distribution functions (red lines) for  $u$  and  $d$  quarks as determined through the global analysis (HERMES, COMPASS, and BELLE data). In the left plots as a function of  $x$ , and in the right plots the unintegrated distribution as a function of  $k_{\perp}$  at a fixed value of  $x$ . The Soffer bound [38] is also shown (blue line), the shaded area is the error band due to the uncertainty in the determination of the free parameters, and the wider band is the uncertainty obtained in the first extraction in Ref [16].

(b) Favored and disfavored Collins FF as determined through the global fit (red lines). In the left plots, the  $z$  dependence of the  $p_{\perp}$  integrated Collins function and normalized to the twice corresponding unpolarized fragmentation function are shown. In the right plots, the  $p_{\perp}$  dependence of the Collins function at fixed value of  $z$  are shown. The  $Q^2$  value is  $2.4 \text{ GeV}^2$  with the assumption that the Collins FF  $Q^2$  evolution is the same as for the  $D$  evolution. The positivity bound [25] (upper line), the uncertainty region, and the uncertainty obtained in Ref [16] are also shown. Note that in this thesis we refer to the transversity function as  $h_1^q$  instead that  $\Delta_{Tq}$ , and to the Collins function as  $H_1^{\perp}$  instead that  $\Delta^N D$ .

<sup>5</sup> $\mathcal{N}_q^T(x) = N_q^T x^{\alpha}(1-x)^{\beta} \frac{(\alpha+\beta)^{\alpha+\beta}}{\alpha^{\alpha}\beta^{\beta}}$ ,  $\mathcal{N}_q^C(z) = N_q^C z^{\gamma}(1-z)^{\delta} \frac{(\gamma+\delta)^{\gamma+\delta}}{\gamma^{\gamma}\delta^{\delta}}$ ,  $h(p_{\perp}) = \sqrt{2}e^{-\frac{p_{\perp}^2}{M_h^2}}$ , and  $|N_q^T|, |N_q^C| \leq 1$ . The coefficients  $N_q^T$  and  $N_q^C$  depend on the quark flavor ( $q = u, d$ ), while all the exponents  $\alpha, \beta, \gamma, \delta$ , and the dimensional parameter  $M$  are taken flavor independent. All these parameters are extracted by the fit.

### 1.3.3 Dihadron fragmentation function

A complementary approach to transversity is provided by semi-inclusive two hadron production,  $ep^\uparrow \rightarrow e'(h_1 h_2)X$ , where the two unpolarized hadrons with momenta  $P_1$  and  $P_2$  emerge from the fragmentation of the struck quark. This mechanism differs from the Collins mechanism in that the transverse spin of the fragmenting quark is transferred to the relative orbital angular momentum of the hadron pair. In addition, by detecting a second hadron, the sensitivity to the quark spin survives integration over transverse momenta. Thus, unlike the Collins effects, collinear models can be used for factorization and the QCD evolution of the fragmentation function is known [39, 40].

The kinematics is similar to the one in single-hadron SIDIS except for the final hadronic state, where now  $z = z_1 + z_2$  is the fractional energy carried by the hadron pair, and vectors  $\mathbf{P}_h = \mathbf{P}_1 + \mathbf{P}_2$  and  $\mathbf{R} = (\mathbf{P}_1 - \mathbf{P}_2)/2$  (see also Fig. 1.6) are introduced, together with the invariant mass  $M_h$  of the pair, which must be considered smaller than the hard scale ( $P_h^2 = M_h^2 \ll Q^2$ ).

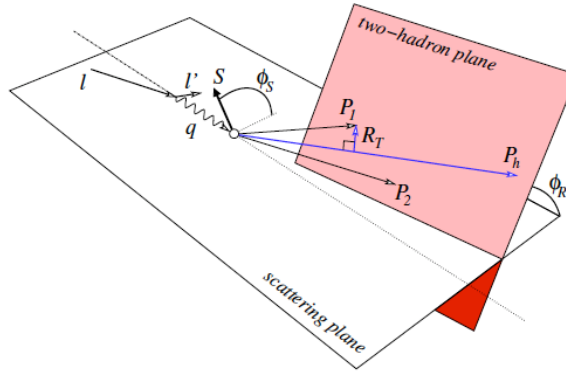


Figure 1.6: Kinematic of the production of two hadrons in SIDIS processes.

In analogy with the Collins function, the expression for unpolarized hadrons ( $h_1, h_2$ ) produced by a transversely polarized quark reads:

$$D_{h_1 h_2 / q^\uparrow}(z, M_h^2, \mathbf{R}_T) = D_1^q(z, M_h^2) - H_1^{\triangleleft q}(z, M_h^2) \frac{\mathbf{S}_{\perp q} \cdot (\hat{\mathbf{p}} \times \mathbf{R}_T)}{M_h}, \quad (1.15)$$

where  $\mathbf{R}_T$  is the component of  $\mathbf{R}$  transverse to  $\mathbf{P}_h$ .

The relevant asymmetry that should be measured in SIDIS is

$$A_{UT}^{\sin(\phi_R + \phi_S) \sin(\theta)} \propto h_1^q(x) \times H_1^{\triangleleft q}(z, M_h^2), \quad (1.16)$$

where  $\theta$  is the angle between  $P_1$  and  $P_2$  in the two hadron center of mass frame, and  $H_1^{\triangleleft}$  is the Interference Fragmentation Function (IFF, chiral-odd function like Collins FF).

As in the single-hadron production case, transversity can be extracted from the asymmetry (1.16) only if the unknown  $H_1^{\triangleleft}$  is independently determined from  $e^+e^-$  annihilation. In this case, two hadron pairs produced in opposite jets are considered:  $e^+e^- \rightarrow$

$(\pi^+\pi^-)_{jet1} (\pi^+\pi^-)_{jet2} X$ , with kinematics depicted in Fig. 1.7 (see also reference [41] for a detailed description).

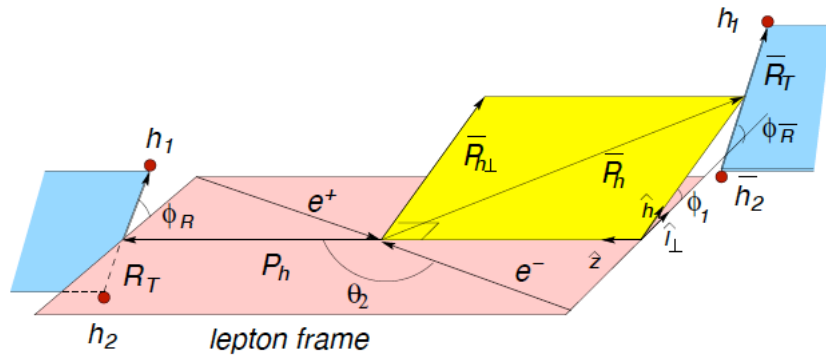


Figure 1.7: Kinematic for the  $e^+e^- \rightarrow (h_1h_2)_{jet1}(\bar{h}_1\bar{h}_2)_{jet2}X$

In this reaction, the orientation of the two hadrons with respect to each other and to the jet direction is an indicator of the transverse spin direction of the quark. Such a correlation is expected to occur due to the strong final state interaction between the two hadrons: different partial waves can interfere and this is expected to give rise to non-vanishing two-hadron IFFs. The leading-twist cross section of this process contains many terms [41], among which there is one involving the product of  $H_1^{\leftarrow}$  for the quark  $q$  and of  $\bar{H}_1^{\leftarrow}$  for the  $\bar{q}$ , weighted by  $\cos(\phi_{\mathbf{R}} + \phi_{\bar{\mathbf{R}}})$ . Thus, this contribution can be extracted by defining the so-called Artru-Collins azimuthal asymmetry [41, 42]:

$$A^{\cos(\phi_{\mathbf{R}}+\phi_{\bar{\mathbf{R}}})}(z, M_h^2, \bar{z}, \bar{M}_h^2) \propto \frac{\sin^2 \theta_2}{1 + \cos^2 \theta_2} \frac{|\mathbf{R}| |\bar{\mathbf{R}}|}{M_h \bar{M}_h} \frac{\sum_q e_q^2 H_1^{\leftarrow q}(z, M_h^2) \bar{H}_1^{\leftarrow q}(\bar{z}, \bar{M}_h^2)}{\sum_q e_q^2 D_1^q(z, M_h^2) \bar{D}_1^q(\bar{z}, \bar{M}_h^2)}, \quad (1.17)$$

where the di-hadron fragmentation function  $D_1^q$  and  $H_1^{\leftarrow q}$  are the same universal functions appearing in the SIDIS asymmetry equation (1.16).

The first measurements of  $A_{UT}^{\sin(\phi_R+\phi_S)\sin(\theta)}$  was performed by the HERMES Collaboration [43], which gave evidence of a non-zero IFF. Preliminary SIDIS data are also available from the COMPASS Collaboration [44, 45] using transversely polarized deuteron and hydrogen targets. In addition, results from measurements of the  $A^{\cos(\phi_R+\phi_{\bar{R}})}$  asymmetry have been recently published by the BELLE Collaboration in Ref. [46].

## 1.4 Summary

As shown in this Chapter, the extraction of the Collins FF ( $H_1^{\perp q}$ ) is a fundamental tool in order to have a complete description of the quarks distribution inside the nucleon. In fact, it allows the extraction of the transversity distribution function ( $h_1^q$ ), which is the least known leading-twist

---

PDF due to its chiral-odd nature. Since only chiral-even objects are observable, the transversity function is always coupled with another chiral-odd function like the Collins FF, as explained in section 1.2. The first measurement of transversity and Collins FF were obtained by Anselmino and collaborators in reference [16, 17] and briefly described in section 1.3.2. Given the complexity of the subject, an independent measurement of the Collins asymmetries by *BABAR*, as described in this dissertation, is advisable in order to both confirm the Belle results and improve the precision of the global fit. To achieve this result, I studied the process  $e^+e^- \rightarrow \pi\pi X$  with charged pion pairs detected in opposite jets. The analysis strategy, systematics checks, and results are discussed in the following chapters.



## Chapter 2

# Fragmentation Functions in $e^+e^-$ annihilation

### 2.1 Introduction

The term “*Fragmentation Functions*” (FFs) is widely used to describe the energy distribution of final-state particles in hard processes [47]. In unpolarized semi-inclusive  $e^+e^-$  annihilation, the cross section at the center-of-mass (CM) energy  $\sqrt{s} = Q$  via an intermediate photon or  $Z$ -boson is given by

$$\frac{1}{\sigma_0} \frac{d^2\sigma^h(e^+e^- \rightarrow \gamma/Z \rightarrow h + X)}{dz d\cos\theta} = \frac{3}{8}(1 + \cos^2\theta)F_T^h + \frac{3}{4}\sin^2\theta F_L^h + \frac{3}{4}\cos\theta F_A^h. \quad (2.1)$$

In this formula,  $z = 2E_h/\sqrt{s}$  is the scaled energy of the hadron  $h$ , and  $\theta$  is the angle relative to the electron beam in the CM frame. The transverse and longitudinal FFs,  $F_T$  and  $F_L$ , represent the contributions from  $\gamma/Z$  polarizations transverse or longitudinal with respect to the direction of motion of the hadron. The parity-violating term with the asymmetric FF  $F_A$  arises from the interference between vector and axial-vector contributions. The normalization factors  $\sigma_0$  used in the literature range from the total cross section  $\sigma_{tot}$  for  $e^+e^- \rightarrow hadrons$  (including all weak and QCD contributions) to  $\sigma_0 = 4\pi\alpha^2 N_c/3s$ ,<sup>1</sup> with  $N_c = 3$ .

Integration of Eq. (2.1) over  $\theta$  yields the total fragmentation function  $F^h = F_T^h + F_L^h$

$$\frac{1}{\sigma_0} \frac{d\sigma^h}{dz} = F^h(z, s) = \sum_i \int_z^1 \frac{dx}{x} C_i(x, \alpha_s(\mu), \frac{s}{\mu^2}) D_i^h(\frac{z}{x}, \mu^2) + \mathcal{O}(\frac{1}{\sqrt{s}}), \quad (2.2)$$

where  $\mu^2$  is the factorization scale,  $i = u, \bar{u}, d, \bar{d}, \dots, g$ ,  $C_i$  are coefficient functions calculated in perturbative QCD,  $D_i^h$  are the parton FFs<sup>2</sup>, and  $\alpha_s$  is the running coupling constant, whose dependence from  $Q^2$  is:

$$\alpha_s(\sqrt{Q^2}) = \frac{12\pi}{(33 - 2N_f) \ln(Q^2/\Lambda^2)}, \quad (2.3)$$

<sup>1</sup>The lowest order QED cross section for  $e^+e^- \rightarrow \mu^+\mu^-$  times the number of colors  $N_c$ .

<sup>2</sup>These functions are the final state analogue to the initial state parton distribution functions (PDFs).

with  $N_f$  the number of quark flavors, and  $\Lambda$  the QCD scale parameter<sup>3</sup>.

The function  $D_i^h(z, \mu^2)$  indicates the probability to find a hadron  $h$  with the energy fraction  $z$ , coming from the fragmentation of parton  $i$ . Beyond the leading order (LO) of perturbative QCD, these universal functions depend on the factorization scheme, with ‘reasonable’ scheme choices retaining certain quark-parton-model constraints such as the momentum sum rule

$$\sum_h \int_0^1 dz z D_i^h(z, \mu^2) = 1. \quad (2.4)$$

The simpler parton model approach would predict scale-independent distributions (‘scaling’) for both the FF  $F^h$  and the parton FF  $D_i^h$ . Perturbative QCD corrections lead to logarithmic scaling violation equations (Dokshitzer-Gribov-Lipatov-Altarelli-Parisi, DGLAP) [48, 49, 50]

$$\frac{\delta}{\delta \ln \mu^2} D_i(z, \mu^2) = \sum_j \int_z^1 \frac{dx}{x} P_{ji}(x, \alpha_s(\mu^2)) D_j\left(\frac{z}{x}, \mu^2\right), \quad (2.5)$$

where  $P_{ji}$  is the splitting function which describes the parton splitting  $j \rightarrow i$  and which can be given also as a power series in  $\alpha_s$ . The effect of the evolution is shown in Fig. 2.1: as the scale increases, one observes a scaling violation in which the  $x$ -distribution is shifted toward lower values.

Measurements of fragmentation in lepton-hadron and hadron-hadron scattering are complementary to those in  $e^+e^-$  annihilation. The latter provides a clean environment (no initial-state hadron remnant) and stringent constraints on the combinations  $D_q^h + D_{\bar{q}}^h$ . However,  $e^+e^-$  annihilation is far less sensitive to  $D_g^h$  and insensitive to the charge asymmetries  $D_q^h - D_{\bar{q}}^h$ . These quantities are best constrained in proton-(anti)proton and electro-proton scattering, respectively.

Moreover, unlike  $e^+e^-$  annihilation where  $q^2 = s$  is fixed by the collider energy, lepton-hadron scattering has two independent scales,  $Q^2 = -q^2$  and the invariant mass  $W^2$  of the hadronic final state, which both can vary by several orders of magnitudes for a given CM energy, thus allowing the study of fragmentation in different environments by a single experiment. In DIS ( $Q^2 \gg 1 \text{ GeV}^2$ ), using the quark-parton-model (QPM), the hadronic fragments of the struck quark can be directly compared with the quark fragmentation in  $e^+e^-$  in a suitable frame (Breit frame [52]<sup>4</sup>).

The comparison of scaling violation in DIS and  $e^+e^-$  experiments shows a general agreement, as can be seen in Fig. 2.2. However, processes in DIS which are not present in  $e^+e^-$  annihilation, such as boson-gluon fusion and initial state QCD radiation, can depopulate the current region of Breit frame. These effects become more prominent at low values of  $Q$  and  $x$ . Hence, when compared with  $e^+e^-$  data at  $\sqrt{s} = 5.2, 6.5 \text{ GeV}$  [53] (not shown here) the DIS particle rates tend to lie below those from  $e^+e^-$  annihilation.

<sup>3</sup> $\Lambda \sim 200 \text{ MeV}$  represents the energy at which  $\alpha_s$  becomes large and perturbative QCD is not longer valid.

<sup>4</sup>The Breit frame is defined as the frame in which the exchanged boson is completely space-like.

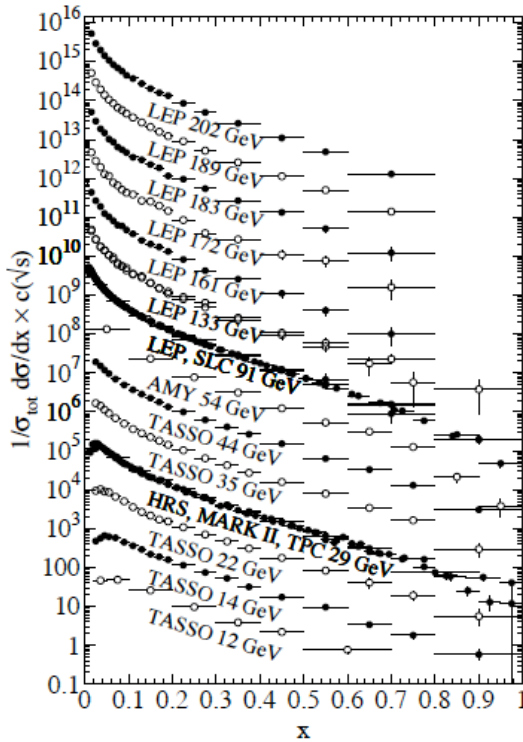


Figure 2.1: Fragmentation function in  $e^+e^-$  annihilation for all charged particles and for different center of mass energies versus  $x = 2E^h/\sqrt{s}$  [51].

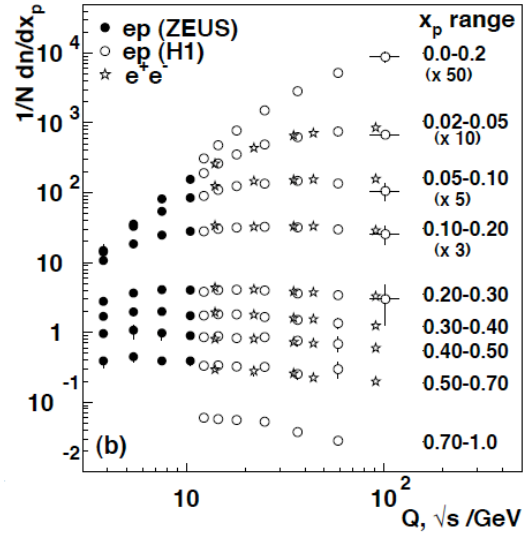


Figure 2.2: Scaling violations of the FF for all charged particles in the current region of Breit frame of DIS and  $e^+e^-$  annihilation [51]. The data are shown as a function of  $\sqrt{s}$  for  $e^+e^-$  results, and as a function of  $Q$  for DIS results.

## 2.2 Fragmentation models

Although the scaling violation can be calculated perturbatively, the parton fragmentation functions are non-perturbative objects. Perturbative evolution gives rise to a shower of quarks and gluons (partons). Phenomenological hadronization (or fragmentation) models are then used to model the carry-over parton momenta and flavor of the hadrons. These models, implemented in the Monte Carlo event generation programs, can be grouped in three classes: independent fragmentation, string fragmentation, and cluster fragmentation, briefly summarized below.

### 2.2.1 Independent fragmentation

Historically, one of the first fragmentation models was the independent fragmentation model of Feynman and Field [54]. In this model, the original quark and antiquark each transform into a jet of hadrons, independently of each other.

Fig. 2.3 illustrates the creation of a jet by independent fragmentation from a quark  $q_0$  created in the process  $e^+e^- \rightarrow q_0\bar{q}_0$ . First, a quark pair  $q_1\bar{q}_1$  is created from the vacuum.  $\bar{q}_1$  and  $q_0$  combine to form a meson, leaving behind  $q_1$ , which has less energy than  $q_0$ . Then, another pair

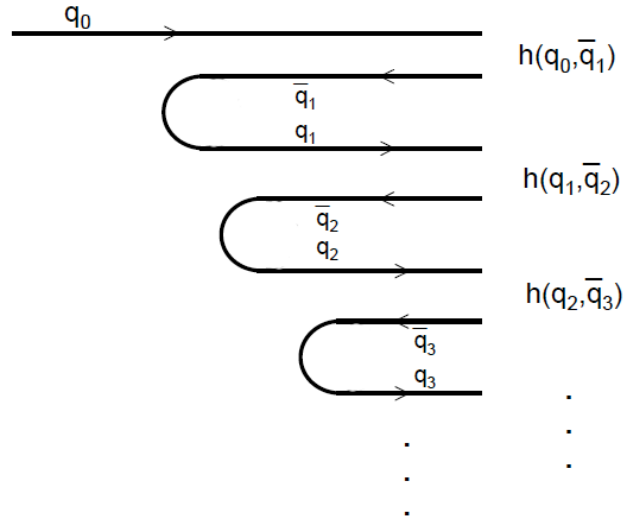


Figure 2.3: Schematic view of the independent fragmentation process into mesons for a jet originated by the quark  $q_0$ .

$q_2\bar{q}_2$  is created, and  $q_1$  and  $\bar{q}_2$  bind together to form another meson, leaving behind  $q_2$  with still less energy. This process repeats itself until the remaining quark has too little energy to form a meson. The same kind of iterative process produces a second jet from  $\bar{q}_0$ .

In this model it is assumed that the quarks and antiquarks created from the vacuum have a transverse momentum that is distributed as a Gaussian with an experimentally determined width  $\sigma_q$ , and that the total transverse momentum of each pair is zero. Another experimentally measured parameter determines the fraction of vector mesons (the remainder being pseudoscalar mesons). A third parameter determines the probability that the created  $q\bar{q}$  pairs are  $s\bar{s}$  or  $w\bar{w}$ ,  $d\bar{d}$ . Another feature of this model is a fragmentation function  $f(z)$ , which is the probability density, at each step in the fragmentation chain, that a fraction  $z$  of the momentum of a quark  $q_i$  goes into the meson  $h_i$ . Its parameterization is

$$f(z) = 1 - a - 3a(1 - z)^2, \quad (2.6)$$

where  $a$  is determined from experiment.

The original Feynman-Field model did not include baryon production and gluon jets, which are introduced by Meyer in reference [55]. However, it has a number of theoretical problems that makes it difficult to use.

### 2.2.2 String fragmentation

The string-fragmentation scheme considers the color field between the partons to be the fragmenting entity rather than the partons themselves. The popular implementation of this model

is the Lund model [56], implemented in the JETSET [57], PYTHIA [58], and UCLA [59] Monte Carlo event generation programs.

The color force fields are modeled by the massless relativistic string with color  $3(q)$  and  $\bar{3}(\bar{q})$  at the endpoints (the gluons ( $g$ , 8 colors) are treated as internal excitations on the string field). The string is uniform along its length; this means that there is a constant force field ( $\mathcal{K} \simeq 1$  GeV/fm) spanned between the original pair. This pair is produced at the origin  $O$ , as shown in Fig. 2.4, and afterwards the  $q_0\bar{q}_0$  are moving apart along the  $x$ -axis.

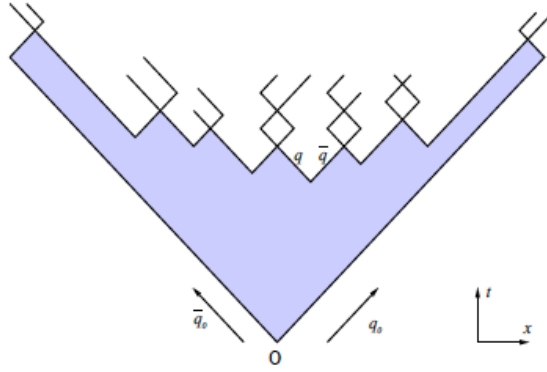


Figure 2.4: String fragmentation and meson production in  $t - x$  space.

When the energy stored in the string is sufficient, a  $q\bar{q}$  pair may be created from the vacuum. Thus, the string breaks up repeatedly into color singlet systems as long as the invariant mass of the string pieces exceeds the on-shell mass of the hadron.

The creation of a quark-antiquark pair at a point violates the energy conservation if the quarks have mass or transverse momentum. Thus, the  $q\bar{q}$  pairs are created according to the probability of tunneling processes

$$P \propto \exp\left(\frac{-\pi m_{q\perp}^2}{\mathcal{K}}\right) \quad (2.7)$$

which depends on the transverse mass squared  $m_{q\perp}^2 \equiv \sqrt{m_q^2 + p_{q\perp}^2}$  and the string tension  $\mathcal{K}$ . The transverse momentum  $p_{q\perp}$  is locally compensated between quark and antiquark. Due to the dependence of the parton mass,  $m_q$ , and/or hadron mass,  $m_h$ , the production of strange and, in particular, heavy-quark hadrons is suppressed.

The longitudinal momenta  $p_l$  of the hadrons are determined by a string fragmentation function, which is a function of the light-cone variable  $E + p_l$ . The first hadron at the end of the string takes a fraction  $z_1$  of the total  $(E + p)_q$  of the entire string:  $(E + p)_1 = z_1(E + p)_q$ . The next hadron created takes another fraction  $z_2$  of the remaining available  $(E + p)_q$  of the unfragmented string system.

An important feature of this model is the requirement that, on average, the fragmentation starting from one end of the string is the same as the fragmentation starting from the other end of the string. This is given by the *Lund Symmetric fragmentation function* [60]

$$f(z) \sim \frac{1}{z}(1-z)^\alpha \exp\left(\frac{-bm_{h\perp}^2}{z}\right), \quad (2.8)$$

where  $a$  and  $b$  are free parameters. These parameters need to be adjusted to bring the fragmentation into accordance with experimental data.

### 2.2.3 Cluster fragmentation

The third class of fragmentation models used in high energy physics are the cluster fragmentation models, implemented in HERWIG [61] and SHERPA [62] Monte Carlo event generators. In this approach, a leading logarithm parton shower is generated and the evolution of the shower stops when the parton virtuality  $Q$  falls below the cutoff  $Q_0$  ( $Q_0 < 1$  GeV). At this point all gluons are split into  $q\bar{q}$  pairs, and adjacent quarks and antiquarks are formed into color-neutral clusters [63]. The cluster thus formed are fragmented into hadrons. If a cluster is too light to decay into two hadrons, it is taken to represent the lightest single hadron of its flavor. Its mass is shifted to the appropriate value by an exchange of 4-momentum with a neighboring cluster in jet. A decay channel is chosen based on phase-space probability, the density of states, and the spin degeneracy of the hadrons.

Cluster fragmentation has a compact description with few parameters, due to the phase space dominance in the hadron formation.

## 2.3 Theoretical aspects of Collins Fragmentation Function in $e^+e^-$ annihilation

After the brief introduction about the physics scenario and the usefulness of the measurement of the Collins asymmetry described so far, in the following sections we summarize the theoretical formalism of the inclusive two-hadrons production in  $e^+e^-$  annihilation up to order  $1/Q$ , where the two hadrons belong to different, back-to-back jets ( $e^+e^- \rightarrow h_1h_2X$ ).

### 2.3.1 General angular dependence

We consider the process  $e^+e^- \rightarrow h_1h_2X$ , where the two leptons annihilate into a photon (or  $Z$  boson) with 4-momentum  $q = l + l'$  ( $l$  and  $l'$  are the electron and positron momenta, respectively). The photon momentum sets the scale  $Q$  ( $Q^2 \equiv q^2$ ) which is much larger than the characteristic hadronic scale. Denoting the momentum of the outgoing hadrons by  $P_h$ , with  $h = 1, 2$ , we define the invariants  $z_h = 2P_h \cdot q/Q^2$  which are analogous to the Bjorken variable.

Note that  $z_h$  are the fractions of the beam energy carried by the hadrons in the  $e^+e^-$  center of mass system, and they obey the following constraint:

$$z_1 < 1, \quad z_2 < 1. \quad (2.9)$$

In the case of unpolarized leptons and hadrons, and two-jet event topology, the normalized differential cross section for the process  $e^+e^- \rightarrow h_1 h_2 X$ , where the two hadrons belong to opposite jets, can be written as:

$$\begin{aligned} \frac{dN}{d\Omega} \equiv \left( \frac{d\sigma}{dz_1 dz_2 d^2\mathbf{q}_T} \right)^{-1} \frac{d\sigma}{dz_1 dz_2 d\Omega d^2\mathbf{q}_T} = & F_1(1 + \cos^2 \theta) + F_2(1 - 3 \cos^2 \theta) + F_3 \cos \theta \quad (2.10) \\ & + F_4 \sin 2\theta \cos \phi + F_5 \sin^2 \theta \cos 2\phi + F_6 \sin \theta \cos \phi \\ & + F_7 \sin 2\theta \sin \phi + F_8 \sin^2 \theta \sin 2\phi + F_9 \sin \theta \sin \phi \end{aligned}$$

The functions  $F_i$  depend on the invariants  $z_h$  and on the squared transverse momentum of the photon with respect to the two hadrons ( $\mathbf{q}_T^2 \equiv Q_T^2$ ). The azimuthal angle  $\phi$  and the polar angle  $\theta$  are given in the lepton pair center of mass frame (or equivalently the photon center of mass frame). If at high  $Q^2$  and  $Q_T^2$  collinear factorization of the cross section is considered, then at tree level (zeroth order in  $\alpha_s$ ) only  $F_1, F_3$  will receive non-zero contributions ( $F_3$  only from  $\gamma - Z$  interference), at first order in  $\alpha_s$   $F_1, \dots, F_6$  receive contributions, and at second order all  $F_i$  are non zero (no transverse beam polarization is assumed). Below we will discuss the differential cross section in more detail.

### 2.3.2 Two-particle inclusive cross section

The square amplitude for  $e^+e^- \rightarrow h_1 h_2 X$  can be split into two parts: the first part is purely leptonic and the second part is purely hadronic:

$$|\mathcal{M}|^2 = \frac{e^4}{Q^4} L_{\mu\nu} H^{\mu\nu}. \quad (2.11)$$

Neglecting the lepton masses and taking into account the helicity conservation, we can write the lepton tensor as<sup>5</sup>:

$$L_{\mu\nu}(l, l') = 2l_\mu l'_\nu + 2l_\nu l'_\mu - Q^2 g_{\mu\nu}. \quad (2.12)$$

For the case of two observed hadrons in the final state, the product of the hadronic current matrix elements is written as:

$$H_{\mu\nu}(P_X; P_1; P_2) = \langle 0 | J_\mu(0) | P_X; P_1; P_2 \rangle \langle P_X; P_1; P_2 | J_\nu | 0 \rangle. \quad (2.13)$$

<sup>5</sup>For unpolarized electron and positron beams

Including the factor  $1/2$  from averaging over the initial state polarization, the cross section for inclusive hadron pair production in  $e^+e^-$  annihilation is given by

$$\frac{P_1^0 P_2^0 d\sigma^{e^+e^-}}{d^3P_1 d^3P_2} = \frac{\alpha^2}{4Q^6} L_{\mu\nu} \mathcal{W}^{\mu\nu}, \quad (2.14)$$

with

$$\mathcal{W}_{\mu\nu}(q; P_1; P_2) = \int \frac{d^3P_X}{(2\pi)^3 2P_X^0} \delta^4(q - P_X - P_1 - P_2) H_{\mu\nu}(P_X; P_1; P_2) \quad (2.15)$$

For the calculation of the hadron tensor it will be convenient to define the *lightlike* directions using the hadronic momenta. We choose two dimensionless light-cone basis vectors (see Appendix A):

$$n_+^\mu = (1, 0, \mathbf{0}_T), \quad n_-^\mu = (0, 1, \mathbf{0}_T), \quad n_+ \cdot n_- = 1, \quad (2.16)$$

and the hadronic momenta  $P_1$  and  $P_2$  can be parametrized as (up to  $Q_T^2/Q^2$  corrections):

$$P_1^\mu \equiv \frac{z_1 Q}{\sqrt{2}} n_-^\mu + \frac{M_1^2}{z_1 Q \sqrt{2}} n_+^\mu, \quad (2.17)$$

$$P_2^\mu \equiv \frac{M_2^2}{z_2 Q \sqrt{2}} n_-^\mu + \frac{z_2 Q}{\sqrt{2}} n_+^\mu, \quad (2.18)$$

$$q^\mu \equiv \frac{Q}{\sqrt{2}} n_-^\mu + \frac{Q}{\sqrt{2}} n_+^\mu + q_T^\mu. \quad (2.19)$$

Vectors transverse to  $n_+$  and  $n_-$  are obtained using the tensors:

$$g_T^{\mu\nu} \equiv g^{\mu\nu} - n_+^{\{\mu} n_-^{\nu\}}, \quad (2.20)$$

$$\epsilon_T^{\mu\nu} \equiv \epsilon^{\mu\nu\rho\sigma} n_{+\rho} n_{-\sigma}, \quad (2.21)$$

where the brackets around the indices indicate symmetrization.

The experimental analysis of the azimuthal asymmetries are not usually performed in the frame in which the two hadrons are collinear, for which the above (Sudakov) decomposition into light-like vectors and transverse parts is most suited. Instead it is much more common to consider angles in the lepton pair center of mass frame. In this case, there is still freedom to select which momentum or linear combination of momenta, is used to define the  $\hat{z}$  axis. Two choices are common: **Gottfried-Jackson frame** (GJ, Fig. 2.5) and **Collins-Soper frame** (CS, Fig. 2.6). We describe first the GJ frame. Later we shall consider the CS frame and, finally, we shall report the results for the frame in which the jet or thrust axis is used to fix the basis.

In order to expand the hadron tensor in terms of independent Lorentz structures, it is convenient to work with vectors orthogonal to  $q$ . A normalized time-like vector is defined by  $q$  and

a normalized space-like vector is defined by  $\tilde{P}^\mu = P^\mu - (P \cdot q/q^2)q^\mu$  for one of the outgoing momenta ( $P_2$  for example):

$$\hat{t}^\mu \equiv \frac{q^\mu}{Q}, \quad (2.22)$$

$$\hat{z}^\mu \equiv \frac{Q}{P_2 \cdot q} \tilde{P}_2^\mu = 2 \frac{P_2^\mu}{z_2 Q} - \frac{q^\mu}{Q}. \quad (2.23)$$

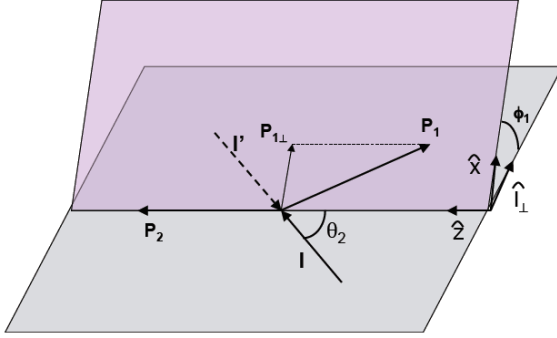


Figure 2.5: **Gottfried-Jackson frame:** Kinematic of the annihilation process in the  $e^+e^-$  center of mass frame.  $P_1$  and  $P_2$  are the momenta of the two hadrons in opposite jets. In this frame  $\hat{x} \equiv \hat{\mathbf{h}}$

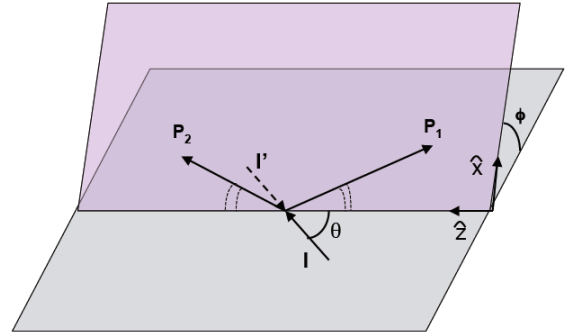


Figure 2.6: **Collins-Soper frame:** Kinematic of the annihilation process in the  $e^+e^-$  center of mass frame.  $P_1$  and  $P_2$  are the momenta of the two hadrons in opposite jets.

This means that in the lepton pair center of mass frame, hadron 2 is moving along the  $\hat{z}$  direction, as in Fig. 2.5. Vectors orthogonal to  $\hat{z}$  and  $\hat{t}$  are obtained using the tensors:

$$g_{\perp}^{\mu\nu} \equiv g^{\mu\nu} - \hat{t}^\mu \hat{t}^\nu + \hat{z}^\mu \hat{z}^\nu \quad (2.24)$$

$$\epsilon_{\perp}^{\mu\nu} \equiv -\epsilon^{\mu\nu\rho\sigma} \hat{t}_\rho \hat{z}_\sigma = \frac{1}{(P_2 \cdot q)} \epsilon^{\mu\nu\rho\sigma} P_{2\rho} q_\sigma. \quad (2.25)$$

Since we have chosen hadron 2 to define the longitudinal direction, we can use the momentum  $P_1$  of hadron 1 to express the directions orthogonal to  $\hat{z}$  and  $\hat{t}$ . We define the normalized vector  $\hat{h}^\mu = g_{\perp}^{\mu\nu} P_{1\nu} / |\mathbf{P}_{1\perp}|$  ( $P_{1\perp}^\mu = g_{\perp}^{\mu\nu} P_{1\nu}$ ), and the second orthogonal direction is given by  $\epsilon_{\perp}^{\mu\nu} \hat{h}_\nu$ . Note that the *transverse* tensors in Eqs. (2.20) and (2.21) are not identical to the *perpendicular* ones defined above if the momentum of the outgoing hadron 1 does not vanish (the differences are of the order  $1/Q$ ).

Azimuthal angles will lie inside the plane orthogonal to  $\hat{t}$  and  $\hat{z}$ . In particular, the azimuthal angle  $\phi$  gives the orientation of  $\hat{l}_{\perp}$ , where  $\hat{l}_{\perp}^\mu$  denotes the normalized perpendicular part of the lepton momentum  $l^\mu$ . As we can see in figure 2.5, the angle  $\phi_1$  is between  $\hat{\mathbf{h}} \propto \mathbf{P}_{1\perp}$  and  $\hat{l}_{\perp}$ , and for a generic vector  $a$  we have:

$$\hat{l}_{\perp} \cdot a_{\perp} = -|\mathbf{a}_{\perp}| \cos \phi_a \quad (2.26)$$

$$\epsilon_{\perp}^{\mu\nu} \hat{l}_{\perp\mu} a_{\perp\nu} = |\mathbf{a}_{\perp}| \sin \phi_a \quad (2.27)$$

where the convention used for the epsilon tensor is  $\epsilon^{0123} = 1$ .

The cross sections are obtained from the hadron tensor after contraction with the lepton tensor. The lepton tensor for unpolarized leptons expressed in the  $e^+e^-$  center of mass is given by:

$$L^{\mu\nu} = Q^2 \left[ -2A(y)g_{\perp}^{\mu\nu} + 4B(y)\hat{z}^{\mu}\hat{z}^{\nu} - 4B(y) \left( \hat{l}^{\mu}\hat{l}^{\nu} + \frac{1}{2}g_{\perp}^{\mu\nu} \right) - 2C(y)D(y)\hat{z}^{\{\mu}\hat{l}^{\nu\}} \right]. \quad (2.28)$$

In this expression, we encounter the function  $y = P_2 \cdot l / P_2 \cdot q \approx l^- / q^-$ , which in the  $e^+e^-$  CM frame is  $y = (1 + \cos\theta^*)/2$ , where  $\theta^* \equiv \theta_2$  is the angle of  $\hat{z}$  with respect to the momentum of the incoming lepton  $l$  (as reported in Fig. 2.5):

$$A(y) = \left( \frac{1}{2} - y + y^2 \right) \stackrel{cm}{=} \frac{1}{4}(1 + \cos^2\theta^*) \quad (2.29)$$

$$B(y) = y(1 - y) \stackrel{cm}{=} \frac{1}{4}\sin^2\theta^* \quad (2.30)$$

$$C(y) = (1 - 2y) \stackrel{cm}{=} -\cos\theta^* \quad (2.31)$$

$$D(y) = \sqrt{y(1 - y)} \stackrel{cm}{=} \frac{1}{2}\sin\theta^* \quad (2.32)$$

Denoting the hadron tensor with  $W^{\mu\nu}$ , we can write the cross section for the process  $e^+e^- \rightarrow h_1h_2X$  in the center of mass frame as:

$$\frac{d\sigma^{(e^+e^-)}}{dz_1 dz_2 d\Omega d^2\mathbf{q}_T} = \frac{\alpha^2}{16Q^4} z_1 z_2 L_{\mu\nu} W^{\mu\nu} \quad (2.33)$$

where  $d\Omega = 2dyd\phi^l$ , with  $\phi^l$  giving the orientation of  $\hat{\mathbf{l}}_{\perp}$ .

As mentioned above, sometimes it may be convenient to choose a rotated set of basis vectors in the lepton center of mass frame: the CS frame shown in Fig. 2.6. In the lepton center of mass frame the  $\hat{z}$  axis points now in the direction that bisects the three-vectors  $\mathbf{P}_2$  and  $-\mathbf{P}_1$ , and the angle of  $\hat{z}$  with respect to the momentum of the incoming lepton  $l$  is  $\theta^* \equiv \theta$ .

Neglecting the mass correction terms, the basis vectors of the CS and GJ frames for  $e^+e^- \rightarrow h_1h_2X$  are the following [64]:

$$\begin{aligned} \hat{t}_{CS}^{\mu} &= \frac{q^{\mu}}{Q} & \hat{t}_{GJ}^{\mu} &= \frac{q^{\mu}}{Q} \\ \hat{z}_{CS}^{\mu} &= \frac{2Q}{\tilde{s}\tilde{Q}} ((P_1 \cdot q)\tilde{P}_2^{\mu} - (P_2 \cdot q)\tilde{P}_1^{\mu}) & \hat{z}_{GJ}^{\mu} &= \frac{Q}{P_2 \cdot q} \tilde{P}_2^{\mu} \\ \hat{x}_{CS}^{\mu} &= \frac{2Q}{\tilde{s}Q_T\tilde{Q}} ((P_1 \cdot q)\tilde{P}_2^{\mu} + (P_2 \cdot q)\tilde{P}_1^{\mu}) & \hat{x}_{GJ}^{\mu} &= \frac{2Q}{\tilde{s}Q_T} ((P_1 \cdot \hat{z}_{GJ})\tilde{P}_2^{\mu} - (P_2 \cdot \hat{z}_{GJ})\tilde{P}_1^{\mu}) \end{aligned} \quad (2.34)$$

where  $\tilde{s} = (P_1 + P_2)^2$  and  $\tilde{Q}^2 = Q^2 + Q_T^2$ . Note that  $\hat{x}_{GJ}$  corresponds to  $\hat{h}$ , and  $\hat{y}_{GJ,CS}$  is defined implicitly by requiring a right-handed basis.

These two basis coincide in the limit  $Q_T \rightarrow 0$ . When  $Q_T \neq 0$  they differ only by a rotation:

$$\hat{z}_{GJ} = \cos \beta \hat{z}_{CS} + \sin \beta \hat{x}_{CS}, \quad (2.35)$$

$$\hat{x}_{GJ} = -\sin \beta \hat{z}_{CS} + \cos \beta \hat{x}_{CS} \quad (2.36)$$

where  $\cos \beta = Q/\tilde{Q}$  and  $\sin \beta = Q_T/\tilde{Q}$ .

In summary, we considered two sets of basis vectors, the first set constructed from the two hadron momenta and the second set from the photon momentum and one of the hadron momenta ( $P_2$ ), both in the  $e^+e^-$  center of mass frame. The respective frames where the momenta  $P_1$  and  $P_2$  (CS frame), or  $q$  and  $P_2$  (GJ frame), are collinear are the natural ones connected to these two sets. The two reference frames are related to each other via a Lorentz transformation. Note that in the CS frame (called also "transverse basis")  $q$  has a transverse component  $q_T$ , while in the GJ frame (or "perpendicular basis")  $P_1$  has a perpendicular component  $P_{1\perp}$ , and they are related as follows:

$$P_{1\perp}^\mu = -z_1 q_T^\mu = z_1 Q_T \hat{h}^\mu. \quad (2.37)$$

### 2.3.3 Hadron tensor

The hadron tensor  $W^{\mu\nu}$  can be expanded in terms of independent Lorentz structures which leads to a parametrization in terms of structure functions  $W_i$ . Ignoring lepton polarization and  $\gamma - Z$  interference, the most general decomposition consists of four structure functions which in the leptonic center of mass frame (or rather the "perpendicular basis") are defined as:

$$W^{\mu\nu} = -g_{\perp}^{\mu\nu} W_T + \hat{z}^\mu \hat{z}^\nu W_L - \hat{z}^{\{\mu} \hat{x}^{\nu\}} W_\Delta - (\hat{x}^{\{\mu} \hat{x}^{\nu\}} - \hat{x}^2 g_{\perp}^{\mu\nu}) W_{\Delta\Delta}. \quad (2.38)$$

such that  $W_\mu^\mu = -(2W_T + W_L)$ . The notation used here is similar to the notation for Drell-Yan process and more explanations can be found in references [65], [66], [67] and [68]. The structure functions  $W_{T,L,\Delta,\Delta\Delta}$  are associated with specific polarizations of the photons [65]:

- $W_T = W^{1,1}$ ,
- $W_L = W^{0,0}$ ,
- $W_\Delta = (W^{0,1} + W^{(1,0)})/\sqrt{2}$ ,
- $W_{\Delta\Delta} = W^{1,-1}$ ,

where the first and the second superscripts denote the photon helicity in the amplitude and its complex conjugate, respectively. Thus,  $W_T$  and  $W_L$  are the structure functions for transverse and longitudinal virtual photons,  $W_\Delta$  is the single-spin flip structure function and  $W_{\Delta\Delta}$  is the

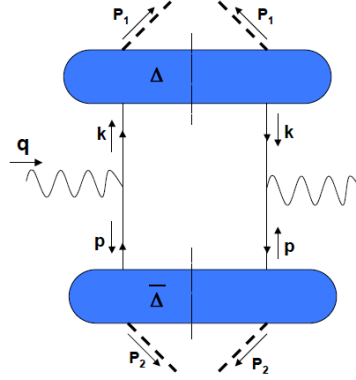


Figure 2.7: Factorized diagram contributing to  $e^+e^-$  annihilation at leading order. The non-perturbative information is encoded in the quark fragmentation correlation function  $\Delta$  ( $\bar{\Delta}$  for antiquark). In these figure,  $q$  is the photon momentum,  $k$  and  $p$  are the momenta of the quark and antiquark respectively, and  $P_{1,2}$  the hadron momentum.

double-spin flip one.

In terms of these structure functions the cross section for the  $e^+e^- \rightarrow h_1 h_2 X$  process becomes:

$$\frac{d\sigma(e^+e^- \rightarrow h_1 h_2 X)}{dz_1 dz_2 d\Omega d^2\mathbf{q}_T} = \frac{3\alpha^2}{4Q^2} z_1^2 z_2^2 \{W_T(1 + \cos^2 \theta^*) + W_L(1 - \cos^2 \theta^*) + W_\Delta \sin 2\theta^* \cos \phi^* + W_{\Delta\Delta} \sin^2 \theta^* \cos 2\phi^*.\} \quad (2.39)$$

Here  $\theta^*$  and  $\phi^*$  indicate the polar and the azimuthal angles in the  $e^+e^-$  center of mass frame (GJ frame, see Fig. 2.5).

### 2.3.4 Cross section

In this section we investigate the  $\phi$  dependence that arises at leading order in  $\alpha_s$  and  $1/Q$  in the cross section of the process  $e^+e^- \rightarrow h_1 h_2 X$ . The cross section involves products of fragmentation functions, which unlike the ordinary collinear functions, include transverse momentum dependence [19]. Non-trivial quark spin effects, which require non-zero partonic transverse momenta, can arise at leading order, as it is the case for the *Collins effect*. Although we are interested in the cross section differential in  $\mathbf{q}_T$ , we shall consider first the case of integration over the transverse momentum of the virtual photon and then the unintegrated cross section.

#### Integration over transverse photon momentum

At tree level one needs to calculate the diagram shown in Fig. 2.7. It depicts the squared amplitude of the process in which the photon produces a quark and an antiquark, which subsequently fragment independently into the hadrons  $h_1$  and  $h_2$ , respectively.

As defined in reference [9], the quark fragmentation correlation function  $\Delta(P_1; k)$  is defined as:

$$\Delta_{ij}(P_h; k) = \sum_X \int \frac{d^4x}{(2\pi)^4} e^{ik \cdot x} \langle 0 | \psi_i(x) | P_h; X \rangle \langle P_h; X | \bar{\psi}_j(0) | 0 \rangle \quad (2.40)$$

where  $k$  is the quark momentum (the average over color indices is implicit). It is also understood that appropriate path-ordered exponential should be included in order to obtain a color gauge invariant quantity<sup>6</sup>.

The above matrix element as function of invariants is assumed to vanish sufficiently fast above a characteristic hadronic scale ( $\mathcal{O}(M)$ ) which is smaller than  $Q$  (this means that  $k^2$ ,  $\mathbf{k} \cdot \mathbf{P}_1 \ll Q^2$ ). Now, making the following Sudakov decomposition for the quark momentum  $k$ :

$$\mathbf{k} \equiv \frac{z_1 Q}{z\sqrt{2}} n_- + \frac{z(k^2 + \mathbf{k}_T^2)}{z_1 Q \sqrt{2}} n_+ + k_T \approx \frac{1}{z} \mathbf{P}_1 + \mathbf{k}_T, \quad (2.41)$$

the Dirac structure of the quark correlation function can be expanded in a number of amplitudes constrained by hermiticity and parity. These amplitudes are functions of invariants built up from the quark and hadron momenta.

In the calculation of the cross section integrated over the transverse momentum of the photon, at leading twist we have only one possible Dirac structure [69]<sup>7</sup>:

$$D_1(z) \equiv \frac{1}{4z} \int dk^+ d^2 \mathbf{k}_T \text{Tr}(\Delta \gamma^-) \Big|_{k^- = P_1^- / z} \quad (2.42)$$

where  $D_1(z)$  is the ordinary unpolarized fragmentation function, which depends only on the light-cone momentum fraction  $z = P_1^- / k^-$ . The fragmentation of an antiquark, denoted with  $\bar{\Delta}_{ij}(P_2; p)$ , is similar to the quark fragmentation. The main difference is the role of  $+$  and  $-$  direction which is reversed.

The four-momentum conservation  $\delta$ -function at the photon vertex is written as:

$$\delta^4(q - k - p) = \delta(q^+ - p^+) \delta(q^- - k^-) \delta^2(\mathbf{p}_T + \mathbf{k}_T - \mathbf{q}_T), \quad (2.43)$$

fixing  $P_2^+ / \bar{z} = p^+ = q^+ = P_2^+ / z_2$  and  $P_1^- / z = k^- = q^- = P_1^- / z_1$ .

The hadron tensor as function of  $\mathbf{q}_T$  is given by

$$W^{\mu\nu} = 3 \int dp^- dk^+ d^2 \mathbf{p}_T d^2 \mathbf{k}_T \delta^2(\mathbf{p}_T + \mathbf{k}_T - \mathbf{q}_T) \text{Tr}(\bar{\Delta}(p) \gamma^\mu \Delta(k) \gamma^\nu), \quad (2.44)$$

where the factor 3 originates from the color summation. In the formula (2.44) we have omitted the flavor summation and the contribution from diagrams with reversed fermion flow, which results from the above expression by replacing  $\mu \leftrightarrow \nu$  and  $q \rightarrow -q$ .

<sup>6</sup>We choose the gauge  $A^- = 0$ , see Appendix B

<sup>7</sup>The generalized parton FFs are obtained as traces of the quark-quark correlation function with the Dirac matrices  $\Gamma$ , as shown in Appendix B

After integration over the transverse photon momentum (or equivalently over the perpendicular momentum of hadron 1:  $\mathbf{P}_{1\perp} = -z_1\mathbf{q}_T$ ), the integration over  $\mathbf{k}_T$  and  $\mathbf{p}_T$  in the equation (2.44) results in:

$$\int d^2\mathbf{q}_T W^{\mu\nu} = -\frac{12}{z_1 z_2} \sum_{a,\bar{a}} e_a^2 g_{\perp}^{\mu\nu} D_1 \bar{D}_1, \quad (2.45)$$

where, now, the summation over flavor indices is included and  $e_a$  is the quark charge. The fragmentation fractions are flavor dependent and depend only on the longitudinal momentum fractions, i.e.  $D_1^a(z_1)\bar{D}_1^a(z_2)$ .

From this hadron tensor one arrives at the following expression for the cross section at leading order in  $\alpha_s$  and  $1/Q$ :

$$\frac{d\sigma(e^+e^- \rightarrow h_1 h_2 X)}{dz_1 dz_2 d\Omega} = \frac{3\alpha^2}{Q^2} A(y) \sum_{a,\bar{a}} e_a^2 D_1 \bar{D}_1. \quad (2.46)$$

### Unintegrated cross section

Now we turn to the cross section differential in the transverse momentum. In this case we consider the correlation function  $\Delta$  integrated only over  $k^+$ . It can be parametrized in terms of transverse momentum dependent (TMD) fragmentation functions ([21, 64, 70]):

$$\begin{aligned} \Delta(z, \mathbf{k}_T) &\equiv \frac{1}{4z} \int dk^+ \Delta(P_1; k) \Big|_{k^- = P_1^- / z, \mathbf{k}_T} = \\ &= \frac{M_1}{4P_1^-} \left\{ D_1(z, \mathbf{k}_T^2) \frac{\not{P}_1}{M_1} + H_1^\perp(z, \mathbf{k}_T^2) \frac{\sigma_{\mu\nu} k_T^\mu P_1^\nu}{M_1^2} \right\} \end{aligned} \quad (2.47)$$

where we report only the fragmentation functions relevant for unpolarized hadron production, whose contributions to the cross section are of leading order in  $1/Q$ . Note that after integration over  $\mathbf{k}_T$  the term with  $H_1^\perp$  drops and the first term reduces to the expression in Eqn. (2.42). Strictly speaking, the TMD fragmentation functions depend on  $z$  and on  $\mathbf{k}'_T$ , where  $\mathbf{k}'_T = -z\mathbf{k}_T$  is the transverse momentum of the hadron in a frame where the quark has no transverse momentum. In order to switch from quark to hadron transverse momentum a Lorentz transformation leaving  $k^-$  and  $P_1^-$  unchanged needs to be performed ([9],[71]).

The Collins function  $H_1^\perp$  implies a correlation between the transverse polarization direction of the quark and the transverse momentum direction of the unpolarized hadron it fragments into [9].

The Collins effect correlates the azimuthal angle of the transverse spin of a fragmenting quark with that of the transverse momentum of the produced hadron, both taken around the quark momentum, via a  $\sin(\phi')$  distribution of their difference angle  $\phi'$  (see Fig. (2.8)). Therefore, the distribution of the final state particles contains information about the spin direction of the fragmenting quark.

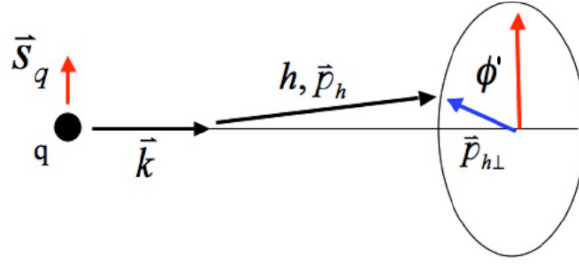


Figure 2.8: Collins effect:  $\vec{S}_q$  and  $\vec{k}$  are the spin and momentum of the fragmenting quark;  $\vec{P}_{h\perp}$  is the transverse momentum of the hadron coming from the quark fragmentation.

The presence of the Dirac matrix anticommutator  $\sigma_{\mu\nu}$  shows that the Collins effect is a chiral-odd state; an interference term between opposite chirality states of the fragmenting quark. The function  $H_1^\perp$  is also often referred to as "time-reversal odd" fragmentation function, due its behavior under time reversal (it does not imply a violation of time reversal symmetry; a detailed discussion is reported in Ref. [72]).

The  $e^+e^- \rightarrow h_1 h_2 X$  reactions involve the product of two Collins fragmentation functions which introduce a  $\cos(2\phi)$  asymmetry, where the cosine modulation arises because we measure the complementary angle of  $\phi'$ . It is an azimuthal "spin" asymmetry in the sense that the asymmetry arises from the correlation of the transverse spin states of the quark-antiquark pair. On average, the quark and antiquark will not be transversely polarized, but for each particular event the spin can have a transverse component and these components will be correlated via the photon polarization state, which in turn is determined by the beam direction. Due to the Collins effect, the direction of the produced hadrons are correlated to the quark and antiquark spin and hence, to the beam direction. This correlation does not average out after summing over all quark polarization states and, as a transverse spin state is a helicity flip state, one deduces that the asymmetry arises from the interference between the photon helicity  $\pm 1$  states (along the quark-antiquark axis) and hence contributes to  $W_{\Delta\Delta}$ <sup>8</sup>.

The Collins effect for unpolarized  $e^+e^- \rightarrow h_1 h_2 X$  shows up at leading order in an azimuthal  $\cos(2\phi)$  asymmetry in the differential cross section [37, 64]:

$$\begin{aligned} \frac{d\sigma(e^+e^- \rightarrow h_1 h_2 X)}{dz_1 dz_2 d\Omega d^2\mathbf{q}_T} &= \frac{3\alpha^2}{Q^2} z_1^2 z_2^2 \left\{ A(y) \mathcal{F}[D_1 \bar{D}_1] + \right. \\ &\quad \left. + B(y) \cos(2\phi_1) \mathcal{F} \left[ (2 \hat{\mathbf{h}} \cdot \mathbf{k}_T \hat{\mathbf{h}} \cdot \mathbf{p}_T - \mathbf{k}_T \cdot \mathbf{p}_T) \frac{H_1^\perp \bar{H}_1^\perp}{M_1 M_2} \right] \right\} \end{aligned} \quad (2.48)$$

where the angle  $\phi_1$  is the azimuthal angle of  $\hat{\mathbf{h}} = \hat{\mathbf{x}}$  (see figure 2.5) and we use the convolution

<sup>8</sup>Such a helicity-flip contribution can also arise from quark mass terms, but those are power suppressed and do not lead to an azimuthal dependence.

notation

$$\mathcal{F}[D\bar{D}] \equiv \sum_{a,\bar{a}} e_a^2 \int d^2\mathbf{k}_T d^2\mathbf{p}_T \delta^2(\mathbf{p}_T + \mathbf{k}_T - \mathbf{q}_T) D^a(z_1; z_1^2 \mathbf{k}_T^2) \bar{D}^{\bar{a}}(z_2; z_2^2 \mathbf{p}_T^2) \quad (2.49)$$

Comparing the previous equation with Eq. (2.39), we find that:

$$W_T = \mathcal{F}[D_1 \bar{D}_1] \quad (2.50)$$

$$W_L = W_\Delta = 0 \quad (2.51)$$

$$W_{\Delta\Delta} = \mathcal{F} \left[ (2 \hat{\mathbf{h}} \cdot \mathbf{k}_T \hat{\mathbf{h}} \cdot \mathbf{p}_T - \mathbf{k}_T \cdot \mathbf{p}_T) \frac{H_1^\perp \bar{H}_1^\perp}{M_1 M_2} \right] \quad (2.52)$$

The convolutions in Eq. (2.48) are not the objects of interest, rather one wants to learn about the FFs depending on  $z$  and  $\mathbf{k}_T$ . This may not be possible without further assumptions about the type of the  $\mathbf{k}_T$  dependence; usually a Gaussian transverse momentum dependence is used. As a way out, it has been suggested [37] to consider specific integrated weighted asymmetries that probe the  $\mathbf{k}_T$  moments of the functions, instead the full transverse momentum dependence. These so called transverse moments are defined as:

$$F^{(n)}(z_1) = \int d^2\mathbf{k}'_T \left( \frac{\mathbf{k}'_T{}^2}{2M_1^2} \right)^n F(z_1, \mathbf{k}'_T{}^2) \quad (2.53)$$

for a generic fragmentation function  $F$ . In particular, the first transverse moment of Collins fragmentation function

$$H_1^{\perp(1)}(z) = z^2 \int d^2\mathbf{k}'_T \left( \frac{\mathbf{k}'_T{}^2}{2M^2} \right) H_1^\perp(z_1, z^2 \mathbf{k}'_T{}^2) \quad (2.54)$$

is the familiar  $\mathbf{k}_T$ -integrated FF.

As shown in [37], considering appropriate weights produces a product of  $\mathbf{k}_T$  moments of FFs, in this case  $H_1^{\perp(1)} \bar{H}_1^{\perp(1)}$  in the Eq. (2.48).

Note that the  $\mathbf{k}_T^2$ -moment  $H_1^{\perp(1)}$  that arise in the above  $e^+e^-$  annihilation expression also appears in the  $Q_T$ -weighted  $\sin(\phi_h + \phi_S)$  asymmetry in semi-inclusive lepton-hadron scattering, in that case multiplied by the transversity distribution function [23].

### 2.3.5 Universality of the Collins effect

It has been shown in references [73, 74] that the *T-odd distribution functions* are process dependent. This follows from their gauge invariant definition as matrix elements of operators involving path-ordered exponentials that are non local off the light-cone. For *T-odd fragmentation functions*, such as the Collins fragmentation function, a similar conclusion was drawn [72]. However, for the particular case  $e^+e^- \rightarrow h_1 h_2 X$  and semi-inclusive DIS, it has been argued using a model (and later also with more general arguments) that the Collins fragmentation functions are identical [75, 76, 77]. This conclusion was also extended to the process  $pp \rightarrow h \text{ jet } X$

[78]. In this sense the Collins function is considered universal.

Assuming the universality of the Collins fragmentation function for the processes  $e^+e^- \rightarrow h_1 h_2 X$  and SIDIS, a simultaneous fit to the Collins effect asymmetry data has been performed, as discussed in section 1.3.2.

### 2.3.6 Higher twist

For a more complete description, in this section we will introduce the terms that arise when going beyond leading order in  $1/Q$ . Insertion of the leading order parameterization of  $\Delta$  (Eqn. (2.47)) in the calculation of the diagram shown in Fig. (2.7) also produces  $1/Q$  contributions. Such  $1/Q$  contribution can already be generated by simply transforming to a different frame. This contribution is not electromagnetically gauge invariant and the full calculation at order  $1/Q$  [37] requires first of all, that the correlation function  $\Delta$  is parametrized further to include higher twist fragmentation functions:

$$\Delta(z, \mathbf{k}_T) = \frac{M_1}{4P_1^-} \left\{ D_1(z, \mathbf{k}_T^2) \frac{\not{P}_1}{M_1} + H_1^\perp(z, \mathbf{k}_T^2) \frac{\sigma_{\mu\nu} k_T^\mu P_1^\nu}{M_1^2} + E1 + D^\perp \frac{\not{k}_T}{M_1} + H \sigma_{\mu\nu} n_-^\mu n_+^\nu \right\} \quad (2.55)$$

where  $E$ ,  $H$  and  $D^\perp$  are twist-3 FFs. In addition, up to order  $1/Q$ , there are other four diagrams shown in Fig. (2.9). These four diagrams involve one gluon which connects to one of the two soft hadronic matrix elements.

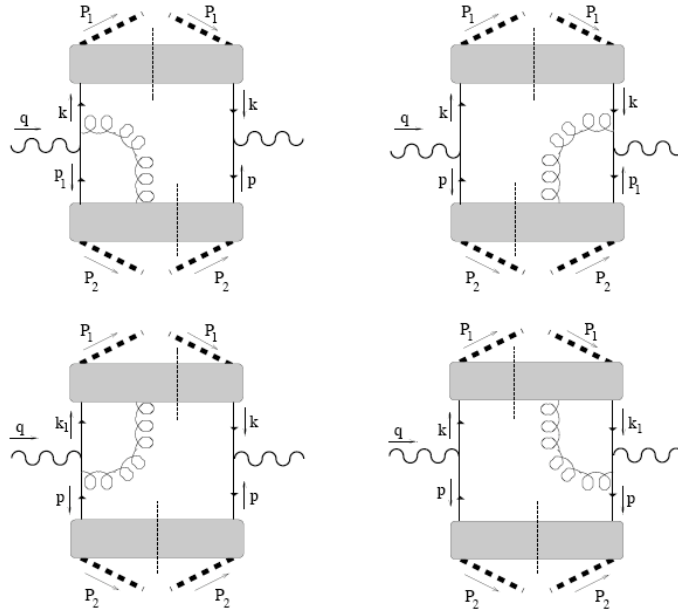


Figure 2.9: Diagrams contributing to  $e^+e^-$  annihilation at order  $1/Q$ , involving one gluon which connects one of the two soft part.

Hence, up to order  $1/Q$ , in addition to the quark-quark correlation function  $\Delta(P_1; k)$ , described

in Eq. (2.40), we have to account also for the quark-gluon correlation function:

$$\begin{aligned} \Delta_{Aij}^\alpha(P_1; k, k_1) &= \sum_X \int \frac{d^4x}{(2\pi)^4} \frac{d^4y}{(2\pi)^4} e^{ik \cdot y + i k_1 \cdot (x-y)} \times \\ &\times \langle 0 | \phi_i(x) g A_T^\alpha(y) | P_1; X \rangle \langle P_1; X | \bar{\phi}_j(0) | 0 \rangle \end{aligned} \quad (2.56)$$

where  $k, k_1$  are the quark momenta and again inclusion of path-ordered exponentials and an averaging over color indices are understood<sup>9</sup>.

In a calculation up to sub-leading order, we only encounter the partly integrated correlation functions  $\int dk^+ \Delta(P_1; k)$  and  $\int dk^+ d^4k_1 \Delta_A^\alpha(P_1; k, k_1)$ . More explanations about the full hadron tensor calculation (including higher twist fragmentation functions) are available in references [37, 64].

In the GJ frame, the cross section at leading order in  $\alpha_s$  including twist-3 contributions becomes [64]:

$$\begin{aligned} \frac{d\sigma(e^+e^- \rightarrow h_1 h_2 X)}{dz_1 dz_2 d\Omega d^2\mathbf{q}_T} &= \frac{3\alpha^2}{Q^2} z_1^2 z_2^2 \left\{ A(y) \mathcal{F}[D_1 \bar{D}_1] + \right. \\ &+ B(y) \cos(2\phi_1) \times \mathcal{F} \left[ (2\hat{\mathbf{h}} \cdot \mathbf{k}_T \hat{\mathbf{h}} \cdot \mathbf{p}_T - \mathbf{k}_T \cdot \mathbf{p}_T) \frac{H_1^\perp \bar{H}_1^\perp}{M_1 M_2} \right] - \\ &- C(y) D(y) \cos(\phi_1) \times \left( \frac{M_1}{Q} \mathcal{F} \left[ \frac{\hat{\mathbf{h}} \cdot \mathbf{k}_T}{M_1} \frac{\tilde{D}^\perp}{z_1} \bar{D}_1 \right] - \frac{M_2}{Q} \mathcal{F} \left[ \frac{\hat{\mathbf{h}} \cdot \mathbf{k}_T}{M_1} H_1^\perp \frac{\bar{H}}{z_2} \right] - \right. \\ &\left. \left. - \frac{M_2}{Q} \mathcal{F} \left[ \frac{\hat{\mathbf{h}} \cdot \mathbf{p}_T}{M_2} D_1 \frac{\bar{D}^\perp}{z_2} \right] + \frac{M_1}{Q} \mathcal{F} \left[ \frac{\hat{\mathbf{h}} \cdot \mathbf{p}_T}{M_2} \frac{\tilde{H}}{z_1} \frac{\bar{H}_1^\perp}{z_1} \right] \right) \right\} \end{aligned} \quad (2.57)$$

where the fragmenting functions indicated with a tilde differ from the corresponding twist-3 functions by a twist-2 part:

$$D^\perp = z D_1 + \tilde{D}^\perp, \quad (2.58)$$

$$H = -\frac{\mathbf{k}_T^2}{M_1^2} z H_1^\perp + \tilde{H}. \quad (2.59)$$

The results obtained in Eqn. (2.57) are the the same as Eqn. (2.48) plus an additional  $\cos(\phi_1)$  asymmetry of order  $M/Q$ . The function  $E$  only contributes in the case of polarized electrons at  $1/Q$  and for unpolarized electrons at the  $1/Q^2$  level.

### 2.3.7 Jet frame asymmetry

In an unpublished study [13] a transverse spin correlation similar to the  $\cos(2\phi)$  in back-to-back jets was investigated using LEP's DELPHI data.

<sup>9</sup>Note that the definition of  $\Delta_A^\alpha$  includes one power of the strong coupling constant  $g$ .

Although the transverse polarization of quark (antiquark) in  $Z^0$  decay is very small ( $O(m_q/M_Z)$ ), there is a non-trivial correlation between transverse polarization of quark and antiquark, and the transverse spin correlation coefficient is given by

$$C_{TT}^{q\bar{q}} = \frac{v_q^2 - a_q^2}{v_q^2 + a_q^2} \quad (2.60)$$

with  $v_q$  and  $a_q$  the vector and axial vector couplings of quarks to the  $Z$ -boson, respectively. The following angular dependence of the differential cross section for correlated hadron production in opposite jets was studied:

$$\frac{d\sigma}{d\cos\theta d\phi d\phi'} \propto 1 + \cos^2\theta + C_{TT}^{q\bar{q}} S \sin^2\theta \cos(\phi + \phi') \quad (2.61)$$

In this equation,  $S$  is the analyzing power<sup>10</sup> of the asymmetry to be determined,  $\theta$  is the polar angle of  $q\bar{q}$  pair with respect to the electron beam direction in the  $Z^0$  (or  $e^+e^-$ ) rest frame, and  $\phi, \phi'$  are the azimuthal angles around the  $q\bar{q}$  axis of two produced hadrons from opposite jets plane.

This  $\cos(\phi + \phi')$  asymmetry differs from the  $\cos(2\phi_1)$  asymmetry discussed so far in that now we need to know the two hadrons momenta and the jet axis, which is necessary for the calculation of the two azimuthal angle  $\phi$  and  $\phi'$ .

The jet-axis is identified as the  $q\bar{q}$  axis, then a measurement of the transverse momenta of the leading particles in the two jets compared to the jet momentum is a determination of the transverse momenta of the quarks compared to the leading hadrons they fragment into. One can keep the cross section differential in the azimuthal angles of the transverse momentum of the quarks, after which the  $\mathbf{q}_T$  integration can be safely done (as opposed to the case of the  $\cos(2\phi)$  asymmetry) and it will not average to zero unless one integrates over the azimuthal angles. In this way one will arrive at an expression involving the moments

$$F^{[n]}(z_i) \equiv \int d|\mathbf{k}_T|^2 \left[ \frac{|\mathbf{k}_T|}{M_i} \right]^2 F(z_i, |\mathbf{k}_T|^2) \quad (2.62)$$

for  $n = 0$  and  $n = 1$ . The latter is often referred to as the *half-momentum* and also written as  $F^{(1/2)}$ .

Making a transformation from the frame in which  $P_1$  and  $P_2$  are collinear into the lepton pair center of mass frame where the  $q\bar{q}$  axis define the  $\hat{z}$  axis, and contracting the hadron with the lepton tensor written in this basis, we have the following differential cross section in case

<sup>10</sup> $S$  is the ratio of spin dependent to spin-independent parts of the fragmentation function.

of unpolarized final state hadrons<sup>11</sup>:

$$\begin{aligned} \frac{d\sigma(e^+e^- \rightarrow h_1 h_2 X)}{dz_1 dz_2 d\cos(\theta_{jet}) d\phi d\phi'} &= \sum_{a \bar{a}} \frac{3\alpha^2}{Q^2} z_1^2 z_2^2 \left\{ (1 + \cos^2 \theta_{jet}) D_1^{[0]a}(z_1) \bar{D}_1^{[0]a}(z_2) \right. \\ &\quad \left. + \sin^2 \theta_{jet} \cos(\phi + \phi') H_1^{\perp[0]a}(z_1) \bar{H}_1^{\perp[0]a}(z_2), \right\} \end{aligned} \quad (2.63)$$

where  $\theta_{jet}$  is the angle between the jet-axis and the beam axis. More details can be found in Ref. [64].

---

<sup>11</sup>Unlike reference [13] we also included the photon contribution (the  $\gamma - Z$  interference was found to be very small at  $\sqrt{s} \sim 10$  GeV [64]).

## Chapter 3

# The *BABAR* Experiment

*BABAR* is an High Energy Physics experiment installed at the Stanford Linear Accelerator Center (SLAC), California. It was designed and build by a large international team of scientists and engineers in the 90s, with a comprehensive physics program consisting of the systematic measurement of  $CP$  violation in the  $B$  meson system, precision measurements of decays of bottom and charm mesons, and of the  $\tau$  lepton, and search for rare processes. The *BABAR* experiment consists of a detector [79] built around the interaction reagon of the high luminosity  $e^+e^-$  collider PEP-II [80]. *BABAR* started taking data in 1999 and finished in year 2008. In this chapter the main features of the final design and performances of PEP-II and *BABAR* are described.

### 3.1 The PEP-II $B$ Factory

The PEP-II  $B$  Factory is an asymmetric-energy  $e^+e^-$  collider designed to operate at a center-of-mass energy of 10.58 GeV, correspondig to the mass of the  $\Upsilon(4S)$  vector meson resonance (see Fig. 3.1). The luminosity  $\mathcal{L}$  of the machine depends on the careful tuning of several parameter. This dependence is expressed as:

$$\mathcal{L} = \frac{nfN_1N_2}{A}, \quad (3.1)$$

where  $n$  is the number of bunches in a ring,  $f$  is the bunch crossing frequency,  $N_1$  and  $N_2$  are the total number of particles in each bunch, and  $A$  is their overlap section ( $A = 4\pi\sigma_x\sigma_y$ ). The design peak luminosity was foreseen to be  $\mathcal{L} = 3 \times 10^{33} \text{ cm}^{-2} \text{ s}^{-1}$  and was reached in 2001, and the record is  $1.2 \times 10^{34} \text{ cm}^{-2} \text{ s}^{-1}$  achieved in 2006.

The effective cross section<sup>1</sup> of the main physics processes in PEP-II are listed in Tab. 3.1( [81]), and for the production of the  $\Upsilon(4S)$  at  $\sqrt{s} = 10.58 \text{ GeV}$  it is about 1.1 nb, where the  $\Upsilon(4S)$  decays almost exclusively into  $B^0\bar{B}^0$  and  $B^+B^-$  pairs.

As shown in Fig. 3.1, at the peak of  $\Upsilon(4S)$  there is a non-negligible amount of  $e^+e^- \rightarrow q\bar{q}$  ( $q = u, d, s, c$ ) and  $e^+e^- \rightarrow l^+l^-$  ( $l = e, \mu, \tau$ ) events. In addition, part of the data is collected

---

<sup>1</sup>This effective cross section is lower of about one third than the peak cross section (3.6 nb) due to the energy spead (3-6 MeV) of the beams and to the initial state radiation.

at the CM energy 40 MeV below the  $\Upsilon(4S)$  peak, where  $B\bar{B}$  production is not allowed. This data sample corresponds to about 1/10 of the sample taken at the  $\Upsilon(4S)$  peak and, in the “conventional” BABAR analysis, is used to study non- $B\bar{B}$  background. In this analysis it is included in the signal sample.

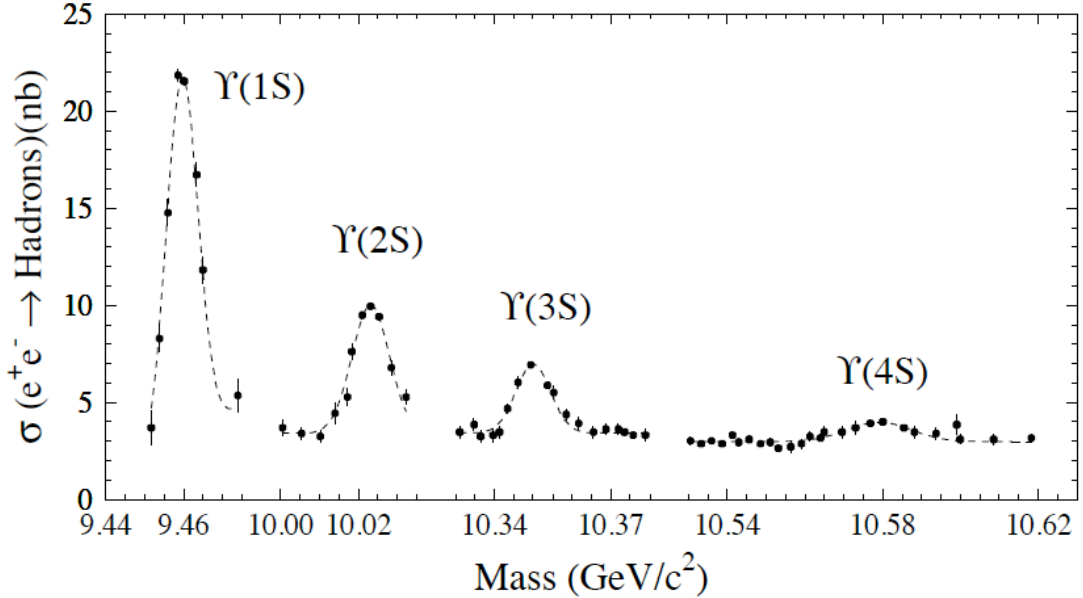


Figure 3.1: The first four S-wave  $\Upsilon$  resonances shown with the hadronic cross section versus center-of-mass energy/ $c^2$  in the  $\Upsilon$  mass region. The  $\Upsilon(4S)$  is the third radial excitation of the ground state. Its larger width is a consequence of the fact that the  $\Upsilon(4S)$  is just above threshold for strongly decaying to  $B^0\bar{B}^0$  and  $B^+B^-$  pairs.

### 3.1.1 PEP-II Layout

In PEP-II, the electron beam of 9.0 GeV collides almost head-on<sup>2</sup> with the positron beam of 3.1 GeV resulting in a boost for the CM system of  $\beta\gamma \approx 0.56$  in the LAB frame. This boost is crucial to study the  $B$ -meson system: it allows to reconstruct the decay vertex of the two  $B$  mesons and to determine their relative decay times, since the average separation between the two  $B$  vertexes is  $\beta\gamma c\tau \approx 250\mu\text{m}$ . One can therefore measure the time-dependent decay rates and CP-asymmetries.

The different beam energies require a two rings configuration, as shown in Fig. 3.2. The parameters of PEP-II rings are summarized in Tab. 3.2

Electron and positron are accelerated from the 3 km long SLAC linear accelerator (LINAC) and accumulated into the two 2.2 km long storage rings, called HER (High-Energy-Ring) and LER

<sup>2</sup>The crossing angle is 20 mrad.

$e^+e^- \rightarrow$	Cross section (nb)
$u\bar{u}$	1.39
$d\bar{d}$	0.35
$s\bar{s}$	0.35
$c\bar{c}$	1.30
$b\bar{b}$	1.10 (effective) - 3.6 (peak)
$e^+e^-$	$\sim 53$
$\mu^+\mu^-$	1.16
$\tau^+\tau^-$	0.94

Table 3.1: Cross section of the main physics processes at the  $\Upsilon(4S)$ . The cross section for  $e^+e^-$  is referred to the volume of *BABAR* electromagnetic calorimeter, which is used to trigger these events.

(Low-Energy Ring), respectively. A fraction of electrons instead of being delivered to the HER is further accelerated to an energy of 30 GeV and sent to a target where positrons are produced.

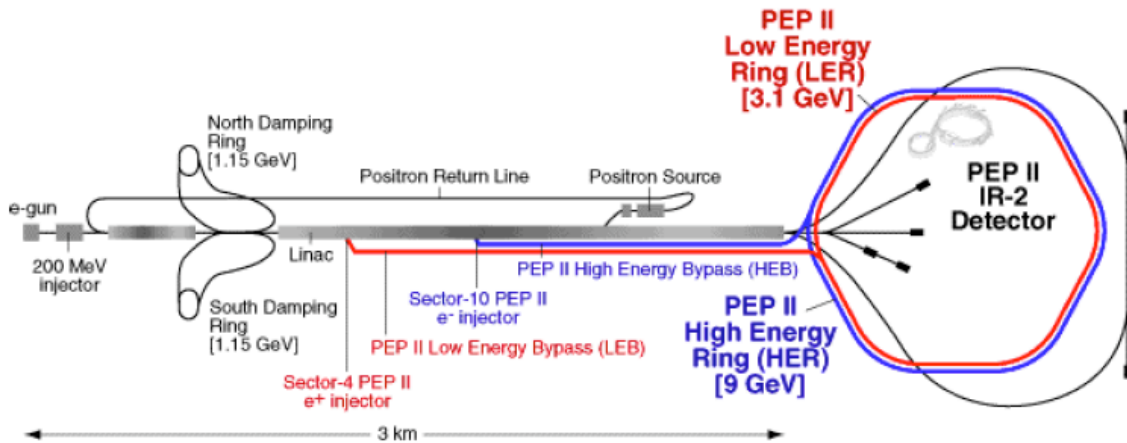


Figure 3.2: The PEP-II asymmetric storage ring and the SLAC linear accelerator. The SLAC LINAC is the injector for PEP-II. The interaction point of PEP-II is at IR-2, where *BABAR* is suited.

In proximity of the interaction region, the beams are focused by a series of offset quadrupoles (indicated with Q in Fig. 3.5) and bent by a pair of samarium-cobalt dipole magnet (B1), which allow the bunches to collide head-on. The B1 dipoles, located at  $\pm 21$  cm on each side of the interaction point (IP), and the Q1 quadrupoles, are permanent magnets which operate inside the field of the *BABAR* superconducting solenoid, while Q2, Q4, and Q5, are located outside or in the fringe field of the solenoid. This configuration is the best compromise

Parameters	Units	Design	$\Upsilon(4S)$ Typical
Energy ( $E$ ) HER/LER	GeV	9.0/3.1	9.0/3.1
Current ( $I$ ) HER/LER	A	0.75/2.15	0.9-1.9/1.3-2.6
# of bunches		1658	1732
$\sigma_x$	$\mu m$	110	120
$\sigma_y$	$\mu m$	3.3	4.1
$\sigma_z$	$\mu m$	11	11-12
$\beta_y^*$	mm	15-25	9-10
$\beta_x^*$	cm	50	40-105
$\xi_y$ HER/LER		0.03/0.03	0.062/0.047
$\xi_x$ HER/LER		0.03/0.03	0.113/0.027
Bunch Spacing	ns	4.2	4.2
Luminosity	$10^{33} cm^{-2} s^{-1}$	3	4.4-10.4

Table 3.2: PEP-II beam parameters[82]. HER and LER refer to the high energy  $e^-$  and low  $e^+$  ring respectively.  $\sigma_x$ ,  $\sigma_y$ , and  $\sigma_z$  refer to the R.M.S. horizontal, vertical, and longitudinal bunch size at the IP.  $\beta_{x,y}^*$  is the horizontal and vertical envelope function at the collision point and  $\xi_{x,y}$  the tune shift. The peak luminosity is proportional to  $E I \xi_y / \beta_y^*$ , assuming the product  $E \cdot I$  roughly equal for the two beams.

between physics and engineers requirements.

The interaction region is enclosed in a water-cooled beam pipe consisting of two thin layers of beryllium (0.83 mm and 0.53 mm) with a 1.48 mm water channel in between.

To attenuate synchrotron radiation, the inner surface of the beam pipe is gold-plated (about 4  $\mu m$ ). Beam pipe, permanent magnets, and Silicon Vertex Tracker (SVT) are assembled, aligned, and then enclosed in a 4.4 m long support tube, which is inserted into the *BABAR* detector.

### 3.1.2 PEP-II performances

PEP-II has delivered luminosity starting from May 1999 till April 2008, and since then *BABAR* has recorded a total integrated luminosity of 531  $fb^{-1}$ , mostly at the  $\Upsilon(4S)$  resonance peak (also called on-peak sample) plus small samples around  $\Upsilon(2S)$  and  $\Upsilon(3S)$  ones, as shown in Fig. 3.3

Some off-peak luminosity has been collected 40 MeV below each resonance peak, and finally an energy scan from  $\Upsilon(4S)$  till 11.2 GeV with 5 MeV steps, for a total amount of 54  $fb^{-1}$ . Every single run of data has been checked and some of them have been rejected because of poor quality due to technical problems with the detector or bad conditions for the machine background. PEP-II has largely surpassed its design performance, with a record peak-luminosity of  $1.2 \cdot 10^{34} cm^{-2} s^{-1}$ , and a monthly integrated luminosity of 20  $fb^{-1}$ , that is, respectively, about a factor four and six with respect to the expectations. The progress in the instantaneous luminosity is

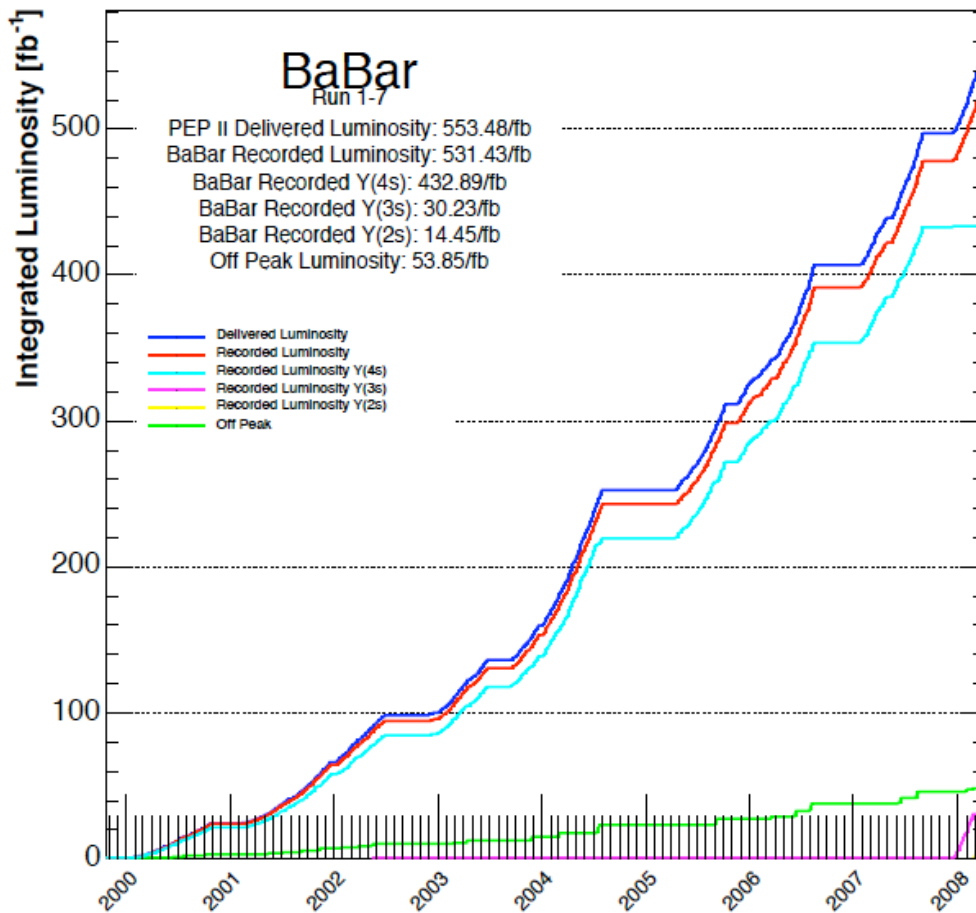


Figure 3.3: Total luminosity delivered by PEP-II from October 1999 to April 2008. The luminosities integrated by *BABAR* at different resonances is also shown.

mainly due to the increase of the beam currents and improved focusing and beam orbits. A significant improvement of the order of 50% of the integrated luminosity has been achieved at the begin of year 2004 with the implementation of a novel mode of operation of PEP-II called *trickle injection* (see Fig. 3.4). Until the end of 2003, PEP-II typically operated in a series of 40 minute fills during which the colliding beam coasted: at the end of each fill, it took about three to five minutes to replenish the beams for the next fill, and during this period the *BABAR* data acquisition system had to be turned off for the high background condition, affecting detector safety and data acquisition dead-time. With the new technique, the *BABAR* detector could take data uninterrupted while the LINAC continuously refilled the beams with small injection at lower rate, replacing particles lost in collisions in the interaction region.

Trickle injection was introduced first in December 2003 in the low energy ring, and in March 2004 it was implemented in the high energy ring. The advantages of this novel mode of op-

eration went beyond just the increase in luminosity. Continuous injection made the storage of particles more stable, so that PEP-II rings were easier to operate and beam losses were far less frequent than with the previous operational mode.

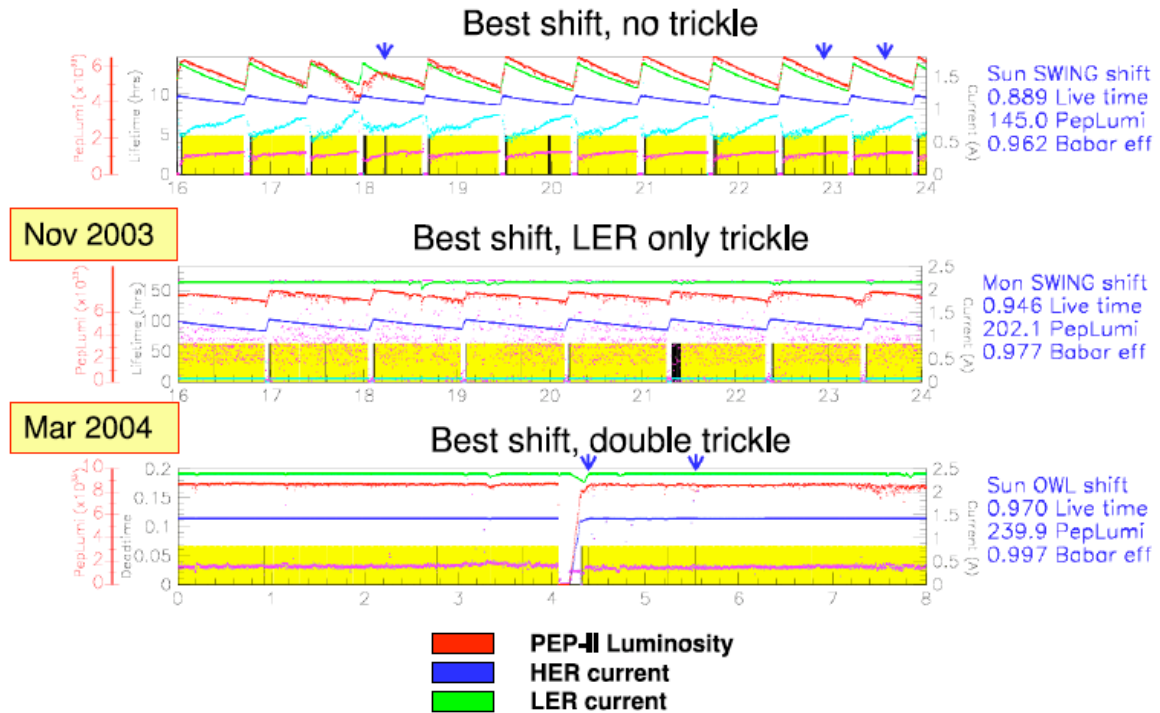


Figure 3.4: Comparison of the best 8-hour periods of data taking for three different mode of operation of PEP-II: no trickle injection (top), trickle injection of the low energy ring (middle), and trickle injection of both beams (bottom).

### 3.1.3 PEP-II background

Beam-generated background causes high single-counting rates, data acquisition dead time, high currents and radiation damage of the *BABAR* detector and electronics. This results in low data quality and can affect the lifetime of the apparatus. For this reason the background generated by PEP-II was studied in detail and the interaction region was carefully designed. The primary sources of the machine-generated background are:

- **synchrotron radiation** in the proximity of the interaction region. A strong source of background is due to beam deflections in the interaction region. This component is limited by channeling the radiation out of the *BABAR* acceptance with a proper design of the interaction region and beam orbits, and placing absorbing masks before the detector components;

- **interaction between beam particles and residual gas** in either rings, originated from beam gas bremsstrahlung and Coulomb scattering. Both types of interaction cause an escape of beam particles from their orbit. This background represents the primary source of radiation damage for the inner vertex detector and the principal background source for the other components. The intrinsic rate of these processes is proportional to the product of the beam current and the residual pressure;
- **Electromagnetic shower generated by beam-beam collision.** These shower are due to  $e^+e^-$  produced by radiative Bhabha scattering and hitting the beam pipe close to the interaction point. This background is proportional to the machine luminosity and it is always monitored.

### 3.2 Overview of the *BABAR* detector

System	Polar angle coverage ( $\theta$ )	Channels	Layers	Segmentation	Performance
SVT	[20.1,150.2] $^\circ$	150K	5	50-100 $\mu\text{m}$ $r - \phi$ 100-200 $\mu\text{m}$ $z$	$\sigma_{d0} = 55 \mu\text{m}$ $\sigma_{z0} = 65 \mu\text{m}$
DCH	[17.2,152.6] $^\circ$	7,104	40	6-8 mm drift distance	$\sigma_\phi = 1 \text{ mrad}$ $\sigma_{\tan \lambda} = 0.001$ $\sigma_{p_T}/P_T = 0.47\%$ $\sigma(dE/dx) = 7.5\%$
DIRC	[25.5,141.4] $^\circ$	10,752	1	$35 \times 17 \text{ mm}^2$ ( $r\Delta\phi \times \Delta r$ ) 144 bars	$\sigma_{\theta_C} = 2.5 \text{ mrad}$ per track
EMC (C)	[27.1,140.8] $^\circ$	$2 \times 5760$	1	$47 \times 47 \text{ mm}^2$ 5760 crystals	$\sigma_E/E = 3.0\%$ $\sigma_\phi = 3.9 \text{ mrad}$
EMC (F)	[15.8,27.1] $^\circ$	$2 \times 820$		820 crystals	$\sigma_\theta = 3.9 \text{ mrad}$
IFR (C)	[47,123] $^\circ$	22K+2K	19+2	20-38 mm	90% $\mu^\pm$ eff. 6-8% $\pi^\pm$ mis-id
IFR (F)	[20,47] $^\circ$	14.5K	18	28-38 mm	(loose selection, 1.5-3.0 GeV/c)
IFR (B)	[123,154] $^\circ$	14.5K	18	28-38 mm	

Table 3.3: Overview of the coverage, segmentation, and performance of the *BABAR* detector system. The notation (C), (F), and (B) refers to the central barrel, forward and backward components of the system, respectively. The detector coverage in the laboratory frame is specified in terms of the polar angle  $\theta$ . Performance numbers are quoted for 1 GeV/c particles, except where noted.

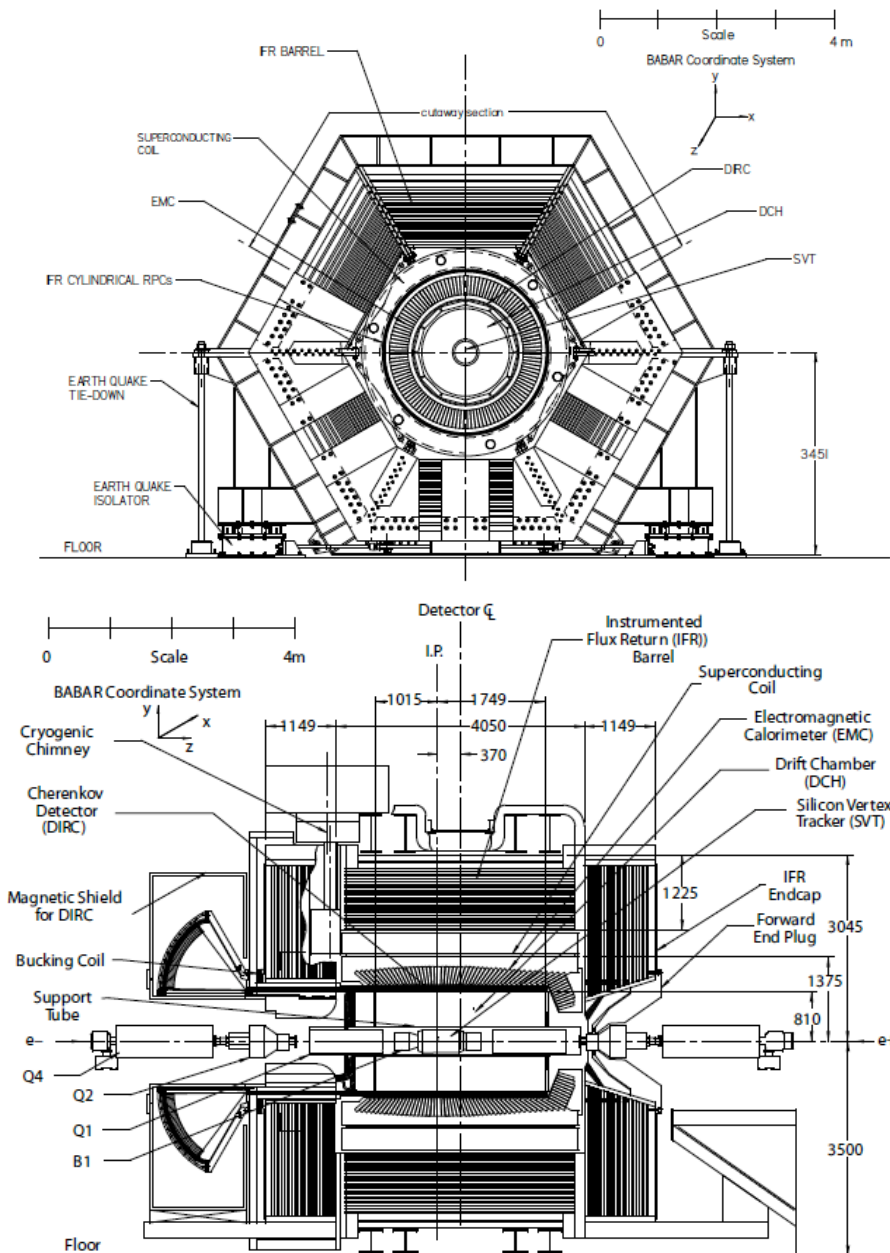


Figure 3.5: Layout of the *BABAR* detector projected along the beam axis (top) and projected in the plane orthogonal to the beam axis (bottom).

The design of the *BABAR* detector has been optimized for CP violation studies, but it is also well suitable for searches of rare decays of  $B$ ,  $\tau$ , and hadronic studies. To achieve the goal of performing accurate event reconstruction there are many requirements:

- a large acceptance and uniform efficiency, in particular down to small polar angles rela-

tive to the boost direction, to avoid particle losses;

- excellent detection efficiency for charged particles down to 60 MeV/c and for photons down to 25 MeV;
- good momentum resolution to kinematically separate signal from background;
- excellent energy and angular resolution for the detection of photons from  $\pi^0$  and  $\eta_0$  decays, and from radiative decays in the range from 25 MeV to 4 GeV;
- very good vertex resolution, both transverse and parallel to the beam;
- identification of electron and muon over a wide range of momentum, primarily for the detection of semi-leptonic decays used to tag the  $B$ -meson flavor and for the study of semi-leptonic and rare decays;
- identification of hadrons over a wide range of momentum;
- a highly efficient, selective trigger system with redundancy so as to avoid significant signal losses and systematic uncertainties.

The *BABAR* detector (see Fig. 3.5), designed and fabricated by a collaboration of 600 physicists of 75 institutions from 9 countries, meets all these requirements, as will be described in the next sections on this chapter. To take into account the boost of PEP-II and maximize the geometric acceptance, the whole detector is displaced in the forward direction (the direction of the highest energy beam) with respect to the interaction point by 37 cm. An overview of the polar angle ( $\theta$ ) coverage, the segmentation and the performance of the *BABAR* detector system is summarized in Tab. 3.3.

The *BABAR* superconducting solenoid, which produces a 1.5 T axial magnetic field, contains a set of nested detectors, which are - going from inside to outside -

- a five layers of silicon vertex detector (SVT),
- a central drift chamber (DCH) for charged particle detections and momentum measurement,
- a ring-imaging Čerenkov radiation detector (DIRC) for charged particle identification, and
- a CsI(Tl) crystal electromagnetic calorimeter (EMC) for the detection of photons and electrons.

The calorimeter has a barrel and an end-cap which extends it into the forward direction ( $e^-$  beam direction), where many of the collision products emerge. All the detector located inside

the magnet have full acceptance in azimuth ( $\phi$ ).

The instrumented flux return (IFR) outside the cryostat is composed of 18 layers of steel, which increase in thickness outwards, with in-between 19 layers of planar resistive plate chambers (RPC) or limited streamer tubes (LST) in the barrel and 18 in the end-caps. The IFR allows the separation of muons and charged hadrons, and also detects penetrating neutral hadrons. As indicated in Fig. 3.5, the right-handed coordinate system is anchored to the main tracking system, the drift chamber, with the  $z$ -axis coinciding with its principal axis. This axis is offset relative to the beam axis by about 20 mrad in the horizontal plane. The positive  $y$ -axis points upward and the positive  $x$ -axis points away from the center of the PEP-II storage rings.

In the following section there is a detailed description of each sub-detector and their performances.

### 3.3 The Silicon Vertex Tracker (SVT)

The SVT sub-detector provides a precise measurement of the decay vertices and of the charged particle trajectories near the interaction region. The mean vertex resolution along the  $z$ -axis must be better than  $80 \mu\text{m}$  in order to avoid a significant impact on the time-dependent CP asymmetry measurements, and a  $100 \mu\text{m}$  resolution in the  $x - y$  transverse plane is necessary in reconstructing decays of bottom and charm mesons, as well as  $\tau$  leptons<sup>3</sup>.

The SVT also provides standalone tracking for particles with transverse momentum too low to reach the outer tracker, like soft pions from  $D^*$  decays and many charged particles produced in multi-body  $B$ -meson decays. The choice of a vertex tracker made of five layers of double-sided silicon strip sensors allows a complete track reconstruction even in the absence of drift chamber information.

Finally, the SVT supplies PID information both for low and high momentum tracks. For low momentum tracks the SVT  $dE/dx$  is the only PID information available, for high momentum tracks the SVT provides the best measurement of the track angles, required to achieve the designed resolution on the Čerenkov angle measured by the DIRC.

#### 3.3.1 Detector layout

The Silicon Vertex Tracker is composed of five layers of  $300 \mu\text{m}$  thick, double-sided micro-strip detectors [83]. The total active silicon area is  $0.96 \text{ m}^2$  and the material traversed by particles at normal incidence is  $4\% X_0$ . The geometrical acceptance is about 90% of the solid angle in the CM system.

<sup>3</sup>For example, in decays of the type  $B^0 \rightarrow D^+ D^-$ , the separation of the two  $D$  vertices is important. The distances between the two  $D$ 's in the  $x - y$  plane for this decay is typically  $\sim 275 \mu\text{m}$ . Hence, the SVT needs to provide resolution of about  $\sim 100 \mu\text{m}$  in the plane perpendicular to the beam line.

The silicon detectors and the associated readout electronics are assembled into mechanical units called *moduls*. The inner three layers have six detector modules and are traditional barrel-style structure. They are placed next to the interaction region, at radii 3.3, 4.0, and 5.9 cm from the beam axis (see Fig. 3.6 and Fig.3.7), and provide an accurate measurement of the track impact parameters along  $z$  and in the  $x - y$  plane.

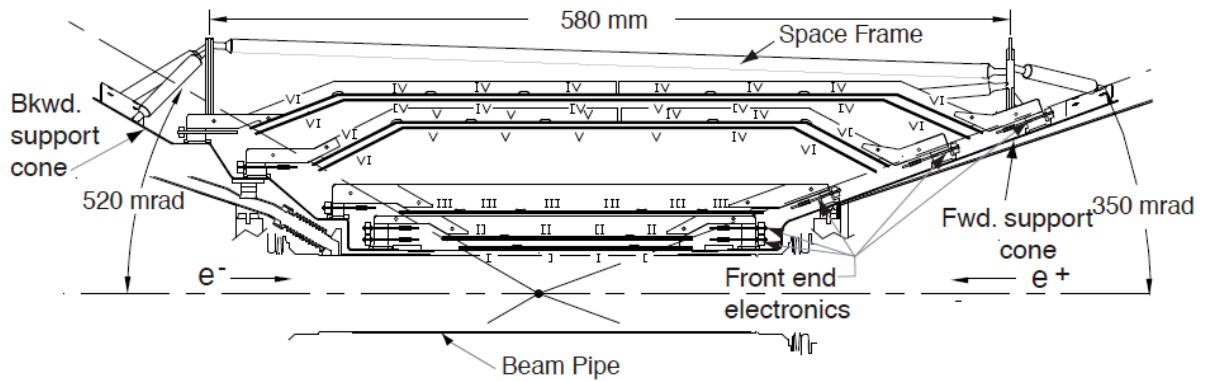


Figure 3.6: Longitudinal section of the SVT detector.

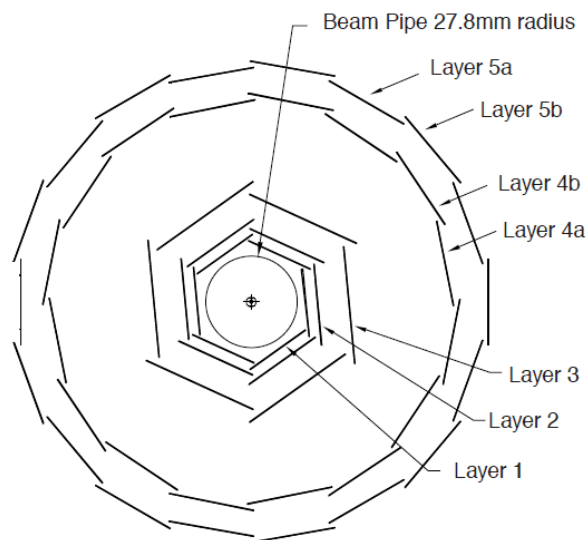


Figure 3.7: Transverse section of the SVT detector.

The outer two layers, composed by 16 and 18 modules, have a peculiar arch structure to reduce the incident angles of particles going in the forward and backward direction, and their barrel parts are placed at radii between 12.7 and 14.6 cm from the beam axis. They permit an accurate polar angle measurement and, along with the inner three layers, enable standalone

tracking for particles with low transverse momentum. Full azimuthal coverage is obtained by partially overlapping adjacent modules, which is also advantageous for alignment. The polar angle coverage in the laboratory frame is  $20.1^\circ < \theta_{LAB} < 150.2^\circ$ .

Each silicon detector consists of a high-resistivity  $n^-$  bulk implanted with  $p^+$  strips on one side and orthogonally-orientated  $n^+$  strips on the other side. The strips are AC-coupled to the electronics via integrated decoupled capacitor, and the strip pitch varies from 50 to 210  $\mu\text{m}$  depending on the layer. The detector are operated in reverse mode at full depletion, with bias voltage ( $V_{bias}$ ) typically 10 V higher than the depletion voltage ( $V_{depl}$ ), which ranges between 25 - 35 V. The strips are biased through polysilicon resistors (4-20  $\text{M}\Omega$ ) and the detector active area is surrounded by an implanted guard ring that collects the edge currents and shapes the electric field in the active region.

### 3.3.2 Detector performance

#### Hit efficiency and resolution

The SVT hit efficiency is determined by comparing the number of hits found by a half-module and assigned to a reconstructed track to the number of tracks crossing the active area of the module. Excluding the readout section which were defective, the combined hardware and software efficiency is measured to be about 97%.

Fig. 3.8 shows the measured SVT spatial hit resolution in the  $z$  and  $r - \phi$  for the five layers, as a function of the track incident angle with respect to the silicon wafer plane. The spatial resolution of SVT hits is determined by measuring the distance between the track trajectory and the hit, using high-momentum tracks in two prong events. The uncertainties due to the track trajectory is subtracted to obtain the hit resolution, which varies between 15 and 50 microns.

#### $dE/dx$ resolution

Limited particle identification (PID) for low momentum particles that do not reach the drift chamber and the Čerenkov detector is provided by the SVT through the measurement of the specific ionization loss,  $dE/dx$ , as derived from the total charge deposited in each silicon layer. It is computed as a truncated mean from the lowest 60% of the individual  $dE/dx$  measurements for tracks with at least 4 associated SVT hits. The resulting SVT  $dE/dx$  distribution as a function of momentum is shown in Fig. 3.9 [84]. The superimposed Bethe-Bloch curves for the individual particle species have been determined using various particle control sample, and a  $2\sigma$  separation between kaons and pions can be achieved up to momenta of 500  $\text{MeV}/c$ .

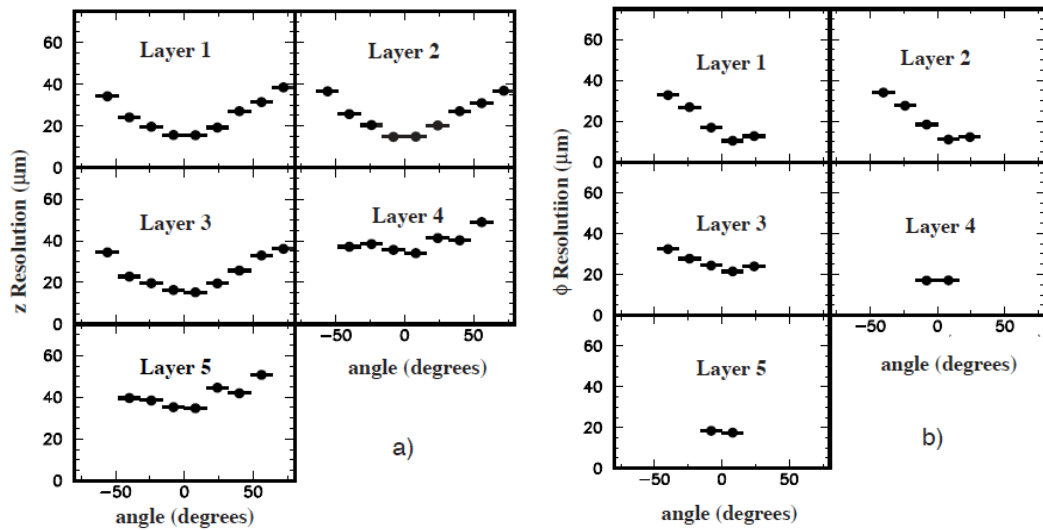


Figure 3.8: SVT hit resolution in the  $z$  (a) and  $\phi$  (b) coordinate in microns, plotted as a function of track incident angle in degrees. Each plot shows a different layer of the SVT. The plots in  $\phi$  coordinate for layers 1-3 are asymmetric around  $\phi = 0$  because of the “pinwheel” design of the inner layers. There are fewer points in the  $\phi$  resolution plots for the outer layers as they subtend smaller angles than the inner layers.

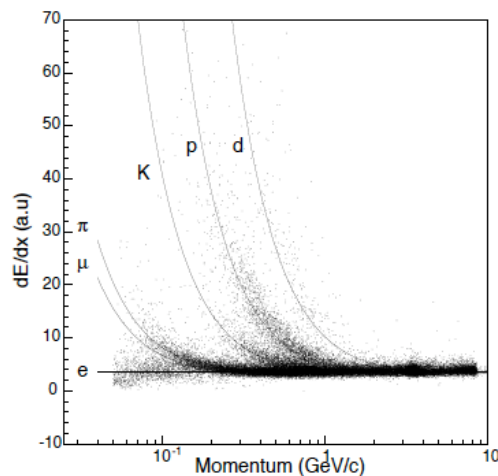


Figure 3.9: Energy loss per unit length ( $dE/dx$ ) as measured in the SVT as a function of momentum. The enhancement of protons is due to beam-gas interactions. The vertical scale is arbitrary.

### 3.4 The Drift Chamber (DCH)

The DCH sub-detectors is the main tracking device for charged particles with transverse momenta  $p_T$  above 120 MeV/c, providing the measurement of  $p_T$  from the curvature of the particle

trajectory inside the solenoid. The DCH also allows the reconstruction of secondary vertices outside the SVT volume, such as those from  $K_S^0 \rightarrow \pi^+\pi^-$  decays. For this purpose, the chamber should be able to measure not only the transverse momenta and position, but also the longitudinal position of the tracks ( $z$ ), with a resolution of  $\sim 1$  mm. Good  $z$  resolution also aids in matching DCH and SVT tracks and in projecting tracks to the DIRC and the calorimeter.

For low momentum particles, the DCH provides PID by measurement of the  $dE/dx$ , thus allowing the  $K/\pi$  separation up to  $\approx 700$  MeV/c. This capability is complementary to that of the DIRC in the barrel region, while in the extreme backward and forward directions, the DCH is the only device to discriminate between different particle hypotheses.

### 3.4.1 Detector layout

The design adopted for the DCH is illustrated in Fig. 3.10. It consists of a 280 cm long cylinder located within the volume inside the DIRC and outside the PEP-II support tube [85]. The active volume provides charged particle tracking over the polar angle range  $17.2^\circ < \theta_{LAB} < 152.6^\circ$ .

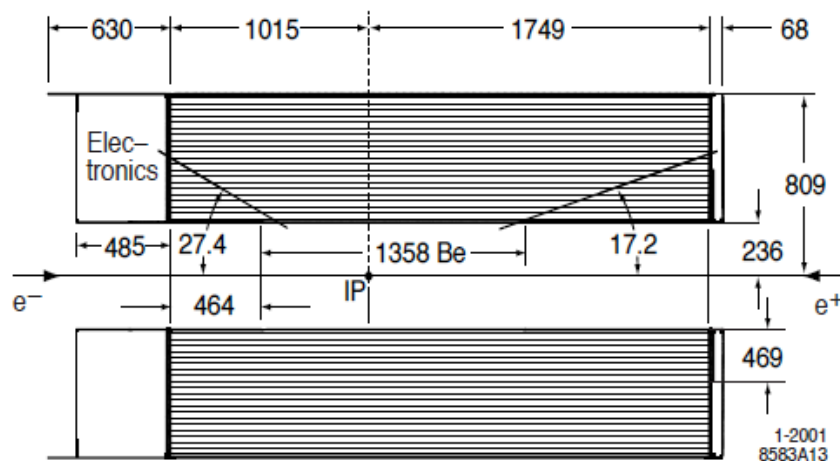


Figure 3.10: Longitudinal section of the drift chamber. Lengths are in mm, angles in degrees.

The drift system consists of 7104 hexagonal cells, approximately 1.8 cm wide by 1.2 cm high, arranged in 40 concentric layers. Each hexagonal cell consists of one sense wire surrounded by six field-shaping wires, as shown in Fig. 3.11(b). In such configuration, an approximated circular symmetry of equipotential contours is reached over a large portion of the cell. Table 3.4 reports the wire specifications. A positive high voltage is applied to the sense wires, while the field wires are at ground potential.

The 40 concentric layers are grouped by 4 into super layers, as shown in Fig. 3.11(a) for the four innermost super-layers. This arrangement enables local segment finding and left-right ambiguity resolution, even if one out of four signals is missing. For this reason two different wire

Type	Material	Diameter ( $\mu\text{m}$ )	Voltage (V)	Tension (g)
Sense	W-Re	20	1960	30
Field	Al	120	0	155
Guard	Al	80	340	74
Clearing	Al	120	825	155

Table 3.4: DCH wire specification. All wires are gold plated.

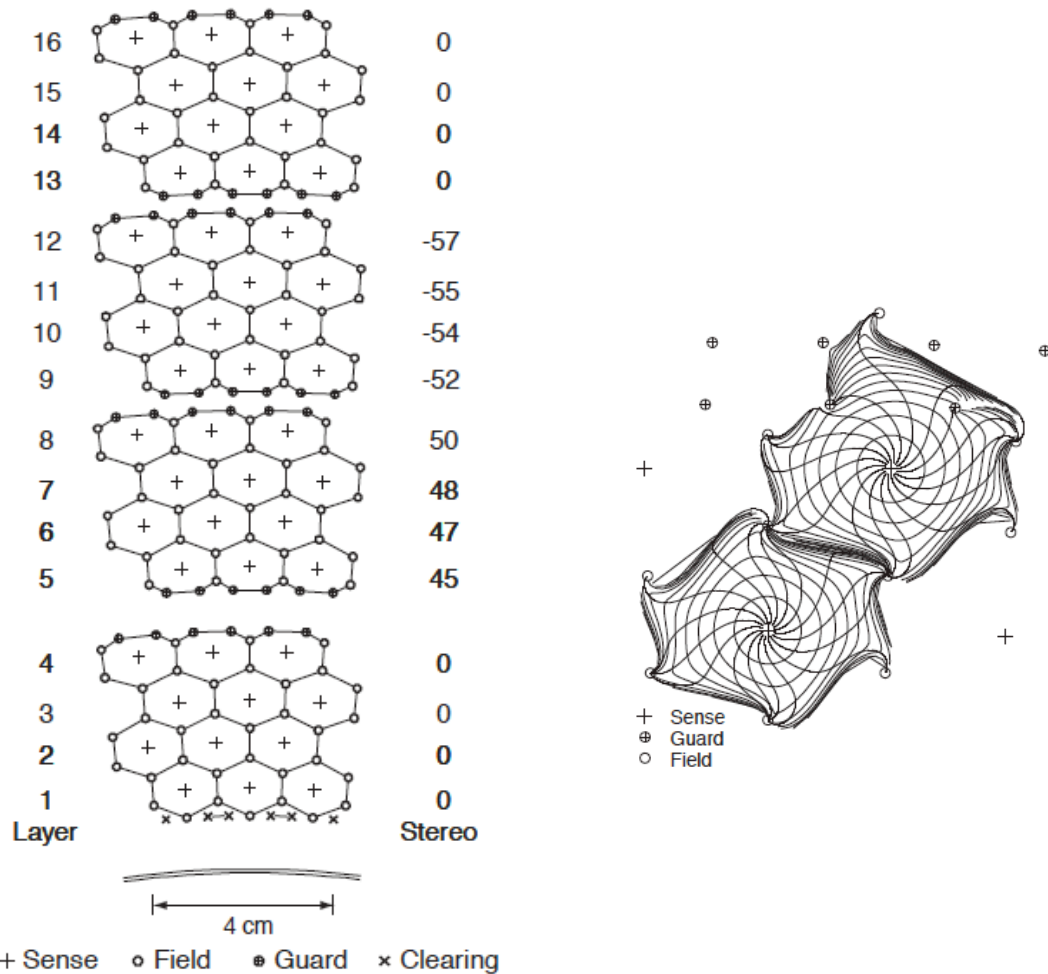
Parameter	Values
Mixture He: C <sub>4</sub> H <sub>10</sub>	80:20
Radiation Length	807 m
Primary Ions	21.2/cm
Drift Velocity	22 $\mu\text{m}/\text{ns}$
Lorentz Angle	32°
$dE/dx$ Resolution	6.9%

Table 3.5: Proprieties of helium-isobutane gas mixture at atmospheric pressure and 20° C. The drift velocity is given for operation without magnetic field, while the Lorentz angle is stated for a 1.5T magnetic field.

types are used: the axial type wires (A), parallel to the  $z$ -axis, provide position measurements in the  $x$ - $y$  plane, while longitudinal position information is obtained with wires placed at small angles with respect to the  $z$ -axis (stereo wires, U or V type). Sense and field wires have the same orientation in each super-layer and are alternating following the scheme AUVAUVAUVA, as shown in Fig. 3.11(a).

The 40 layers provide up to 40 spatial and ionization loss measurements for charged particles with  $p_T$  greater than 180 MeV/c. In order to reduce the impact of multiple scattering on  $p_T$  resolution, material within the chamber volume has been minimized (0.2%  $X_0$ ) using low-mass aluminum field-wires and a helium-isobutane gas mixture. The main proprieties of the gas are listed in Tab. 3.5.

The inner cylindrical wall of the DCH is kept thin to facilitate the matching of the SVT and DCH tracks, to improve the track resolution for high momentum tracks, and minimize the background from photon conversion and interaction. In addition, the HV distribution and all the readout electronics are mounted on the backward endplate of the chamber, in order to minimize the material in the forward direction, so as not to degrade the DIRC and EMC performances.



(a) DCH cell configuration in the first 16 layers

(b) DCH cell structure with 100 ns isochrones.

Figure 3.11: *BABAR* DCH cell configuration. In the left plot (a), lines have been added between field wires to aid in visualization of the cells, and the number on its right side give the stereo angles (mrad) of sense wires in each layer. The 1 mm-thick beryllium inner cylinder is also shown inside the first layer. In the right plot, is shown the cell structure. The plus sign, open circles, filled circles, and crosses denote sense wire, field wires, guard wires and clearing wires, respectively.

### 3.4.2 Detector performance

#### Tracking efficiency and resolution

The drift chamber reconstruction efficiency has been measured on data in selected samples of multi-hadron events by exploiting the fact that the tracks can be reconstructed independently in the SVT and in the DCH. The absolute DCH tracking efficiency is determined as the fraction of all the tracks detected in the SVT which are also reconstructed by the DCH when they fall

within its acceptance. In Fig. 3.12 [79] is shown its dependency on the transverse momentum and polar angle. At the design voltage of 1960 V the DCH efficiency averages to  $98 \pm 1\%$  for tracks above 200 MeV/c and polar angle  $\theta > 500$  mrad ( $29^\circ$ ). At the typical operating voltage of 1930 V it decreases by about 2%.

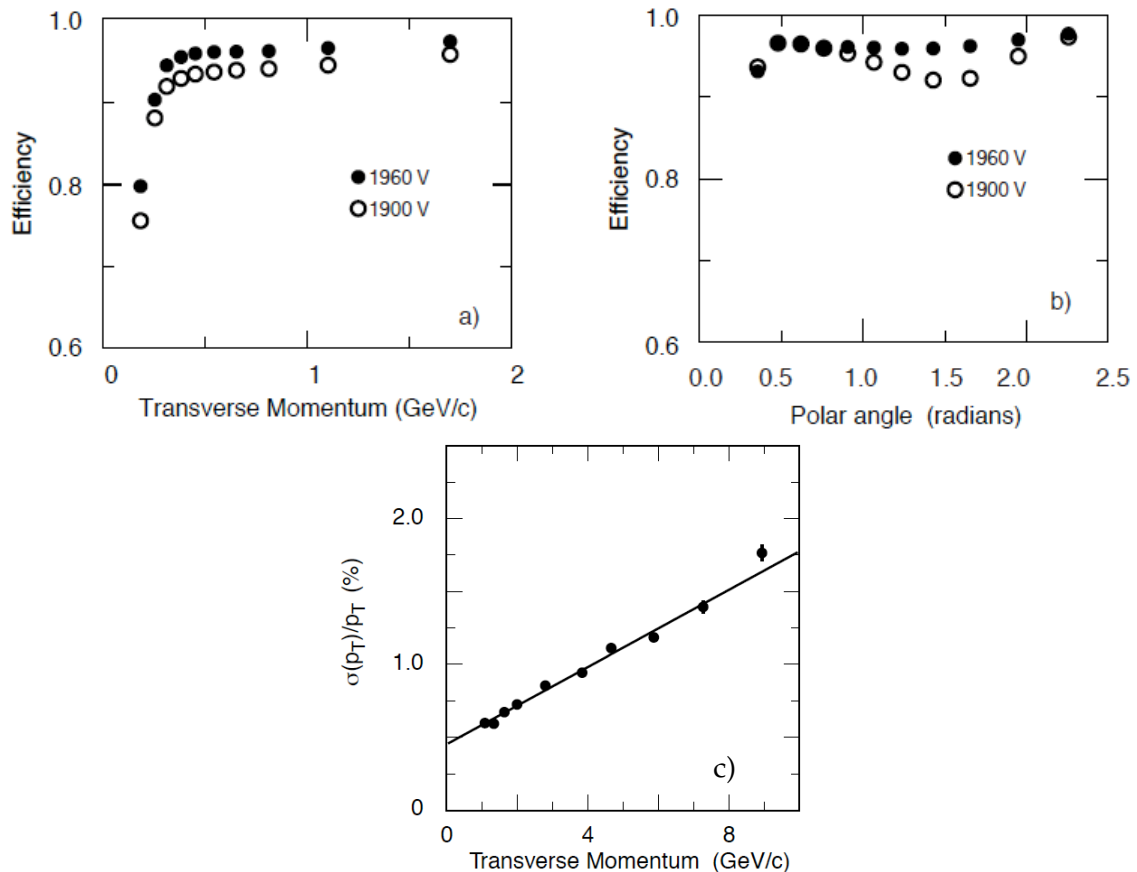


Figure 3.12: Track reconstruction efficiency in the DCH at operating voltages of 1900V and 1960V, as a function of (a) transverse momentum, and (b) polar angle. In plot c) the  $p_T$  resolution determined from cosmic ray muons is shown.

The  $p_T$  resolution, directly related to the curvature resolution, is measured as a function of  $p_T$  in cosmic ray studies (see Fig. 3.12c). The data are well represented by a linear function:

$$\frac{\sigma p_T}{p_T} = (0.13 \pm 0.01)\% \cdot p_T + (0.45 \pm 0.03)\% \quad (3.2)$$

where  $p_T$  is measured in GeV/c. The first contribution (dominating at high transverse momentum) comes from the curvature error due to the finite spatial measurement resolution. The second term (dominating at low momenta) is due to multiple Coulomb scattering.

### $dE/dx$ resolution

The specific energy loss,  $dE/dx$ , for charged particles traversing the DCH is derived from measurement of the total charge deposited in each drift cell. It is computed as a truncated mean from the lowest 80% of the individual  $dE/dx$  measurements. Various corrections are applied to remove sources of bias (as changes in the gas gain due to temperature and pressure variations, differences in cell geometry,...) that would degrade the accuracy of the primary ionization measurement.

The left plot (a) of Fig. 3.13 shows the distribution of the reconstructed and corrected  $dE/dx$  from the DCH as a function of the track momenta. The superimposed Bethe-Bloch prediction for different masses have been determined using various particle control samples. The achieved resolution is typically 7.5% (as shown in the right plot (b) of Fig. 3.13 for  $e^\pm$  from Bhabha scattering), limited by the number of samples and Landau fluctuations. A  $3\sigma$  separation between kaons and pions can be achieved up to momenta of about 700 MeV/c [86].

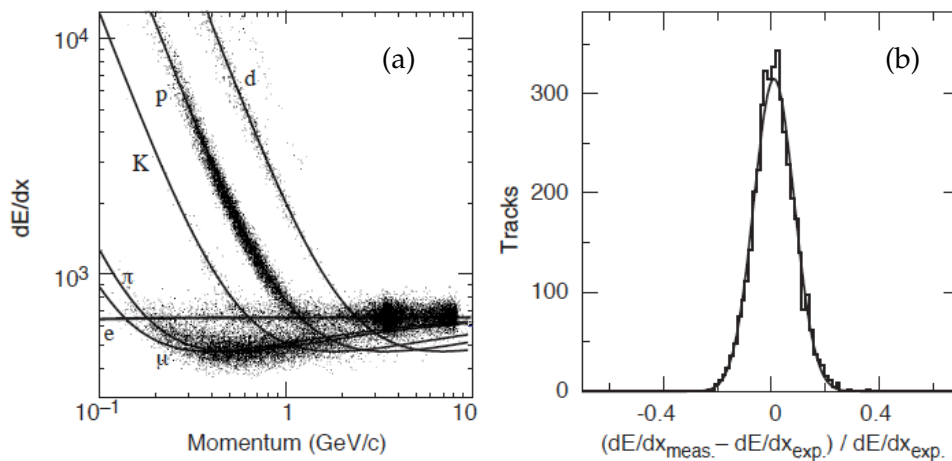


Figure 3.13: (a)  $dE/dx$  as a function of track momentum. The data include large samples of beam background triggers, as evident from the high rate of protons. The unit of the  $dE/dx$  curve is arbitrary due to the corrections for the deposited charge in individual DCH cells. (b) Difference between the measured and expected  $dE/dx$  for  $e^\pm$  from Bhabha scattering. The curve is the result of the fit to the data described in the text.

## 3.5 The Čerenkov light detector

The PID at low momenta exploits primarily the  $dE/dx$  measurements in the DCH and SVT. For momenta above 700 MeV/c, the  $dE/dx$  information does not allow to separate pions and kaons and, therefore, a dedicated PID sub-detector is needed.

The Detector of Internally Reflecting Čerenkov Radiation (DIRC), has been designed to provide  $K/\pi$  separation of  $\gtrsim 3\sigma$ , for all tracks with momenta from the pion Čerenkov threshold

up to more than 4 GeV/c.

### 3.5.1 Detector layout

The DIRC [87] is a novel type of ring-imaging Čerenkov detector, based on the principle that the magnitude of angles are maintained upon reflection from a flat surface.

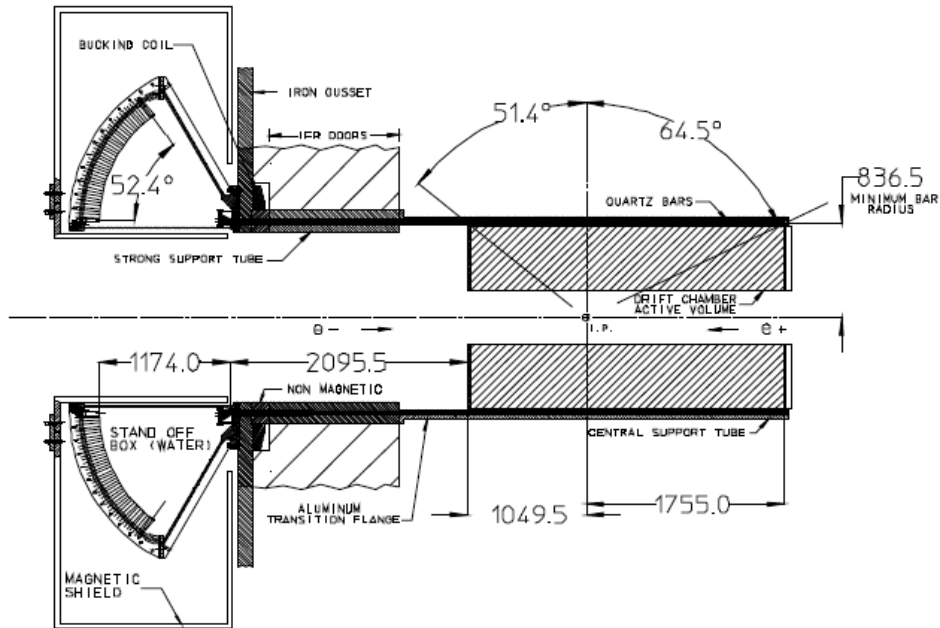


Figure 3.14: Schematics of the DIRC mechanical support structure.

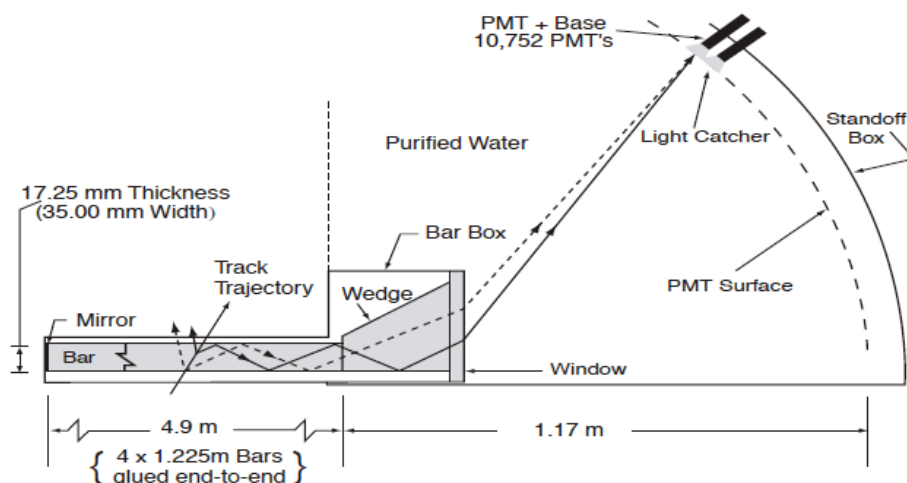


Figure 3.15: Schematics of the DIRC fused silica radiator bar and imaging region.

Fig. 3.14 shows the schematic geometry of the DIRC, while Fig. 3.15 illustrates the principles of light production, transport, and imaging.

The radiator material of the DIRC is synthetic fused silica in the form of long, thin bars with rectangular cross section. The bars, which are 17 mm-thick, 35 mm-wide, and 4.9 m-long, are placed into 12 hermetically sealed containers, called *bar boxes*, made of very thin aluminum-hexcel panels. Each bar box contains 12 bars, for a total of 144 bars.

The solid angle subtended by the radiator bars corresponds to 94% of the azimuth and 83% of the cosine of the polar angle in the CM system. The total thickness of the DIRC material (bars and support structure) at normal incidence is only 8 cm, corresponding to 17%  $X_0$ . Such a thin Čerenkov detector allows a larger inner tracking volume, which is needed to achieve the desired momentum resolution, and a compact outer electromagnetic calorimeter with improved angular and energy resolution and limited costs.

The bars serve both as radiators and as light pipes for the portion of the light trapped in the radiator by total internal reflection, where the internal reflection coefficient of the bar surfaces is greater than 0.9992 per bounce.

A charged particles with velocity  $v > c/n$ , traversing the fused silica bar (refraction index  $n = 1.473$ ), generates a cone of Čerenkov photons of half-angle  $\theta_c$  with respect to the particle direction, where  $\theta_c$  is the Čerenkov angle and  $\cos \theta_c = 1/\beta n$  ( $\beta = v/c$ ,  $v$  is the velocity of the particle). For particles with  $\beta \approx 1$ , some photons will always lie within the total internal reflection limit, and will be transported to either one or both ends of the bar, depending on the particle incident angle. To avoid instrumenting both ends of the bars with photon detectors, a mirror is placed at the forward end, perpendicular to the bar axis, to reflect incident photons to the backward, instrumented end.

Once photons arrive at the instrumented end, most of them emerge into a water-filled expansion region, called *standoff box*, containing 6000 liters of purified water ( $n=1.346$ ). A fused silica wedge at the exit of the bar reflect photons at large angles relative to the bar axis, reducing the size of the required detection surface. The photons are detected by an array of densely packed photon-multiplier tubes (PMTs), each surrounded by reflecting "light catcher" cones to capture light that would otherwise miss the active area of the PMT. The PMTs are placed at a distance of about 1.2 m from the bar end. The expected Čerenkov light pattern at this surface is essentially a conic section, where the opening angle is the Čerenkov production angle modified by refraction at the exit from the fused silica window.

### 3.5.2 Detector performance

In the absence of correlated systematic errors, the resolution ( $\sigma_{C,track}$ ) on the track Čerenkov angle should scale as

$$\sigma_{C,track} = \frac{\sigma_{C,\gamma}}{\sqrt{N_\gamma}}, \quad (3.3)$$

where  $\sigma_{C,\gamma}$  is the single photon Čerenkov angle resolution, and  $N_\gamma$  is the number of detected photons.

The single photon Čerenkov resolution has been measured in di-muon events to be 10.2 mrad (see Fig. 3.16(a) [79]). The main contributions to it come from the geometry of the detector (the size of the bars, the diameter of the PMTs, and the distance between the bars and the PMTs give a 7 mrad contribution) and from the spread of the photon production angle, dominated by a 5.4 mrad chromatic term. The measured time resolution (Fig. 3.16(b)) is 1.7 ns, close to the intrinsic 1.5 ns transit time spread of the PMTs.

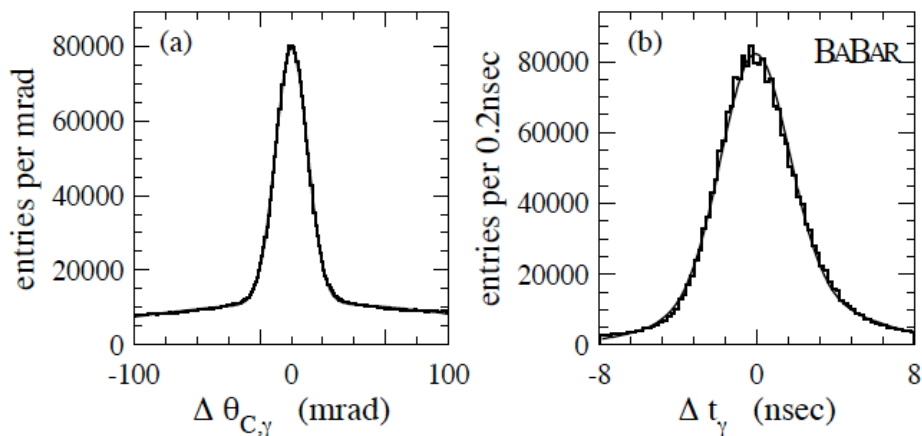


Figure 3.16: The difference between the measured and expected values of the Čerenkov angle for single photons,  $\Delta\theta_{C,\gamma}$  (a), and the measured and expected photon arrival time, for single muons in  $\mu^+\mu^-$  events (b).

In Fig. 3.17 the number of detected photons is shown as a function of the polar angle. It increases from a minimum of about 16 at the center of the barrel ( $\theta \approx 90^\circ$ ) to well over 50 at large polar angles (in the forward and backward direction), corresponding to the fact that the path-length in the radiator is longer for tracks emitted at large dip angles (greater number of Čerenkov photons produced in the bars) and the fraction of photons trapped by total internal reflection rises. This feature is very useful in the *BABAR* environment, where the particles are emitted preferentially in the forward direction as a consequence of the boost of the CM. The bump at  $\cos\theta = 0$  is a result of the fact that for tracks at small angles internal reflection of the Čerenkov photons occurs in both the forward and backward direction. The small decrease of the number of photons from the backward direction to the forward one is a consequence of the photon absorption along the bar before reaching the stand-off box in the backward end.

The combination of the single photon Čerenkov angle resolution, the distribution of the number of detected photons versus the polar angle, and the polar angle distribution of the charged tracks yield a typical track Čerenkov angle resolution which is about 2.5 mrad for muons in di-muon events.

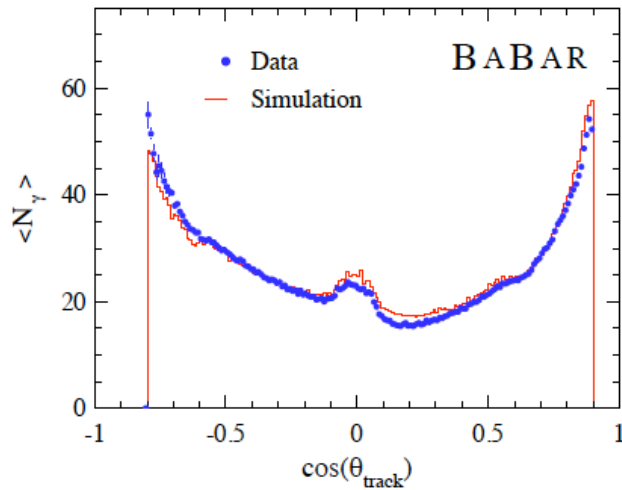


Figure 3.17: Number of detected photons versus track polar angle for reconstructed tracks in di-muon events compared to the Monte Carlo simulation.

The efficiency for correctly identifying a charged kaons that traverses a radiator bar, and the probability to wrongly identify a pion as a kaon, are determined using  $D^{*\pm} \rightarrow D^0\pi^\pm$  ( $D^0 \rightarrow K^\mp\pi^\pm$ ) decays reconstructed in data, where  $K^\mp/\pi^\pm$  tracks are identified through the charge correlation with the  $\pi^\pm$  from the  $D^{*\pm}$  decay.

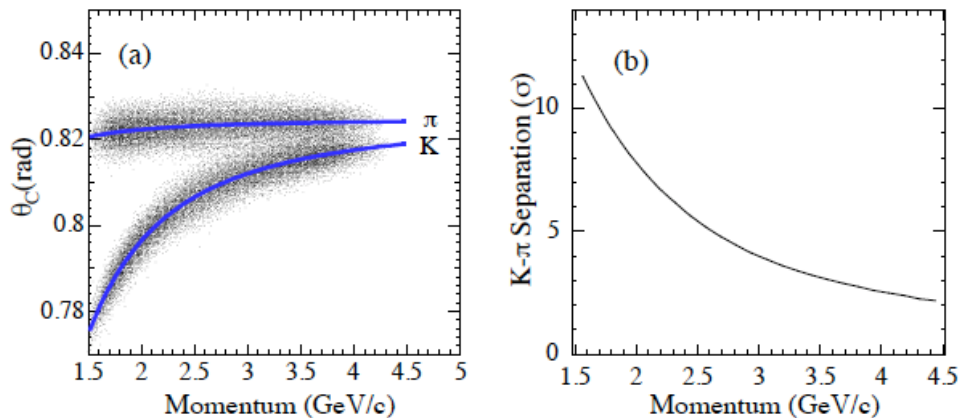


Figure 3.18: (a) The measured Čerenkov angle for pions (upper band) and kaons (lower band) from  $D^{*\pm} \rightarrow D^0\pi^\pm$ ,  $D^0 \rightarrow K^\mp\pi^\pm$  decays reconstructed in data. The curves show the expected angle  $\theta_C$  as a function of LAB momentum, for  $K$  and  $\pi$  mass hypothesis. (b) The average difference between the expected value of  $\theta_C$  for pions and kaons divided by the uncertainties ( $|\theta_C^K - \theta_C^\pi|/\sigma_{\theta_C}$ ), as a function of momentum.

The distribution of the Čerenkov angle for pions and kaons as a function of the momentum is shown in Fig. 3.18(a), while Fig. 3.18(b) reports the separation between kaons and pions,

which is about 4.3 standard deviations at 3 GeV/c.

The DIRC is intrinsically a three-dimensional imaging device, using position and arrival time of the PMT signals. In order to associate the photon signals with the track traversing a bar, the vector pointing from the center of the bar end to the center of each PMT is taken as a measurement of the photon propagation angles ( $\alpha_x, \alpha_y, \alpha_z$ ). As the track position and angles are known from the tracking system, these three angles can be used to determine the two Čerenkov angles ( $\theta_C, \phi_C$ ). This constraint on  $\theta_C$  and  $\phi_C$  is particularly useful in suppressing hits from beam-generated background and from other tracks in the same event and also in resolving some ambiguities in the association between the PMT hits and the track (for instances, the forward-backward ambiguity between photons that have or have not been reflected by the mirror at the forward end of the bars).

The observable used to distinguish between signal and background photons is the difference between the measured and the expected photon time ( $\Delta t_\gamma$ , shown in Fig. 3.16). The expected photon arrival time is calculated for each photon using the track time-of-flight assuming it to be a charged pion, and the photon propagation time within the bar, the wedge, and the water filled standoff box. The measured photon arrival time is obtained from the recorded time of the candidate signal in the PMT, after calibration. The effect of applying the PMT time information in a di-muon event [79] is shown in Fig. 3.19. The background hits, principally due to the low energy photons from the accelerator, are reduced by about a factor 40.

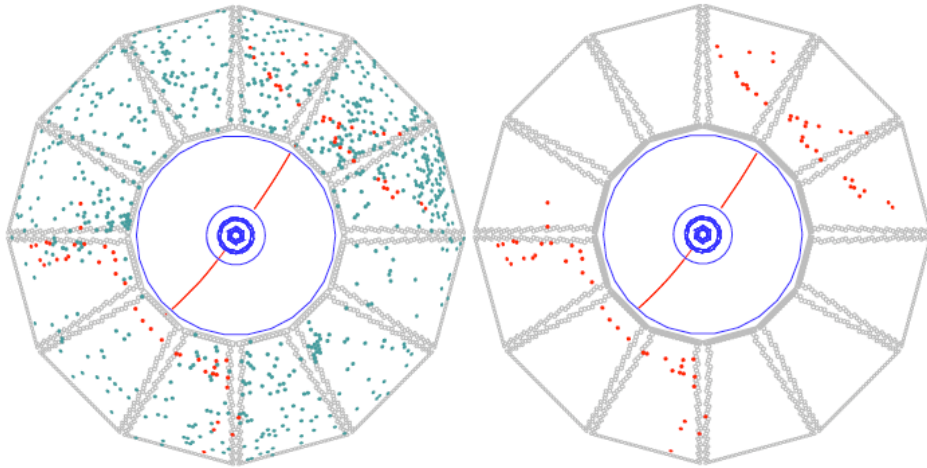


Figure 3.19: Display of an  $e^+e^- \rightarrow \mu^+\mu^-$  event reconstructed with two different time cuts. On the left, all DIRC PMTs with signal within 300 ns of the trigger time window are shown. On the right, only DIRC PMTs with signal within 8 ns of the expected Čerenkov photon arrival time are displayed.

### 3.6 The Electromagnetic Calorimeter

The *BABAR* electromagnetic calorimeter (EMC) is designed to measure electromagnetic showers with high efficiency, and excellent energy and angular resolution over an energy range between 20 MeV (low photons from  $\pi^0$  mesons from  $B$ -meson decays) and 9 GeV (electrons from Bhabha scattering). It is also the primary sub-detector providing electron-hadron separation.

Energy deposit clusters in the EMC with lateral shape consistent with the expected pattern from an electromagnetic shower are identified as photons if they are not associated with any charged tracks extrapolated from the tracking devices (DCH and SVT). Otherwise, they are identified as electrons if they are matched to a charged track and the ratio between the energy  $E$  measured in the EMC and the momentum  $p$  measured by the tracking system is  $E/p \approx 1$ .

The measurement of extremely rare decays of  $B$  mesons containing  $\pi^0$ s (e.g.,  $B^0 \rightarrow \pi^0\pi^0$ ) pose the most stringent requirements on energy resolution, namely of order 1-2%. The  $\pi^0$  mass resolution is dominated by the energy resolution for  $\pi^0$  of energy less than 2 GeV, and by the angular resolution at higher energies. Therefore, the angular resolution is required to be a few milliradians in order to maintain good  $m_\pi^0$  resolution at all energies ( $\sigma_{m_\pi^0} \approx 6.5$  MeV).

In addition, excellent photon identification at low energy ( $\sim 20$  MeV) is required for efficient reconstruction of decays containing multiple  $\pi^0$  and  $\eta$ . Similar precision is required for efficient separation of electrons and hadrons, with purity required at the 0.1% level for momentum as low as 500 MeV/ $c$ .

The need for high efficiency requires hermetic coverage of the acceptance region, while excellent resolution is achieved by minimizing the material in front of, and between, the active detector elements.

#### 3.6.1 Detector layout

The *BABAR* EMC [88] contains a cylindrical barrel and a conical endcap containing a total of 6580 CsI crystals doped with thallium (Tl) at 1% level. The main properties of CsI(Tl) are summarized in Tab. 3.6. The high light yield and the small Molière radius give the excellent energy and angular resolution required, while the short radiation length allows shower containment at the *BABAR* energies with a relatively compact design. Furthermore, the high light yield and the emission spectrum permit efficient use of silicon photodiodes readout. The transverse size of the crystals is chosen to be comparable to the Molière radius in order to achieve the required angular resolution at low energies. This choice is the best compromise, since the electromagnetic shower has a natural lateral spread of the Molière radius and the energy resolution would degrade if the transverse crystal size were chosen smaller than this radius, due to the summing of the electronic noise from several crystals.

Each crystal is a truncated trapezoidal pyramid, whose length increases from 29.6 cm (16  $X_0$ ) in the backward to 32.4 cm (17.5  $X_0$ ) in the forward direction to limit the effects of shower

Parameter	Values
Radiation Length	1.85 cm
Molière Radius	3.8 cm
Density	4.53 g/cm <sup>3</sup>
Light Yield	50000 $\gamma$ /MeV
Light Yield Temp. Coeff.	0.28%/°C
Peak Emission $\lambda_{max}$	565 nm
Refractive Index ( $\lambda_{max}$ )	1.80
Signal Decay Time	680 ns (64%) 3.3 $\mu$ s (36%)

Table 3.6: Proprieties of CsI(Tl).

leakage from increasingly higher energy particles (see Fig. 3.20a). To minimize the material in front of the calorimeter, the support structure of the crystals (made in carbon fiber) and the front-end electronic are located at the outer radius of the EMC. To recover the small fraction of light that is not internally reflected, each crystal is wrapped with a white diffuse reflector (TYVEK), 25  $\mu$ m aluminum foil and 13  $\mu$ m Mylar foil for insulation. The scintillation light generated inside each crystal is detected by two independent silicon PIN diodes.

The barrel contains 5760 crystals arranged in 48 distinct rows containing 120 identical crystals, with an inner radius of 90 cm, as shown in Fig. 3.20b. The forward end is closed by a separable endcap holding nine additional rows (1080 crystals). This geometry provides full azimuthal coverage, while the polar angle coverage is  $15.8^\circ < \theta_{LAB} < 140.8^\circ$ .

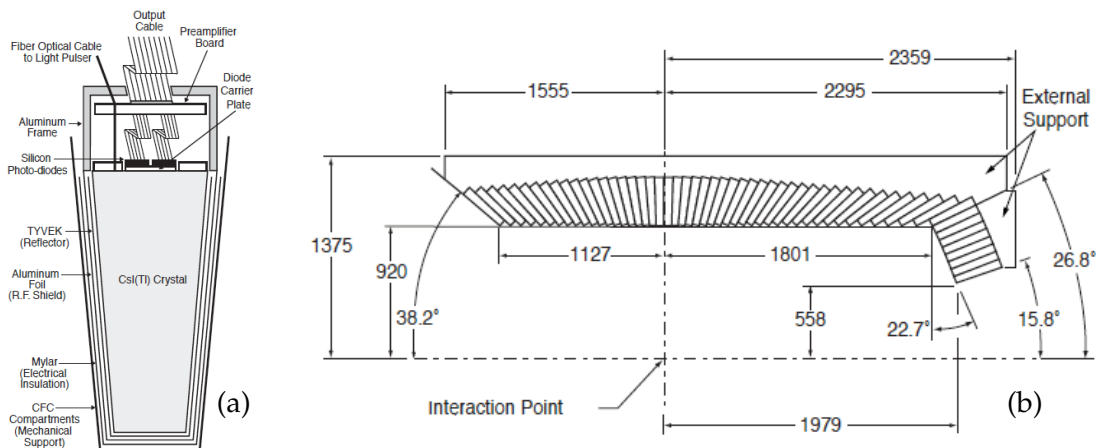


Figure 3.20: (a) Schematic view of one EMC crystal module. (b) Longitudinal cross section of the EMC (only the top half is shown). The detector is axially symmetric around the  $z$ -axis. All dimensions are given in mm.

### 3.6.2 Detector performance

The reconstruction of energy deposits in the calorimeter, is based on the concept of EMC cluster: it is defined as a contiguous array of crystals, all with energy above 0.5 MeV, whose total energy exceeds the threshold of 20 MeV in order to suppress background processes.

#### Energy resolution

The energy resolution of a homogeneous calorimeter is determined by fluctuations in the electromagnetic shower propagation and, for the *BABAR* EMC detector, is empirically described as a quadric sum of a stochastic term  $\sigma_1$  and a constant term  $\sigma_2$ :

$$\frac{\sigma_E}{E} = \frac{\sigma_1}{\sqrt[4]{E(\text{GeV})}} \oplus \sigma_2, \quad (3.4)$$

where  $E$  and  $\sigma_E$  refer to the energy of a photon and to its rms error.

The stochastic term  $\sigma_1 E^{-\frac{1}{4}}$ , which is dominant at low energies, arises primarily from the fluctuation in photon statistics, but it also depends on electron noise of the photon detector and electronics. The constant term  $\sigma_2$  is dominant at higher energies ( $> 1$  GeV). It arises from non uniformity in light collection, leakage or absorption in the material between and in front of the crystals, and uncertainties in the calibrations.

In *BABAR*, the energy resolution of the EMC is measured on data selected control samples, including electrons and positrons from Bhabha scattering (energies between 3 and 9 GeV), photons from  $\pi^0$  and  $\eta$  decays (energies below 2 GeV), and from the decay  $\chi_{c1} \rightarrow J\phi\gamma$  ( $E \approx 500$  MeV). At low energies the resolution is determined through weekly calibrations performed with a radioactive source ( $^{16}\text{O}^*$ ) of 6.13 MeV photons.

A fit to the resolution dependence on the energy with the empirical parametrization of Eq. (3.4), shown in Fig. 3.21(a), yields:

$$\frac{\sigma_E}{E} = \frac{(2.32 \pm 0.30)\%}{\sqrt[4]{E(\text{GeV})}} \oplus (1.85 \pm 0.12)\%, \quad (3.5)$$

which is in reasonable agreement with the Monte Carlo studies of the expected resolution.

#### Angular resolution

The angular resolution is determined by the transverse crystal size and the distance from the interaction point, and improves as the transverse size of the crystal decreases.

The measurement of the angular resolution is based on the analysis of  $\pi^0$  and  $\eta$  decays to two photons of approximately equal energy. The result is reported in Fig. 3.21. The resolution varies between about 12 mrad at low energies and 3 mrad at high energies. The data fits the

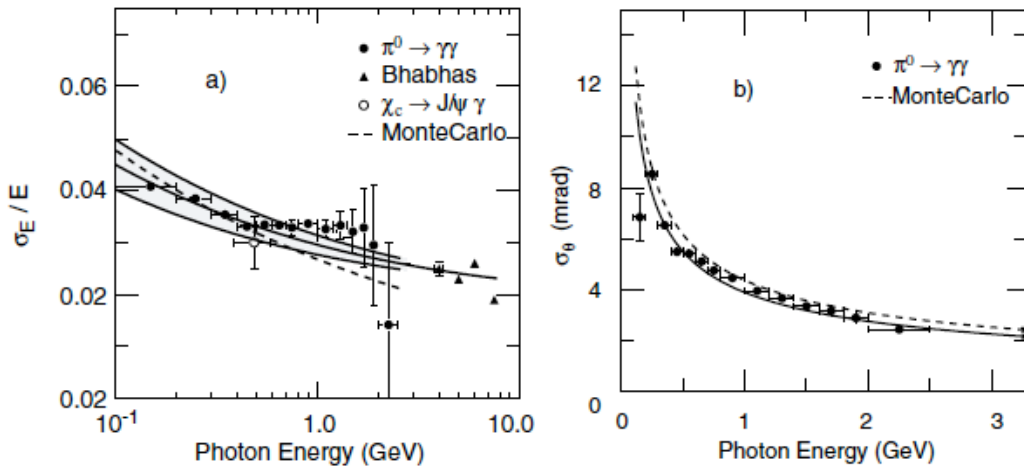


Figure 3.21: (a) Energy resolution for the EMC measured for photons and electrons from various processes. The solid curve is a fit to Eqn. (3.4) and the shaded area denotes the one sigma error of the fit. (b) EMC angular resolution measured using photon candidates from  $\pi^0$  decays. The solid curve is a fit to Eqn. (3.6).

empirical parameterization:

$$\sigma_\theta = \sigma_\phi = \left( \frac{3.87 \pm 0.07}{\sqrt{E(\text{GeV})}} + (0.00 \pm 0.04) \right) \text{ mrad.} \quad (3.6)$$

### Electron-Hadron separation

Electrons are separated from charged hadrons primarily on the basis of the shower energy, lateral shower moments, and track momentum. The most important variable for the discrimination of hadrons is the ratio of the shower energy to the track momentum ( $E/p$ ). Fig. 3.22 shows the efficiency for electron identification and the pion misidentification probability as a function of the track momentum and polar angle. The electron efficiency is measured using electrons from radiative Bhabha and  $e^+e^- \rightarrow e^+e^-e^+e^-$  events. The pion misidentification probability is measured using charged pions from  $K_S^0$  decays and three-prong  $\tau$  decay. For momenta above 1 GeV/c the electron identification is about 91% with an average pion misidentification of 0.2%.

## 3.7 The Instrumented Flux Return

The Instrumented Flux Return (IFR) is designed to identify muons and detect neutral hadrons (primarily  $K_L^0$ ) over a wide range of momenta and angles. The principal requirements for the IFR are large solid angle coverage, good efficiency, and high background rejection for muons down to momenta below 1 GeV/c. For neutral hadron, high efficiency and good angular resolution are crucial.

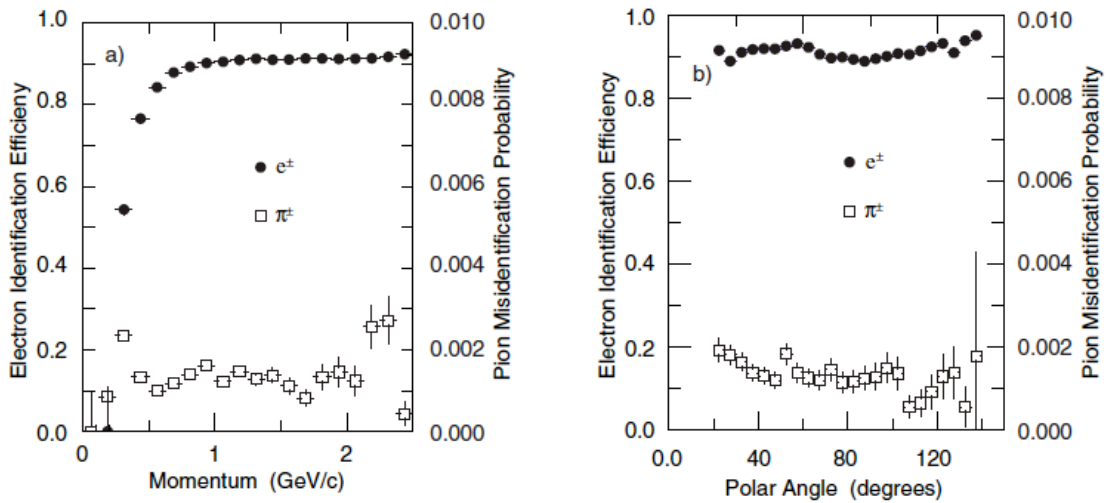


Figure 3.22: Electron efficiency and pion misidentification probability as a function of a) the particle momentum and b) the polar angle, measured in the laboratory system.

### 3.7.1 Detector layout

The IFR uses the steel flux return of the magnet as a muon filter and hadron absorber. Single gap Resistive Plate Chambers [89] (RPCs) with two-coordinate readout have been chosen as detector. RPCs detect streamers from ionizing particles via capacitive readout strips. They offer the advantage of simple, low cost construction and the possibility of covering odd shapes with minimal dead space. Further benefits are large signals and fast response allowing for simple and robust front end electronics and good time resolution, typically 1-2 ns. The position resolution, of the order of few millimeters, depends primarily on the segmentation of the readout strips. A cross section of an RPC is shown schematically in Fig. 3.23.

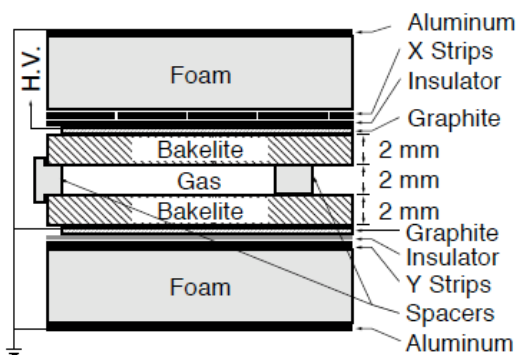


Figure 3.23: Cross section of a planar RPC with the schematics of the HV connection.

The planar RPC consists of two 2 mm-thick bakelite sheets, separated by a gap of 2 mm.

The bulk resistivity of the bakelite sheets has been especially tuned to  $10^{11} - 10^{12} \Omega\text{cm}$ , and the external surfaces are coated with graphite to achieve a surface resistivity of  $\sim 100 \text{ k}\Omega/\text{square}$ . The two graphite surface are connected to high voltage ( $\sim 8 \text{ kV}$ ) and protected by a insulating mylar film. The bakelite surfaces facing the gap are treated with linseed oil.

The RPC detectors are operated in limited streamer mode and the signals are read out capacitively on both sides of the gap, by external electrodes made of aluminum strips on a mylar substrate.

The RPCs are installed in the gaps of the finely segmented steel of the barrel and the two end doors of the iron for the magnetic flux return [90], as illustrated in Fig. 3.24. The steel is segmented into 18 plates, increasing in thickness from 2 cm of the inner 9 plates to 10 cm of outermost plates, for a total of 65 cm (60 cm in the endcap), which corresponds to about 4 interaction lengths. In addition, two layers of RPCs are installed between the EMC and the magnet cryostat to detect particles exiting the EMC. The configuration has been optimized on the basis of Monte Carlo studies of muon penetration and charged and neutral hadron interaction.

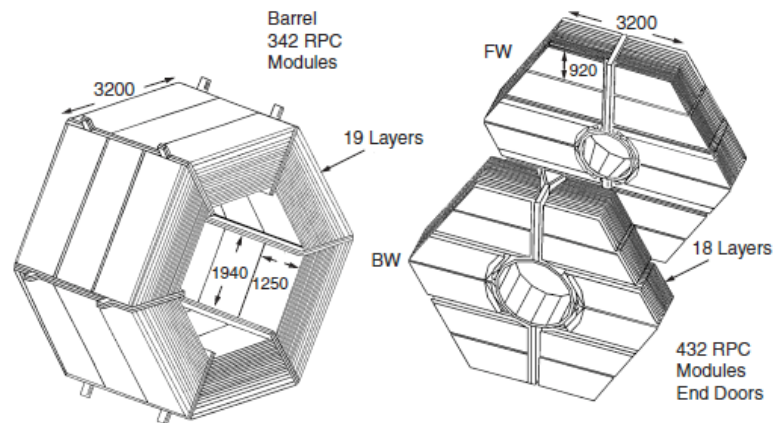


Figure 3.24: Overview of the IFR. On the left, is shown the barrel sectors and, on the right, the forward and backward end doors. The shape of the RPC modules and their dimensions are indicated.

Soon after the installation (Summer 1999), the efficiency of a large number of chambers (initially greater than 90%) has started to deteriorate at a rate of 0.5-1% per month. In order to solve this loss of efficiency, an extensive improvement program has been developed with multiple solutions. The RPCs in the forward end-cap region have been replaced in Summer 2002 with new ones based on the same base concept but with improved fabrication technique. The RPCs in the barrel region have been replaced with Limited Streamer Tube (LST) detectors [91]. The research and design phase started in 2002 with the first installation phase in Summer 2004 and the second phase in Autumn 2006. In particular, in the first installation phase, the RPCs



capability, wire surface quality and uniformity. Final results led to the configuration detailed above and a ternary gas mixture of Ar/C<sub>4</sub>H<sub>10</sub>/CO<sub>2</sub> (3/8/89)% was chosen.

### 3.7.2 Detector performance

#### Muon efficiency

The efficiency of RPCs and LSTs is evaluated using di-muon events collected both in normal condition data ( $e^+e^- \rightarrow \mu^+\mu^-$ ) and monthly dedicated cosmic ray runs. The efficiency is found by counting the number of times a hit is found in a certain chamber when a charged tracks is expected to traverse it, based on information from the other tracking system. The absolute efficiency at the nominal working voltage (typically 7.6 kV for RPC and 5.5 for LST) is stored in the *BABAR* condition database for use in the event reconstruction software.

As previously said, soon after the installation, a progressive efficiency deterioration has been observed in a significant fraction of the RPC chambers, as shown in Fig. 3.26. Several tests were performed in order to understand the causes of the loss of efficiency, and it was found that a number of prototype RPCs developed similar efficiency problems after being operated above a temperature of 36°C for a period of two weeks<sup>4</sup>. In some of these modules evidence was found that the linseed oil had accumulated at various spots under the influence of the electric field[93].

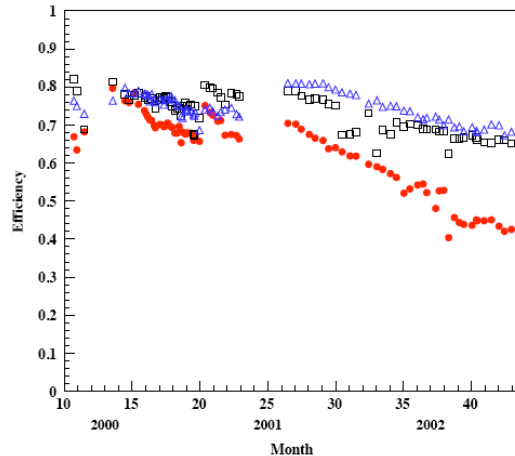


Figure 3.26: The average RPC efficiency in the barrel (red circles), forward end cap (blue triangles), and backward end cap (black squares) are shown as a function of time until summer 2002. The efficiency is evaluated using  $\mu^+\mu^-$  pairs from collision data.

After the installation of the LST detector, a stable muon efficiency was recovered, as shown in Fig. 3.27. The overall average efficiency at the end of the *BABAR* data-taking was about 88%,

<sup>4</sup>Similar temperature had been reached inside the iron during the first summer of operation due to the temperature in the experimental hall and the absence of water cooling system.

slightly below the designed efficiency. Beside the geometrical effect, the main sources of inefficiency are broken strips and wires which have been disconnected or kept to a lower voltage.

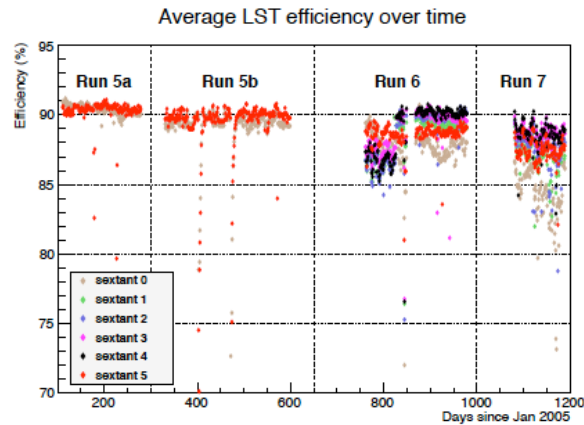


Figure 3.27: Time evolution of the average sextant detection efficiency of the LST detector. The inefficiency is localized in particular in the two innermost layers; for this reason it didn't affect the muon identification quality.

### Muon identification

While muon identification relies entirely on the IFR, other detector systems provide complementary information. Charged particles are reconstructed in the SVT and DCH and muon candidates are required to meet the criteria for minimum ionizing particles in the EMC. Charged tracks that are reconstructed in the tracking system are extrapolated to the IFR taking into account the non-uniform magnetic field, multiple scattering, and the average energy loss. The projected intersections of a track with the RPC and LST planes are computed and, for each readout plane, all clusters (groups of adjacent hits) detected within a predefined distance from the predicted intersection are associated with the track. Quantities used for  $\pi/\mu$  discrimination, in addition to the penetration depth in the iron of the track, are the average number and r.m.s. of the distribution of the RPC and LST hits per layer. The hits multiplicity per layer is expected to be larger for pions, producing an hadronic interaction, than for muons.

The performance of muon identification has been tested on samples of muons from  $\mu\mu ee$  and  $\mu\mu\gamma$  final state and pions from three-prong  $\tau$  decays and  $K_S \rightarrow \pi^+\pi^-$  decays. The typical muon identification efficiency and the pion mis-identification probability as a function of the track momentum and polar angle are shown in Fig. 3.28, while Fig. 3.29 displays the performances of a muon selector based on a neural network in the forward and barrel region, for different years of data taking. Due to the problems and replacement described above, the efficiency of the IFR detector shows large fluctuation through the years.

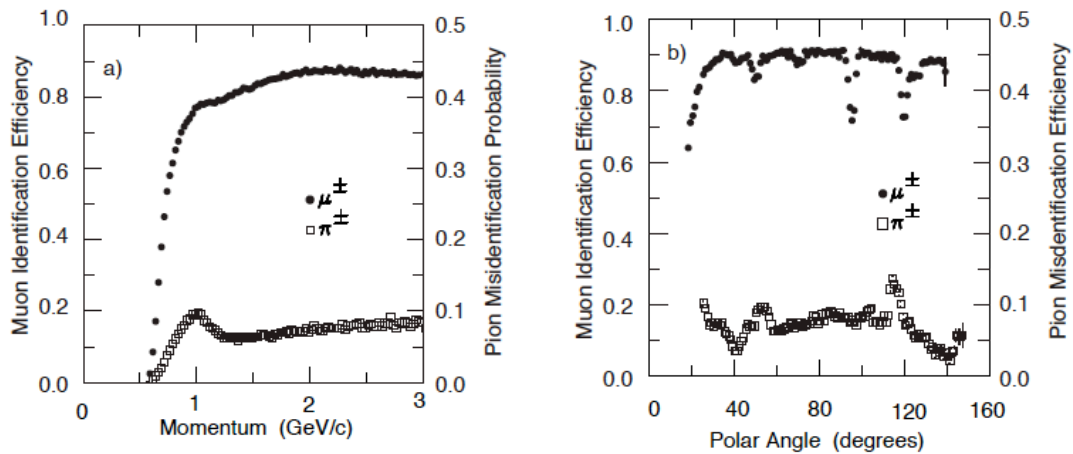


Figure 3.28: Muon efficiency (left scale) and pion misidentification probability (right scale) as a function of a) the laboratory track momentum, and b) the polar angle (for  $1.5 << 3.0$  GeV/c momentum).

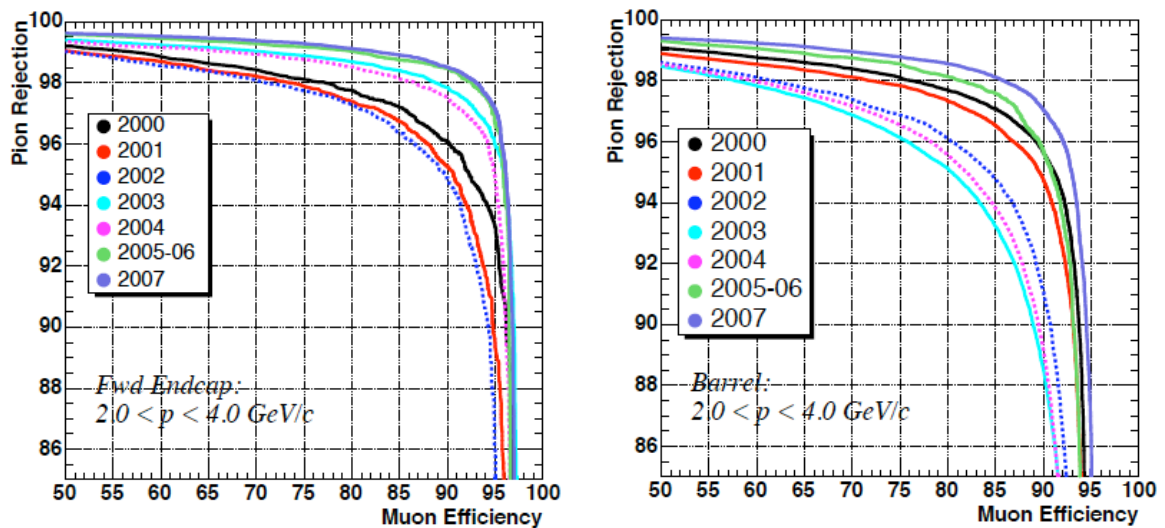


Figure 3.29: Pion mis-identification vs. muon efficiency rate of neural network algorithm for different period of *BABAR* data taking.

### Neutral Hadron Detection

Neutral hadrons interacting in the steel of the IFR are identified as clusters that are not associated with a charged track. Since a significant fraction of neutral hadrons interact before reaching the IFR, information from the EMC and the IFR is combined: neutral showers in the EMC are associated with the neutral hadrons detected in the IFR if their production angles, taken from the first interaction point in the detector, are consistent with each other. The  $K_L^0$  detection efficiency and angular resolution are measured on a control sample of  $K_L^0$  produced in

$e^+e^- \rightarrow \phi\gamma \rightarrow K_L^0 K_S^0 \gamma$  processes, where the  $K_L^0$  direction is inferred from the missing momentum calculated from the particles that are reconstructed in the final state ( $\gamma$  and  $K_S^0$ ). The  $K_L^0$  reconstruction efficiency increases roughly linearly with momentum between 20% at 1 GeV/c and 40% at 4 GeV/c (EMC and IFR combined), and the angular resolution is of the order of 50 mrad.

### 3.8 The *BABAR* Trigger

The *BABAR* trigger is designed to select a large variety of physics processes rejecting background events and keeping a total event rate around 300 Hz so as do not overload the downstream processing. The trigger must select the physics events of interest with very high and/or well understood efficiency, depending on the particular mode.

The trigger system is implemented as two-level hierarchy, an hardware based Level 1 (L1) followed by a software based Level 3 (L3)<sup>5</sup>. The goal of the L1 hardware trigger is to reduce the rate to a level acceptable for the L3 software trigger, which runs on a farm of commercial processors. The L1 trigger is optimized for simplicity and speed, and is designed to provide an output trigger rate of the order of 2 kHz or less. The L1 trigger selection is based on charged tracks in the DCH, showers in the EMC, and tracks detected in the IFR. Its maximum response latency for a given collision is 11  $\mu$ s.

Based on both the complete event and L1 trigger information, the L3 software algorithms select events of interest allowing them to be transferred to mass storage for further analysis. Dedicated L1 trigger processors receive data which are continuously clocked in from the DCH, EMC, and IFR detector subsystem. The L1 trigger processor produces a 30 MHz clocked output to the *Fast Control and Timing System* (FCTS) that can optimally mask or prescale input triggers. Tab. 3.7 summarizes the cross section, production rates and L1 trigger rates for the main physical processes at the  $\Upsilon(4S)$  resonance for the design luminosity  $\mathcal{L} = 3 \cdot 10^{33} \text{ cm}^{-2}\text{s}^{-1}$ .

The L3 trigger is implemented as a software that makes use of the complete event information for taking its decision, including the output of the L1 trigger processors and of the FCTS. The selection decision is primarily taken by two set of orthogonal filters, one exclusively based on the DCH information, the other based on the EMC data only. The DCH filters select events containing at least one high  $p_T$  track ( $p_T > 600 \text{ MeV}/c$ ) or two low  $p_T$  tracks, originating from the interaction point. The all-neutral trigger for L3 is based on information from the EMC. The EMC filter identifies energy clusters with a sensitivity sufficient for finding minimum ionizing particles. To filter out noise, individual crystal signals below an energy threshold 20 MeV or which lie outside a 1.3  $\mu$ s time window around the event are rejected. Cluster with a total energy above 100 MeV are retained, and the energy weighted centroid and average time, the

<sup>5</sup>An intermediate Level 2 (L2) software trigger was originally foreseen in the very early step of *BABAR* design, but it was soon merged in the L3 trigger.

Event type	Cross section nb	Production Rate Hz	L1 Trigger Rate Hz
$b\bar{b}$	1.1	3.2	3.2
other $q\bar{q}$	3.4	10.2	10.1
$e^+e^-$	$\sim 53$	159	156
$\mu^+\mu^-$	1.2	3.5	3.1
$\tau^+\tau^-$	0.9	2.8	2.4

Table 3.7: Effective cross section, production rates, and trigger rates for the principal physics processes at the  $\Upsilon(4S)$  for a luminosity of  $\mathcal{L} = 3 \cdot 10^{33} \text{ cm}^{-2}\text{s}^{-1}$ .

L3 trigger	$\epsilon_{b\bar{b}}$	$\epsilon_{B \rightarrow \pi^0 \pi^0}$	$\epsilon_{B \rightarrow \tau \nu}$	$\epsilon_{c\bar{c}}$	$\epsilon_{uds}$	$\epsilon_{\tau\tau}$
1 track filter	89.9	69.9	85.5	89.2	88.2	94.1
2 track filter	98.9	84.1	94.5	96.1	93.2	87.6
Combined DCH filters	99.4	89.1	96.6	97.1	95.4	95.5
2 cluster filter	25.8	91.2	14.2	39.2	48.7	34.3
4 cluster filter	93.5	95.2	62.3	87.4	85.5	37.8
Combined EMC filters	93.5	95.7	62.3	87.4	85.6	46.3
Combined DCH+EMC filters	>99.9	99.3	98.1	99.0	97.6	97.3
Combined L1+L3	>99.9	99.1	97.8	98.9	95.8	92.0

Table 3.8: L3 trigger efficiency (%) for various physics processes, derived from Monte Carlo simulation.

number of crystals, and a lateral moment describing the shower shape for the particle identification are calculated. The L3 trigger efficiency for MonteCarlo simulated events are shown in Tab. 3.8 for events that passed L1.



## Chapter 4

# Collins Asymmetry: analysis strategy

As reported in chapter 2, the Collins fragmentation function describes the production of a hadron with transverse momentum  $\mathbf{P}_{h\perp}$  from a transversely polarized quark with spin  $\mathbf{S}_q$  and momentum  $\mathbf{k}$ .

Following the Trento convention [94], the number densities for finding an hadron  $h$  produced from a transversely polarized quark  $q$  is defined as:

$$D_{h,q\uparrow} = D_1^q(z, P_{h\perp}^2) + H_1^{\perp q}(z, P_{h\perp}^2) \frac{(\hat{\mathbf{k}} \times \mathbf{P}_{h\perp}) \cdot \mathbf{S}_q}{zM_h}. \quad (4.1)$$

The first term in Eq.(4.1) is the unpolarized fragmentation function, where  $z = 2E_h/Q$  is the fractional energy of the hadron in the  $e^+e^-$  CM frame. The second term contains the Collins fragmentation function  $H_1^{\perp q}(z, P_{h\perp}^2)$  and the spin orientation of the quark. It changes sign when the quark spin is flipped, and thus generates a single spin asymmetry. The triple product introduces a  $\cos \phi$  modulation, where  $\phi$  is the azimuthal angle spanned by the hadron transverse momentum and the plane normal to the quark spin along the quark momentum<sup>1</sup>. In  $e^+e^-$  annihilation with unpolarized beams, the quark polarization is unknown, therefore the Collins asymmetries in single jets will yield a zero result as the modulation will average to zero in large event samples. The Collins spin effect can instead be observed in the production of two hadrons detected in opposite jets, produced by the fragmentation of a correlated quark-antiquark pair. This correlation results in a cosine modulation of the distribution of the azimuthal angles of the two hadrons.

In this analysis we therefore consider the process  $e^+e^- \rightarrow h_1 h_2 X$ , where  $h_1$  and  $h_2$  are pions, performing the measurement of Collins Asymmetry in two different reference frames: the thrust reference frame (called *RF12*) and the second-hadron momentum frame (*RF0*), which correspond to the jet reference frame and Gottfried-Jackson frame introduced in Chapter 2. The description of the azimuthal angles in the two reference frames are reported in Fig. 4.1.

---

<sup>1</sup>Note that we have a cosine modulation instead a sine modulation as shown in Fig. 2.8, because there is a  $\pi/2$  difference in the azimuthal angle definition.

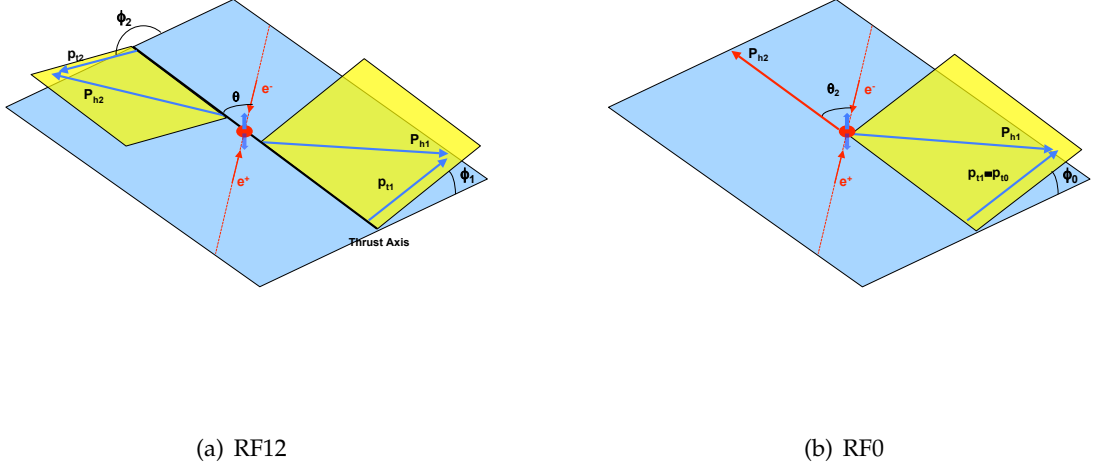


Figure 4.1: Definition of the azimuthal angles  $\phi_1$ ,  $\phi_2$  in the thrust reference frame (RF12), and  $\phi_0$  in the second hadron momentum frame (RF0).

#### 4.1 Thrust Reference Frame: RF12

The thrust reference frame is shown in Fig. 4.1(a). The azimuthal angles  $\phi_1$  and  $\phi_2$  are the angles between the scattering plane and the transverse hadron momenta  $p_{ti}$  around the thrust axis<sup>2</sup>. The  $\theta = \theta_{th}$  angle is defined as the angle between the beam axis and the thrust axis. In this reference frame the azimuthal angles are defined as:

$$\phi_{1,2} = \text{sign}[\hat{\mathbf{n}} \cdot \{(\hat{\mathbf{z}} \times \hat{\mathbf{n}}) \times (\hat{\mathbf{n}} \times \hat{\mathbf{P}}_{h_1, h_2})\}] \times \arccos \left( \frac{\hat{\mathbf{z}} \times \hat{\mathbf{n}}}{|\hat{\mathbf{z}} \times \hat{\mathbf{n}}|} \cdot \frac{\hat{\mathbf{n}} \times \mathbf{P}_{h_{1,2}}}{|\hat{\mathbf{n}} \times \mathbf{P}_{h_{1,2}}|} \right); \quad (4.2)$$

where  $\hat{\mathbf{z}}$  is the unitary vector defined by the  $e^+e^-$  direction. In order to extract the Collins function, we need to consider the process  $e^+e^- \rightarrow q\bar{q}$  and the initial momentum of the quark-antiquark pair. The quark directions are, however, not accessible to a direct measurement and are thus approximated by the thrust axis of the event, indicated by the unitary vector  $\hat{\mathbf{n}}$ . It is the vector along which the following expression is maximized:

$$\text{thrust} = \max \left| \frac{\sum_{i=1}^N |(\hat{\mathbf{n}} \cdot \mathbf{P}_i)|}{\sum_{i=1}^N |\mathbf{P}_i|} \right|; \quad (4.3)$$

where  $N$  is the number of particles used in the calculation and  $\mathbf{P}_i$  is the 3-momentum of the particle  $i$ . The value of the event thrust is therefore a measurement of the alignment of the

<sup>2</sup>Note that in this reference frame, assuming that the thrust axis is the same as the  $q\bar{q}$  axis,  $p_{ti}$  coincide with  $P_{i\perp}$  defined in Sec. 2.3

particles within an event along a common axis, and falls in the range (0.5, 1). The lower is the thrust, the more spherical the event is; the higher the thrust, the more jet-like the event.

The Collins asymmetries can be extracted in this reference frame by measuring a  $\cos(\phi_1 + \phi_2)$  modulation of hadron pairs distribution on top of the flat distribution due to the unpolarized part of the fragmentation function. The normalized distribution is defined as:

$$R_{12} = \frac{N(\phi_1 + \phi_2)}{\langle N_{12} \rangle}, \quad (4.4)$$

with  $N(\phi_1 + \phi_2)$  the di-hadron yield, and  $\langle N_{12} \rangle$  the average bin content. The corresponding differential cross section depends on fractional energies  $z_1$ ,  $z_2$  of the two hadrons, and on the sum of the previously defined azimuthal angles,  $\phi_1 + \phi_2$ , and can be written as:

$$\begin{aligned} \frac{d\sigma(e^+e^- \rightarrow h_1 h_2 X)}{dz_1 dz_2 d(\phi_1 + \phi_2) d\cos(\theta)} &= \sum_{q, \bar{q}} \frac{3\alpha^2}{Q^2} \frac{e_q^2}{4} z_1^2 z_2^2 \{ (1 + \cos^2 \theta) D_1^{q,[0]}(z_1) \bar{D}_1^{q,[0]}(z_2) + \\ &+ \sin^2 \theta \cos(\phi_1 + \phi_2) H_1^{q,[1]}(z_1) \bar{H}_1^{q,[1]}(z_2) \}; \end{aligned} \quad (4.5)$$

where the summation runs over all quark flavors accessible at the center of mass energy and the antiquark fragmentation is denoted by a bar. Note that the fragmentation functions do not appear in the cross section directly but as the zeroth and first moments in the absolute value of the corresponding transverse momenta [64]:

$$F^{[n]}(z) = \int d|\mathbf{k}_T^2| \left( \frac{|\mathbf{k}_T|}{M} \right)^n F(z, \mathbf{k}_T^2). \quad (4.6)$$

In this equation, the transverse hadron momentum has been rewritten in terms of the intrinsic transverse momentum of the process:  $\mathbf{P}_{h\perp} = z\mathbf{k}_T$  and the mass  $M$  is the mass of the detected hadron (in this analysis the pion mass).

## 4.2 Second-hadron momentum Reference Frame: RF0

The *RF0* frame is shown in Fig. 4.1(b). The azimuthal angle  $\phi_0$  is defined as the angle between the plane spanned by the beam axis and the second hadron  $\mathbf{P}_2$ , and the transverse momentum  $\mathbf{p}_{t0}$  ( $\mathbf{p}_{t0} \equiv \mathbf{p}_{t1}$ ) of the first hadron around the second hadron direction<sup>3</sup>. The angle  $\theta = \theta_2$  is defined in this case as the angle between the beam axis and the momentum  $\mathbf{P}_2$  of the second hadron. The azimuthal angle is calculated as:

$$\phi_0 = \text{sign}[\mathbf{P}_{h2} \cdot \{(\hat{\mathbf{z}} \times \mathbf{P}_{h2}) \times (\mathbf{P}_{h2} \times \mathbf{P}_{h1})\}] \times \arccos \left( \frac{\hat{\mathbf{z}} \times \mathbf{P}_{h2}}{|\hat{\mathbf{z}} \times \mathbf{P}_{h2}|} \cdot \frac{\mathbf{P}_{h2} \times \mathbf{P}_{h1}}{|\mathbf{P}_{h2} \times \mathbf{P}_{h1}|} \right), \quad (4.7)$$

<sup>3</sup>Note that in this reference frame,  $\mathbf{p}_{t0}$  does not coincide with  $\mathbf{P}_{1\perp}$ , but they can be kinematically related, as shown for example in Ref. [16].

and the corresponding normalized distribution  $R_0$  is :

$$R_0 = \frac{N(2\phi_0)}{\langle N_0 \rangle}. \quad (4.8)$$

At leading order in  $\alpha_s$  and  $1/Q^2$ , the differential cross section is given by [37]:

$$\begin{aligned} \frac{d\sigma(e^+e^- \rightarrow h_1 h_2 X)}{dz_1 dz_2 d^2\mathbf{q}_T d\cos(\theta) d\phi_0} &= \frac{3\alpha^2}{Q^2} z_1^2 z_2^2 \left\{ A(y) \mathcal{F}(D_1(z_1) \overline{D}_2(z_2)) + \right. \\ &\left. + B(y) \cos(2\phi_0) \mathcal{F} \left[ (2\hat{\mathbf{h}} \cdot \mathbf{k}_T \hat{\mathbf{h}} \cdot \mathbf{p}_T - \mathbf{k}_T \cdot \mathbf{p}_T) \frac{H_1^\perp(z_1) \overline{H}_2^\perp(z_2)}{M_1 M_2} \right] \right\}, \end{aligned} \quad (4.9)$$

where  $Q_t = |\mathbf{q}_T|$  is the transverse momentum of the virtual photon from  $e^+e^-$  annihilation in the center of mass of the two hadrons. The convolution integral over the transverse momenta  $\mathbf{k}_T = z_1 \mathbf{P}_{h_1\perp}$  and  $\mathbf{p}_T = z_2 \mathbf{P}_{h_2\perp}$  is:

$$\mathcal{F}(X) = \sum_{a, \bar{a}} e_a^2 \int d^2\mathbf{k}_T d^2\mathbf{p}_T \delta^2(\mathbf{p}_T + \mathbf{k}_T - \mathbf{q}_T) X; \quad (4.10)$$

the kinematic factors  $A(y)$  and  $B(y)$  are described in the theoretical section 2.3, and  $\hat{\mathbf{h}}$  is a unit vector in the direction of the transverse momentum of the first hadron relative to the axis defined by the second hadron.

Note that the cross sections given in Eq.(4.5) and Eq.(4.9) are related. Integrating Eq.(4.5) over the azimuthal angles ( $\phi_1, \phi_2$ ) and Eq.(4.9) over the azimuthal angle and the transverse photon momentum ( $\phi_0, q_T$ ), the same unpolarized cross section is obtained.

Similarly, the Collins contributions can be related to each other; however, due to the additional convolutions of transverse momenta, it is necessary to know the intrinsic transverse momentum dependence of the Collins function. The majority of authors assume that the Collins function is a Gaussian in  $k_T$ , as for the unpolarized FF, but with different width than the unpolarized case. More details can be found, for example, in Refs. [21, 95, 96].

In the following sections, after a brief discussion of the particle reconstruction and identification at *BABAR*, the selection criteria and the methods for the extraction of the asymmetry are described.

### 4.3 Analysis strategy and selection criteria

We focus on the measurement of the Collins effect in light quark fragmentation where it is expected to be dominant, as helicity is conserved only for nearly massless quarks, while for heavier quarks the correlation between the quark and the antiquark side may be lost. The process to be studied is  $e^+e^- \rightarrow \pi\pi X$ , with the two charged pions detected in two opposite hemispheres, and the asymmetries is measured in bins of fractional energy and of transverse pion momentum.

The analysis is performed using an integrated luminosity of  $424 \text{ fb}^{-1}$  of data collected at 10.58 GeV CM energy, which corresponds to the mass of  $\Upsilon(4S)$  resonance, and a luminosity of  $44 \text{ fb}^{-1}$  collected 40 MeV below the  $\Upsilon(4S)$ . In addition a number of physics processes have been simulated with the Monte Carlo (MC) technique. Systematic effects in the analysis method, event selection and event reconstruction, and the contribution of possible background sources are studied using specifically selected data control samples and MC simulations. All used data samples are summarized in Tab. 4.1. The simulation of hadronic events in non-resonant  $e^+e^-$  annihilation, is performed using the `Jetset` [57] generator. Separate MC samples are generated for light quarks,  $e^+e^- \rightarrow q\bar{q}$ , ( $q = u, d, s$ ), that we call generic  $uds$  MC, and heavy quarks,  $e^+e^- \rightarrow c\bar{c}$ . The `EvtGen` [97] generator has been used to simulate  $B\bar{B}$  events with generic  $B$  decays. Finally,  $e^+e^- \rightarrow \tau^+\tau^-$ , and  $e^+e^- \rightarrow \mu^+\mu^-$  event samples are produced with the `KK2F` [98] generator, and the decay of the  $\tau$  leptons are simulated with the `TAUOLA` [99] generator.

MC $uds$	$\mathcal{L}_{equiv.} = 937.8/fb$
Full data sample	$\mathcal{L} = 468/fb$
MC $c\bar{c}$	$\mathcal{L}_{equiv} = 468/fb$
MC $B^+B^-$	$\mathcal{L}_{equiv} = 234/fb$
MC $B^0\bar{B}^0$	$\mathcal{L}_{equiv} = 234/fb$
MC $\tau^+\tau^-$	$\mathcal{L} = 468/fb$
$D^*$ enhanced: MC $c\bar{c}$	$\mathcal{L}_{equiv} = 468/fb$
$D^*$ enhanced: MC $B^+B^-$	$\mathcal{L}_{equiv} = 234/fb$
$D^*$ enhanced: MC $B^0\bar{B}^0$	$\mathcal{L}_{equiv} = 234/fb$
$D^*$ enhanced: full data sample	$\mathcal{L} = 468/fb$
$\mu^+\mu^-$ data	$\mathcal{L} = 44.8/fb$

Table 4.1: Data and MC samples used in the analysis. For MC production it is reported the equivalent luminosity  $\mathcal{L}_{equiv} = N/\sigma$ , where N is the number of generated events, and the cross section  $\sigma$  are taken from Tab. 3.1.

### 4.3.1 Charged particle reconstruction

Charged particle tracks are reconstructed by processing the information from both the SVT and the DCH. The track finding and the fitting procedures use the *Kalman fitter algorithm* [100] that takes into account the detailed description of the material in the detector and the full magnetic field map. Using a sequence of modules to refine the fitting procedure, the final result is the creation of the track-candidate list used in the analysis (the basic list is *charged tracks*). Further requirements are applied to obtain a list of tracks coming from the interaction region (called *Good Tracks Loose*) and for tracks within the detector acceptance region, called *Good Tracks Acc*

*Loose*, which satisfy the following selection criteria:

- tracks with a polar angle in the laboratory system between  $0.410 < \theta < 2.54$ ;
- minimum transverse momentum of  $0.1 \text{ GeV}/c$  with respect to the beam axis, and maximum momentum of  $10 \text{ GeV}/c$ ;
- minimum number of hits in the DCH of 12;
- maximum distance of closest approach (DOCA) to the beam spot<sup>4</sup> in the  $x - y$  plane of  $1.5 \text{ cm}$ , and  $z$  DOCA between  $-10 \text{ cm}$  and  $10 \text{ cm}$ ;

### 4.3.2 Particle identification

All *BABAR* detectors contribute in a complementary way to particle identification (PID): the SVT and DCH provide  $dE/dx$  and momentum measurements for charged particles; the DIRC is a Čerenkov ring-imaging device, the electromagnetic calorimeter discriminates electrons from muons and charged hadrons according to energy deposit and shower shape; finally, the IFR characterizes muons and hadrons according to their different transverse and longitudinal interaction pattern in the segmented iron.

A good identification is obtained using advanced technique methods (likelihood ratio, neural network,...) that combine all the information coming from each sub-detector. A series of selectors for different particle hypothesis are built upon these informations and optimized for different physics analysis.

A selector is a category related to a selection method with certain parameters and criteria. In general, for each method four or more nested selectors are defined, with different performances:

- *looser* selection: higher efficiency but also higher mis-identification rate;
- *tighter* selection: lower efficiency but also lower mis-identification rate.

Each track satisfies or not a specific selector if it respects its criteria.

### Charged hadrons identification

Separation among different charged hadrons ( $\pi$ ,  $K$ , and  $p$ ) is provided mainly by the tracking system and by the DIRC.

- For each track intersecting the DIRC, from the reconstructed image and the track crossing angle, the corresponding Čerenkov angle and its error are determined, and a confidence

---

<sup>4</sup>The beam spot is the size of luminosity region, which is calculated run-by-run. It can be approximated by an ellipsoid with a Gaussian distribution along the three axes, with  $\sigma_z \simeq 1 \text{ cm}$ ,  $\sigma_x \simeq 100 \mu\text{m}$ , and  $\sigma_y \simeq 5 \mu\text{m}$ .

level for each mass hypothesis ( $e$ ,  $\mu$ ,  $\pi$ ,  $K$ , and  $p$ ) is calculated. A charged track is identified by the hypothesis with the highest confidence level.

- The SVT and DCH detectors provide PID information combining the measurement of  $dE/dx$  and track momentum as explained in sections 3.3.2 and 3.4.2 . A likelihood and significance level for a given mass hypothesis are obtained independently for each detector.
- All the informations coming for each sub-detector are combined together in order to produce the PID selectors, which are used to accept or reject a given track.

### Electron identification

Electrons are discriminated from charged hadrons by taking into account the ratio of the energy  $E$  deposited in the EMC to the track momentum  $p$  measured in the DCH. This quantity ( $E/p$ ) should be compatible with unity for electrons, since all their energy is deposited in the calorimeter. The other charged tracks should appear as minimum ionizing particles, unless they have hadronic interactions in the calorimeter crystals. Muons and charged hadrons therefore have values of  $E/p$  significantly lower than unity.

To further separate electrons from hadrons a variable describing the shape of the energy deposit in the EMC is used (LAT), since the lateral energy distribution of hadronic showers differs significantly from those of electromagnetic showers. The LAT variable is defined as:

$$LAT = \frac{\sum_{i=3}^N E_i r_i^2}{\sum_{i=3}^N E_i r_i^2 + E_1 r_0^2 + E_2 r_0^2} \quad (4.11)$$

where  $r_0$  is the average distance between two crystals,  $N$  is the number of crystals associated with the shower,  $E_i$  is the energy deposit in the  $i$ -th crystal, and  $r_i$  is the radial distance from the shower center. Electrons deposit most of their energy in two or three crystals, so that the value of LAT is small for electromagnetic showers.

In addition, the measured specific ionization in the DCH and Čerenkov angle in the DIRC are required to be consistent with the values expected for an electron. This offers a good  $e/\pi$  separation in a wide momentum range.

### Muon identification and $\mu/\pi$ discrimination in the IFR

Charged particles that are reconstructed in the tracking system and meet criteria for minimum ionization in the EMC are potential muon candidates. Their trajectories are extrapolated to the IFR taking into account the non-uniform magnetic field, the multiple scattering, and the average energy loss. The discrimination between muons and charged hadrons is obtained combining in a likelihood function or in a neural network the following information:

- the number of IFR layers associated with the track;
- the total number of interaction lengths traversed from the IP to the last RPC or LST layer with an associated cluster;
- the transverse size of the cluster, which identifies the showering hadrons;
- the number and position of detector layers with no hits associated with the track (“missed” planes), which may be caused by neutral particles coming from the hadronic shower.

### Photon and $\pi^0$ reconstruction

Photons are identified as well reconstructed clusters in the EMC, not associated to any track extrapolated from the tracking volume to the inner surface of the EMC. Two particles with small angular separation create energy deposits that overlap. To resolve this situation, regions of local maxima in the energy deposit of a cluster are located and referred to as bumps. Therefore, a bump represents the energy deposit of a single particle and contains one and only one local maximum.

The lateral distribution of energy (LAT variable of Eq. 4.11) within a cluster depends heavily on the nature of the incident particle. Electromagnetic particles deliver a regular and symmetric shape in the lateral distribution, with the fall-off in energy from the center being exponential. In contrast, hadronic particles produce irregular and less predictable energy deposits, often resulting in more than one cluster for incident hadron.

Decays of  $\pi^0$ s into two photons fall into two categories:

- for  $\pi^0$  energies below 1 GeV, the two photons are sufficiently far apart to produce two well-separated clusters, and the  $\pi^0$  is reconstructed from the two photon 4-momenta;
- for  $\pi^0$  energies beyond 1.5 GeV, the two photons have decreasing separation, and they are no longer distinguishable as separate clusters. In these cases the two bumps have to be identified.

### 4.3.3 Analysis strategy

The analysis strategy consists of the following main points:

#### 1. Event preselection:

- We use the standard list for charged particles **GoodTracksAccLoose**. Neutral particles are used in this analysis only for the calculation of the event thrust. In particular we select neutral candidates with  $0.410 < \theta_{lab} < 2.54$  rad., lateral moment smaller than 1.1, and an energy greater than 0.030 GeV.

- We select multi-hadrons events using the TagBGMultiHadron background filter flags: it requires more than two charged tracks in the event and a value of the second Fox-Wolfram momentum [101], calculated from charged tracks only,  $R'_2 < 0.98$ . This variable is a measure of event sphericity ranging between 0 and 1, with more spheric events, as  $\Upsilon(4S)$  decays, having a small  $R'_2$  value. On the contrary, lepton pairs events have  $R'_2$  close to 1, and would produce a huge spike in the distribution shown in Fig. 4.2(a) if no cut off by the multi-hadron selection.

Figure 4.3 compares the distribution of the number of tracks in the data sample (Fig. 4.3(a)), with respect to the number of tracks in the  $uds$  MC sample (Fig. 4.3(b)), for selected multi-hadron events. The two distributions differ by a peak at number of tracks equal to four in the data sample, which is due to the  $\tau\tau$  events (in Fig. 4.3(c) the MC simulation is reported). The  $\tau$  contribution to the asymmetries will be estimated in section 5.2.

- We require the visible energy of the event ( $E_{vis}$ ) to be higher than 7 GeV, in order to suppress some background sources as  $e^+e^- \rightarrow \tau^+\tau^-$ ,  $\gamma\gamma$  processes, and events characterized by hard Initial State Radiation. Figure 4.2(b) shows the distribution of the visible energy in the LAB frame. The shoulder at low value of energy is due to  $\gamma\gamma$  events.

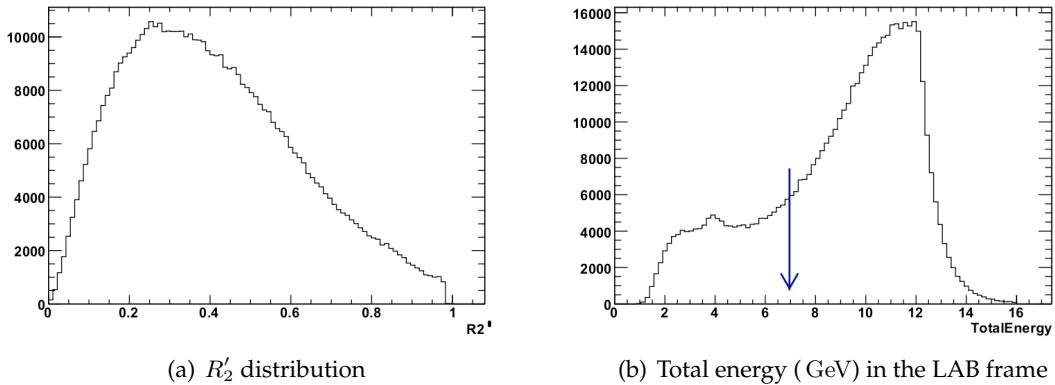


Figure 4.2: (a) The  $R'_2$  distribution for multi-hadrons events (charged tracks  $\geq 2$  and  $R'_2 < 0.98$ ). (b) The visible energy for multi-hadrons events in the LAB frame. In this analysis we require a total energy higher than 7 GeV, as indicated by the blue arrow.

2. Since the correlation between the  $q\bar{q}$  pair is lost in case of emission of energetic gluons, we look for a two-jet topology, and suppress  $e^+e^- \rightarrow q\bar{q}g$  events requiring a value of the event thrust greater than 0.8, with the thrust calculated using all charged tracks and neutral particles. As seen, in fact, in Fig. 4.4(a) most of the light  $q\bar{q}$  production appears in

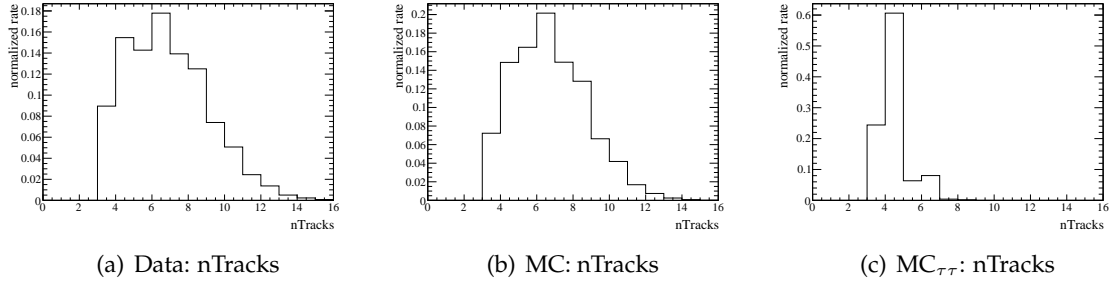


Figure 4.3: Number of tracks in the (a) data sample, (b) MC sample, and (c)  $\tau\tau$  MC sample. All the distributions are normalized to the number of events.

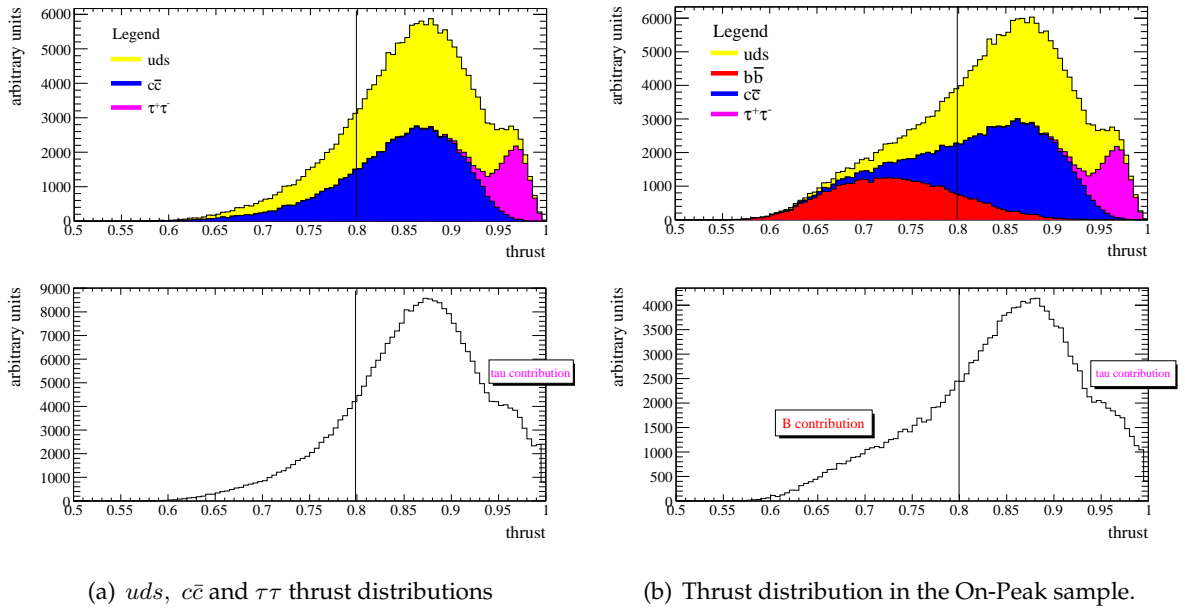


Figure 4.4: Left: thrust distribution for simulated events at  $\sqrt{s} = 10.54$  GeV:  $e^+e^- \rightarrow c\bar{c}$  (blue),  $e^+e^- \rightarrow q\bar{q}$ ,  $q = uds$  (yellow) and  $e^+e^- \rightarrow \tau\tau$  (magenta) processes. In the lower plot is reported the thrust distribution for a small Off-Peak sample, as comparison. Right plots: (top) thrust distribution at  $\sqrt{s} = 10.58$  GeV with in addition the  $e^+e^- \rightarrow B\bar{B}$  (red) channel. The lower plot shows the corresponding distribution obtained for a small sample of On-Peak data ( $\mathcal{L} \sim 148 \text{ pb}^{-1}$ ). The difference at high thrust values between data and MC are due to  $e^+e^- \rightarrow \mu^+\mu^-$  and Bhabha events, not included in the simulation. The vertical black line is the cut applied in this analysis ( $thrust > 0.8$ ).

a two-jet topology and is characterized by high thrust values, with the long tail at lower values due to hard gluon emission. The requirement  $thrust > 0.8$  has been chosen also because for low thrust values the assignment of tracks to the right jet is more difficult, and because it will remove the majority of the more spheric  $B\bar{B}$  events (see Fig. 4.4(b)). Events with charm quarks have, instead, a shape similar to the light quarks. The charm

contribution to the asymmetry must be carefully evaluated and eventually subtracted. Events from  $e^+e^- \rightarrow \tau^+\tau^-$  reaction populate the region at high *thrust* values, and their contribution to the asymmetry must be subtracted, too.

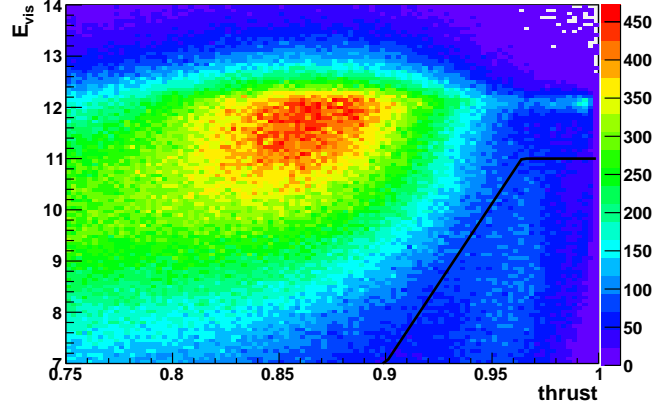


Figure 4.5: Total visible energy of the events as a function of the thrust value for the on-resonance data sample. The events at high thrust value and low total energy are due to the  $e^+e^- \rightarrow \tau^+\tau^-$  process. The black line is the cut applied in the analysis in order to remove this background. The peak at  $E_{tot} \sim 12$  GeV and high thrust values, is due to radiative Bhabha and  $\mu^+\mu^-(\gamma)$  events, and it is removed applying a veto on electrons and muons.

3. We select tracks consistent to be produced at the primary vertex, which is calculated on event-by-event basis fitting all reconstructed tracks. In particular, the distance of closest approach of the track to the primary vertex in the transverse plane must be  $d_{xy} < 2$  mm and that along the beam axis  $d_z < 1.5$  cm. In addition, tracks are identified as pions if they satisfy the tight criteria of the pion **KM selector** [102].
4. The range of applicability for fragmentation function as discussed in this thesis is limited to medium-to-large values of hadrons' fractional energies  $z_{1,2} = \frac{2E_{h_{1,2}}}{Q}$  [26]. For small  $z$  values the mass correction terms proportional to  $M_h/(zQ^2)$  becomes important.

Previous studies, including the preliminary results that we showed at the Transversity2011 workshop [103, 104], limit the measurement of the Collins asymmetries to tracks with  $z > 0.2$ . However, it may be of interest to extend the study to lower  $z$  values, in order to assess when the mass correction terms start to play a significant role. On the other hand, low momentum tracks pose severe experimental difficulties, as described below, so that reliable measurements of the asymmetries in the present analysis could be obtained only for  $z > 0.15$ .

5. One of the most important contributions to the Collins asymmetry originates from low

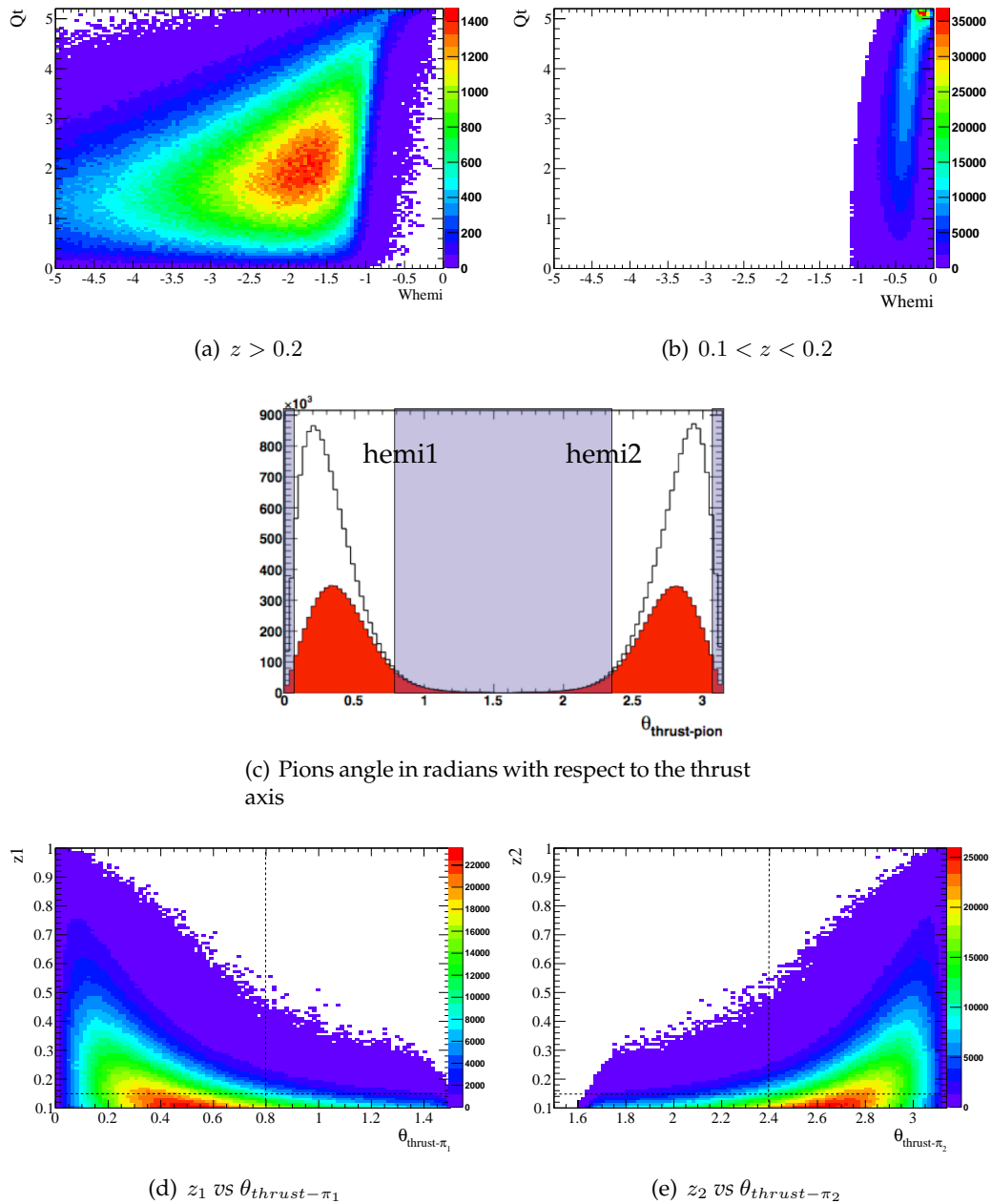


Figure 4.6: (a)  $Q_t$  vs  $W_{hemi}$  distribution for pion pairs with  $z > 0.2$ . (b) The same distribution as in (a) for pion pairs with  $z < 0.2$ . All the pairs with lower fractional energy are distributed for  $W_{hemi} < -1$  and higher values of  $Q_t$ , which corresponds to an higher probability of hemispheres mis-identification. (c) Angle between pions and thrust axis in radians. The red histogram refers to pions with  $z < 0.2$ , and the highlighted region indicates the cut applied. (d), (e) Opening angle in radians between the thrust and pion in the first and second hemispheres respectively. The dotted black lines indicate the cuts applied in the analysis.

energetic gluon radiation  $e^+e^- \rightarrow q\bar{q}g$  which does not manifest itself in a third jet but introduces additional azimuthal modulation. As shown in Ref. [64, 67], the angular distribution of the gluon radiation process  $e^+e^- \rightarrow q\bar{q}g \rightarrow h_1h_2X$  is given by:

$$\frac{dN}{d\Omega} \propto \frac{Q_t^2}{Q^2 + Q_t^2} \sin\theta_{CS} \cos(2\phi_{CS}), \quad (4.12)$$

where the subscript CS refers to the Collins-Soper frame described in Fig. 2.6. In addition, all the formalism used so far is valid in the region where the transverse momentum  $Q_t$  is small compared to the hard scale  $Q$  ( $Q_t^2 \ll Q^2$ ) [64]. For these reasons, a safe choice is to require  $Q_t < 3.5$  GeV/ $c$ .

6. Figure 4.5, which reports the total visible energy for the on-peak data sample versus the thrust value for events having at least one good hadron pair, shows that the bulk of the signal  $uds$  events is clearly separated by two background sources. The peak at about 12 GeV of energy and high thrust values is in fact due to radiative Bhabha and  $\mu^+\mu^-(\gamma)$  events, while the small accumulation visible at lower energies and  $T > 0.94$  (corresponding to the peak visible at  $T \simeq 0.96$  in Fig. 4.4(a)) is due to  $\tau^+\tau^-$  events. The first kind of background is suppressed removing from the final sample tracks identified as electrons or muons. The majority of the  $\tau^+\tau^-$  events are instead removed applying a cut around the  $\tau^+\tau^-$  peak region, as shown in Fig. 4.5; the dilution of the measured asymmetry due to the remaining  $\tau^+\tau^-$  background is discussed in Sec.5.2.
7. We assume the thrust axis ( $\hat{n}$ ) as the  $q\bar{q}$  direction, we separate charged pions in opposite hemispheres according to that axis, and we pair those pions that satisfy the condition:

$$W_{hemi} = (\mathbf{P}_1 \cdot \hat{n}) (\mathbf{P}_2 \cdot \hat{n}) < 0, \quad (4.13)$$

where  $\mathbf{P}_{1,2}$  are the momenta of selected pions. For pairs with values of  $W_{hemi}$  near to zero there is a higher probability that one of the two tracks has been assigned to the wrong hemisphere. Most of these pairs are effectively removed by the requirement  $Q_t < 3.5$  GeV/ $c$ , as can be deduced by looking at the two top plots of Fig. 4.6, where  $Q_t$  is plotted versus  $W_{hemi}$ , for pion pairs with both pions having  $z > 0.2$  on the left plot, and for pairs with both pions having  $0.1 < z < 0.2$  on the right. It is clearly evident that the two distributions are very different from each other, and that when both pions have very low momentum  $W_{hemi}$  is close to zero also for low  $Q_t$ .

The problem with assigning the correct hemisphere to low momentum tracks is better understood from Fig. 4.6(c), which reports the opening angle between the track and the thrust axis. The black histogram is the distribution for all tracks, while the filled red histogram refers only to tracks with  $0.1 < z < 0.2$ . It is seen that the region around  $\theta = \pi/2$ ,

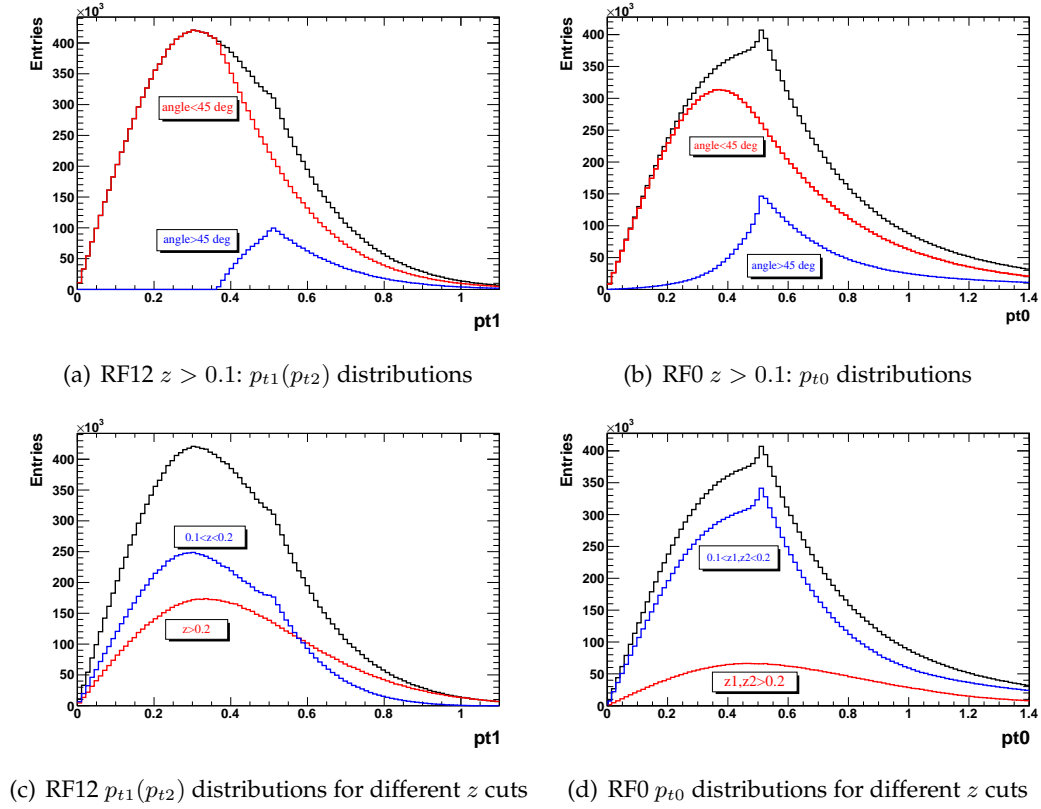


Figure 4.7: (a,b) transverse momentum distribution for pions with  $z > 0.1$  within (red lines) and out (blu lines) the cone of  $45^\circ$  with respect to the thrust axis. (c,d) transverse momentum distribution for pions with  $z > 0.2$  (red lines) and with  $0.1 < z < 0.2$  (blu lines). The black histogram is the full distribution.

where the imaginary plane that divides the two hemispheres is located, is populated almost exclusively by tracks with low  $z$ . The requirement that the pions are emitted within a cone of  $45^\circ$  around the thrust axis removes these ambiguous tracks, which account for about 14% of selected pions with  $0.1 < z < 0.2$ , and for only 0.4% of pions with  $z > 0.2$ . (see also Fig. 4.6(d) and Fig. 4.6(e), which show the pion fractional energy as a function of the pion-thrust opening angle).

We remove also a very small fraction of tracks flying within a cone with opening angle of  $2^\circ$  around the thrust axis, because of the large uncertainty in the determination of the azimuthal angles for these tracks. For pions with higher fractional energy, for which the thrust axis is very close to the 3-momentum vector, this effect dilutes the measured asymmetries.

It is interesting also to study the transverse momentum distributions for different cuts on the pions fractional energy and opening angle. Figures 4.7(a) and 4.7(b), for example, report the  $p_t$  distribution for pions with  $z > 0.1$  and for the two reference frames. The

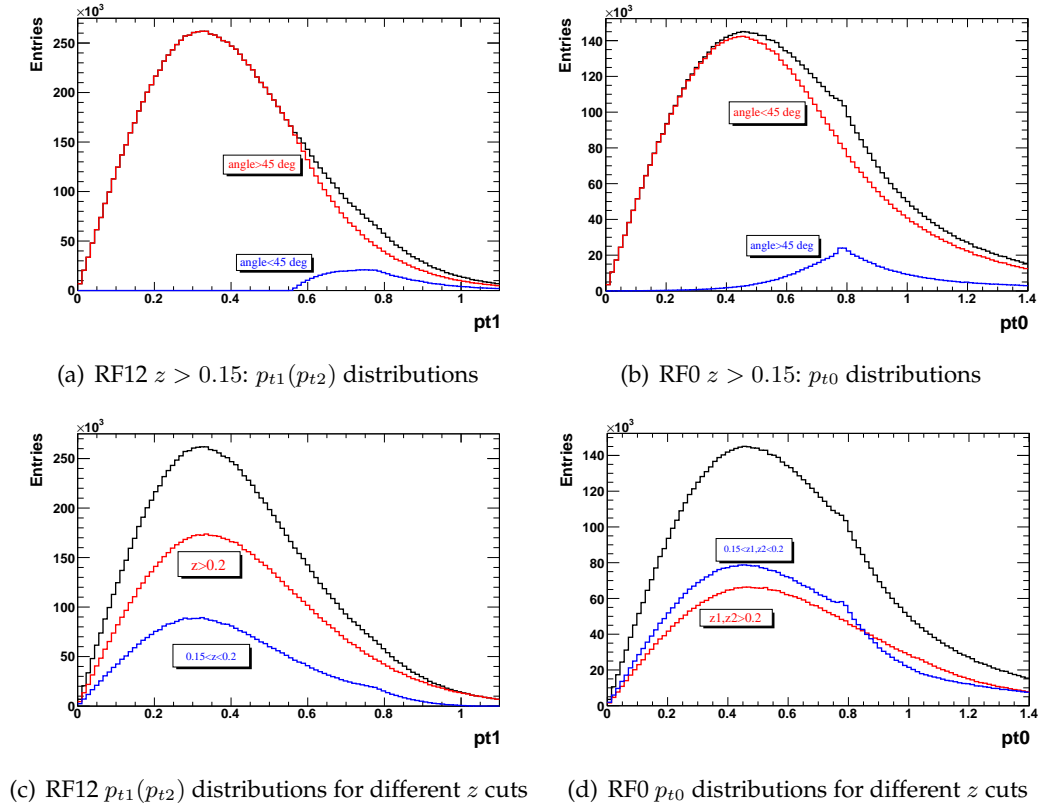


Figure 4.8: (a,b) transverse momentum distribution for pion with  $z > 0.15$  within (red lines) and out (blu lines) the cone of  $45^\circ$  with respect to the thrust axis. (c,d) transverse momentum distribution for pions with  $z > 0.2$  (red lines) and with  $0.15 < z < 0.2$  (blu lines). The black histogram is the full distribution.

black histograms give the full distribution, while the red and blue histograms refer to pions within and outside the cone of  $45^\circ$  around the thrust axis, respectively. Both the black and blue histograms show a peak, much more evident for  $p_{t0}$ , at about  $0.5 \text{ GeV}/c$ , while the pions with small opening angle present a smooth distribution (red histogram). We can deduce that the peak is due to particles with the lowest energy ( $z \simeq 0.1$ ) and emitted at about  $90^\circ$  with respect to the thrust axis.

The bottom plots in the same figure, showing the  $p_t$  distributions for pions with  $z > 0.2$  (red line) and  $0.1 < z < 0.2$  (blue line), confirm that the peak is due to very low energy pions. Figure 4.8 shows the analogous  $p_t$  distributions for pions with a minimum fractional energy of  $z = 0.15$ . The peaks are present also in this case, even if they are less evident and shifted to  $p_t \simeq 0.8 \text{ GeV}/c$ , which is the minimum value for pions perpendicular to the thrust axis. We note also that the fraction of particles with large opening angle is significantly lower than in Fig. 4.7.

These distributions show therefore that the cut on the pion-thrust axis opening angle is

necessary in order to have smooth distributions when tracks with small  $z$  are used.

Finally, the approximation of the  $q\bar{q}$  direction with the thrust axis brings to a significant dilution of the asymmetry, in particular for the thrust reference frame, as explained later in section 5.3.

8. We then calculate the azimuthal angles  $\phi_i$  of the selected pion pairs according to Eq.(4.2) in RF12, and (4.7) in RF0, and fit the asymmetries taking care of the detector acceptances.

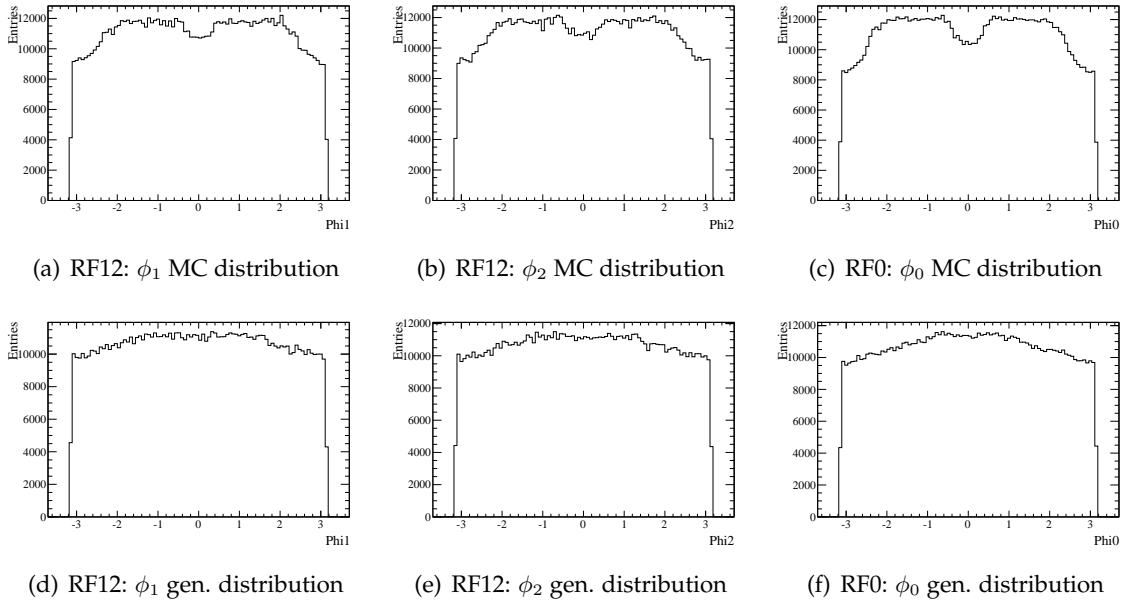


Figure 4.9: Azimuthal angle distributions of reconstructed MC sample for (a)  $\phi_1$  and (b)  $\phi_2$  in the thrust reference frame (RF12), and (c)  $\phi_0$  in the second hadron momentum frame (RF0). The angles are calculated following Eq. (4.2) in RF12, and Eq. (4.7) in RF0. The hole at  $\phi = 0$  and at larger  $\phi$  values are due to detector effects. For comparison, the plots (d,e,f) show the corresponding azimuthal angles for generated events. In particular,  $\phi_1$  and  $\phi_2$  are calculated with respect to the real  $q\bar{q}$  axis.

The azimuthal angles in the two reference frames are shown in Figs. 4.9(a,b,c) and compared with the respective generated distributions (d,e,f). The holes at  $\phi = 0$  and higher  $|\phi|$  values, visible only for reconstructed sample, are due to acceptance effects.

The  $\phi_1 + \phi_2$  and the  $2\phi_0$  distribution, which are sensitive to the Collins effects, are plotted in Figs. 4.10(a) and 4.10(b) (see Eq. (4.5) for RF12 and Eq. (4.9) for RF0). The dotted red histogram refers to the distributions for generated particles associated to the reconstructed ones, for which the azimuthal angles are calculated with respect to the  $q\bar{q}$  axis instead of the thrust axis of the event. The generated and reconstructed distributions are different in RF12, because of the discrepancy between the  $q\bar{q}$  and thrust axis direction. The influence on the measurement of the azimuthal asymmetries due to the thrust axis reconstruction

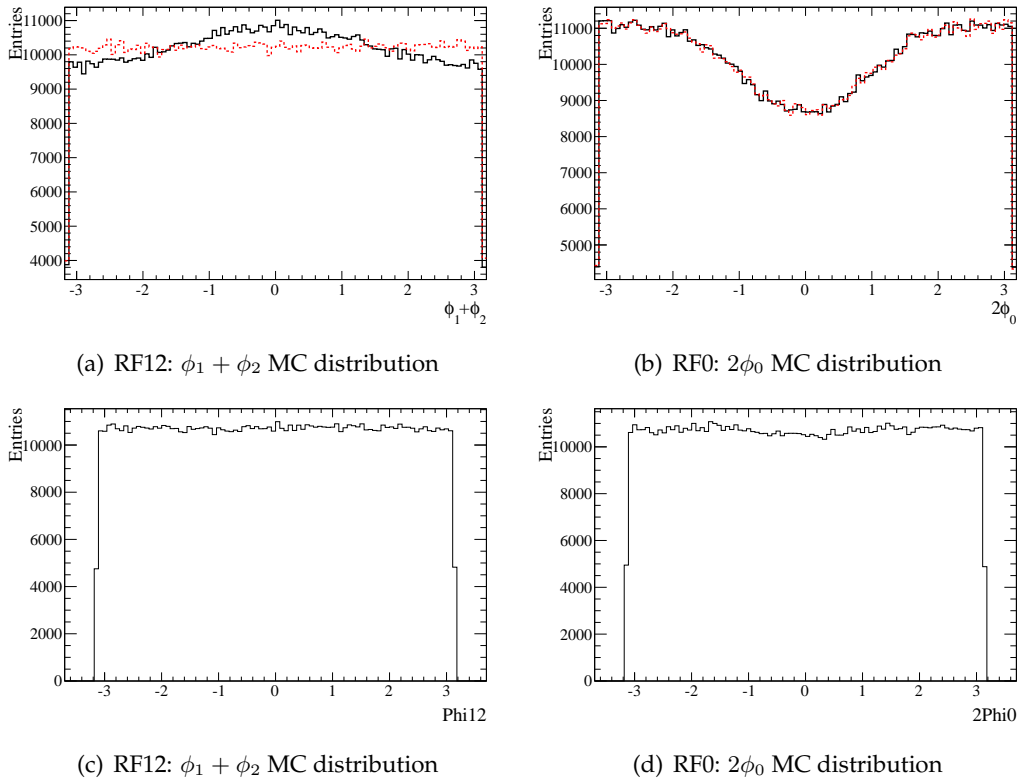


Figure 4.10: (a)  $\phi_1 + \phi_2$  azimuthal distribution in the RF12 frame and (b)  $2\phi_0$  distribution in the RF0 frame. The red dotted histogram refers to the generate associated angles, which are calculated with respect to the  $q\bar{q}$  axis. (c, d) For comparison, the same azimuthal distributions for generated pion pairs for which no detector effects are included.

are discussed in section 5.3. In the RF0 frame, instead, the two distributions are very similar and the only differences are due to the track resolution and particle identification. The true azimuthal distributions, which do not contain resolution or acceptance effects, can be obtained looking at generated events before the detector response is simulated. These distribution are shown in Figs. 4.10(c) and 4.10(d).

Table 4.2 summarizes all the cuts applied in this analysis.

## 4.4 Raw Asymmetries

The possibility to select pion pairs with same charge or opposite charge, allows to be sensitive to favored and disfavored fragmentation functions. Favored FF describe the fragmentation of a quark of flavor  $q$  into an hadron with a valence quark of the same flavor: i.e.  $u \rightarrow \pi^+$  and  $d \rightarrow \pi^-$ . Instead, we refer to  $u \rightarrow \pi^-$  and  $d \rightarrow \pi^+$  as disfavored fragmentation processes. Consider, for example, the production of unlike-sign charged pions from a  $u\bar{u}$  pair :  $e^+e^- \rightarrow u\bar{u} \rightarrow$

Track acceptance cut	$0.410 < \theta_{lab} < 2.54$ rad.
Multi-hadron events	number of charged tracks $> 2$ $R'_2 < 0.98$
Visible energy of the event	$E_{vis} > 7$ GeV
Thrust	$thrust > 0.8$
Pion selector	tight KM selector
Electrons and muons veto	very tight BDT selector very tight KM selector
Pion fractional energy	$z > 0.15$
Pion-thrust opening angle	$\theta_{thrust-\pi} < 45^\circ$
Pion-reference axis opening angle	$\theta_{axis-\pi} > 2^\circ$
Pion pairs in opposite hemispheres	$W_{hemi} < 0$
$Q_t$ transverse momentum	$Q_t < 3.5$ GeV/ $c$

Table 4.2: Summary of the cuts used in this analysis

$\pi^\pm\pi^\mp X$ . The pion pair can be either created through two favored fragmentation processes ( $\pi^+\pi^- X$ ) or through two disfavored fragmentation processes ( $\pi^-\pi^+ X$ ).

Introducing the favored FF  $D_1^{fav} \equiv D^{fav}(z_1) = D_u^{\pi^+}(z_1)$  and  $D_2^{fav} \equiv D^{fav}(z_2) = D_u^{\pi^-}(z_2)$  as well as the disfavored FF  $D_1^{dis} = D^{dis}(z_1) = D_u^{\pi^-}(z_1)$  and  $D_2^{dis} = D^{dis}(z_2) = D_u^{\pi^+}(z_2)$ , the cross section for charged pion pair production can be written as:

$$\begin{aligned}
N^U(\phi) &= \frac{d\sigma(e^+e^- \rightarrow \pi^\pm\pi^\mp X)}{d\Omega dz_1 dz_2} \approx \sum_q e_q^2 \left[ (1 + \cos^2 \theta) (D_1^{fav} \bar{D}_2^{fav} + D_1^{dis} \bar{D}_2^{dis}) \right. \\
&\quad \left. + \sin^2(\theta) \cos(\phi) (H_1^{fav} \bar{H}_2^{fav} + H_1^{dis} \bar{H}_2^{dis}) \right] \quad (4.14) \\
N^L(\phi) &= \frac{d\sigma(e^+e^- \rightarrow \pi^\pm\pi^\pm X)}{d\Omega dz_1 dz_2} \approx \sum_q e_q^2 \left[ (1 + \cos^2 \theta) (D_1^{fav} \bar{D}_2^{dis} + D_1^{dis} \bar{D}_2^{fav}) \right. \\
&\quad \left. + \sin^2(\theta) \cos(\phi) (H_1^{fav} \bar{H}_2^{dis} + H_1^{dis} \bar{H}_2^{fav}) \right] \\
N^C(\phi) &= \frac{d\sigma(e^+e^- \rightarrow \pi\pi X)}{d\Omega dz_1 dz_2} \approx \sum_q e_q^2 \left[ (1 + \cos^2 \theta) (D_1^{fav} + D_1^{dis}) (\bar{D}_2^{fav} + \bar{D}_2^{dis}) \right. \\
&\quad \left. + \sin^2(\theta) \cos(\phi) (H_1^{fav} + H_1^{dis}) (\bar{H}_2^{fav} + \bar{H}_2^{dis}) \right]
\end{aligned}$$

where  $\pi$  stands for a pion of any charge,  $\phi$  is the azimuthal angle  $\phi_1 + \phi_2$  in RF12 or  $\phi_0$  in RF0, and  $N^i$  is the di-hadron yield, for Unlike, Like, and Charged pion pairs, respectively. The  $N^i(\phi)$

are normalized to the average yield per bin  $\langle N^i \rangle$ , which is due to the unpolarized part of the fragmentation function, in order to obtain the normalized distributions  $R_\alpha^i$  defined in Eq.(4.4) and (4.8). Following Eq.(4.5) and (4.9), the normalized yields can be parametrized as:

$$R_\alpha^i = b_\alpha + a_\alpha \cos(\beta_\alpha), \quad (\alpha = 0, 12; i = U, L, C). \quad (4.15)$$

Here  $\beta$  is the azimuthal angles combination  $\phi_1 + \phi_2$  or  $2\phi_0$ , according to the used reference frame. The parameter  $b_\alpha$  should be consistent with unity, while  $a_\alpha$  gives the amplitude of the raw asymmetry. The parameters  $a_\alpha$  are found to be large as shown in Fig. 4.11 for unlike-sign

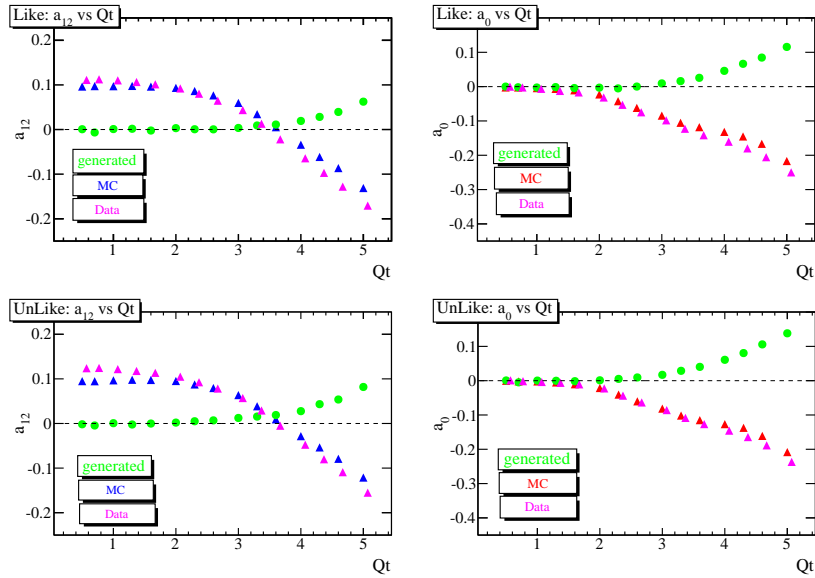


Figure 4.11: Raw asymmetry parameters  $a_{12,0}$  for like-sign pion pairs (upper plots) and for unlike-sign pion pairs (lower plots) as a function of the transverse virtual photon momentum  $Q_t$ . The green points refer to the generated events, the magenta and blue triangles to the reconstructed MC and data pion pairs, respectively.

and like-sign distributions as a function of  $Q_t$ . In particular, the figure compares the asymmetry for data with respect to the asymmetry for Monte Carlo and generated pion pairs. The raw asymmetries for generated MC events are almost consistent with zero for low  $Q_t$  values and increase for higher values due to radiative effects included in the simulation. A large difference between the asymmetries calculated from generated events and those obtained from MC events after GEANT simulation of the detector response and track reconstruction is clearly evident. This discrepancy is due to the large acceptance effects.

Figure 4.12 reports the azimuthal distributions for MC and off-peak data sample. Since the polarized FF are not included at the generation level, we expect to see a flat distribution in the MC azimuthal angles. Instead, we observe a modulation which is due essentially to the detector acceptance effects, more or less the same shape for both MC and data sample. In principle,

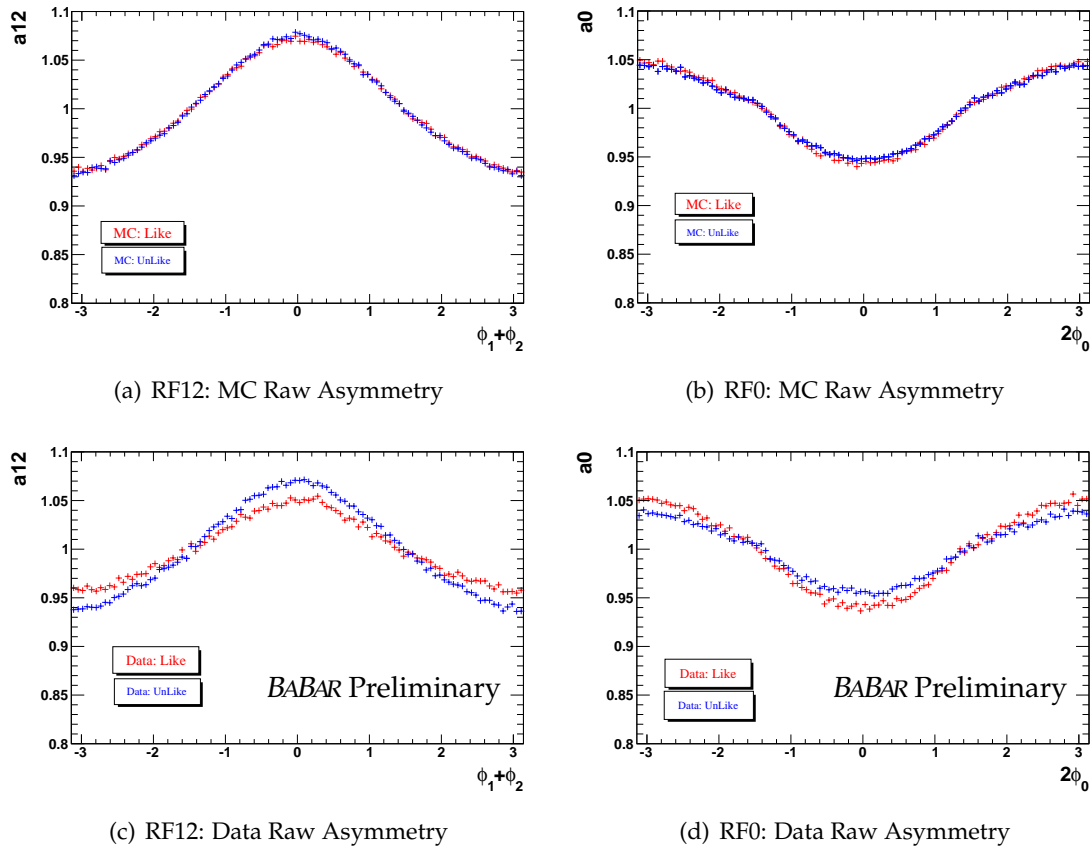


Figure 4.12: Raw asymmetries: in red is reported the distribution for like-sign pion pairs and in blue the distribution for unlike-sign pion pairs. The upper plots refer to MC sample and the lower plots to data sample for the two reference frames described in the text (left plots for RF12, and right plots for RF0).

we can try to estimate these effects in the MC sample and correct consequently the measured asymmetries in the data sample. However, this procedure introduces large uncertainties, and the problem on how well MC describes data. We can move around these problems by noting that the  $R^L$  and  $R^U$  distributions are almost coincident in the case of MC sample, while a clear difference is observed in the data (which it is the azimuthal asymmetry produced by the Collins FFs). This observation suggests the possibility to perform suitable double ratios of asymmetries, as explained in the next section, in order to obtain a MC independent measurement.

## 4.5 Double Ratios

Given the difficulties to separate the true Collins effects from asymmetries produced by detector acceptances and radiative effects, we exploit the fact that instrumental effects cancel making

ratios of asymmetries, as, for example, the ratio of unlike-sign over like-sign asymmetries:

$$\begin{aligned} \frac{R_{12}^U}{R_{12}^L} &= \frac{1 + \frac{\sin^2 \theta}{1 + \cos^2 \theta} \cos(\phi_1 + \phi_2) G^U}{1 + \frac{\sin^2 \theta}{1 + \cos^2 \theta} \cos(\phi_1 + \phi_2) G^L} \\ &\simeq 1 + \frac{\sin^2 \theta}{1 + \cos^2 \theta} \cos(\phi_1 + \phi_2) \{G^U - G^L\}, \end{aligned} \quad (4.16)$$

where the approximation above is true only for small asymmetries values, and

$$\begin{aligned} G^U &= \frac{\sum_q e_q^2 \mathcal{F}(H_1^{fav} \bar{H}_2^{fav} + H_1^{dis} \bar{H}_2^{dis})}{\sum_q e_q^2 (D_1^{fav} \bar{D}_2^{fav} + D_1^{dis} \bar{D}_2^{dis})}, \\ G^L &= \frac{\sum_q e_q^2 \mathcal{F}(H_1^{fav} \bar{H}_2^{dis} + H_1^{dis} \bar{H}_2^{fav})}{\sum_q e_q^2 (D_1^{fav} \bar{D}_2^{dis} + D_1^{dis} \bar{D}_2^{fav})}. \end{aligned} \quad (4.17)$$

It should be noted that the asymmetries generated by QCD radiative events and acceptance effects do not depend on the charge combination of the pion pairs, as will be shown in the section of systematic studies, so that the new asymmetry amplitudes, resulting from the ratio, depend only on a different combination of favored and disfavored FFs.

Similarly, the double ratio of unlike sign and any charged (C) (i.e ++, +- and charge-conjugate combinations) pion pairs is given by:

$$\frac{R_{12}^U}{R_{12}^C} \simeq 1 + \frac{\sin^2 \theta}{1 + \cos^2 \theta} \cos(\phi_1 + \phi_2) \times \{G^U - G^C\}, \quad (4.18)$$

with

$$G^C = \frac{\sum_q e_q^2 \mathcal{F}[(H_1^{fav} + H_1^{dis}) \cdot (\bar{H}_2^{fav} + \bar{H}_2^{dis})]}{\sum_q e_q^2 [(D_1^{fav} + D_1^{dis}) \cdot (\bar{D}_2^{fav} + \bar{D}_2^{dis})]}. \quad (4.19)$$

This double ratio contains different combination of favored and disfavored fragmentation functions thanks to which we can derive information about their relative sign [96]. Analogous expressions can be obtained in the  $RF0$  reference frame, with the modulation of  $\cos(2\phi_0)$  instead of  $\cos(\phi_1 + \phi_2)$ .

The double ratios are still parametrized by a cosine function:

$$\frac{R_\alpha^i}{R_\alpha^j} = B_\alpha^{ij} + A_\alpha^{ij} \cdot \cos(\beta_\alpha), \quad (4.20)$$

where  $i, j = U, L, C$ ;  $\alpha$  represent the used reference frame (RF12 or RF0);  $B$  and  $A$  are free parameters.

The constant term  $B$  should be consistent with unity and the  $A$  parameter contains only the Collins effect and higher-order radiative effects. Figure 4.13 shows the double ratio of unlike over like sign pion pairs for MC (upper plots) and data (lower plots) samples. As mentioned

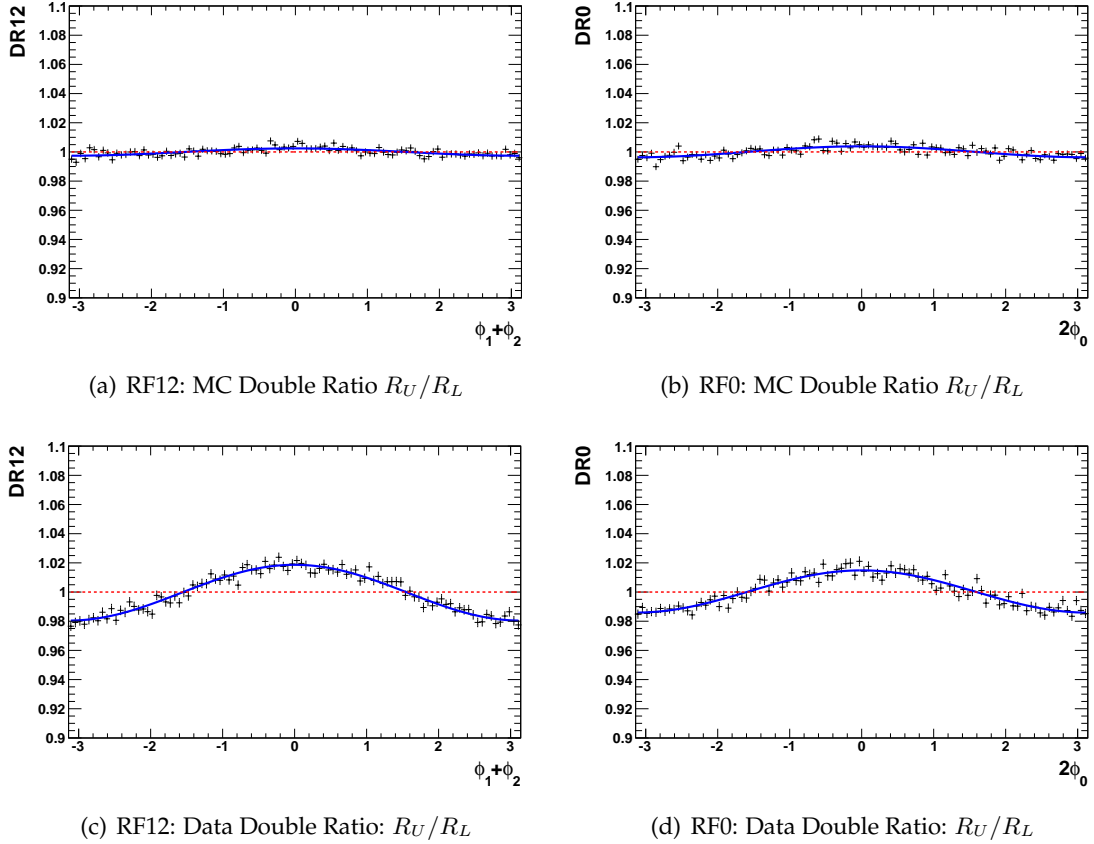


Figure 4.13:  $R^U/R^L$ : (a,b) double ratio asymmetries from Monte Carlo simulation for both the reference frame. The measured asymmetry is of the order of  $0.2 - 0.3\%$ . (c,d) double ratio results for the off-peak data sample. In this case, the asymmetry is of the order of  $1.5 - 2\%$ .

in the previous section, we expect to observe no cosine modulation in simulation. However, a slight deviation from zero asymmetry is observed. The origin and the effect of this possible bias on the measured asymmetry will be studied in detail in section 5.1.

Thanks to the large amount of data (about  $10^9$  events) we can study the dependence of the asymmetry as a function of fractional energies and of transverse momenta of the selected pions ( $z_1$  and  $z_2$ ,  $p_{t1}$  and  $p_{t2}$ , and  $p_{t0}$ ). Table 4.3 reports the chosen  $z$ -bin subdivision (36 independent ( $z_1, z_2$ ) bins or 21 symmetric bins) in the two reference frames. In particular, we choose the following  $z$  intervals:  $[0.15 - 0.2]$ ,  $[0.2 - 0.3]$ ,  $[0.3 - 0.4]$ ,  $[0.4 - 0.5]$ ,  $[0.5 - 0.7]$ ,  $[0.7 - 1]$ . Note that we keep in a separate bin the tracks with  $z < 0.2$ . In this way, our results can be easily combined with the SIDIS and Belle data, which start from  $z > 0.2$ , for the extraction of transversity and Collins FF with a global analysis, as done by the author of Ref. [16, 17]. Similarly, Table 4.4 reports the ( $p_{t1}, p_{t2}$ ) bins: 16 bins or 10 symmetric bins used in the RF12 frame. For RF0, where the transverse momentum of only one pion is meaningful, we choose the following four  $p_{t0}$  bins:  $[0 - 0.25]$ ,  $[0.25 - 0.5]$ ,  $[0.5 - 0.75]$ , and  $[> 0.75]$ .

$z_2$	0.15	0.2	0.3	0.4	0.5	0.7	1	$z_1$
1	6	11	15	18	20	21		
0.7	5	10	14	17	19	20		
0.5	4	9	13	16	17	18		
0.4	3	8	12	13	14	15		
0.3	2	7	8	9	10	11		
0.2	1	2	3	4	5	6		
0.15								

Table 4.3:  $z$ -bin subdivision: in this analysis we divide the asymmetry results in 6x6 bins of  $z_1$  and  $z_2$  as summarized above, or in 21 symmetric  $z$ -bins.

$p_{t2}$	0.	0.25	0.5	0.75	3	$p_{t1}$
3		4	7	9	10	
0.75		3	6	8	9	
0.5		2	5	6	7	
0.25		1	2	3	4	
0.						

Table 4.4:  $p_t$ -bin subdivision: in this analysis we divide the asymmetry results in 4x4 bins of  $p_{t1}$  and  $p_{t2}$  (or in 10 symmetric  $p_t$ -bins) in the RF12 frame. We used only 4  $p_{t0}$ -bins in the RF0 frame.

Following these  $z$  and  $p_t$  bin subdivisions, the asymmetries for data and MC samples (U/L and U/C double ratio) are compared in Fig. 4.14 for  $(z_1, z_2)$ -bin subdivision, in Fig. 4.15 for  $(p_{t1}, p_{t2})$ -bin, and in Fig 4.16 for  $p_{t0}$  bin. In particular, the blue triangles refer to the data asymmetry calculated in the RF12 and RF0 frames, and the green squares to the MC asymmetry. Note that the MC bias plays a marginal role and this contribution will be studied in the next section.

The data report only the statistical errors and are not yet corrected for the background contribution, such as charm, tau, and bottom decays.

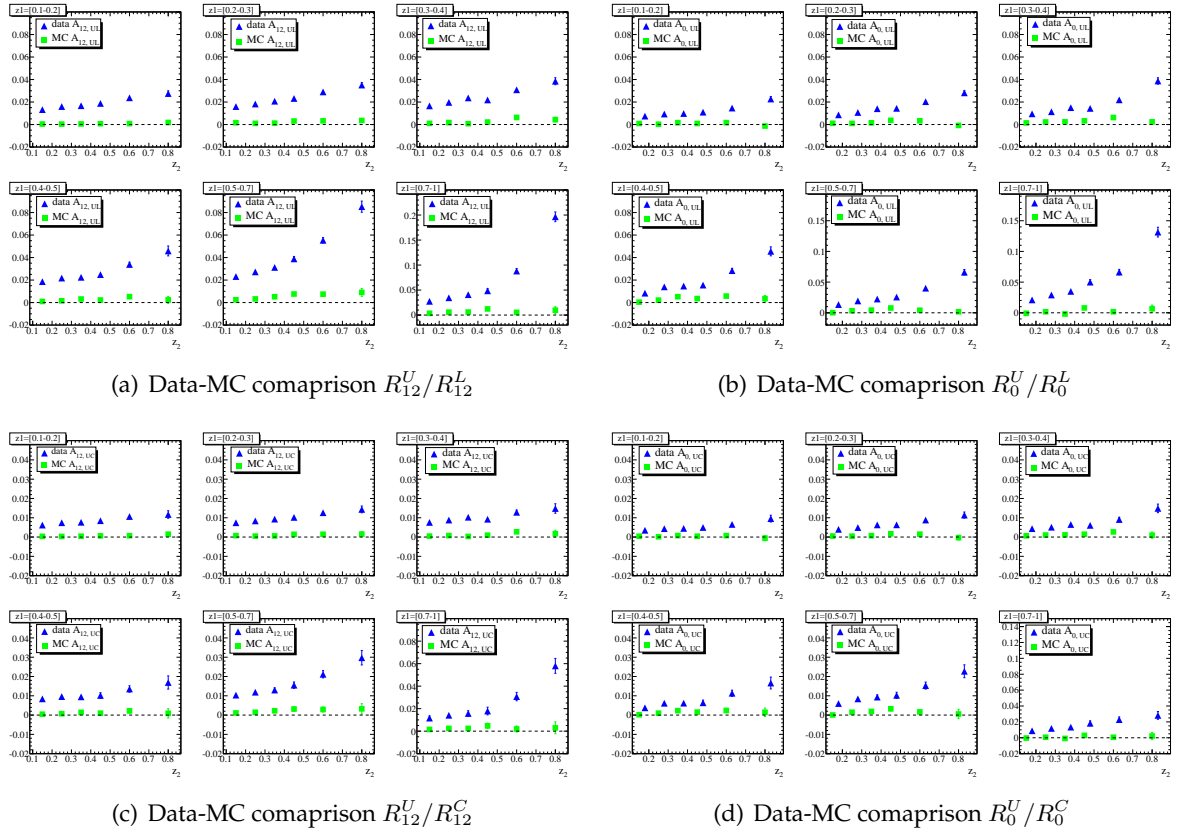


Figure 4.14: Comparison of asymmetries as a function of  $6 \times 6$  ( $z_1, z_2$ )-bin subdivision calculated in data (blue triangles) and MC samples (green squares). The upper two plots show the U/L double ratio, and the last two plots show the U/C double ratio.

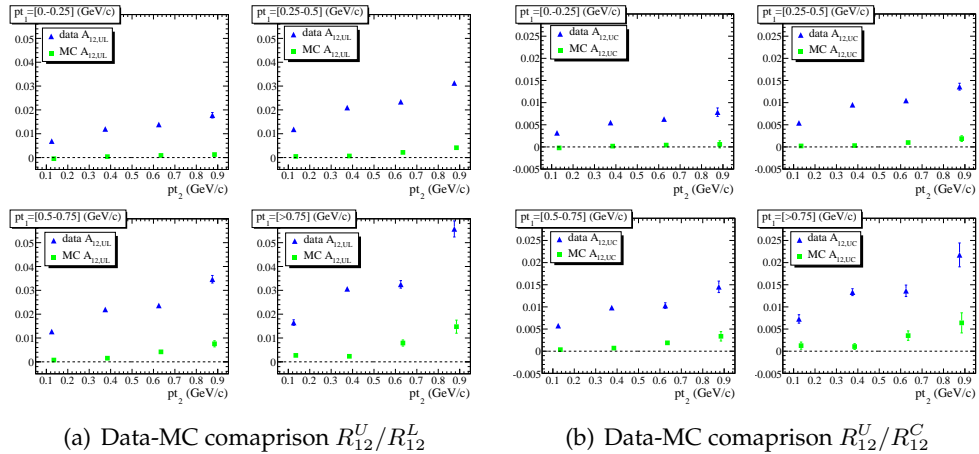


Figure 4.15: RF12: comparison of asymmetries as a function of  $4 \times 4$  ( $p_{t1}, p_{t2}$ )-bin subdivision calculated in data (blue triangles) and MC samples (green squares). The plot on the left shows the U/L double ratio, and the plot on the right shows the U/C double ratio.

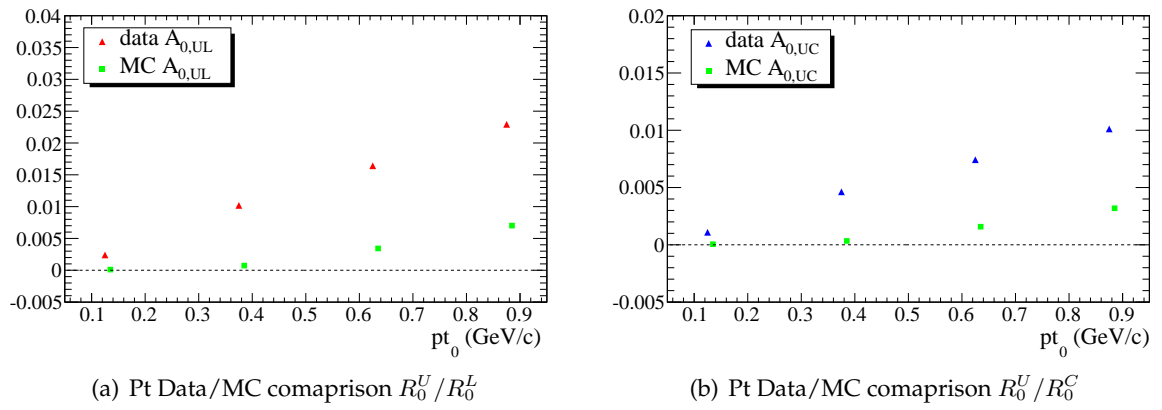


Figure 4.16: RF0: comparison of asymmetries as a function of four  $p_{t0}$ -bin calculated in data (blue triangles) and MC samples (green squares). The plot on the left shows the U/L double ratio, and the plot on the right shows the U/C double ratio.



# Chapter 5

## Study of systematic effects

### 5.1 Asymmetries in the $uds$ Monte Carlo

An important test of the analysis method is the extraction of double ratio from MC. The MC generator describes the radiative gluon effects, but does not contain any polarized function needed for the generation of azimuthal asymmetries, such as the asymmetries based on the Collins effect. Therefore, we expect that the cosine parameter of the fitting function (see Eq.(4.20)) will be consistent with zero when the fit is performed on a sample of simulated  $e^+e^- \rightarrow q\bar{q}$  ( $q = u, d, s$ ) events. The MC generated events undergo a detailed simulation of the *BABAR* detector based on the *GEANT* [105] simulation package, which takes into account the conditions of the detector and the level of machine background in the different data taking periods. We classify six main data taking periods, referring to them as Run1 to Run6, from the older to the newer.

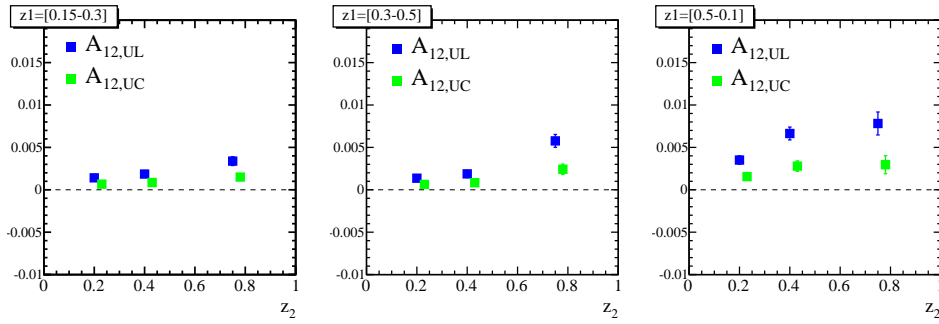
Off-Peak sample			On-Peak sample		
	# events ( $\cdot 10^3$ )	$\mathcal{L}_{equiv.} (fb^{-1})$		# events ( $\cdot 10^3$ )	$\mathcal{L}_{equiv.} (fb^{-1})$
Run1	12400	5.93	Run1	85000	40.76
Run2	31800	15.21	Run2	256200	122.67
Run3	11800	5.64	Run3	134800	64.59
Run4	34200	16.36	Run4	416200	199.23
Run5	59800	28.61	Run5	553200	264.78
Run6	33000	15.79	Run6	327400	157.74
total $\mathcal{L}_{equiv.} \sim (2 \cdot 468.9) fb^{-1}$					

Table 5.1: Number of events and equivalent luminosity ( $\mathcal{L} = N/\sigma$ ) for each  $uds$  MC run. In the left side of the table are summarized the values for the off-peak sample, and in the right side the on-peak values.

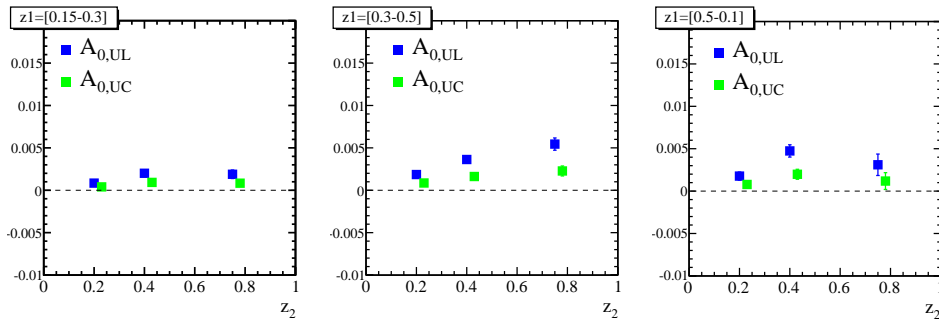
In order to have a simulation as consistent with data as possible, in all studies reported in this

dissertation unless otherwise specified, we use an admixture of MC samples from different Runs, where every Run contributes with a number of events equivalent to twice the corresponding integrated luminosity, as reported in Tab. 5.1.

The simulated events are then reconstructed and analysed as the experimental data. The results of the fits to the asymmetry for the  $uds$  MC are reported in Fig. 5.1 and in Tab. 5.2. In these plots, we coupled two adjacent bins of fractional energy to improve the measurements, since the asymmetry results are consistent for near  $z$ -bins (see also Fig. 4.14, where the  $uds$  MC are compared to the data sample in all the 36 bins of fractional energy). The enlarged  $(z_1, z_2)$  bin subdivision is the following:  $[0.15 - 0.3]$ ,  $[0.3 - 0.5]$ , and  $[0.5 - 0.1]$ . The top three plots (Fig. 5.1(a)) show the asymmetry parameters obtained in this enlarged  $(z_1, z_2)$  intervals, for the U/L and U/C ratios in the thrust reference frame. The bottom three plots (Fig. 5.1(b)) show the same quantities for the second hadron momentum frame. Values of the asymmetries slightly different from zero are seen in various bins, especially for the U/L ratio at high  $z$  values, where they almost reach the 1% level.



(a) RF12: thrust reference frame



(b) RF0: second hadron momentum frame

Figure 5.1: Double ratio asymmetries measured on MC sample in different  $(z_1, z_2)$  bins in the RF12 frame (a) and in the RF0 frame (b). The blue and green squares refer to the U/L and U/C double ratios, respectively.

We also studied the asymmetry as a function of  $p_t$ -bins. The result of the fits to the double ratios in the 16  $(p_{t1}, p_{t2})$  bins and in the 4  $p_{t0}$  bins are shown in Fig. 5.2, where the blue and

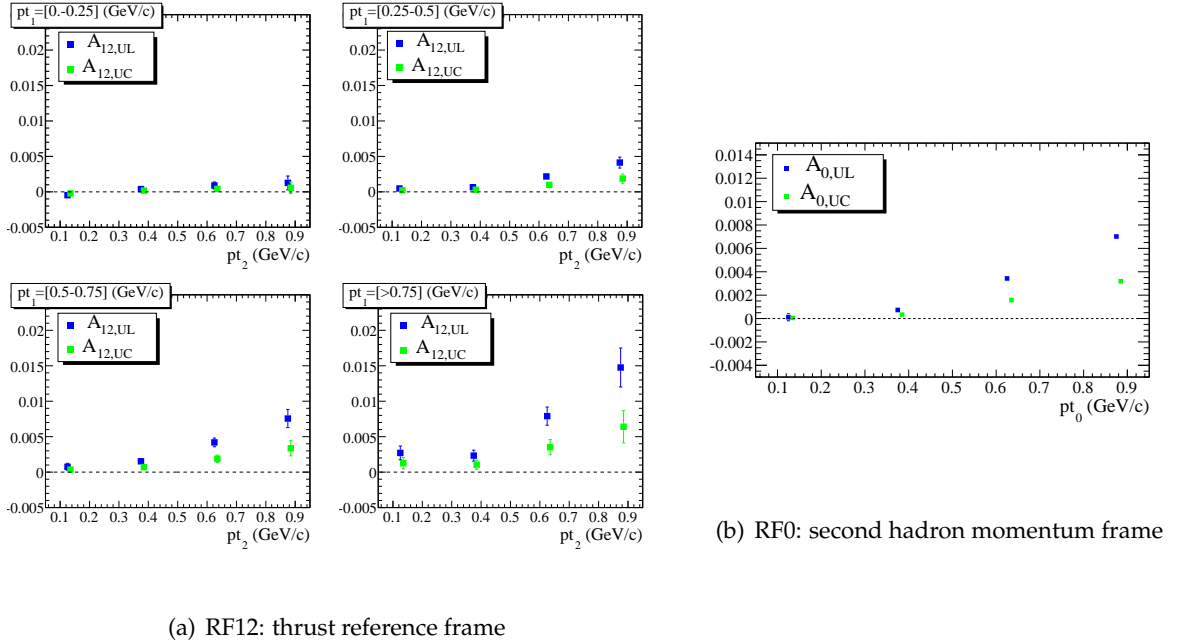


Figure 5.2: MC double ratio study as a function of 16 bins of  $(p_{t1}, p_{t2})$ (a), and as a function of 4  $p_{t0}$  bins (b). The blue squares refer to the U/L ratio, and the green squares to the U/C ratio. The asymmetry increase for higher  $p_t$  values.

green squares refer to the U/L and U/C ratios, and summarized in Tab. 5.3.

Also in these cases non zero asymmetries are seen, and it seems that they are due to pions with transverse momentum  $p_t > 0.5$  GeV/c. To cross check this hypothesis, we separate the reconstructed pions in two MC samples requiring their transverse momentum with respect to the thrust axis to be either  $p_{ti} < 0.5$  GeV/c or  $p_{ti} > 0.5$  GeV/c, and fit again the double ratio in the two samples. The results are shown in Figs. 5.3 and 5.4 for the RF12 and RF0 frames, respectively. In both cases the cosine modulation of the azimuthal distributions for the higher transverse momenta are clear (red fit in figures). On the contrary, the distributions for lower  $p_t$  show negligible asymmetries and can be fitted also with a flat function (blue fits in the same figures).

In order to understand if the observed bias is related to the detector response, we varied the selection criteria and repeated the analysis after each variation. In particular, we performed the analysis:

- using different selectors for pions and/or electron and muon vetos;
- removing sequentially most of the cuts;
- changing the requirement on the minimum number of charged tracks ( $nTracks > 3, 4, \dots$ );

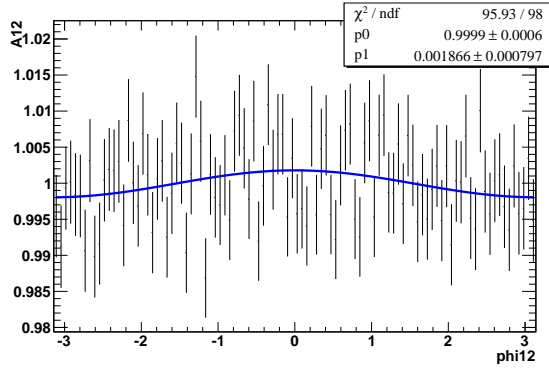
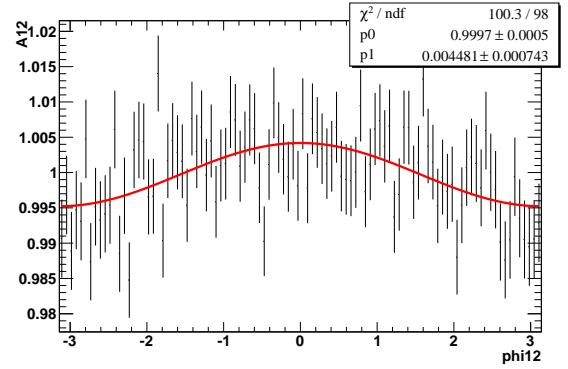
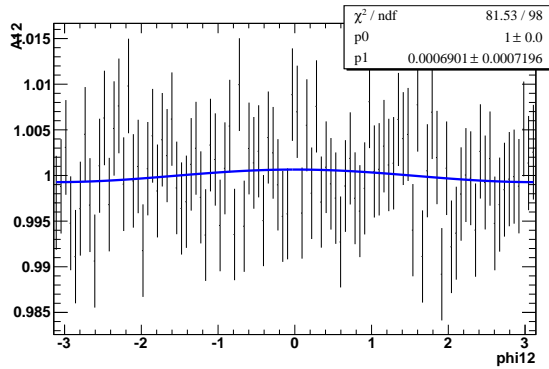
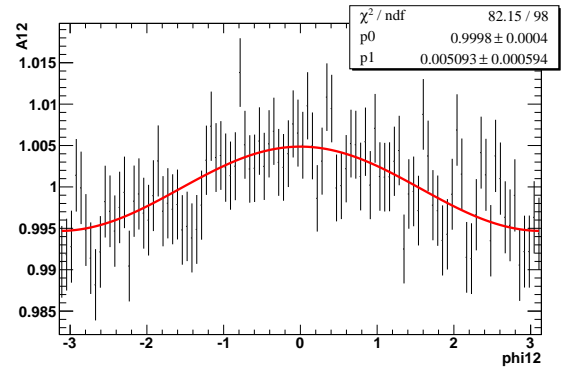
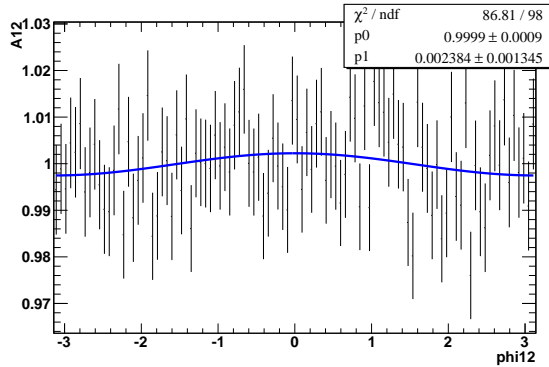
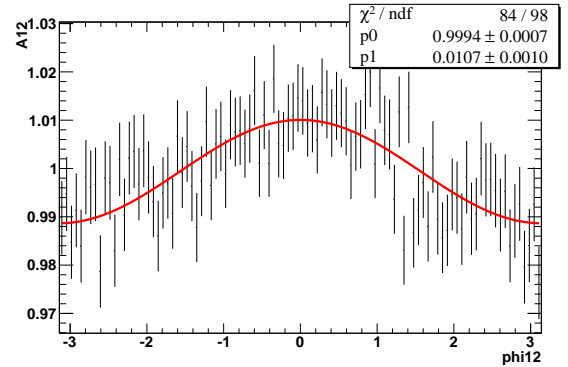
(a)  $p_{t1,2} < 0.5$  GeV/c:  $(z_1; z_2) = (0.15-0.3; 0.5-0.1)$ (b)  $p_{t1,2} > 0.5$  GeV/c:  $(z_1; z_2) = (0.15-0.3; 0.5-0.1)$ (c)  $p_{t1,2} < 0.5$  GeV/c:  $(z_1; z_2) = (0.3-0.5; 0.3-0.5)$ (d)  $p_{t1,2} > 0.5$  GeV/c:  $(z_1; z_2) = (0.3-0.5; 0.3-0.5)$ (e)  $p_{t1,2} < 0.5$  GeV/c:  $(z_1; z_2) = (0.5-1.; 0.3-0.5)$ (f)  $p_{t1,2} > 0.5$  GeV/c:  $(z_1; z_2) = (0.5-1.; 0.3-0.5)$ 

Figure 5.3: RF12: comparison of distribution obtained selecting pions with  $p_{t1,2} < 0.5$  GeV/c (plots on the left, blue fits) and distribution for pions with  $p_{t1,2} > 0.5$  GeV/c (plots on the right, red fits). For pions with higher transverse momentum it is clearly evident the cosine modulation, not observed in the low  $p_t$  distribution, which is the origin of the bias.

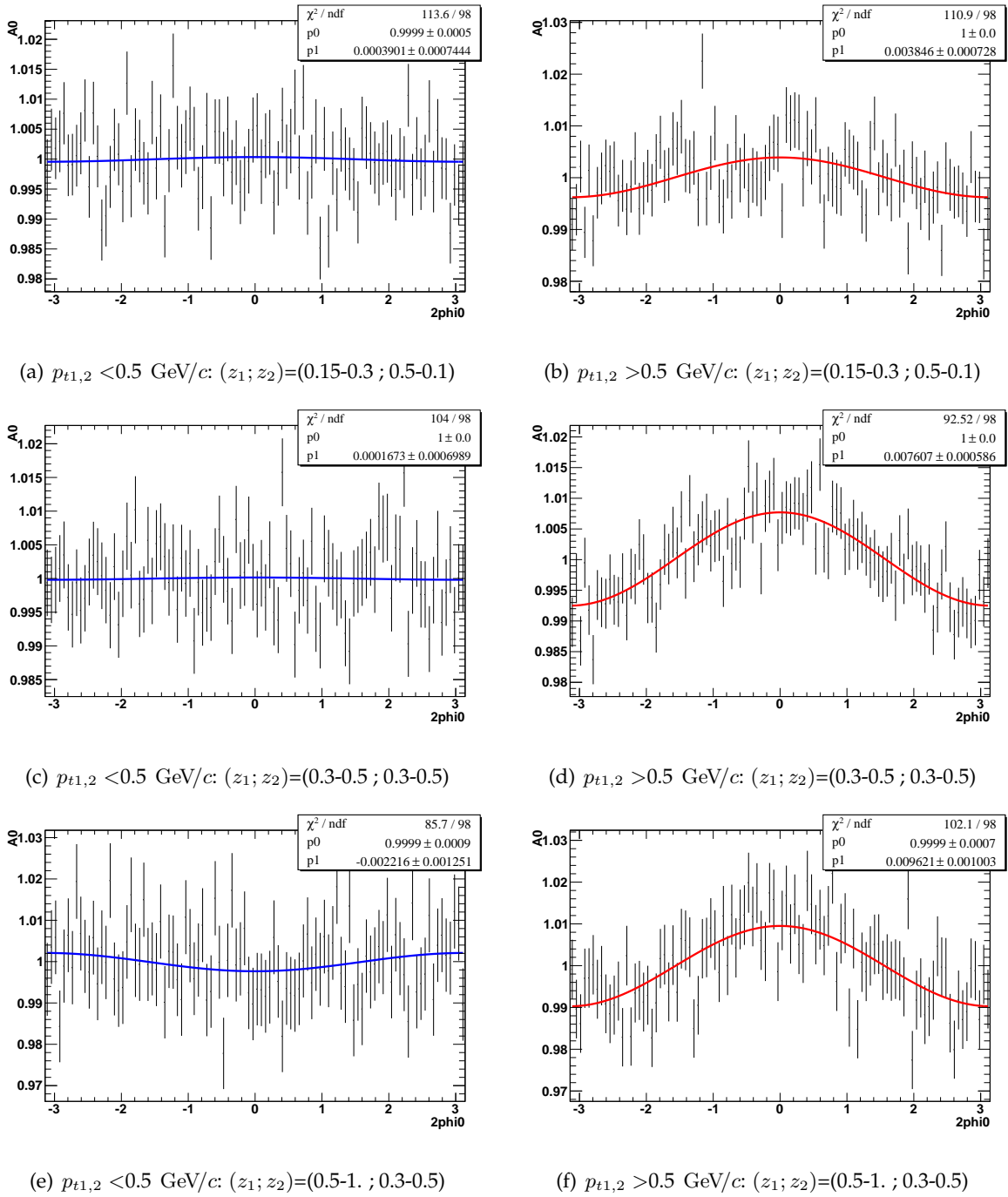


Figure 5.4: RF0: comparison of distribution obtained selecting pions with  $p_{t1,2} < 0.5$  GeV/c (plots on the left, blue fits) and distribution for pions with  $p_{t1,2} > 0.5$  GeV/c (plots on the right, red fits). For pions with higher transverse momentum it is clearly evident the cosine modulation, not observed in the low  $p_t$  distribution, which is the origin of the bias.

- dividing the MC sample in different sub-samples, by data taking period;
- varying the  $z$ -bins range;
- selecting events well contained in the detector, with the requirement of a polar angle of the thrust axis higher than  $70^\circ$ .

None of them turn out to be an evident source of the observed bias.

We can remove the effect of particle reconstruction and identification measuring the azimuthal asymmetries at generator level, that is using the particles' true momenta, as produced by the generator before the GEANT simulation is performed.

We perform two different studies: for the first we consider all charged pions coming directly from the fragmenting  $q\bar{q}$  pair, while for the second study we used only the true pions matching the reconstructed tracks. In addition, to calculate the "true" azimuthal angles in the RF12 reference frame, we used the  $q\bar{q}$  axis instead of the thrust axis.

The results of these studies in terms of fitted asymmetry parameters for the usual  $(z_1/z_2)$ ,  $(p_{t1}p_{t2})$  and  $p_{t0}$  bins, are reported in Figs.5.5 and 5.6.

The asymmetries resulting from the sample of all generated pions (shown on the left of the figures) are consistent with zero in every bin, with few exceptions, and no particular path of the deviations from zero is observed. That is compatible with the assumption that only minimal, if not negligible effects are expected in pure MC due to gluon radiative corrections implemented in the generator model.

Looking at the asymmetries obtained from the sample of generated pions which are associated to effectively reconstructed tracks (shown on the right side of the 5.5 and 5.6) a different behavior is seen in the two reference frames. In fact, the measured asymmetries are essentially consistent with zero in each bin for RF12, but they show values very similar to those obtained fitting the reconstructed pions (see Figs.5.1(b) and 5.2(b)) for RF0.

From these observations we conclude that the small biases seen measuring the Collins asymmetries in the  $uds$  MC samples are real and origin from the experimental method used, different for the two reference frames.

In RF12, the bias is mainly due to the fact that the *true* reference axis, that is the  $q\bar{q}$  direction, cannot be experimentally accessed, and it is therefore approximated by the thrust axis. In RF0, instead, the main effect is the loss of particles outside the detector acceptance, not fully compensated in the ratio of the azimuthal distributions. In both cases pions with higher  $z$  and  $p_t$  are more affected by these experimental limitations.

In conclusion, we decide to correct the asymmetries measured in the data for the bias obtained fitting the double ratio in the fully reconstructed  $uds$  MC sample. The correction is applied on a bin-by-bin basis and, because track resolution and track and PID efficiencies are not perfectly reproduced by the detector simulation, we conservatively assign to the applied

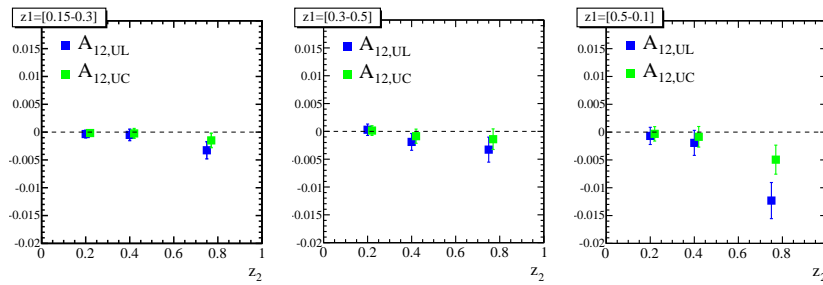
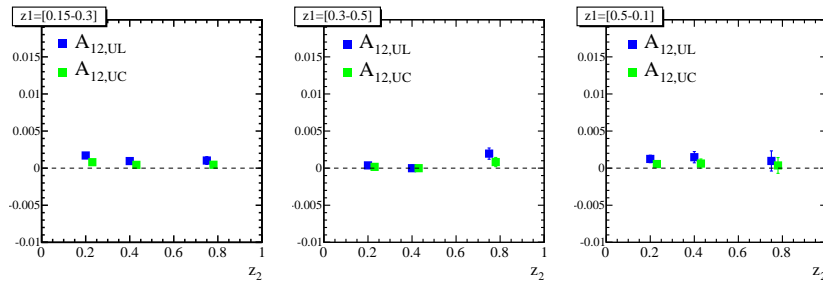
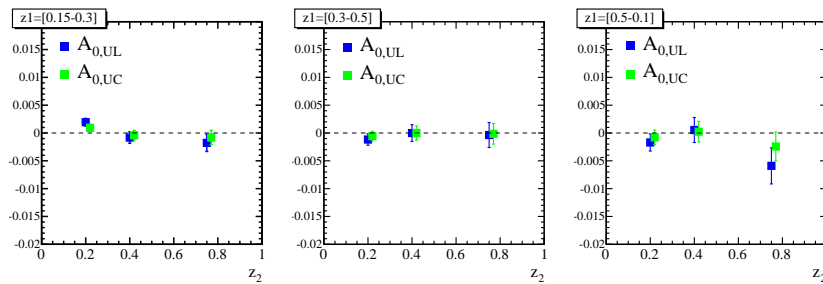
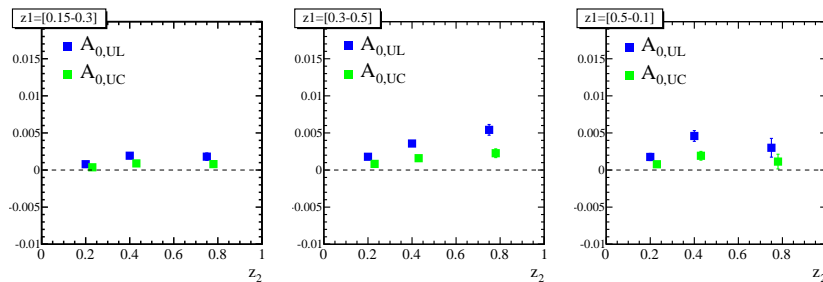
(a) RF12: generated pions  $vs$  ( $z_1, z_2$ )(b) RF12: generated associated pions  $vs$  ( $z_1, z_2$ )(c) RF0: generated pions  $vs$  ( $z_1, z_2$ )(d) RF0: generated associated pions  $vs$  ( $z_1, z_2$ )

Figure 5.5: Distribution as a function of  $(z_1, z_2)$  for generate associated pions (a) and (c), and distribution and for generated pions (b) and (d). Blue and green squares refer to the U/L and U/C double ratio, respectively.

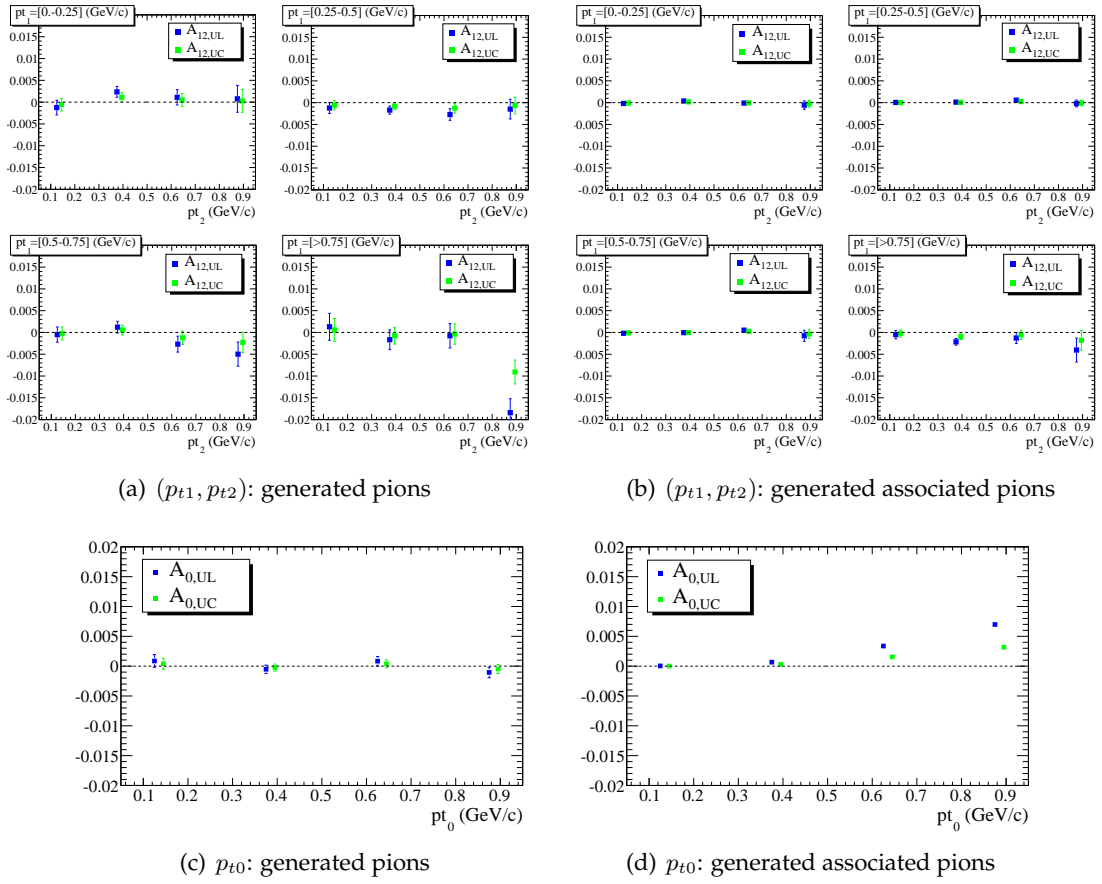


Figure 5.6: Distribution as a function of  $(p_{t1}, p_{t2})$  for generate pions (a) and (c), and distribution for generated associated pions (b) and (d). Blue and green squares refer to the U/L and U/C double ratio, respectively.

corrections the result of the combination in quadrature of the statistical error and the bias measured in each bin as systematic error.

Bins	$(z_1, z_2)$	$A_{12}^{UL}$	$A_0^{UL}$	$A_{12}^{UC}$	$A_0^{UC}$
1	[0.15-0.2][0.15-0.2]	0.0014±0.0002	0.0008±0.0002	0.0007±0.0002	0.0004±0.0002
2	[0.15-0.2][0.2-0.3]	0.0014±0.0002	0.0008±0.0002	0.0007±0.0002	0.0004±0.0002
3	[0.15-0.2][0.3-0.4]	0.0019±0.0003	0.0020±0.0003	0.0009±0.0003	0.0009±0.0003
4	[0.15-0.2][0.4-0.5]	0.0019±0.0003	0.0020±0.0003	0.0009±0.0003	0.0009±0.0003
5	[0.15-0.2][0.5-0.7]	0.0034±0.0006	0.0019±0.0006	0.0015±0.0004	0.0008±0.0004
6	[0.15-0.2][0.7-1.0]	0.0034±0.0006	0.0019±0.0006	0.0015±0.0004	0.0008±0.0004
7	[0.2-0.3][0.15-0.2]	0.0014±0.0002	0.0008±0.0002	0.0007±0.0002	0.0004±0.0002
8	[0.2-0.3][0.2-0.3]	0.0014±0.0002	0.0008±0.0002	0.0007±0.0002	0.0004±0.0002
9	[0.2-0.3][0.3-0.4]	0.0019±0.0003	0.0020±0.0003	0.0009±0.0003	0.0009±0.0003
10	[0.2-0.3][0.4-0.5]	0.0019±0.0003	0.0020±0.0003	0.0009±0.0003	0.0009±0.0003
11	[0.2-0.3][0.5-0.7]	0.0034±0.0006	0.0019±0.0006	0.0015±0.0004	0.0008±0.0004
12	[0.2-0.3][0.7-1.0]	0.0034±0.0006	0.0019±0.0006	0.0015±0.0004	0.0008±0.0004
13	[0.3-0.4][0.15-0.2]	0.0014±0.0003	0.0019±0.0003	0.0006±0.0003	0.0009±0.0003
14	[0.3-0.4][0.2-0.3]	0.0014±0.0003	0.0019±0.0003	0.0006±0.0003	0.0009±0.0003
15	[0.3-0.4][0.3-0.4]	0.0019±0.0004	0.0036±0.0004	0.0008±0.0004	0.0016±0.0003
16	[0.3-0.4][0.4-0.5]	0.0019±0.0004	0.0036±0.0004	0.0008±0.0004	0.0016±0.0003
17	[0.3-0.4][0.5-0.7]	0.0058±0.0008	0.0054±0.0007	0.0024±0.0006	0.0023±0.0006
18	[0.3-0.4][0.7-1.0]	0.0058±0.0008	0.0054±0.0007	0.0024±0.0006	0.0023±0.0006
19	[0.4-0.5][0.15-0.2]	0.0014±0.0003	0.0019±0.0003	0.0006±0.0003	0.0009±0.0003
20	[0.4-0.5][0.2-0.3]	0.0014±0.0003	0.0019±0.0003	0.0006±0.0003	0.0009±0.0003
21	[0.4-0.5][0.3-0.4]	0.0019±0.0004	0.0036±0.0004	0.0008±0.0004	0.0016±0.0003
22	[0.4-0.5][0.4-0.5]	0.0019±0.0004	0.0036±0.0004	0.0008±0.0004	0.0016±0.0003
23	[0.4-0.5][0.5-0.7]	0.0058±0.0008	0.0054±0.0007	0.0024±0.0006	0.0023±0.0006
24	[0.4-0.5][0.7-1.0]	0.0058±0.0008	0.0054±0.0007	0.0024±0.0006	0.0023±0.0006
25	[0.5-0.7][0.15-0.2]	0.0035±0.0003	0.0018±0.0005	0.0016±0.0004	0.0008±0.0008
26	[0.5-0.7][0.2-0.3]	0.0035±0.0003	0.0018±0.0005	0.0016±0.0004	0.0008±0.0008
27	[0.5-0.7][0.3-0.4]	0.0066±0.0004	0.0047±0.0007	0.0028±0.0006	0.0020±0.0020
28	[0.5-0.7][0.4-0.5]	0.0066±0.0004	0.0047±0.0007	0.0028±0.0006	0.0020±0.0020
29	[0.5-0.7][0.5-0.7]	0.0078±0.0008	0.0031±0.0013	0.0030±0.0011	0.0012±0.0012
30	[0.5-0.7][0.7-1.0]	0.0078±0.0008	0.0031±0.0013	0.0030±0.0011	0.0012±0.0012
31	[0.7-1.0][0.15-0.2]	0.0035±0.0003	0.0018±0.0005	0.0016±0.0004	0.0008±0.0008
32	[0.7-1.0][0.2-0.3]	0.0035±0.0003	0.0018±0.0005	0.0016±0.0004	0.0008±0.0008
33	[0.7-1.0][0.3-0.4]	0.0066±0.0004	0.0047±0.0007	0.0028±0.0006	0.0020±0.0020
34	[0.7-1.0][0.4-0.5]	0.0066±0.0004	0.0047±0.0007	0.0028±0.0006	0.0020±0.0020
35	[0.7-1.0][0.5-0.7]	0.0078±0.0008	0.0031±0.0013	0.0030±0.0011	0.0012±0.0012
36	[0.7-1.0][0.7-1.0]	0.0078±0.0008	0.0031±0.0013	0.0030±0.0011	0.0012±0.0012

Table 5.2: Fit results of  $uds$  MC asymmetries as a function of 36  $(z_1, z_2)$ , calculated used the larger  $z$ -bins subdivision.

Bins	$(p_{t1}, p_{t2})$	$A_{12}^{UL}$	$A_{12}^{UC}$
1	[0.-0.25][0.-0.25]	-0.0005±0.0005	-0.0002±0.0004
2	[0.-0.25][0.25-0.5]	0.0004±0.0003	0.0002±0.0003
3	[0.-0.25][0.5-0.75]	0.0009±0.0005	0.0004±0.0004
4	[0.-0.25][>0.75]	0.0012±0.0010	0.0006±0.0008
5	[0.25-0.5][0.-0.25]	0.0005±0.0003	0.0002±0.0003
6	[0.25-0.5][0.25-0.5]	0.0007±0.0002	0.0003±0.0002
7	[0.25-0.5][0.5-0.75]	0.0022±0.0004	0.0009±0.0003
8	[0.25-0.5][>0.75]	0.0041±0.0008	0.0019±0.0006
9	[0.5-0.75][0.-0.25]	0.0007±0.0005	0.0003±0.0004
10	[0.5-0.75][0.25-0.5]	0.0015±0.0004	0.0007±0.0003
11	[0.5-0.75][0.5-0.75]	0.0042±0.0006	0.0019±0.0005
12	[0.5-0.75][>0.75]	0.0075±0.0013	0.0034±0.0010
13	[>0.75][0.-0.25]	0.0027±0.0010	0.0012±0.0008
14	[>0.75][0.25-0.5]	0.0023±0.0008	0.0010±0.0006
15	[>0.75][0.5-0.75]	0.0079±0.0013	0.0035±0.0010
16	[>0.75][>0.75]	0.0147±0.0027	0.0064±0.0022
	$p_{t0}$	$A_0^{UL}$	$A_0^{UC}$
1	[0.-0.25]	0.0001±0.0003	0.0000±0.0002
2	[0.25-0.5]	0.0007±0.0002	0.0003±0.0002
3	[0.5-0.75]	0.0034±0.0002	0.0016±0.0002
4	[>0.75]	0.0070±0.0003	0.0032±0.0002

Table 5.3: Fit results of  $uds$  MC asymmetries as a function of 16  $(p_{t1}, p_{t2})$  in the first part of table, and as a function of 4  $p_{t0}$  bins in the second part.

## 5.2 Contribution of $c\bar{c}$ , $B\bar{B}$ , and $\tau^+\tau^-$ events to the asymmetries

The presence of background processes produces a dilution of the azimuthal asymmetry  $A_\alpha$ ,  $\alpha = 12, 0$ , so that the measured asymmetry  $A_\alpha^{meas}$  results from the combination of the azimuthal distributions produced by the different physics processes contributing to the final sample, and can be written as:

$$A_\alpha^{meas} = \left(1 - \sum_i F_i\right) \cdot A_\alpha + \sum_i F_i \cdot A_\alpha^i \quad (5.1)$$

where  $A_\alpha^i$  and  $F_i$  are the asymmetry and the fraction of pion pairs in the selected sample due to the  $i^{th}$  background component, which must be estimated in order to extract the Collins asymmetries for light quark fragmentation. The background processes giving a significant contribution are  $e^+e^- \rightarrow \tau^+\tau^-$ ,  $e^+e^- \rightarrow c\bar{c}$ , and  $e^+e^- \rightarrow \mathcal{Y}(4S) \rightarrow B\bar{B}$  events surviving the selection procedure. We refer to them as the  $\tau$ , charm and bottom background, respectively. In the former process azimuthal asymmetries can arise from the weak decay of heavy leptons, while for the charm processes also the Collins effects may contribute, even if suppressed because of the heavy mass of the fragmenting quarks (the Collins effect for the  $b$ -quark is suppressed even more).

The study of the azimuthal asymmetries for this kind of processes would therefore be interesting by its own, but larger statistics and an optimized analysis would be necessary to perform precise measurements.

The asymmetries and the fraction  $F_i$  are determined using both MC and data control sample specific to each background process.

### Charm and bottom contribution to the asymmetries

The contribution of  $e^+e^- \rightarrow c\bar{c}$  to the total hadronic cross section is about 40% ( $\sim 30\%$  at the peak of the  $\mathcal{Y}(4S)$ , see Tab.3.1).

Because of the cut on the event thrust value and the requirements on the track selection, the fraction of pion pairs coming from  $B\bar{B}$  decays amounts at most to 2.5% at small fractional energies, and is negligible for  $z_i > 0.5$ . For this reason, we can safely consider the very small contribution of bottom background together with the charm correction, assuming null bottom-quark asymmetries:  $A_\alpha^B = 0$ .

We use the generic  $c\bar{c}$  and  $B\bar{B}$  ( $B^+B^-$  plus  $B^0\bar{B}^0$ ) MC simulation for determining the relative contribution  $D$ , and  $B$  in the data sample:

$$D = \frac{N_{c\bar{c}}}{N_{meas}}, \quad B = \frac{N_{b\bar{b}}}{N_{meas}}, \quad (5.2)$$

where  $N_{c\bar{c}}$  ( $N_{b\bar{b}}$ ) are the number of pion pairs in the  $c\bar{c}$  ( $b\bar{b}$ ) MC sample scaled to match the luminosity of the data sample, and  $N_{meas}$  are the number of pion pairs in the full data sample.

In addition, we select a charm-enhanced data sample requiring at least one  $D^*$  from the decay  $D^{*\pm} \rightarrow D^0 \pi^\pm$ , with the  $D^0$  ( $M_{D^0}^{PDG} \simeq 1864.8 \text{ MeV}/c^2$  [51]) reconstructed in four decay channels:

- *mode 1*:  $D^0 \rightarrow K^- \pi^+$  ( $\mathcal{B} = 3.89\%$ ),
- *mode 2*:  $D^0 \rightarrow K^- \pi^+ \pi^- \pi^+$  ( $\mathcal{B} = 8.1\%$ ),
- *mode 3*:  $D^0 \rightarrow K^- \pi^+ \pi^0$  ( $\mathcal{B} = 13.9\%$ ),
- *mode 4*:  $D^0 \rightarrow K_S^0 \pi^+ \pi^-$  ( $\mathcal{B} = 2.99\%$ ).

The  $D^0$ 's are reconstructed starting from the following lists of composite particles for the four  $D^0$  decay modes:

*mode 1*  $D^0 \rightarrow K^- \pi^+$  : we use the *D0ToKPiDefault* list, which requires:

- pion list: *GoodTracksVeryLoose*,
- kaon list: *GoodTracksVeryLoose*,
- $D^0$  mass selection:  $(M_{D^0}^{PDG} - 0.040 : M_{D^0}^{PDG} + 0.040) \text{ MeV}/c^2$ ;

*mode 2*  $D^0 \rightarrow K^- \pi^+ \pi^- \pi^+$ : we use the *D0ToK3PiDefault* list:

- pion list: *GoodTracksVeryLoose*,
- kaon list: *KLHNotPion*. It is a PID selector list that satisfy  $L_K/(L_K + L_\pi) > 0.20$  or  $L_p/(L_p + L_\pi) > 0.20$ , where  $L_{K,\pi,p}$  is the Likelihood for the corresponding hypothesis mass.
- fitting algorithm: Add4 (this is the normal four-vector addition),
- $D^0$  mass selection:  $(M_{D^0}^{PDG} - 0.040 : M_{D^0}^{PDG} + 0.040) \text{ MeV}/c^2$ ;

*mode 3* :  $D^0 \rightarrow K^- \pi^+ \pi^0$  we construct our list as follow:

- pion list: *GoodTracksVeryLoose*,
- kaon list: *KLHNotPion*,
- $\pi^0$  list ( $\pi^0 \rightarrow \gamma\gamma$ ): *pi0LooseMass*, with the mass of the two photons constrained to the  $\pi^0$  mass ( $m_{\pi^0}^{PDG} \simeq 135.0 \text{ MeV}/c^2$ ), and with energy in the laboratory frame higher than 0.2 GeV. Add4 fitting algorithm is used to constrain mass, momentum, and primary vertex;
- fitting algorithm: Add4,
- $D^0$  mass selection:  $(M_{D^0}^{PDG} - 0.090 : M_{D^0}^{PDG} + 0.090) \text{ MeV}/c^2$ ;

*mode 4* :  $D^0 \rightarrow K_S^0 \pi^+ \pi^-$  we construct our list as follow:

- pion list: *GoodTracksVeryLoose*,
- $K_S^0$  list ( $K_S^0 \rightarrow \pi\pi$ ): *KsDefaultMass*, with the mass of the two pions constrained to the  $K_S^0$  mass ( $m_{K_S^0}^{PDG} \simeq 497.6 \text{ MeV}/c^2$ ). The fitting algorithm used to constrain mass, momentum, and primary vertex is the *TreeFitter* algorithm, which consider the global decay chain based on a *Kalman filter*;
- fitting algorithm: *Add4*,
- $D^0$  mass selection:  $(M_{D^0}^{PDG} - 0.090 : M_{D^0}^{PDG} + 0.090) \text{ MeV}/c^2$ .

Figure 5.7 and Fig. 5.9(a) show the mass distribution of the  $D^0$  reconstructed in the four decay modes, in the MC sample and in the off-peak data sample, respectively. The fits use the sum of a narrow Gaussian, plus a wider one, plus a second order polynomial background. Table 5.4 summarized the fit parameters.

$D^{*\pm}$  are then reconstructed by adding one charged pion with momentum less than  $0.6 \text{ GeV}/c$  to the four-momentum of the  $D^0$  candidate coming from the merged list as before. Figure 5.8 shows the  $\Delta M$  distributions calculated in the  $c\bar{c}$  and  $b\bar{b}$  MC samples, where  $\Delta M = (M_{D^*} - M_{D^0})$  ( $\Delta M = 145.421 \pm 0.010 \text{ MeV}$  [51]). Also in this case, the fit functions are a sum of a narrow Gaussian, plus a wider one, plus the typical background shape function for  $D^* - D^0$  mass difference. Figure 5.9(b) shows the same distribution obtained in the off-peak data sample. The fit parameters for the 4 decay modes are summarized in Tab. 5.5.

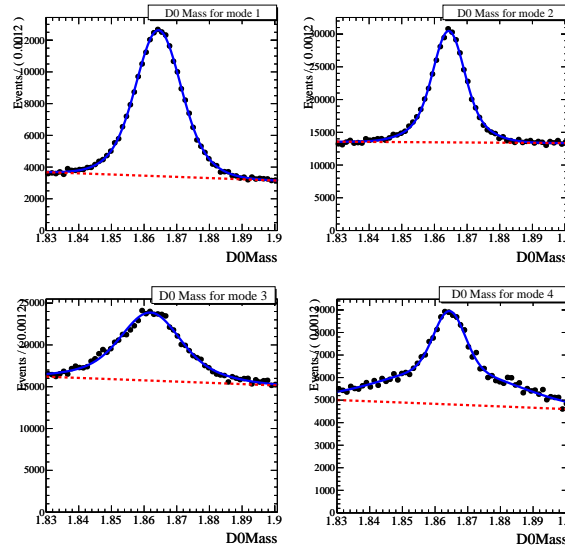


Figure 5.7:  $D^0$  mass for the decay mode  $D^0 \rightarrow K\pi$  (mode 1),  $D^0 \rightarrow K3\pi$  (mode 2),  $D^0 \rightarrow K\pi\pi^0$  (mode 3), and  $D^0 \rightarrow K_S\pi\pi$  (mode 4). The  $D^0$  mass is fitted with a double gaussian and the dashed red line is the background parameterization.

Finally, for the selection of the enhanced  $D^*$  sample, we apply the following cuts:

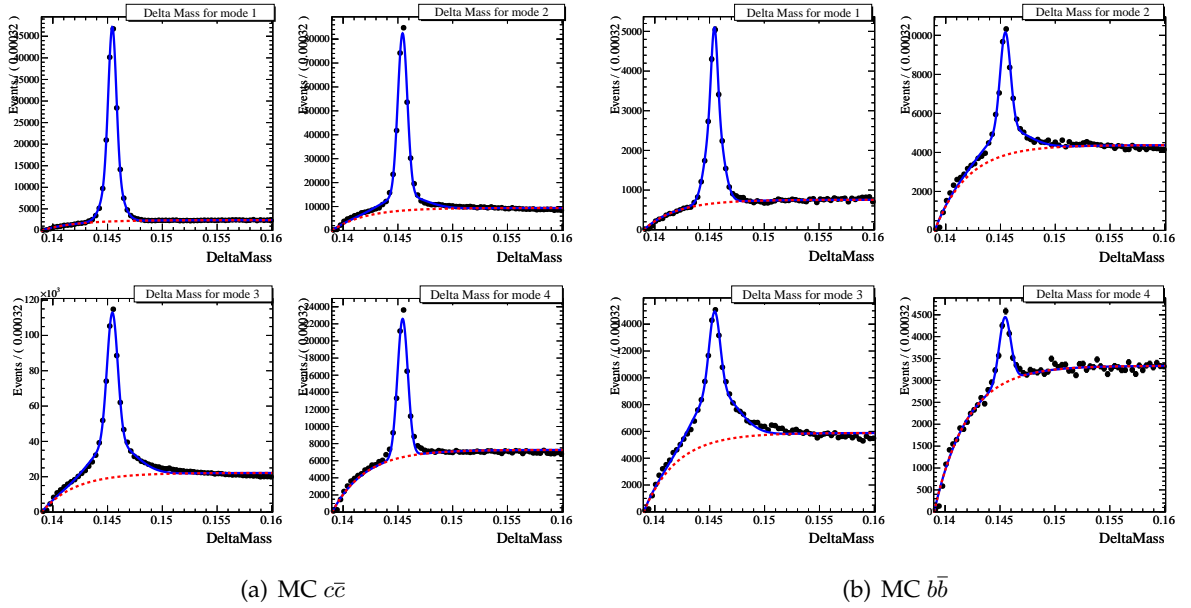


Figure 5.8: Monte Carlo distributions of  $\Delta M$  reconstructed in the  $c\bar{c}$  (a) and  $B\bar{B}$  (b) samples, where  $\Delta M = (M_{D^*} - M_{D^0})$  and  $\Delta M_{pdg} = 145.421 \pm 0.010$  MeV. The fit functions are a sum of a narrow Gaussian, plus a wider one, plus an exponential function for the background parameterization (dashed red line).

- *mode 1*

- $\chi^2$ -probability for fitting the  $D^*$  vertex  $>0.001$
- $1.835 < M_{D^0} < 1.90$  GeV/ $c^2$
- $0.1425 < \Delta M < 0.149$  GeV/ $c^2$

- *mode 2*

- $\chi^2$ -probability for fitting the  $D^*$  vertex  $>0.001$
- $1.83 < M_{D^0} < 1.90$  GeV/ $c^2$
- $0.1425 < \Delta M < 0.148$  GeV/ $c^2$

- *mode 3*

- $\chi^2$ -probability for fitting the  $D^*$  vertex  $>0.001$
- $1.83 < M_{D^0} < 1.90$  GeV/ $c^2$
- $0.1425 < \Delta M < 0.149$  GeV/ $c^2$
- $0.120 < M_{\pi^0} < 0.150$  GeV/ $c^2$

- *mode 4*

- $\chi^2$ -probability for fitting the  $D^*$  vertex  $>0.001$
- $1.835 < M_{D^0} < 1.895 \text{ GeV}/c^2$
- $0.1425 < \Delta M < 0.149 \text{ GeV}/c^2$
- $0.492 < M_{K_S^0} < 0.502 \text{ GeV}/c^2$

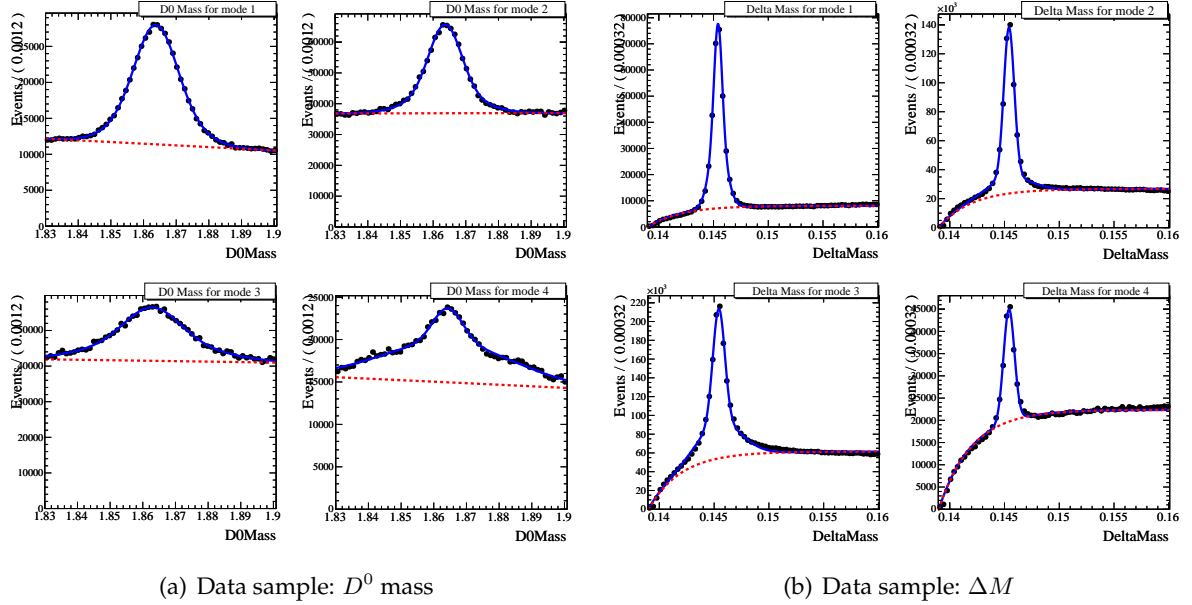


Figure 5.9: Distributions of (a)  $M_{D^0}$  and (b)  $\Delta M$  reconstructed in the off-peak data sample.

Similarly as for the full data sample, we calculate the  $c\bar{c}$  and  $b\bar{b}$  contribution to this enhanced sample:

$$d = \frac{N_{c\bar{c}(D^*)}}{N_{D^*}}, \quad b = \frac{N_{b\bar{b}(D^*)}}{N_{D^*}}. \quad (5.3)$$

In this case,  $N_{c\bar{c}(D^*)}$  ( $N_{b\bar{b}(D^*)}$ ) and  $N_{D^*}$  are the number of pion pairs in the enhanced MC and data sample, respectively.

Measuring the double ratio asymmetries  $A_{meas}$  and  $A_{D^*}$  respectively in the full and in the  $D^*$  enhanced data sample, and assuming that the charm asymmetry is the same in both samples and zero for bottom quark, we can write the following two equations:

$$\begin{aligned} A_{meas} &= (1 - D - B) \cdot A_{uds} + D \cdot A_{charm} \\ A_{D^*} &= d \cdot A_{charm} + (1 - d - b) \cdot A_{uds} \end{aligned} \quad (5.4)$$

The relative contributions  $D$ ,  $d$ ,  $B$ , and  $b$  for the various  $z$ - and  $p_t$ -bins are summarized in Tab. 5.6 and in Tab. 5.7, respectively.

Note that the two equations (5.4) are not yet complete. We need also to take into account the contribution coming from the  $\tau$  background, described in the next paragraph.

$M_{D^0}$ : MC $c\bar{c}$ sample					
mode num.	$M_{D^0}$ (MeV/ $c^2$ )	$\sigma_{gn}$ (MeV/ $c^2$ )	$\sigma_{gw}$ (MeV/ $c^2$ )	$f_n$	$f_w$
1	$1864.39 \pm 0.03$	$6.20 \pm 0.11$	$10.47 \pm 0.44$	$0.241 \pm 0.019$	$0.176 \pm 0.017$
2	$1864.36 \pm 0.03$	$4.44 \pm 0.11$	$9.03 \pm 0.50$	$0.116 \pm 0.009$	$0.086 \pm 0.007$
3	$1861.93 \pm 0.08$	$7.93 \pm 0.39$	$15.42 \pm 0.80$	$0.081 \pm 0.011$	$0.079 \pm 0.014$
4	$1864.39 \pm 0.08$	$4.72 \pm 0.11$	$4.72 \pm 0.11$	$0.068 \pm 0.002$	$0.166 \pm 0.054$
$M_{D^0}$ : off-peak data sample					
mode num.	$M_{D^0}$ (MeV/ $c^2$ )	$\sigma_{gn}$ (MeV/ $c^2$ )	$\sigma_{gw}$ (MeV/ $c^2$ )	$f_n$	$f_w$
1	$1863.79 \pm 0.03$	$6.09 \pm 0.31$	$9.78 \pm 0.80$	$0.241 \pm 0.019$	$0.176 \pm 0.017$
2	$1863.68 \pm 0.02$	$4.88 \pm 0.09$	$9.89 \pm 0.50$	$0.116 \pm 0.009$	$0.086 \pm 0.007$
3	$1862.84 \pm 0.07$	$8.09 \pm 0.48$	$16.70 \pm 2.501$	$0.081 \pm 0.011$	$0.079 \pm 0.014$
4	$1864.29 \pm 0.08$	$4.53 \pm 0.11$	$7.77 \pm 0.21$	$0.035 \pm 0.001$	$0.164 \pm 0.004$

Table 5.4:  $M_{D^0}$  fit parameters for  $c\bar{c}$  MC and for the off-peak data sample, which is used as example. The function used is a sum of a narrow Gaussian, with mean  $M_{D^0}$  and width  $\sigma_{gn}$ , plus a wider one, with the same mean and width  $\sigma_{gw}$ . The  $f_n$  and  $f_w$  parameters are the signal fractions for the relative Gaussian. The background fit parameters are not reported in the table.

$\Delta M(M_{D^*} - M_{D^0})$ : MC $c\bar{c}$ sample					
mode num.	$\Delta M$ (MeV/ $c^2$ )	$\sigma_{gn}$ (MeV/ $c^2$ )	$\sigma_{gw}$ (MeV/ $c^2$ )	$f_n$	$f_w$
1	$145.434 \pm 0.001$	$0.357 \pm 0.004$	$0.792 \pm 0.011$	$0.321 \pm 0.007$	$0.227 \pm 0.007$
2	$145.426 \pm 0.001$	$0.431 \pm 0.001$	$2.301 \pm 0.022$	$0.268 \pm 0.001$	$0.112 \pm 0.001$
3	$145.439 \pm 0.001$	$0.489 \pm 0.002$	$2.241 \pm 0.011$	$0.154 \pm 0.001$	$0.165 \pm 0.001$
4	$145.431 \pm 0.003$	$0.473 \pm 0.004$	—	$0.127 \pm 0.001$	—
$\Delta M(M_{D^*} - M_{D^0})$ : MC $b\bar{b}$ sample					
mode num.	$\Delta M$ (MeV/ $c^2$ )	$\sigma_{gn}$ (MeV/ $c^2$ )	$\sigma_{gw}$ (MeV/ $c^2$ )	$f_n$	$f_w$
1	$145.443 \pm 0.005$	$0.284 \pm 0.019$	$0.728 \pm 0.019$	$0.077 \pm 0.010$	$0.219 \pm 0.010$
2	$145.441 \pm 0.007$	$0.473 \pm 0.009$	$2.241 \pm 0.059$	$0.069 \pm 0.002$	$0.068 \pm 0.002$
3	$145.451 \pm 0.007$	$0.500 \pm 0.010$	$2.213 \pm 0.028$	$0.065 \pm 0.002$	$0.140 \pm 0.002$
4	$145.447 \pm 0.018$	$0.526 \pm 0.021$	—	$0.032 \pm 0.001$	—
$\Delta M(M_{D^*} - M_{D^0})$ : off-peak data sample					
mode num.	$\Delta M$ (MeV/ $c^2$ )	$\sigma_{gn}$ (MeV/ $c^2$ )	$\sigma_{gw}$ (MeV/ $c^2$ )	$f_n$	$f_w$
1	$145.413 \pm 0.001$	$0.632 \pm 0.004$	$0.763 \pm 0.008$	$0.174 \pm 0.005$	$0.206 \pm 0.005$
2	$145.411 \pm 0.001$	$0.477 \pm 0.001$	$2.03 \pm 0.022$	$0.188 \pm 0.001$	$0.081 \pm 0.001$
3	$145.430 \pm 0.001$	$0.546 \pm 0.002$	$1.997 \pm 0.006$	$0.114 \pm 0.001$	$0.127 \pm 0.001$
4	$145.410 \pm 0.003$	$0.495 \pm 0.003$	—	$0.072 \pm 0.001$	—

Table 5.5:  $\Delta M$  fit parameters for  $c\bar{c}$ ,  $b\bar{b}$  MC, and for the off-peak data sample, which is used as example. The function used is a sum of a narrow Gaussian, with mean  $\Delta M$  and width  $\sigma_{gn}$ , plus a wider one, with the same mean and width  $\sigma_{gw}$  for the first three modes, and a single Gaussian for the last. The  $f_n$  and  $f_w$  parameters are the signal fractions for the relative Gaussian. The background fit parameters are not shown in the table.

### $e^+e^- \rightarrow \tau^+\tau^-$ contribution to the asymmetries

Since weak decays are well described in MC, we can use the  $\tau^+\tau^-$  MC to evaluate possible effects due to  $\tau$  decays. The asymmetries measured in the  $\tau$  MC sample have a very small

central value and are consistent with zero within about two standard deviations:

- $A_{12,UL}^{\tau MC} = (0.0027 \pm 0.0010)$ ,  $A_{12,UC}^{\tau MC} = (0.0014 \pm 0.0008)$ ;
- $A_{0,UL}^{\tau MC} = (0.0028 \pm 0.0010)$ ,  $A_{0,UC}^{\tau MC} = (0.0014 \pm 0.0008)$ .

We check for possible effects also in data, performing the analysis on the sample of events sitting in the lower-right side of the  $E_{tot}$  vs  $Thrust$  distribution of Fig. 4.5. This region, which is rejected by the event selection because of the high background from  $e^+e^- \rightarrow \tau^+\tau^-$  (in particular by the cut shown in the same picture as the black line), provides a natural  $\tau$ -enhanced data sample. Figure 5.10 shows the event thrust distribution of the  $\tau$ -enhanced data sample (black histogram). Using the  $\tau$ -MC sample, shown as the dashed histogram we estimate a purity of the selected  $\tau$  sample of about 80%.

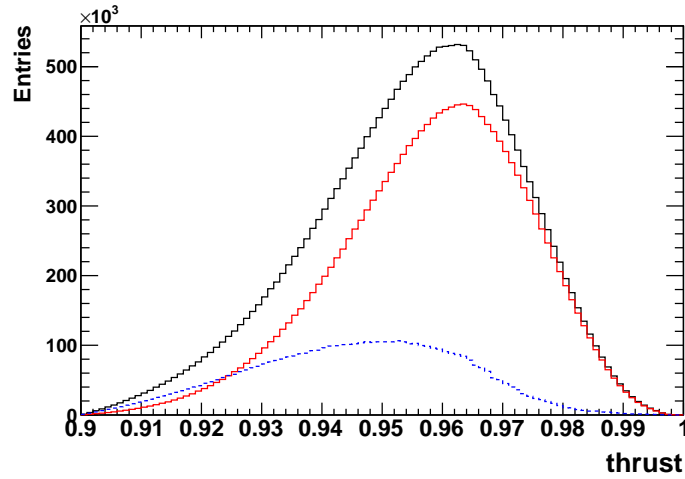


Figure 5.10: Event thrust distribution for the  $\tau$ -enhanced data sample (black) described in the text. The dashed red histogram is the distribution for pure  $\tau^+\tau^-$  events obtained from the  $\tau$  MC sample normalized to the data integrated luminosity, and the dotted blue line is their difference, thus representing the light quarks contamination of the  $\tau$ -enhanced sample.

The asymmetries measured in this enhanced sample are  $A_{12,UL}^{\tau} = (-0.0030 \pm 0.0015)$ ,  $A_{12,UC}^{\tau} = (-0.0015 \pm 0.0012)$ ,  $A_{0,UL}^{\tau} = (-0.0022 \pm 0.0015)$ ,  $A_{0,UC}^{\tau} = (-0.0011 \pm 0.0012)$ , and in Fig. 5.11 are shown, as example, the results for the UL ratio in the two frames.

Following the same procedure described in the previous section, we calculate the fraction of pion pairs in the whole selected data sample from  $\tau^+\tau^-$  events:

$$T = \frac{N_{\tau^+\tau^-}}{N_{meas}}, \quad (5.5)$$

where  $N_{\tau^+\tau^-}$  are the number of pion pairs in the  $\tau$  MC sample scaled to the data integrated luminosity. We found  $T \sim 2\%$  on average, with the value in the various  $z$  and  $p_t$  bins ranging

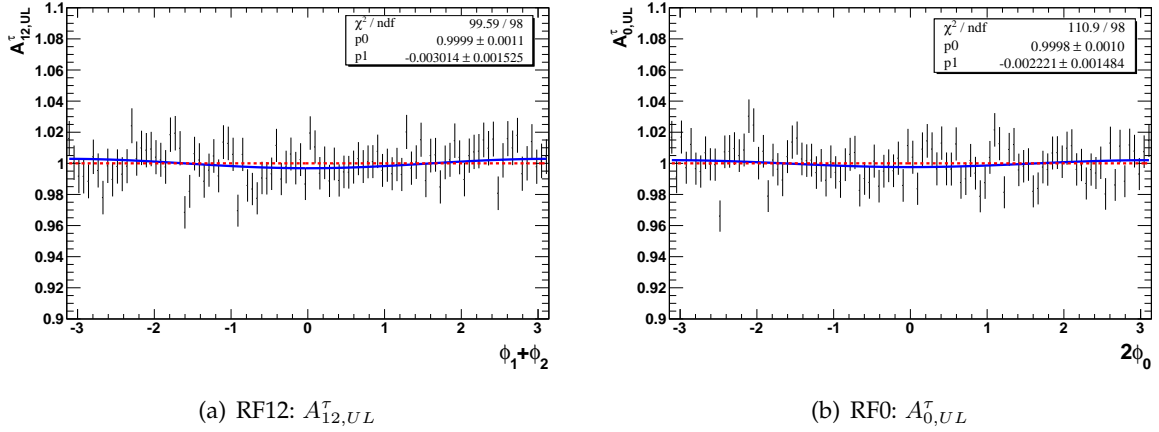


Figure 5.11: U/L double ratio asymmetries for (a) RF12 and (b) RF0 calculated in the  $\tau$  MC samples.

from about 1% at low  $z_i$  to more than 15% at high  $z_i$ , and being more or less independent from the  $p_t$  values, as can be seen in Tab. 5.6 and in Tab. 5.7, respectively.

Considering that the asymmetries measured in both MC and  $\tau$ -enhanced samples are consistent with zero or give only very small deviations from zero, and that the contamination from  $\tau^+\tau^-$  events is significant only at large  $z_i$ , where the Collins effect is much larger as seen in Fig. 4.14, the contribution of the  $\tau$  asymmetry  $A_\alpha^\tau$  to Eq.(5.1) is negligible, and we can safely assume  $A_\alpha^\tau = 0$ .

### Corrections to the measured asymmetries

Taking into account also this contribution, the Eqs.(5.4) become:

$$\begin{aligned} A_{meas} &= (1 - D - B - T) \cdot A_{uds} + D \cdot A_{charm} \\ A_{D^*} &= d \cdot A_{charm} + (1 - d - b) \cdot A_{uds}, \end{aligned} \quad (5.6)$$

where  $A_\tau = A_{bottom} = 0$ . From these two equations we can extract the true Collins asymmetry  $A_{uds}$  and the charm contribution  $A_{charm}$ :

$$\begin{aligned} A_{uds} &= \frac{d \cdot A_{meas} - D \cdot A_{D^*}}{d - D - dB - dT + Db} \\ A_{charm} &= \frac{(1 - D - B - T) \cdot A_{D^*} - (1 - d - b) \cdot A_{meas}}{d - D - dB - dT + Db}. \end{aligned} \quad (5.7)$$

The relative contributions to the full data sample of the  $c\bar{c}$  ( $D$ ),  $B\bar{B}$  ( $B$ ),  $\tau^+\tau^-$  ( $T$ ), and light quark ( $UDS$ ) events, where  $UDS = 1 - D - B - T$  are reported in Tab. 5.6, in columns 2 to 5, respectively. The analogous quantities obtained in the  $D^*$ -enhanced data sample are in columns 6 to 8. We note that in this latter sample, the  $\tau^+\tau^-$  events do not contribute.

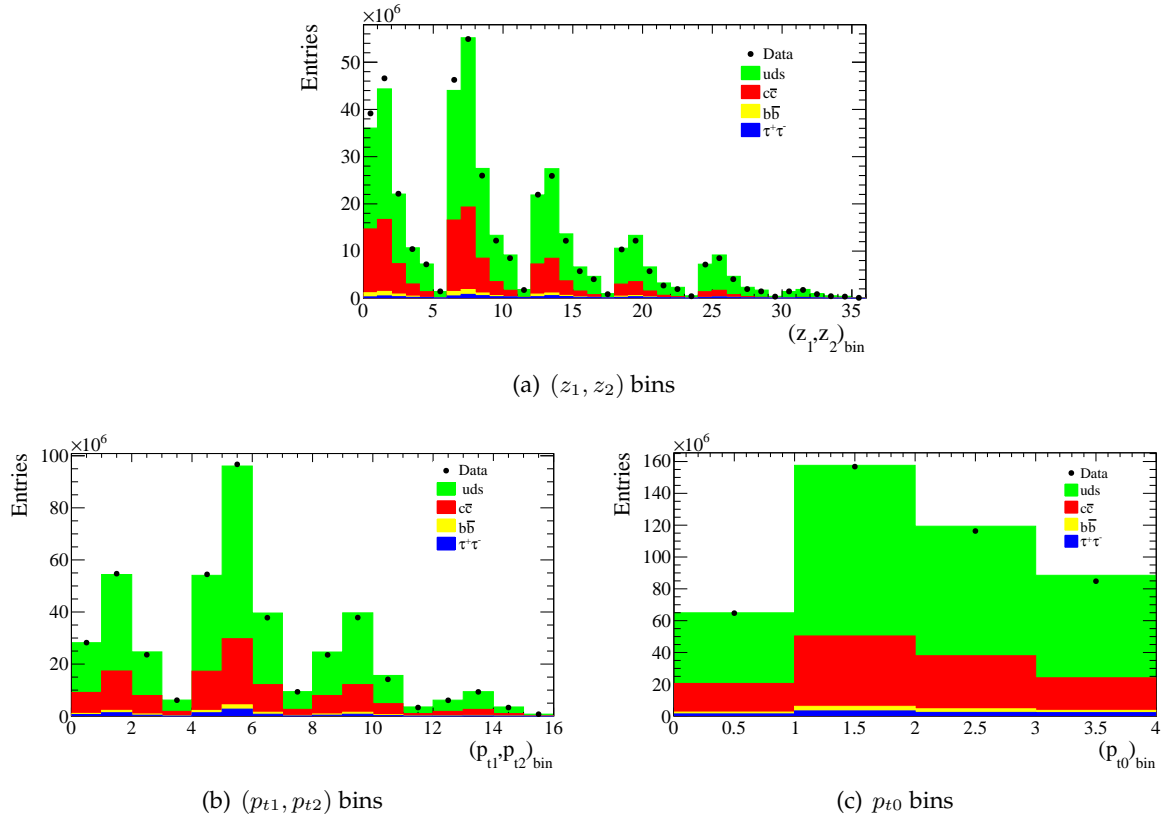


Figure 5.12: Comparison between the number of pion pairs in the data sample (black dots) and the relative contribution due to  $\tau^+\tau^-$  events (blue histogram), plus  $B\bar{B}$  (yellow histogram), plus  $c\bar{c}$  (red histogram), plus  $uds$  (green histogram). Similar plots are obtained for the  $D^*$  enhanced sample. The difference between data and MC are assigned to the charm and tau fractions as systematic errors.

A significant source of systematic error in this procedure can arise from the fractions  $F_i$ , which are estimated from MC simulation. The cross sections of  $e^+e^- \rightarrow q\bar{q}$  processes are known at few percent level, and only a fraction of all charmed-hadrons and  $B$ -meson decays have been measured and included in the MC generators used by the *BABAR* simulation. Also  $\tau$  decays with many hadrons in the final state are known with significant uncertainties. In order to understand how large could be the effect of these uncertainties, we compare bin-by-bin in Fig. 5.12 the number of pion pairs selected in the data with those selected in the  $uds$ ,  $\tau$ , charm, and bottom MC samples, summed according to the nominal production cross sections. The observed data-MC differences are at most at few percent level. Since the number of  $B\bar{B}$  events is negligible if compared to the  $c\bar{c}$  and  $\tau^+\tau^-$  events, we assign errors to the charm ( $D$ , and  $d$ ) and tau ( $T$ ) fractions equal to the observed data-MC differences, and propagate them together with the statistical errors through Eq.(5.7). This conservative choice has a very little effect on the final result.

Figures 5.13 and 5.14 show the Collins asymmetries for light quarks after the background corrections (following Eq. (5.7)) as a function of the  $z$  bins and the  $p_t$  bins, respectively. The blue triangles refer to the U/L double ratio, and the green triangles refer to the U/C double ratio. All these results are summarized in Tables 5.8 - 5.13.

The charm asymmetries (see also Eq. (5.7)) as a function of  $z$  bins are shown in Fig. 5.15. Since the asymmetry does not change significantly for near bins of fractional energy, we decide to evaluate the double ratio in the  $D^*$  enhanced sample coupling two adjacent  $z$  bins in order to reduce the statistical uncertainties. Note that the statistical error of the control sample is the largest source of uncertainties in these measurements. Finally, Fig. 5.16 shows the charm asymmetries as a function of  $p_t$ . Also in these cases, blue and green triangles refers to U/L and U/C double ratio, respectively. The results as a function of  $z$  bins are summarized again in Tables 5.8 - 5.13.

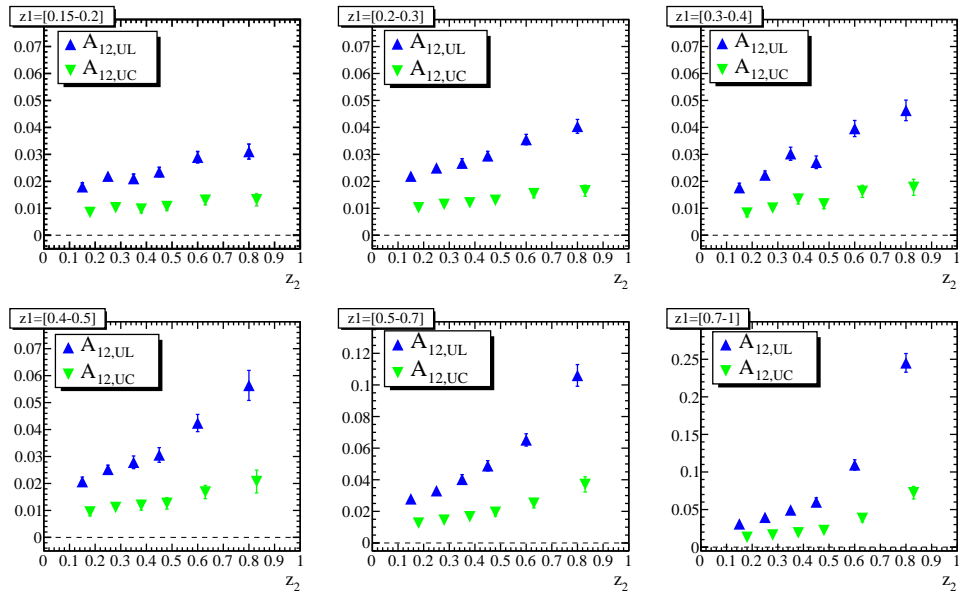
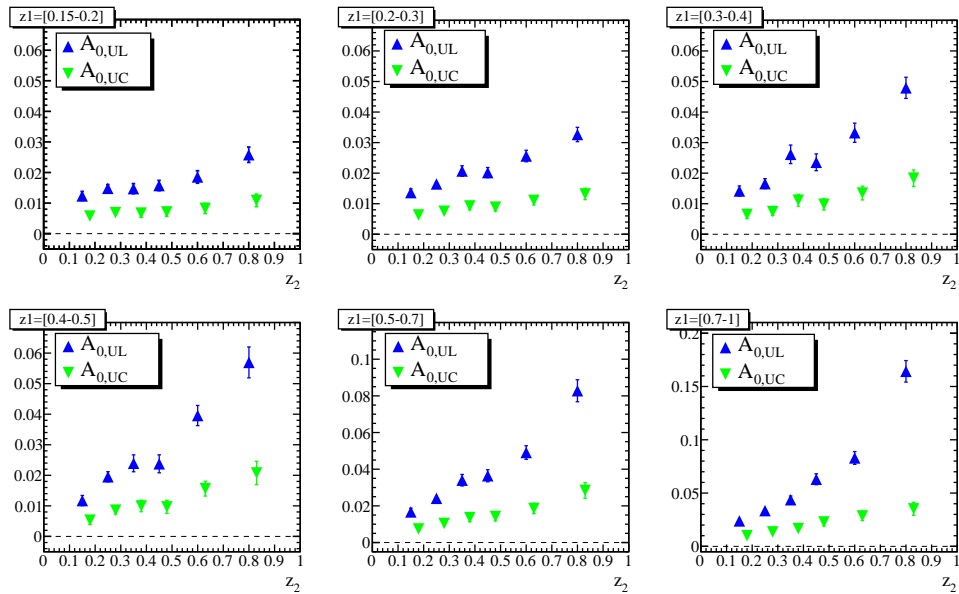
(a) RF12:  $A_{uds}$  Collins asymmetries(b) RF0:  $A_{uds}$  Collins asymmetries

Figure 5.13: Light quark asymmetries as a function of fractional energies, after the correction of charm, bottom and tau contributions (Eq. (5.7)): (a) in the thrust reference frame and (b) in the second momentum hadron frame. The blue triangles refer to the U/L double ratio, and the green triangles refer to the U/C double ratio.

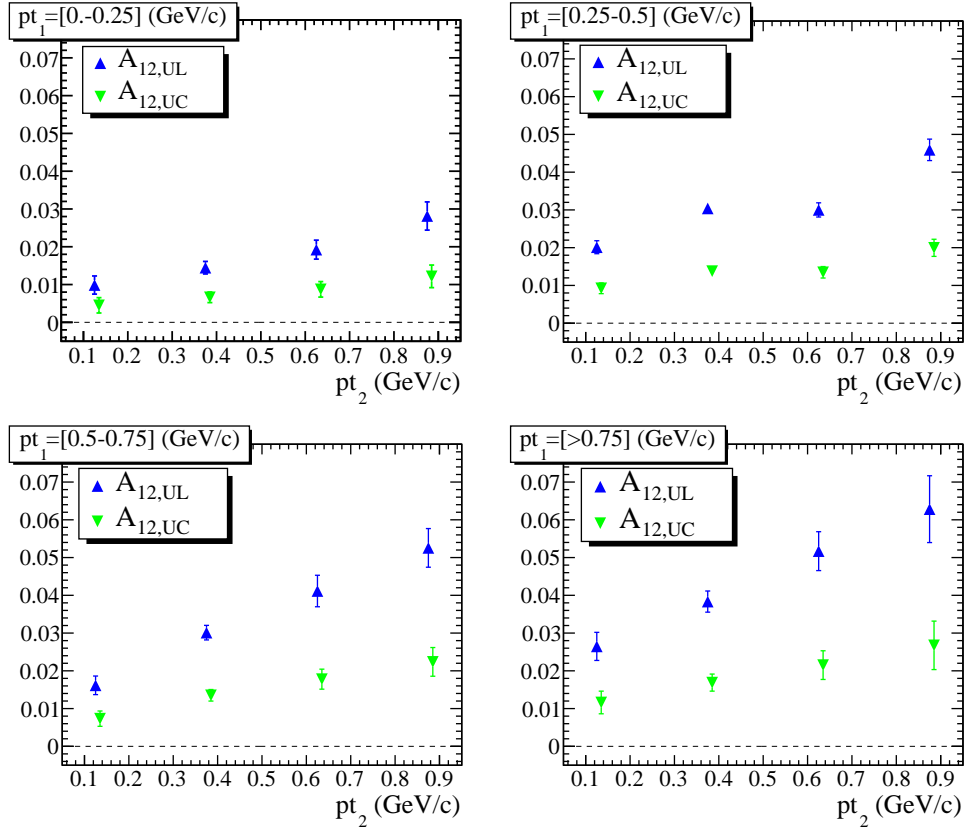
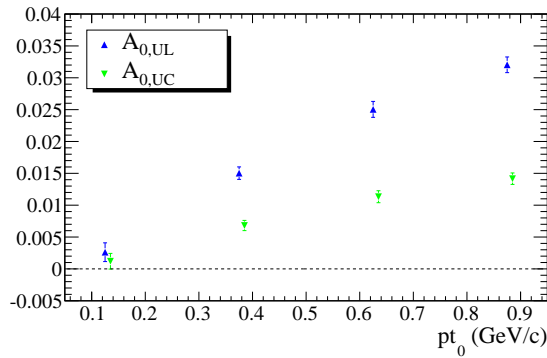
(a) RF12:  $A_{uds}$  Collins asymmetries(b) RF0:  $A_{uds}$  Collins asymmetries

Figure 5.14: Light quark asymmetries as a function of  $p_{t_i}$ , after the correction of charm, bottom and tau contributions (Eq. (5.7)): (a) in the thrust reference frame and (b) in the second momentum hadron frame. The blue triangles refer to the U/L double ratio, and the green triangles refer to the U/C double ratio.

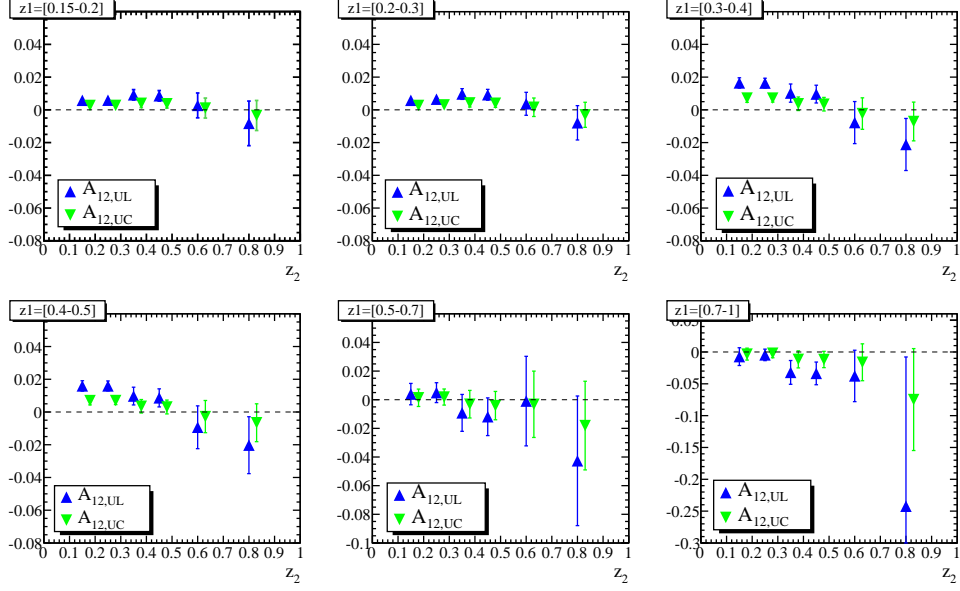
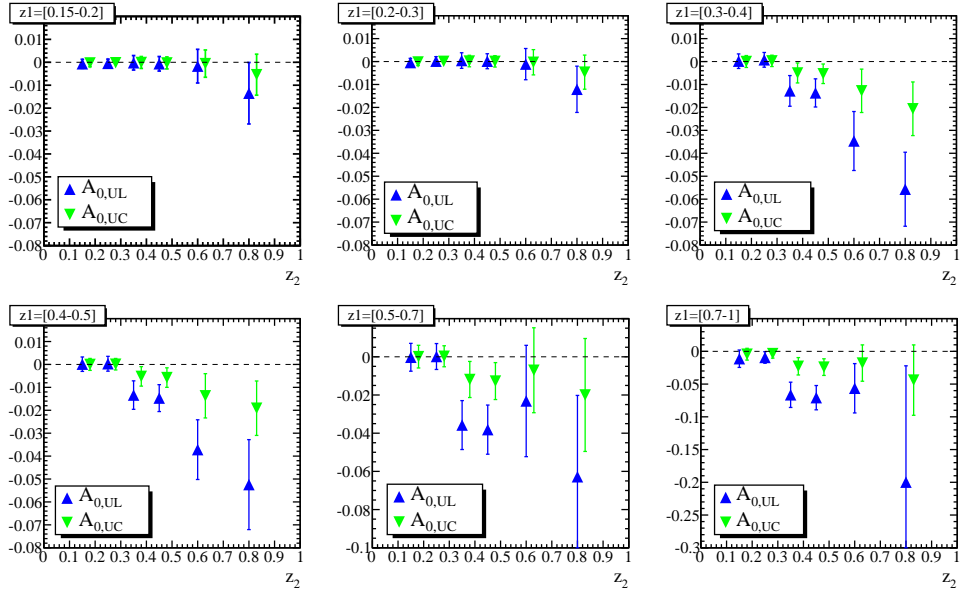
(a) RF12:  $A_{charm}$  asymmetries(b) RF0:  $A_{charm}$  asymmetries

Figure 5.15: Charm asymmetries as a function of fractional energies, calculated following Eq. (5.7): (a) in the thrust reference frame and (b) in the second momentum hadron frame. The blue and green triangles refer to the U/L and U/C double ratio, respectively.

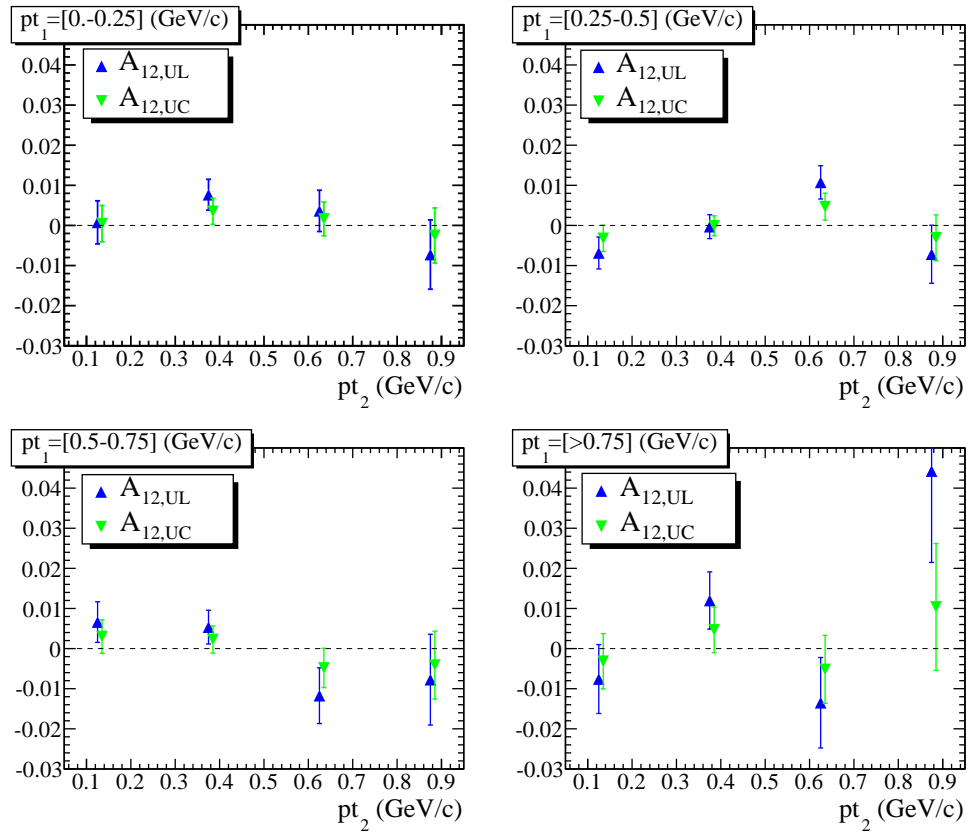
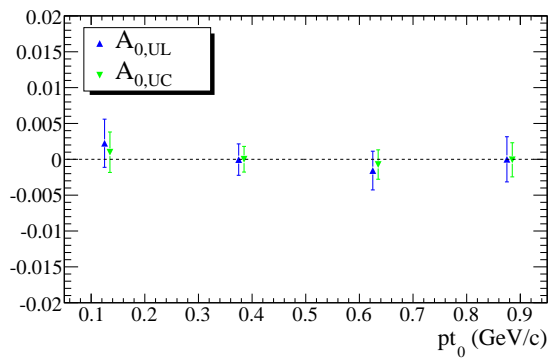
(a) RF12:  $A_{charm}$  asymmetries(b) RF0:  $A_{charm}$  asymmetries

Figure 5.16: Charm asymmetries as a function of  $p_t$ , calculated following Eq. (5.7): (a) in the thrust reference frame and (b) in the second momentum hadron frame. The blue and green triangles refer to the U/L and U/C double ratio, respectively.

$(z_1, z_2)$	Full data sample				$D^*$ -enhanced data sample		
	D	B	T	UDS	d	b	uds
1	34.513 ± 3.006	2.242 ± 0.002	0.770 ± 0.068	62.476 ± 3.007	87.841 ± 1.800	3.307 ± 0.022	8.853 ± 1.800
2	32.722 ± 1.659	2.058 ± 0.002	1.079 ± 0.056	64.141 ± 1.660	90.369 ± 1.432	3.295 ± 0.021	6.337 ± 1.432
3	29.054 ± 0.110	2.542 ± 0.003	1.532 ± 0.008	66.872 ± 0.110	88.609 ± 3.254	4.571 ± 0.036	6.820 ± 3.254
4	24.738 ± 0.637	2.449 ± 0.005	1.962 ± 0.054	70.850 ± 0.640	87.510 ± 1.511	3.682 ± 0.048	8.808 ± 1.512
5	16.864 ± 0.179	0.015 ± 0.000	2.641 ± 0.032	80.481 ± 0.182	86.162 ± 3.706	0.010 ± 0.003	13.829 ± 3.706
6	3.691 ± 0.120	0.000 ± 0.000	6.525 ± 0.205	89.783 ± 0.237	62.822 ± 13.888	0.000 ± 0.000	37.178 ± 13.888
7	32.696 ± 1.665	2.051 ± 0.002	1.080 ± 0.056	64.173 ± 1.666	90.017 ± 1.077	3.269 ± 0.021	6.714 ± 1.077
8	31.815 ± 0.186	1.880 ± 0.002	1.512 ± 0.010	64.793 ± 0.187	94.536 ± 5.778	3.242 ± 0.020	2.223 ± 5.778
9	28.385 ± 1.598	2.180 ± 0.003	2.154 ± 0.123	67.281 ± 1.602	93.773 ± 8.400	4.341 ± 0.033	1.886 ± 8.400
10	24.084 ± 2.062	2.090 ± 0.004	2.724 ± 0.236	71.102 ± 2.075	93.195 ± 6.970	3.453 ± 0.044	3.352 ± 6.970
11	16.396 ± 1.223	0.012 ± 0.000	3.587 ± 0.271	80.005 ± 1.253	91.653 ± 3.012	0.009 ± 0.003	8.339 ± 3.012
12	3.777 ± 0.214	0.000 ± 0.000	8.586 ± 0.475	87.637 ± 0.521	70.470 ± 7.531	0.000 ± 0.000	29.530 ± 7.531
13	29.065 ± 0.094	2.541 ± 0.003	1.543 ± 0.007	66.851 ± 0.094	88.771 ± 3.539	4.687 ± 0.037	6.542 ± 3.539
14	28.363 ± 1.596	2.179 ± 0.003	2.158 ± 0.123	67.300 ± 1.601	93.430 ± 8.159	4.379 ± 0.034	2.191 ± 8.159
15	25.281 ± 2.728	1.975 ± 0.004	3.067 ± 0.334	69.677 ± 2.748	92.702 ± 10.546	4.979 ± 0.053	2.319 ± 10.546
16	21.184 ± 2.901	1.747 ± 0.006	3.880 ± 0.536	73.189 ± 2.950	91.240 ± 8.237	3.567 ± 0.066	5.193 ± 8.237
17	14.169 ± 1.849	0.020 ± 0.001	5.036 ± 0.662	80.776 ± 1.964	90.344 ± 5.565	0.023 ± 0.007	9.633 ± 5.565
18	3.275 ± 0.408	0.000 ± 0.000	12.077 ± 1.473	84.648 ± 1.528	73.370 ± 4.309	0.031 ± 0.031	26.599 ± 4.309
19	24.716 ± 0.630	2.429 ± 0.005	1.976 ± 0.053	70.878 ± 0.632	88.206 ± 1.875	3.566 ± 0.048	8.228 ± 1.875
20	24.047 ± 2.060	2.096 ± 0.004	2.739 ± 0.238	71.118 ± 2.074	92.506 ± 6.451	3.432 ± 0.044	4.061 ± 6.451
21	21.228 ± 2.925	1.741 ± 0.006	3.897 ± 0.542	73.134 ± 2.975	92.048 ± 8.830	3.547 ± 0.066	4.406 ± 8.830
22	17.548 ± 2.982	1.213 ± 0.007	4.975 ± 0.852	76.263 ± 3.101	89.583 ± 6.149	2.401 ± 0.081	8.016 ± 6.150
23	11.304 ± 1.834	0.061 ± 0.002	6.341 ± 1.033	82.294 ± 2.105	88.146 ± 4.390	0.059 ± 0.017	11.795 ± 4.390
24	2.561 ± 0.420	0.000 ± 0.000	15.127 ± 2.402	82.312 ± 2.438	77.753 ± 9.677	0.000 ± 0.000	22.247 ± 9.677
25	16.838 ± 0.188	0.015 ± 0.000	2.645 ± 0.033	80.502 ± 0.191	86.474 ± 3.208	0.007 ± 0.003	13.519 ± 3.208
26	16.365 ± 1.225	0.012 ± 0.000	3.594 ± 0.272	80.029 ± 1.254	92.101 ± 3.639	0.010 ± 0.003	7.888 ± 3.639
27	14.117 ± 1.836	0.019 ± 0.001	5.042 ± 0.660	80.822 ± 1.951	89.667 ± 5.122	0.013 ± 0.005	10.321 ± 5.122
28	11.370 ± 1.849	0.059 ± 0.002	6.318 ± 1.032	82.253 ± 2.117	87.093 ± 3.441	0.078 ± 0.019	12.830 ± 3.441
29	7.170 ± 1.111	0.002 ± 0.000	7.832 ± 1.213	84.996 ± 1.645	84.491 ± 1.244	0.000 ± 0.000	15.509 ± 1.244
30	1.670 ± 0.257	0.000 ± 0.000	17.267 ± 2.509	81.063 ± 2.522	65.056 ± 8.684	0.000 ± 0.000	34.944 ± 8.684
31	3.698 ± 0.121	0.000 ± 0.000	6.596 ± 0.208	89.706 ± 0.241	62.165 ± 14.860	0.000 ± 0.000	37.835 ± 14.860
32	3.745 ± 0.219	0.000 ± 0.000	8.650 ± 0.495	87.605 ± 0.542	73.481 ± 4.469	0.000 ± 0.000	26.519 ± 4.469
33	3.231 ± 0.405	0.001 ± 0.000	12.188 ± 1.494	84.581 ± 1.548	65.635 ± 5.655	0.000 ± 0.000	34.365 ± 5.655
34	2.549 ± 0.422	0.000 ± 0.000	15.268 ± 2.444	82.183 ± 2.480	68.442 ± 4.734	0.000 ± 0.000	31.558 ± 4.734
35	1.653 ± 0.257	0.000 ± 0.000	17.344 ± 2.544	81.003 ± 2.557	68.090 ± 5.339	0.000 ± 0.000	31.910 ± 5.339
36	0.468 ± 0.038	0.000 ± 0.000	18.932 ± 0.841	80.600 ± 0.842	48.387 ± 22.468	0.000 ± 0.000	51.613 ± 22.468

Table 5.6: Fraction of pion pairs in the data sample as a function of  $(z_1, z_2)$  bins (36 bins): D: relative contribution due to the  $c\bar{c}$  events, B: relative contribution due to the  $b\bar{b}$  events, T: relative contribution due to the  $\tau^+\tau^-$  events, and UDS: relative contribution due to the light quarks. In the last three columns are summarized the relative contribution in the  $D^*$  enhanced data sample coming from  $c\bar{c}$  (d),  $b\bar{b}$  (b), and light quarks (uds). In the errors of D, T, and d is included the difference between data and MC, as shown in Fig. 5.12.

$(p_{t2}, p_{t1})$	Full data sample				$D^*$ -enhanced data sample		
	D	B	T	UDS	d	b	uds
1	28.534 ± 0.040	1.572 ± 0.002	2.182 ± 0.005	67.712 ± 0.040	90.069 ± 4.966	3.235 ± 0.030	6.696 ± 4.966
2	27.643 ± 0.172	1.656 ± 0.002	2.411 ± 0.016	68.290 ± 0.173	89.078 ± 3.355	3.330 ± 0.022	7.592 ± 3.356
3	29.971 ± 1.403	2.002 ± 0.003	1.591 ± 0.076	66.436 ± 1.405	93.837 ± 6.777	3.488 ± 0.031	2.674 ± 6.777
4	27.063 ± 0.252	2.032 ± 0.006	0.829 ± 0.011	70.076 ± 0.252	95.156 ± 4.957	2.715 ± 0.046	2.129 ± 4.957
5	27.662 ± 0.198	1.655 ± 0.002	2.397 ± 0.019	68.286 ± 0.198	88.966 ± 3.226	3.336 ± 0.022	7.698 ± 3.226
6	26.250 ± 0.181	1.711 ± 0.001	2.792 ± 0.020	69.247 ± 0.182	87.242 ± 1.250	3.356 ± 0.016	9.402 ± 1.250
7	28.063 ± 1.341	2.035 ± 0.002	1.938 ± 0.094	67.965 ± 1.344	91.949 ± 4.616	3.552 ± 0.024	4.499 ± 4.616
8	24.973 ± 0.198	2.052 ± 0.005	0.951 ± 0.010	72.025 ± 0.198	92.081 ± 1.761	2.794 ± 0.038	5.125 ± 1.761
9	30.016 ± 1.411	2.008 ± 0.003	1.589 ± 0.077	66.388 ± 1.413	93.962 ± 6.881	3.528 ± 0.031	2.510 ± 6.881
10	28.047 ± 1.352	2.036 ± 0.002	1.931 ± 0.095	67.987 ± 1.356	91.954 ± 4.617	3.540 ± 0.024	4.506 ± 4.617
11	30.007 ± 3.183	2.439 ± 0.004	1.521 ± 0.164	66.033 ± 3.188	95.528 ± 6.947	3.589 ± 0.036	0.883 ± 6.948
12	26.571 ± 1.791	2.667 ± 0.009	0.919 ± 0.066	69.844 ± 1.792	92.819 ± 2.120	3.264 ± 0.062	3.917 ± 2.121
13	27.077 ± 0.270	2.044 ± 0.006	0.824 ± 0.011	70.055 ± 0.270	94.838 ± 4.620	2.831 ± 0.047	2.331 ± 4.621
14	24.947 ± 0.221	2.056 ± 0.005	0.947 ± 0.011	72.050 ± 0.221	92.291 ± 2.031	2.874 ± 0.038	4.835 ± 2.031
15	26.581 ± 1.821	2.676 ± 0.009	0.923 ± 0.067	69.819 ± 1.822	93.251 ± 2.371	3.191 ± 0.062	3.558 ± 2.372
16	23.654 ± 0.818	3.358 ± 0.022	0.888 ± 0.039	72.100 ± 0.819	92.732 ± 1.314	3.353 ± 0.122	3.915 ± 1.319

$(p_{t2}, p_{t1})$	Full data sample				$D^*$ -enhanced data sample		
	D	B	T	UDS	d	b	uds
1	27.787 ± 0.095	1.795 ± 0.002	2.186 ± 0.009	68.237 ± 0.095	89.673 ± 3.262	3.349 ± 0.019	6.978 ± 3.262
2	28.191 ± 0.149	1.845 ± 0.001	2.100 ± 0.012	67.783 ± 0.149	90.157 ± 3.218	3.371 ± 0.012	6.472 ± 3.218
3	28.657 ± 0.747	1.942 ± 0.001	2.029 ± 0.054	67.219 ± 0.749	91.756 ± 4.463	3.451 ± 0.014	4.793 ± 4.463
4	24.123 ± 1.056	1.669 ± 0.001	2.622 ± 0.116	72.026 ± 1.063	91.096 ± 3.886	3.165 ± 0.016	5.739 ± 3.886

Table 5.7: Fraction of pion pairs in the data sample as a function of  $(p_{t1}, p_{t2})$  bins (16 bins) and  $p_{t0}$  bins (4 bins): D: relative contribution due to the  $c\bar{c}$  events, B: relative contribution due to the  $b\bar{b}$  events, T: relative contribution due to the  $\tau^+\tau^-$  events, and UDS: relative contribution due to the light quarks. In the last three columns are summarized the relative contribution in the  $D^*$  enhanced data sample coming from  $c\bar{c}$  (d),  $b\bar{b}$  (b), and light quarks (uds). In the errors of D, T, and d is included the difference between data and MC, as shown in Fig. 5.12

$A_{12}^{UL}$				
$(z_1, z_2)$	$A_{meas} \pm \delta A_{meas}$	$A_{D^*} \pm \delta A_{D^*}$	$A_{uds} \pm \delta A_{uds}$	$A_{charm} \pm \delta A_{charm}$
1	$0.0132 \pm 0.0005$	$0.0067 \pm 0.0016$	$0.0180 \pm 0.0015$	$0.0058 \pm 0.0020$
2	$0.0160 \pm 0.0004$	$0.0067 \pm 0.0016$	$0.0219 \pm 0.0012$	$0.0059 \pm 0.0019$
3	$0.0167 \pm 0.0006$	$0.0096 \pm 0.0027$	$0.0210 \pm 0.0017$	$0.0092 \pm 0.0032$
4	$0.0188 \pm 0.0009$	$0.0096 \pm 0.0027$	$0.0235 \pm 0.0017$	$0.0086 \pm 0.0032$
5	$0.0238 \pm 0.0011$	$0.0063 \pm 0.0062$	$0.0289 \pm 0.0021$	$0.0027 \pm 0.0076$
6	$0.0276 \pm 0.0024$	$0.0063 \pm 0.0062$	$0.0310 \pm 0.0028$	$-0.0083 \pm 0.0136$
7	$0.0160 \pm 0.0004$	$0.0067 \pm 0.0016$	$0.0219 \pm 0.0012$	$0.0058 \pm 0.0019$
8	$0.0182 \pm 0.0004$	$0.0067 \pm 0.0016$	$0.0250 \pm 0.0012$	$0.0065 \pm 0.0021$
9	$0.0207 \pm 0.0006$	$0.0096 \pm 0.0027$	$0.0267 \pm 0.0017$	$0.0097 \pm 0.0033$
10	$0.0231 \pm 0.0008$	$0.0096 \pm 0.0027$	$0.0294 \pm 0.0017$	$0.0092 \pm 0.0033$
11	$0.0290 \pm 0.0010$	$0.0063 \pm 0.0062$	$0.0355 \pm 0.0019$	$0.0037 \pm 0.0070$
12	$0.0351 \pm 0.0022$	$0.0063 \pm 0.0062$	$0.0404 \pm 0.0026$	$-0.0079 \pm 0.0105$
13	$0.0166 \pm 0.0006$	$0.0158 \pm 0.0027$	$0.0176 \pm 0.0017$	$0.0164 \pm 0.0031$
14	$0.0197 \pm 0.0006$	$0.0158 \pm 0.0027$	$0.0223 \pm 0.0015$	$0.0163 \pm 0.0030$
15	$0.0237 \pm 0.0008$	$0.0102 \pm 0.0047$	$0.0302 \pm 0.0024$	$0.0102 \pm 0.0056$
16	$0.0218 \pm 0.0012$	$0.0102 \pm 0.0047$	$0.0271 \pm 0.0023$	$0.0096 \pm 0.0054$
17	$0.0309 \pm 0.0014$	$-0.0032 \pm 0.0111$	$0.0396 \pm 0.0030$	$-0.0078 \pm 0.0129$
18	$0.0385 \pm 0.0031$	$-0.0032 \pm 0.0111$	$0.0463 \pm 0.0038$	$-0.0212 \pm 0.0159$
19	$0.0186 \pm 0.0009$	$0.0158 \pm 0.0027$	$0.0207 \pm 0.0017$	$0.0159 \pm 0.0032$
20	$0.0218 \pm 0.0008$	$0.0158 \pm 0.0027$	$0.0252 \pm 0.0016$	$0.0159 \pm 0.0030$
21	$0.0224 \pm 0.0012$	$0.0102 \pm 0.0047$	$0.0279 \pm 0.0023$	$0.0097 \pm 0.0054$
22	$0.0248 \pm 0.0018$	$0.0102 \pm 0.0047$	$0.0306 \pm 0.0027$	$0.0086 \pm 0.0055$
23	$0.0339 \pm 0.0021$	$-0.0032 \pm 0.0111$	$0.0424 \pm 0.0032$	$-0.0093 \pm 0.0131$
24	$0.0459 \pm 0.0044$	$-0.0032 \pm 0.0111$	$0.0564 \pm 0.0056$	$-0.0203 \pm 0.0174$
25	$0.0231 \pm 0.0011$	$0.0072 \pm 0.0062$	$0.0279 \pm 0.0021$	$0.0039 \pm 0.0075$
26	$0.0273 \pm 0.0010$	$0.0072 \pm 0.0062$	$0.0331 \pm 0.0019$	$0.0049 \pm 0.0069$
27	$0.0312 \pm 0.0014$	$-0.0041 \pm 0.0110$	$0.0402 \pm 0.0030$	$-0.0092 \pm 0.0129$
28	$0.0388 \pm 0.0021$	$-0.0041 \pm 0.0110$	$0.0488 \pm 0.0032$	$-0.0119 \pm 0.0132$
29	$0.0554 \pm 0.0024$	$0.0093 \pm 0.0260$	$0.0652 \pm 0.0039$	$-0.0010 \pm 0.0313$
30	$0.0852 \pm 0.0050$	$0.0093 \pm 0.0260$	$0.1060 \pm 0.0069$	$-0.0427 \pm 0.0452$
31	$0.0274 \pm 0.0024$	$0.0072 \pm 0.0062$	$0.0309 \pm 0.0028$	$-0.0073 \pm 0.0140$
32	$0.0346 \pm 0.0022$	$0.0072 \pm 0.0062$	$0.0397 \pm 0.0025$	$-0.0046 \pm 0.0090$
33	$0.0408 \pm 0.0031$	$-0.0041 \pm 0.0110$	$0.0494 \pm 0.0038$	$-0.0321 \pm 0.0187$
34	$0.0485 \pm 0.0044$	$-0.0041 \pm 0.0110$	$0.0600 \pm 0.0056$	$-0.0336 \pm 0.0178$
35	$0.0880 \pm 0.0049$	$0.0093 \pm 0.0260$	$0.1094 \pm 0.0069$	$-0.0376 \pm 0.0404$
36	$0.1965 \pm 0.0097$	$0.0093 \pm 0.0260$	$0.2452 \pm 0.0125$	$-0.2424 \pm 0.2345$

Table 5.8: Thrust reference frame (RF12): double ratio of U/L pion pairs as a function of  $(z_1, z_2)$ -bins. In the second and third columns are reported the measured asymmetries in the full data sample ( $A_{meas}$ ) and in the  $D^*$  enhanced sample ( $A_{D^*}$ ). Since the asymmetry does not change significantly for adjacent bins of fractional energy, we evaluated the double ratio in the  $D^*$  sample coupling two adjacent  $z$ -bins, in order to reduce the statistical uncertainties. In the last two columns are reported the light quark and the charm asymmetries obtained following Eq. (5.7).

$A_0^{UL}$				
$(z_1, z_2)$	$A_{meas} \pm \delta A_{meas}$	$A_{D^*} \pm \delta A_{D^*}$	$A_{uds} \pm \delta A_{uds}$	$A_{charm} \pm \delta A_{charm}$
1	$0.0075 \pm 0.0005$	$0.0005 \pm 0.0016$	$0.0123 \pm 0.0015$	$-0.0007 \pm 0.0020$
2	$0.0093 \pm 0.0004$	$0.0005 \pm 0.0016$	$0.0148 \pm 0.0012$	$-0.0005 \pm 0.0019$
3	$0.0098 \pm 0.0006$	$0.0008 \pm 0.0027$	$0.0147 \pm 0.0017$	$-0.0002 \pm 0.0032$
4	$0.0110 \pm 0.0009$	$0.0008 \pm 0.0027$	$0.0157 \pm 0.0017$	$-0.0007 \pm 0.0032$
5	$0.0146 \pm 0.0010$	$0.0011 \pm 0.0061$	$0.0185 \pm 0.0020$	$-0.0017 \pm 0.0074$
6	$0.0227 \pm 0.0022$	$0.0011 \pm 0.0061$	$0.0258 \pm 0.0025$	$-0.0135 \pm 0.0134$
7	$0.0086 \pm 0.0004$	$0.0005 \pm 0.0016$	$0.0136 \pm 0.0012$	$-0.0005 \pm 0.0019$
8	$0.0107 \pm 0.0004$	$0.0005 \pm 0.0016$	$0.0165 \pm 0.0011$	$0.0002 \pm 0.0020$
9	$0.0141 \pm 0.0006$	$0.0008 \pm 0.0027$	$0.0207 \pm 0.0017$	$0.0004 \pm 0.0034$
10	$0.0144 \pm 0.0008$	$0.0008 \pm 0.0027$	$0.0202 \pm 0.0017$	$0.0001 \pm 0.0033$
11	$0.0203 \pm 0.0010$	$0.0011 \pm 0.0061$	$0.0256 \pm 0.0019$	$-0.0011 \pm 0.0068$
12	$0.0282 \pm 0.0020$	$0.0011 \pm 0.0061$	$0.0326 \pm 0.0023$	$-0.0121 \pm 0.0101$
13	$0.0095 \pm 0.0006$	$0.0011 \pm 0.0027$	$0.0142 \pm 0.0017$	$0.0002 \pm 0.0032$
14	$0.0114 \pm 0.0006$	$0.0011 \pm 0.0027$	$0.0166 \pm 0.0016$	$0.0008 \pm 0.0032$
15	$0.0150 \pm 0.0008$	$-0.0113 \pm 0.0046$	$0.0262 \pm 0.0030$	$-0.0128 \pm 0.0067$
16	$0.0143 \pm 0.0012$	$-0.0113 \pm 0.0046$	$0.0236 \pm 0.0028$	$-0.0137 \pm 0.0061$
17	$0.0219 \pm 0.0014$	$-0.0281 \pm 0.0108$	$0.0332 \pm 0.0031$	$-0.0347 \pm 0.0129$
18	$0.0387 \pm 0.0028$	$-0.0281 \pm 0.0108$	$0.0479 \pm 0.0035$	$-0.0557 \pm 0.0161$
19	$0.0083 \pm 0.0009$	$0.0011 \pm 0.0027$	$0.0117 \pm 0.0017$	$0.0001 \pm 0.0032$
20	$0.0140 \pm 0.0008$	$0.0011 \pm 0.0027$	$0.0195 \pm 0.0017$	$0.0003 \pm 0.0032$
21	$0.0147 \pm 0.0012$	$-0.0113 \pm 0.0046$	$0.0239 \pm 0.0028$	$-0.0134 \pm 0.0062$
22	$0.0155 \pm 0.0017$	$-0.0113 \pm 0.0046$	$0.0238 \pm 0.0029$	$-0.0147 \pm 0.0059$
23	$0.0284 \pm 0.0020$	$-0.0281 \pm 0.0108$	$0.0396 \pm 0.0033$	$-0.0372 \pm 0.0130$
24	$0.0455 \pm 0.0040$	$-0.0281 \pm 0.0108$	$0.0569 \pm 0.0051$	$-0.0524 \pm 0.0196$
25	$0.0134 \pm 0.0010$	$0.0020 \pm 0.0061$	$0.0167 \pm 0.0020$	$-0.0003 \pm 0.0073$
26	$0.0193 \pm 0.0010$	$0.0020 \pm 0.0061$	$0.0241 \pm 0.0019$	$0.0001 \pm 0.0068$
27	$0.0224 \pm 0.0014$	$-0.0285 \pm 0.0107$	$0.0340 \pm 0.0031$	$-0.0357 \pm 0.0128$
28	$0.0256 \pm 0.0020$	$-0.0285 \pm 0.0107$	$0.0364 \pm 0.0033$	$-0.0381 \pm 0.0129$
29	$0.0401 \pm 0.0023$	$-0.0119 \pm 0.0242$	$0.0491 \pm 0.0037$	$-0.0231 \pm 0.0292$
30	$0.0661 \pm 0.0044$	$-0.0119 \pm 0.0242$	$0.0828 \pm 0.0060$	$-0.0628 \pm 0.0426$
31	$0.0210 \pm 0.0022$	$0.0020 \pm 0.0061$	$0.0239 \pm 0.0025$	$-0.0113 \pm 0.0133$
32	$0.0290 \pm 0.0020$	$0.0020 \pm 0.0061$	$0.0335 \pm 0.0023$	$-0.0093 \pm 0.0088$
33	$0.0349 \pm 0.0028$	$-0.0285 \pm 0.0107$	$0.0438 \pm 0.0035$	$-0.0664 \pm 0.0193$
34	$0.0500 \pm 0.0040$	$-0.0285 \pm 0.0107$	$0.0630 \pm 0.0051$	$-0.0708 \pm 0.0185$
35	$0.0663 \pm 0.0044$	$-0.0119 \pm 0.0242$	$0.0830 \pm 0.0060$	$-0.0564 \pm 0.0377$
36	$0.1314 \pm 0.0079$	$-0.0119 \pm 0.0242$	$0.1642 \pm 0.0101$	$-0.1998 \pm 0.1777$

Table 5.9: Second hadron momentum frame (RF0): double ratio of U/L pion pairs as a function of  $(z_1, z_2)$ -bins. In the second and third columns are reported the measured asymmetries in the full data sample ( $A_{meas}$ ) and in the  $D^*$  enhanced sample ( $A_{D^*}$ ). Since the asymmetry does not change significantly for adjacent bins of fractional energy, we evaluated the double ratio in the  $D^*$  sample coupling two adjacent  $z$ -bins, in order to reduce the statistical uncertainties. In the last two columns are reported the light quark and the charm asymmetries obtained following Eq. (5.7).

$A_{12}^{UC}$				
$(z_1, z_2)$	$A_{meas} \pm \delta A_{meas}$	$A_{D^*} \pm \delta A_{D^*}$	$A_{uds} \pm \delta A_{uds}$	$A_{charm} \pm \delta A_{charm}$
1	0.0062 ± 0.0004	0.0031 ± 0.0014	0.0084 ± 0.0012	0.0027 ± 0.0016
2	0.0074 ± 0.0004	0.0031 ± 0.0014	0.0102 ± 0.0010	0.0027 ± 0.0016
3	0.0077 ± 0.0005	0.0042 ± 0.0022	0.0097 ± 0.0014	0.0040 ± 0.0026
4	0.0085 ± 0.0007	0.0042 ± 0.0022	0.0106 ± 0.0014	0.0037 ± 0.0027
5	0.0106 ± 0.0009	0.0027 ± 0.0051	0.0130 ± 0.0017	0.0011 ± 0.0061
6	0.0117 ± 0.0019	0.0027 ± 0.0051	0.0132 ± 0.0022	-0.0034 ± 0.0092
7	0.0074 ± 0.0004	0.0031 ± 0.0014	0.0102 ± 0.0010	0.0027 ± 0.0016
8	0.0084 ± 0.0003	0.0031 ± 0.0014	0.0114 ± 0.0009	0.0030 ± 0.0015
9	0.0093 ± 0.0005	0.0042 ± 0.0022	0.0120 ± 0.0013	0.0042 ± 0.0025
10	0.0102 ± 0.0007	0.0042 ± 0.0022	0.0130 ± 0.0013	0.0040 ± 0.0025
11	0.0126 ± 0.0008	0.0027 ± 0.0051	0.0154 ± 0.0016	0.0016 ± 0.0056
12	0.0143 ± 0.0018	0.0027 ± 0.0051	0.0165 ± 0.0021	-0.0030 ± 0.0077
13	0.0076 ± 0.0005	0.0069 ± 0.0022	0.0082 ± 0.0014	0.0072 ± 0.0026
14	0.0088 ± 0.0005	0.0069 ± 0.0022	0.0101 ± 0.0012	0.0072 ± 0.0024
15	0.0103 ± 0.0007	0.0038 ± 0.0037	0.0134 ± 0.0018	0.0037 ± 0.0041
16	0.0092 ± 0.0010	0.0038 ± 0.0037	0.0116 ± 0.0018	0.0034 ± 0.0041
17	0.0128 ± 0.0012	-0.0005 ± 0.0085	0.0163 ± 0.0023	-0.0023 ± 0.0096
18	0.0148 ± 0.0025	-0.0005 ± 0.0085	0.0178 ± 0.0030	-0.0071 ± 0.0118
19	0.0084 ± 0.0007	0.0069 ± 0.0022	0.0094 ± 0.0014	0.0070 ± 0.0026
20	0.0096 ± 0.0007	0.0069 ± 0.0022	0.0111 ± 0.0013	0.0070 ± 0.0025
21	0.0095 ± 0.0010	0.0038 ± 0.0037	0.0119 ± 0.0018	0.0035 ± 0.0041
22	0.0102 ± 0.0014	0.0038 ± 0.0037	0.0126 ± 0.0021	0.0031 ± 0.0042
23	0.0135 ± 0.0017	-0.0005 ± 0.0085	0.0168 ± 0.0025	-0.0028 ± 0.0098
24	0.0169 ± 0.0034	-0.0005 ± 0.0085	0.0207 ± 0.0042	-0.0066 ± 0.0116
25	0.0103 ± 0.0009	0.0029 ± 0.0051	0.0126 ± 0.0017	0.0013 ± 0.0061
26	0.0119 ± 0.0008	0.0029 ± 0.0051	0.0144 ± 0.0015	0.0019 ± 0.0056
27	0.0130 ± 0.0012	-0.0011 ± 0.0084	0.0166 ± 0.0022	-0.0031 ± 0.0096
28	0.0155 ± 0.0017	-0.0011 ± 0.0084	0.0194 ± 0.0025	-0.0041 ± 0.0099
29	0.0212 ± 0.0019	0.0012 ± 0.0193	0.0252 ± 0.0030	-0.0032 ± 0.0232
30	0.0297 ± 0.0037	0.0012 ± 0.0193	0.0370 ± 0.0048	-0.0180 ± 0.0310
31	0.0116 ± 0.0019	0.0029 ± 0.0051	0.0131 ± 0.0022	-0.0033 ± 0.0094
32	0.0141 ± 0.0017	0.0029 ± 0.0051	0.0162 ± 0.0020	-0.0019 ± 0.0071
33	0.0157 ± 0.0024	-0.0011 ± 0.0084	0.0190 ± 0.0030	-0.0116 ± 0.0134
34	0.0179 ± 0.0034	-0.0011 ± 0.0084	0.0221 ± 0.0043	-0.0118 ± 0.0128
35	0.0307 ± 0.0037	0.0012 ± 0.0193	0.0383 ± 0.0048	-0.0162 ± 0.0290
36	0.0580 ± 0.0066	0.0012 ± 0.0193	0.0724 ± 0.0083	-0.0747 ± 0.0801

Table 5.10: Thrust reference frame (RF12): double ratio of U/C pion pairs as a function of  $(z_1, z_2)$ -bins. The same caption as Tab. 5.8.

$A_0^{UC}$				
$(z_1, z_2)$	$A_{meas} \pm \delta A_{meas}$	$A_{D^*} \pm \delta A_{D^*}$	$A_{uds} \pm \delta A_{uds}$	$A_{charm} \pm \delta A_{charm}$
1	0.0035 ± 0.0004	0.0003 ± 0.0014	0.0058 ± 0.0012	-0.0003 ± 0.0016
2	0.0043 ± 0.0003	0.0003 ± 0.0014	0.0069 ± 0.0010	-0.0002 ± 0.0016
3	0.0045 ± 0.0005	0.0004 ± 0.0022	0.0067 ± 0.0014	-0.0001 ± 0.0026
4	0.0050 ± 0.0007	0.0004 ± 0.0022	0.0071 ± 0.0014	-0.0003 ± 0.0026
5	0.0066 ± 0.0009	0.0006 ± 0.0049	0.0083 ± 0.0017	-0.0006 ± 0.0059
6	0.0096 ± 0.0018	0.0006 ± 0.0049	0.0109 ± 0.0020	-0.0054 ± 0.0089
7	0.0040 ± 0.0003	0.0003 ± 0.0014	0.0063 ± 0.0010	-0.0002 ± 0.0016
8	0.0049 ± 0.0003	0.0003 ± 0.0014	0.0075 ± 0.0009	0.0001 ± 0.0015
9	0.0063 ± 0.0005	0.0004 ± 0.0022	0.0093 ± 0.0013	0.0002 ± 0.0025
10	0.0063 ± 0.0007	0.0004 ± 0.0022	0.0089 ± 0.0013	0.0001 ± 0.0025
11	0.0088 ± 0.0008	0.0006 ± 0.0049	0.0111 ± 0.0015	-0.0003 ± 0.0055
12	0.0114 ± 0.0016	0.0006 ± 0.0049	0.0132 ± 0.0019	-0.0046 ± 0.0074
13	0.0044 ± 0.0005	0.0004 ± 0.0022	0.0065 ± 0.0014	0.0000 ± 0.0026
14	0.0051 ± 0.0005	0.0004 ± 0.0022	0.0074 ± 0.0013	0.0003 ± 0.0025
15	0.0065 ± 0.0007	-0.0044 ± 0.0036	0.0111 ± 0.0019	-0.0050 ± 0.0043
16	0.0061 ± 0.0010	-0.0044 ± 0.0036	0.0098 ± 0.0019	-0.0053 ± 0.0043
17	0.0091 ± 0.0011	-0.0102 ± 0.0083	0.0135 ± 0.0022	-0.0128 ± 0.0095
18	0.0149 ± 0.0022	-0.0102 ± 0.0083	0.0184 ± 0.0027	-0.0206 ± 0.0117
19	0.0038 ± 0.0007	0.0004 ± 0.0022	0.0053 ± 0.0014	0.0000 ± 0.0026
20	0.0061 ± 0.0007	0.0004 ± 0.0022	0.0086 ± 0.0013	0.0001 ± 0.0025
21	0.0062 ± 0.0010	-0.0044 ± 0.0036	0.0100 ± 0.0019	-0.0052 ± 0.0042
22	0.0064 ± 0.0014	-0.0044 ± 0.0036	0.0097 ± 0.0021	-0.0057 ± 0.0043
23	0.0113 ± 0.0016	-0.0102 ± 0.0083	0.0156 ± 0.0024	-0.0137 ± 0.0097
24	0.0166 ± 0.0031	-0.0102 ± 0.0083	0.0208 ± 0.0038	-0.0191 ± 0.0119
25	0.0060 ± 0.0009	0.0011 ± 0.0050	0.0074 ± 0.0017	0.0001 ± 0.0059
26	0.0084 ± 0.0008	0.0011 ± 0.0050	0.0104 ± 0.0015	0.0003 ± 0.0055
27	0.0093 ± 0.0011	-0.0092 ± 0.0082	0.0136 ± 0.0022	-0.0119 ± 0.0094
28	0.0102 ± 0.0016	-0.0092 ± 0.0082	0.0142 ± 0.0024	-0.0127 ± 0.0097
29	0.0153 ± 0.0018	-0.0031 ± 0.0185	0.0186 ± 0.0029	-0.0070 ± 0.0222
30	0.0227 ± 0.0033	-0.0031 ± 0.0185	0.0284 ± 0.0043	-0.0200 ± 0.0296
31	0.0088 ± 0.0018	0.0011 ± 0.0050	0.0100 ± 0.0020	-0.0044 ± 0.0090
32	0.0118 ± 0.0016	0.0011 ± 0.0050	0.0136 ± 0.0019	-0.0034 ± 0.0070
33	0.0134 ± 0.0022	-0.0092 ± 0.0082	0.0167 ± 0.0027	-0.0228 ± 0.0133
34	0.0182 ± 0.0031	-0.0092 ± 0.0082	0.0229 ± 0.0039	-0.0241 ± 0.0127
35	0.0228 ± 0.0033	-0.0031 ± 0.0185	0.0286 ± 0.0043	-0.0179 ± 0.0277
36	0.0282 ± 0.0049	-0.0031 ± 0.0185	0.0352 ± 0.0061	-0.0439 ± 0.0538

Table 5.11: Thrust reference frame (RF12): double ratio of U/C pion pairs as a function of  $(z_1, z_2)$ -bins. The same caption as Tab. 5.9.

$A_{12}^{UL}$				
$(p_{t1}, p_{t2})$	$A_{meas} \pm \delta A_{meas}$	$A_{D^*} \pm \delta A_{D^*}$	$A_{uds} \pm \delta A_{uds}$	$A_{charm} \pm \delta A_{charm}$
1	$0.0069 \pm 0.0005$	$0.0014 \pm 0.0047$	$0.0099 \pm 0.0024$	$0.0008 \pm 0.0054$
2	$0.0120 \pm 0.0004$	$0.0079 \pm 0.0033$	$0.0145 \pm 0.0017$	$0.0076 \pm 0.0038$
3	$0.0139 \pm 0.0006$	$0.0039 \pm 0.0047$	$0.0192 \pm 0.0025$	$0.0036 \pm 0.0052$
4	$0.0178 \pm 0.0012$	$-0.0063 \pm 0.0080$	$0.0281 \pm 0.0037$	$-0.0073 \pm 0.0086$
5	$0.0118 \pm 0.0004$	$-0.0046 \pm 0.0033$	$0.0201 \pm 0.0017$	$-0.0069 \pm 0.0040$
6	$0.0210 \pm 0.0003$	$0.0026 \pm 0.0025$	$0.0304 \pm 0.0012$	$-0.0003 \pm 0.0030$
7	$0.0234 \pm 0.0005$	$0.0112 \pm 0.0036$	$0.0300 \pm 0.0019$	$0.0107 \pm 0.0041$
8	$0.0313 \pm 0.0009$	$-0.0043 \pm 0.0065$	$0.0459 \pm 0.0028$	$-0.0072 \pm 0.0072$
9	$0.0127 \pm 0.0006$	$0.0066 \pm 0.0046$	$0.0162 \pm 0.0025$	$0.0066 \pm 0.0051$
10	$0.0220 \pm 0.0005$	$0.0063 \pm 0.0036$	$0.0301 \pm 0.0019$	$0.0054 \pm 0.0042$
11	$0.0236 \pm 0.0008$	$-0.0109 \pm 0.0055$	$0.0411 \pm 0.0042$	$-0.0117 \pm 0.0070$
12	$0.0347 \pm 0.0016$	$-0.0051 \pm 0.0103$	$0.0526 \pm 0.0051$	$-0.0078 \pm 0.0113$
13	$0.0165 \pm 0.0012$	$-0.0066 \pm 0.0079$	$0.0265 \pm 0.0037$	$-0.0076 \pm 0.0086$
14	$0.0306 \pm 0.0009$	$0.0129 \pm 0.0064$	$0.0383 \pm 0.0028$	$0.0120 \pm 0.0071$
15	$0.0325 \pm 0.0016$	$-0.0107 \pm 0.0102$	$0.0517 \pm 0.0052$	$-0.0135 \pm 0.0113$
16	$0.0558 \pm 0.0034$	$0.0435 \pm 0.0208$	$0.0628 \pm 0.0089$	$0.0442 \pm 0.0228$
$A_0^{UL}$				
$(p_{t1}, p_{t2})$	$A_{meas} \pm \delta A_{meas}$	$A_{D^*} \pm \delta A_{D^*}$	$A_{uds} \pm \delta A_{uds}$	$A_{charm} \pm \delta A_{charm}$
1	$0.0024 \pm 0.0004$	$0.0022 \pm 0.0029$	$0.0026 \pm 0.0015$	$0.0022 \pm 0.0034$
2	$0.0102 \pm 0.0002$	$0.0009 \pm 0.0019$	$0.0150 \pm 0.0010$	$-0.0000 \pm 0.0022$
3	$0.0164 \pm 0.0003$	$-0.0002 \pm 0.0021$	$0.0250 \pm 0.0012$	$-0.0016 \pm 0.0027$
4	$0.0229 \pm 0.0003$	$0.0018 \pm 0.0025$	$0.0320 \pm 0.0012$	$-0.0000 \pm 0.0032$

Table 5.12: In the first part of the table are reported the double ratio of U/L pion pairs as a function of  $(p_{t1}, p_{t2})$  bins obtained in the RF12 frame. In the second part, are summarized the results for the same double ratio in the RF0 frame, as a function of  $p_{t0}$ . In particular, are compared the asymmetries measured ( $A_{meas}$ ) in the full data, the asymmetries measured in the  $D^*$  enhanced sample ( $A_{D^*}$ ), the light quark ( $A_{uds}$ ) and charm ( $A_{charm}$ ) asymmetries. The last two are obtained following Eq. 5.7.

$A_{12}^{UC}$				
$(p_{t1}, p_{t2})$	$A_{meas} \pm \delta A_{meas}$	$A_{D^*} \pm \delta A_{D^*}$	$A_{uds} \pm \delta A_{uds}$	$A_{charm} \pm \delta A_{charm}$
1	$0.0032 \pm 0.0004$	$0.0007 \pm 0.0040$	$0.0045 \pm 0.0020$	$0.0004 \pm 0.0045$
2	$0.0055 \pm 0.0003$	$0.0036 \pm 0.0028$	$0.0066 \pm 0.0014$	$0.0035 \pm 0.0032$
3	$0.0063 \pm 0.0005$	$0.0017 \pm 0.0039$	$0.0087 \pm 0.0020$	$0.0016 \pm 0.0042$
4	$0.0078 \pm 0.0010$	$-0.0021 \pm 0.0064$	$0.0122 \pm 0.0030$	$-0.0025 \pm 0.0069$
5	$0.0054 \pm 0.0003$	$-0.0022 \pm 0.0028$	$0.0092 \pm 0.0014$	$-0.0032 \pm 0.0033$
6	$0.0095 \pm 0.0002$	$0.0012 \pm 0.0021$	$0.0138 \pm 0.0010$	$-0.0001 \pm 0.0025$
7	$0.0105 \pm 0.0004$	$0.0049 \pm 0.0030$	$0.0135 \pm 0.0015$	$0.0047 \pm 0.0034$
8	$0.0136 \pm 0.0008$	$-0.0018 \pm 0.0052$	$0.0200 \pm 0.0023$	$-0.0031 \pm 0.0057$
9	$0.0058 \pm 0.0005$	$0.0030 \pm 0.0039$	$0.0073 \pm 0.0020$	$0.0030 \pm 0.0042$
10	$0.0098 \pm 0.0004$	$0.0027 \pm 0.0030$	$0.0135 \pm 0.0015$	$0.0023 \pm 0.0034$
11	$0.0103 \pm 0.0006$	$-0.0045 \pm 0.0044$	$0.0178 \pm 0.0026$	$-0.0048 \pm 0.0049$
12	$0.0145 \pm 0.0013$	$-0.0029 \pm 0.0077$	$0.0224 \pm 0.0038$	$-0.0041 \pm 0.0085$
13	$0.0073 \pm 0.0010$	$-0.0027 \pm 0.0064$	$0.0116 \pm 0.0030$	$-0.0032 \pm 0.0069$
14	$0.0133 \pm 0.0008$	$0.0051 \pm 0.0052$	$0.0169 \pm 0.0023$	$0.0047 \pm 0.0057$
15	$0.0136 \pm 0.0013$	$-0.0041 \pm 0.0078$	$0.0215 \pm 0.0038$	$-0.0052 \pm 0.0085$
16	$0.0217 \pm 0.0027$	$0.0107 \pm 0.0145$	$0.0267 \pm 0.0064$	$0.0104 \pm 0.0158$
$A_0^{UC}$				
$(p_{t1}, p_{t2})$	$A_{meas} \pm \delta A_{meas}$	$A_{D^*} \pm \delta A_{D^*}$	$A_{uds} \pm \delta A_{uds}$	$A_{charm} \pm \delta A_{charm}$
1	$0.0011 \pm 0.0003$	$0.0010 \pm 0.0024$	$0.0012 \pm 0.0012$	$0.0010 \pm 0.0028$
2	$0.0046 \pm 0.0002$	$0.0004 \pm 0.0016$	$0.0068 \pm 0.0008$	$0.0000 \pm 0.0018$
3	$0.0074 \pm 0.0002$	$-0.0001 \pm 0.0018$	$0.0113 \pm 0.0009$	$-0.0007 \pm 0.0020$
4	$0.0101 \pm 0.0003$	$0.0007 \pm 0.0020$	$0.0142 \pm 0.0009$	$-0.0001 \pm 0.0024$

Table 5.13: In the first part of the table are reported the double ratio of U/C pion pairs as a function of  $(p_{t1}, p_{t2})$  bins obtained in the RF12 frame. In the second part, are summarized the results for the same double ratio in the RF0 frame, as a function of  $p_{t0}$ . In particular, are compared the asymmetries measured ( $A_{meas}$ ) in the full data, the asymmetries measured in the  $D^*$  enhanced sample ( $A_{D^*}$ ), the light quark ( $A_{uds}$ ) and charm ( $A_{charm}$ ) asymmetries. The last two are obtained following Eq. 5.7.

### 5.3 Monte Carlo Re-weighted sample

As already pointed out, the experimental method used assumes that the event thrust axis coincides with the true  $q\bar{q}$  axis, but this is only a rough approximation. In fact, as can be seen in Fig. 5.17, the distribution of the opening angle between the two axis shows a peak at approximately 0.1 rad and a long tail at higher values.

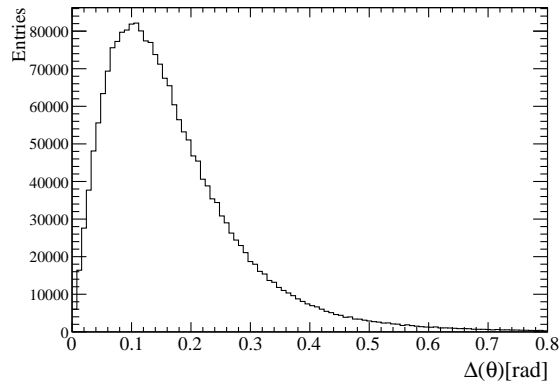


Figure 5.17: Opening angle  $\Delta(\theta)$  between the thrust axis and the real  $q\bar{q}$  axis. The peak is at about 0.1 rad with an r.m.s. of about 0.05 rad.

Figure 5.18(a) shows the scatter plot of the  $\phi_{1, reco} + \phi_{2, reco}$  combinations for reconstructed pions, with the angles calculated with respect to the thrust axis, and the true values, that is the  $\phi_{1, gen} + \phi_{2, gen}$  combinations obtained from the generated momentum of the pions and the  $q\bar{q}$  axis. If the assumption that the thrust axis coincides with the  $q\bar{q}$  axis is correct, the data should be distributed along the diagonal of the 2D-plot, while we observe a large smearing effect. Much better agreement between reconstructed and true azimuthal angles is observed for the RF0 reference frame, because  $2\phi_0$  is calculated with respect to the plane constructed with the beam axis and the second pion momentum, instead of the plane containing the thrust axis as for the RF12. For this reason, the thrust axis mis-reconstruction does not influence the measurement in the RF0 frame, and only small smearing effects related to PID and tracking resolution remain.

The above illustrated smearing effects produce a dilution of the asymmetries which has to be estimated and corrected for. The MC generator does not include spin effects, as it would have been needed in order to perform detailed studies. We overcome this limitation simulating the azimuthal asymmetries with a proper re-weighting of the generated angular distributions. The applied weights are defined as:

$$w^i = 1 + a^i \cdot \cos(\phi_{\alpha, gen}) \quad (5.8)$$

with  $i = U, L, C$ , and  $\alpha = 12, 0$ . Note that the angles  $\phi_{\alpha, gen}$  are the azimuthal angles for generated particles calculated with respect to the true  $q\bar{q}$  axis. Analyzing the double ratios,

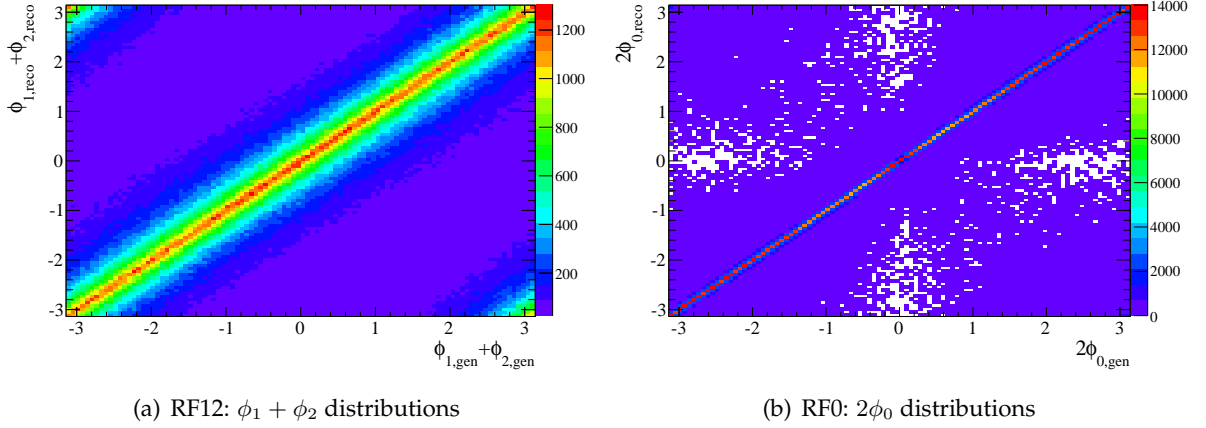


Figure 5.18: Distributions of the reconstructed  $\phi_1 + \phi_2$  (a) and  $2\phi_0$  (b) combination, versus the corresponding values for the generated tracks. The reconstructed azimuthal angles  $\phi_1$  and  $\phi_2$  are calculated with respect to the plane containing the beam axis and the thrust axis, instead the real  $q\bar{q}$  axis is used in the generated azimuthal distributions. In the RF0 frame, the reconstructed (generated)  $2\phi_0$  angle is calculated with respect to the plane determined by the beam axis and the second reconstructed (generated) pion momentum.

for example, with generated weights  $w^U = 1\%$  and  $w^L = -1\%$  the reconstructed  $U/L$  double ratios should ideally return a 2% asymmetry.

We perform this study using the  $uds$  MC sample, and evaluate the correction factors, indicated with  $\zeta$ , dividing the sample according to the following  $z_i$  intervals:  $[0.15 - 0.2]$ ,  $[0.2 - 0.3]$ ,  $[0.3 - 0.5]$ ,  $[0.5 - 1.0]$ ; and  $p_{ti}$  intervals:  $[0.1 - 0.25]$ ,  $[0.25 - 0.5]$ ,  $[0.5 - 0.75]$ ,  $[0.75 - 5.0]$  GeV/ $c$ . In particular, since the kinematic distributions are very different for pion pairs with very low fractional energy ( $z_i < 0.2$ , as shown in Fig. 4.6(a), and in Fig. 4.6(b)), we evaluate separately the correction factor for the  $z$ -bin  $[0.15 - 0.2]$ . For the same reasons, all correction factors as a function of  $p_t$  are obtained selecting pions with  $z > 0.2$ , assuming that the inclusion of pion pairs with lower  $z$  does not influence significantly the determination of  $\zeta$ .

We introduce the following weights:

- $w^i = \pm 0.01$ , which corresponds to an asymmetry of 2%,
- $w^i = \pm 0.02$ , which corresponds to an asymmetry of 4%,
- $w^i = \pm 0.03$ , which corresponds to an asymmetry of 6%, and
- $w^i = \pm 0.05$ , which corresponds to an asymmetry of 10%,

and fit the reconstructed double ratio distributions for each weight. Taking into account the small MC bias described in Sec.5.1, the fraction of the original asymmetry returned by the fit is given by:

$$W^\alpha = \frac{A_w^\alpha}{A_{intr.} + A_{bias}}, \quad (5.9)$$

where  $\alpha = UL, UC$ ,  $A_w$  is the fitted asymmetry,  $A_{intr.}$  is the asymmetry introduced with the weight in the simulation (2%, 4%, 6% or 10%), and  $A_{bias}$  is the bias measured in the  $uds$  MC sample.

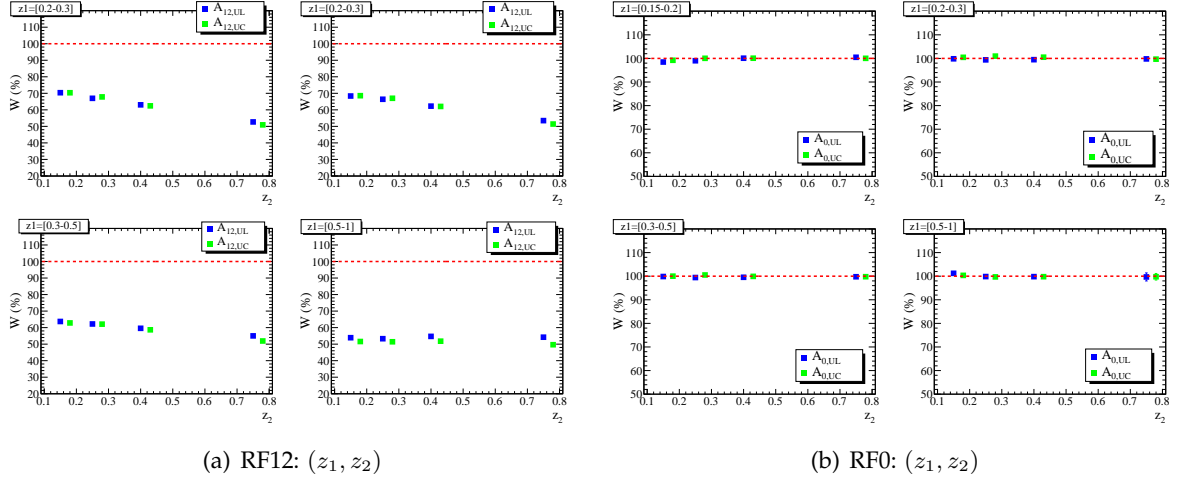


Figure 5.19: Average fraction (%) of asymmetries results, in the RF12 (a) and RF0 (b) frames, as a function of  $(z_1, z_2)$  subdivision for the reconstructed light quark MC events, re-weighted as described in the text. Blue and green squares refers to the U/L and U/C double ratios, respectively.

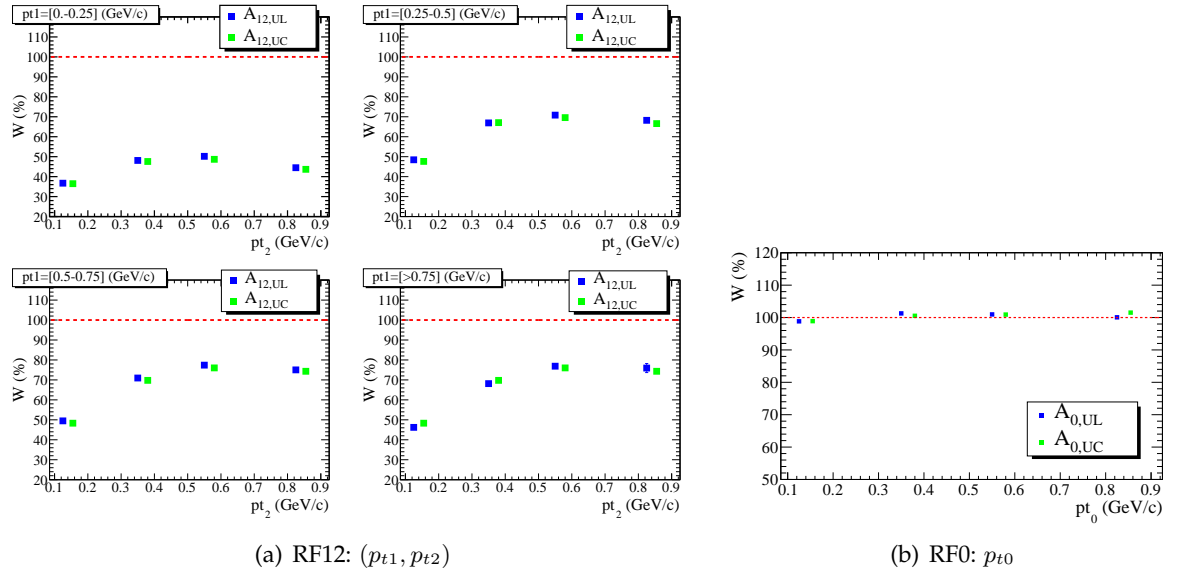


Figure 5.20: Average fraction (%) of asymmetries results, in the RF12 (a) and RF0 (b) frames, as a function of  $p_t$  bins subdivision for the reconstructed light quark MC events, re-weighted as described in the text. Blue and green squares refers to the U/L and U/C double ratios, respectively.

The results for different applied weights are consistent with each other, we therefore calculate the average fractions  $\langle W \rangle$  and get the corrections  $\zeta = 1 / \langle W \rangle$ . The average fractions are reported in Figs. 5.19 and 5.20. As expected, we observe essentially no effect in the RF0 frame, where the fitted asymmetries are consistent with the generated ones in every  $z_i$  or  $p_{ti}$  intervals, and therefore no corrections are applied to the asymmetries measured in the data sample. On the contrary, the average fractions of the asymmetries measured in the RF12 frame are significantly lower than unity, and show also a pattern as a function of  $z$  and  $p_t$ . In fact they seem to decrease smoothly from about 70% to 50% with increasing values of  $z$ , and seems to increase from about 40 to 75% with increasing  $p_t$  values. The results for all measured  $W$ 's and correction  $\zeta$ 's are reported in Tables 5.14 - 5.16

RF12					
Bins	$(z_1, z_2)$	$A^{UL} : \%$	Corr. $\zeta_{12}^{UL}$	$A^{UC} : \%$	Corr. $\zeta_{12}^{UC}$
1	[0.15,0.2][0.15,0.2]	$70.37 \pm 0.46$	$1.421 \pm 0.009$	$70.34 \pm 0.40$	$1.422 \pm 0.008$
2	[0.15,0.2][0.2,0.3]	$66.97 \pm 0.43$	$1.493 \pm 0.010$	$67.83 \pm 0.37$	$1.474 \pm 0.008$
3	[0.15,0.2][0.3,0.5]	$63.03 \pm 0.47$	$1.586 \pm 0.012$	$62.42 \pm 0.40$	$1.602 \pm 0.010$
4	[0.15,0.2][0.5,1.]	$52.69 \pm 0.80$	$1.898 \pm 0.029$	$50.92 \pm 0.68$	$1.964 \pm 0.026$
5	[0.2,0.3][0.15,0.2]	$68.37 \pm 0.43$	$1.463 \pm 0.009$	$68.56 \pm 0.37$	$1.459 \pm 0.008$
6	[0.2,0.3][0.2,0.3]	$66.40 \pm 0.41$	$1.506 \pm 0.009$	$67.00 \pm 0.35$	$1.493 \pm 0.008$
7	[0.2,0.3][0.3,0.5]	$62.24 \pm 0.44$	$1.607 \pm 0.011$	$62.06 \pm 0.38$	$1.611 \pm 0.010$
8	[0.2,0.3][0.5,1.]	$53.48 \pm 0.74$	$1.870 \pm 0.026$	$51.41 \pm 0.63$	$1.945 \pm 0.024$
9	[0.3,0.5][0.15,0.2]	$63.71 \pm 0.47$	$1.570 \pm 0.012$	$62.83 \pm 0.40$	$1.592 \pm 0.010$
10	[0.3,0.5][0.2,0.3]	$62.20 \pm 0.44$	$1.608 \pm 0.011$	$62.10 \pm 0.38$	$1.610 \pm 0.010$
11	[0.3,0.5][0.3,0.5]	$59.58 \pm 0.49$	$1.678 \pm 0.014$	$58.67 \pm 0.41$	$1.704 \pm 0.012$
12	[0.3,0.5][0.5,1.]	$55.00 \pm 0.80$	$1.818 \pm 0.027$	$51.91 \pm 0.68$	$1.927 \pm 0.025$
13	[0.5,1.][0.15,0.2]	$53.89 \pm 0.80$	$1.856 \pm 0.028$	$51.59 \pm 0.68$	$1.938 \pm 0.026$
14	[0.5,1.][0.2,0.3]	$53.29 \pm 0.74$	$1.877 \pm 0.026$	$51.43 \pm 0.63$	$1.944 \pm 0.024$
15	[0.5,1.][0.3,0.5]	$54.69 \pm 0.81$	$1.828 \pm 0.027$	$51.79 \pm 0.69$	$1.931 \pm 0.026$
16	[0.5,1.][0.5,1.]	$54.20 \pm 1.37$	$1.845 \pm 0.047$	$49.65 \pm 1.15$	$2.014 \pm 0.047$

Table 5.14: Thrust reference frame (RF12): estimated average fractions of the asymmetry measured fitting the double ratios U/L and U/C as a function of  $(z_1, z_2)$  and corresponding correction factors  $\zeta$ .

RF0					
Bins	$(z_1, z_2)$	$A^{UL} : \%$	Corr. $\zeta_0^{UL}$	$A^{UC} : \%$	Corr. $\zeta_0^{UC}$
1	[0.15,0.2][0.15,0.2]	$98.47 \pm 0.48$	$1.016 \pm 0.005$	$99.21 \pm 0.41$	$1.008 \pm 0.004$
2	[0.15,0.2][0.2,0.3]	$99.01 \pm 0.47$	$1.010 \pm 0.005$	$100.05 \pm 0.40$	$1.000 \pm 0.004$
3	[0.15,0.2][0.3,0.5]	$100.09 \pm 0.53$	$0.999 \pm 0.005$	$100.09 \pm 0.45$	$0.999 \pm 0.004$
4	[0.15,0.2][0.5,1.]	$100.48 \pm 0.91$	$0.995 \pm 0.009$	$100.04 \pm 0.76$	$1.000 \pm 0.008$
5	[0.2,0.3][0.15,0.2]	$99.84 \pm 0.47$	$1.002 \pm 0.005$	$100.46 \pm 0.40$	$0.995 \pm 0.004$
6	[0.2,0.3][0.2,0.3]	$99.39 \pm 0.48$	$1.006 \pm 0.005$	$100.97 \pm 0.41$	$0.990 \pm 0.004$
7	[0.2,0.3][0.3,0.5]	$99.47 \pm 0.53$	$1.005 \pm 0.005$	$100.52 \pm 0.45$	$0.995 \pm 0.004$
8	[0.2,0.3][0.5,1.]	$99.79 \pm 0.91$	$1.002 \pm 0.009$	$99.69 \pm 0.77$	$1.003 \pm 0.008$
9	[0.3,0.5][0.15,0.2]	$99.86 \pm 0.52$	$1.001 \pm 0.005$	$100.01 \pm 0.44$	$1.000 \pm 0.004$
10	[0.3,0.5][0.2,0.3]	$99.43 \pm 0.52$	$1.006 \pm 0.005$	$100.51 \pm 0.45$	$0.995 \pm 0.004$
11	[0.3,0.5][0.3,0.5]	$99.54 \pm 0.57$	$1.005 \pm 0.006$	$99.92 \pm 0.49$	$1.001 \pm 0.005$
12	[0.3,0.5][0.5,1.]	$99.76 \pm 0.98$	$1.002 \pm 0.010$	$99.78 \pm 0.83$	$1.002 \pm 0.008$
13	[0.5,1.][0.15,0.2]	$101.22 \pm 0.93$	$0.988 \pm 0.009$	$100.35 \pm 0.76$	$0.997 \pm 0.008$
14	[0.5,1.][0.2,0.3]	$99.84 \pm 0.89$	$1.002 \pm 0.009$	$99.70 \pm 0.76$	$1.003 \pm 0.008$
15	[0.5,1.][0.3,0.5]	$99.81 \pm 0.97$	$1.002 \pm 0.010$	$99.79 \pm 0.83$	$1.002 \pm 0.008$
16	[0.5,1.][0.5,1.]	$99.68 \pm 1.70$	$1.003 \pm 0.017$	$99.76 \pm 1.39$	$1.002 \pm 0.014$

Table 5.15: Second pion momentum frame (RF0): estimated average fractions of the asymmetry measured fitting the double ratios U/L and U/C as a function of  $(z_1, z_2)$  and corresponding correction factors  $\zeta$ .

RF12					
Bins	$(z_1, z_2)$	$A^{UL} : \%$	Corr. $\zeta_{12}^{UL}$	$A^{UC} : \%$	Corr. $\zeta_{12}^{UC}$
1	[0,0.25][0,0.25]	$36.71 \pm 0.76$	$2.724 \pm 0.056$	$36.47 \pm 0.64$	$2.742 \pm 0.048$
2	[0,0.25][0.25,0.5]	$48.11 \pm 0.55$	$2.079 \pm 0.024$	$47.58 \pm 0.46$	$2.102 \pm 0.020$
3	[0,0.25][0.5,0.75]	$50.16 \pm 0.72$	$1.994 \pm 0.029$	$48.67 \pm 0.62$	$2.055 \pm 0.026$
4	[0,0.25][> 0.75]	$44.70 \pm 1.20$	$2.237 \pm 0.061$	$43.66 \pm 1.11$	$2.290 \pm 0.058$
5	[0.25,0.5][0,0.25]	$48.43 \pm 0.54$	$2.065 \pm 0.023$	$47.62 \pm 0.46$	$2.100 \pm 0.020$
6	[0.25,0.5][0.25,0.5]	$66.89 \pm 0.42$	$1.495 \pm 0.009$	$67.02 \pm 0.35$	$1.492 \pm 0.008$
7	[0.25,0.5][0.5,0.75]	$70.81 \pm 0.57$	$1.412 \pm 0.011$	$69.56 \pm 0.49$	$1.438 \pm 0.010$
8	[0.25,0.5][> 0.75]	$68.75 \pm 0.85$	$1.455 \pm 0.018$	$66.57 \pm 0.89$	$1.502 \pm 0.020$
9	[0.5,0.75][0,0.25]	$49.47 \pm 0.73$	$2.022 \pm 0.030$	$48.31 \pm 0.62$	$2.070 \pm 0.026$
10	[0.5,0.75][0.25,0.5]	$70.93 \pm 0.58$	$1.410 \pm 0.011$	$69.76 \pm 0.49$	$1.434 \pm 0.010$
11	[0.5,0.75][0.5,0.75]	$77.39 \pm 0.84$	$1.292 \pm 0.014$	$76.01 \pm 0.73$	$1.316 \pm 0.013$
12	[0.5,0.75][> 0.75]	$75.10 \pm 1.27$	$1.332 \pm 0.022$	$74.32 \pm 1.38$	$1.346 \pm 0.025$
13	[> 0.75][0,0.25]	$46.19 \pm 1.28$	$2.165 \pm 0.060$	$44.52 \pm 1.10$	$2.246 \pm 0.055$
14	[> 0.75][0.25,0.5]	$68.13 \pm 1.06$	$1.468 \pm 0.023$	$66.71 \pm 0.91$	$1.499 \pm 0.020$
15	[> 0.75][0.7,0.75]	$76.86 \pm 1.56$	$1.301 \pm 0.026$	$75.17 \pm 1.38$	$1.330 \pm 0.024$
16	[> 0.75][> 0.75]	$76.09 \pm 2.26$	$1.314 \pm 0.039$	$75.06 \pm 2.61$	$1.332 \pm 0.046$
RF0					
Bins	$p_{t0}$	$A^{UL} : \%$	Corr. $\zeta_0^{UL}$	$A^{UC} : \%$	Corr. $\zeta_0^{UC}$
1	[0,0.25]	$98.83 \pm 0.64$	$1.012 \pm 0.007$	$98.87 \pm 0.53$	$1.011 \pm 0.005$
2	[0.25,0.5]	$101.23 \pm 0.40$	$0.988 \pm 0.004$	$100.45 \pm 0.34$	$0.996 \pm 0.003$
3	[0.5,0.75]	$100.93 \pm 0.39$	$0.991 \pm 0.004$	$100.89 \pm 0.34$	$0.991 \pm 0.003$
4	[> 0.75]	$100.04 \pm 0.39$	$1.000 \pm 0.004$	$101.51 \pm 0.35$	$0.985 \pm 0.003$

Table 5.16: Estimated average fractions of the asymmetry measured fitting the double ratios U/L and U/C as a function of  $(p_{t1}, p_{t2})$  (RF12) in the first part of the table, and as a function of  $p_{t0}$  (RF0) in the second part of the table. It is also summarized the corresponding correction factors  $\zeta$ .

## 5.4 Particle Identification

As introduced in section 4.3.2, a series of selectors for different particle hypothesis are built in order to provide particle identification (PID). In this analysis, we select pions that satisfied the KM-selector, which offer six tightness levels of discrimination. In order to check if the measured asymmetries are sensitive to some of the cuts applied for the PID, we compare the results obtained with our standard selection which use the tight (T) selector, with those obtained using a PID selector based on looser (L) criteria. We find good agreement among these selectors for all  $z$  and  $p_t$  bins, and we assign the absolute value of the differences, shown in Fig. 5.21 as systematic errors.

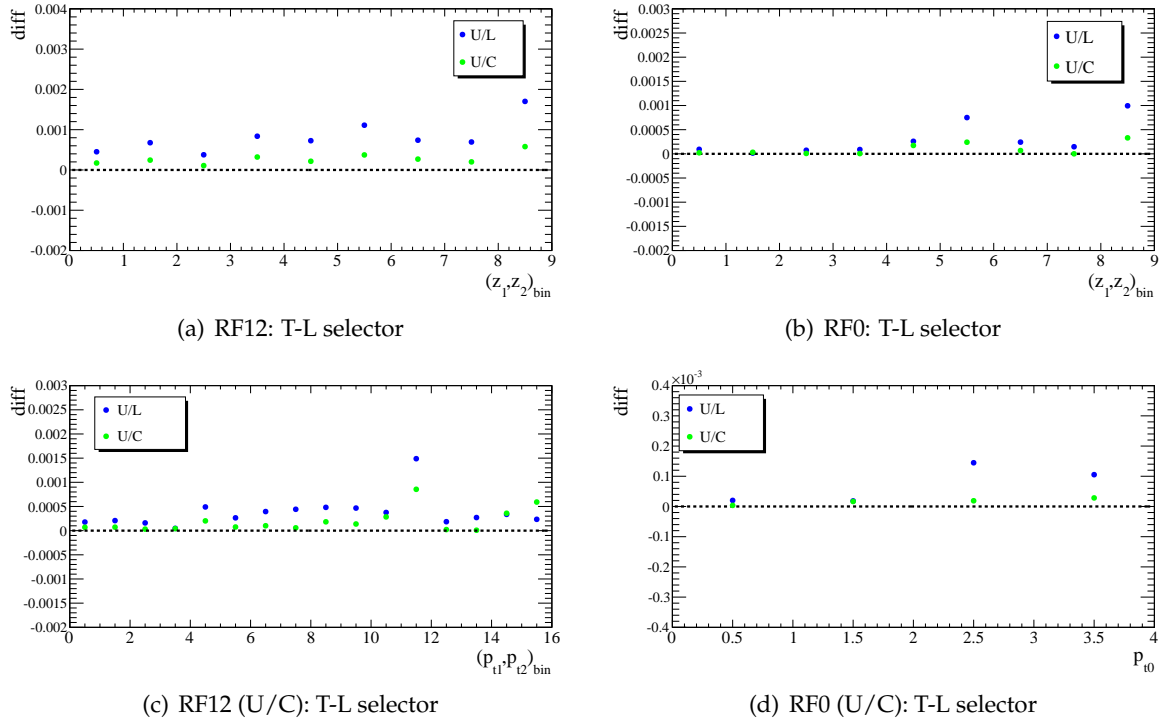


Figure 5.21: Absolute values of the difference between the asymmetries calculated using tight pions selection (selection chosen in this analysis) and the asymmetries calculated using looser selection. Plots (a) and (b) show these difference as a function of  $z$  bins, where two adjacent bins of fractional energy are grouped together in order to reduce the statistical fluctuations. Plots (c) and (d) show the difference as a function of  $p_t$  bins. Blue circles and green circles refer to the U/L and U/C double ratio, respectively.

The average differences between the two selectors criteria are:

- $A_{12}^{U/L}$ : PID systematic uncertainty = 0.00053 (relative contribution=2.7%),
- $A_0^{U/L}$ : PID systematic uncertainty = 0.00003 (relative contribution=0.2%),

- $A_{12}^{U/C}$ : PID systematic uncertainty = 0.00026 (relative contribution=2.7%),
- $A_0^{U/C}$ : PID systematic uncertainty = 0.000001 (relative contribution=0.15%).

As mentioned in Sec.4.3.3, we also apply a veto on electrons and muons because we find a contamination from these sources which affects significantly the measurement at higher  $z$  bins, as shown in Fig. 5.22.

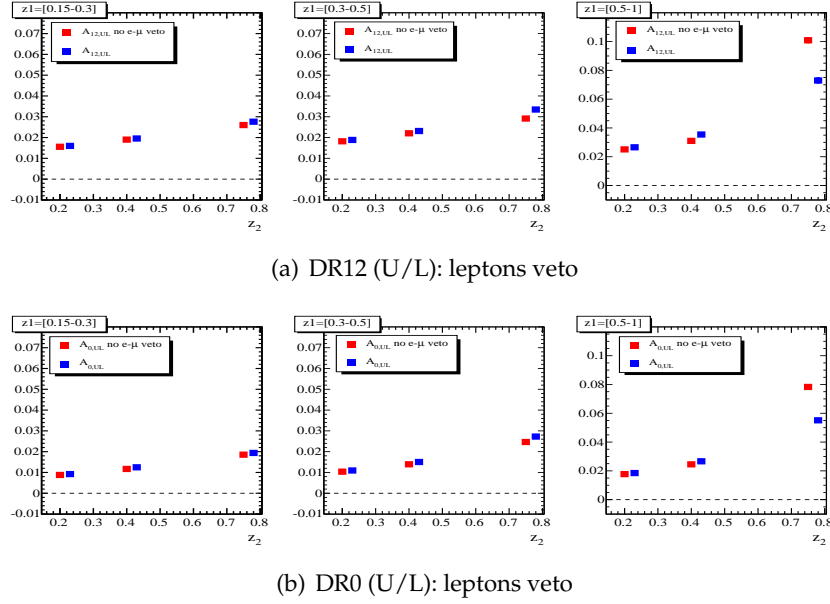


Figure 5.22: Comparison of  $z$ -binned asymmetries measured with (blue circles) or without (red circles) veto on muons and electrons. The leptons contamination affects higher value of fractional energy.

## 5.5 Bin size

The extraction of asymmetry may depend on the choice of the bin size. In order to study this effect we consider three different subdivisions in the azimuthal angles ( $\phi_{12} = \phi_1 + \phi_2$  and  $2\phi_0$ ): 10,40, and 100 bins; the latter being the default bin size.

The difference between 100 and 10 bins subdivisions (which is the largest one) is shown in Fig. 5.23 and is taken as systematic error, and the average value for each double ratio and reference frame is:

- $A_{12}^{U/L}$ : systematic binning uncertainty = 0.0003 (relative contribution=1.5%),
- $A_0^{U/L}$ : systematic binning uncertainty = 0.0002 (relative contribution=1.5%),
- $A_{12}^{U/C}$ : systematic binning uncertainty = 0.000014 (relative contribution=1.5%),

- $A_0^{U/C}$ : PID systematic uncertainty = 0.00001 (relative contribution=1.4%).

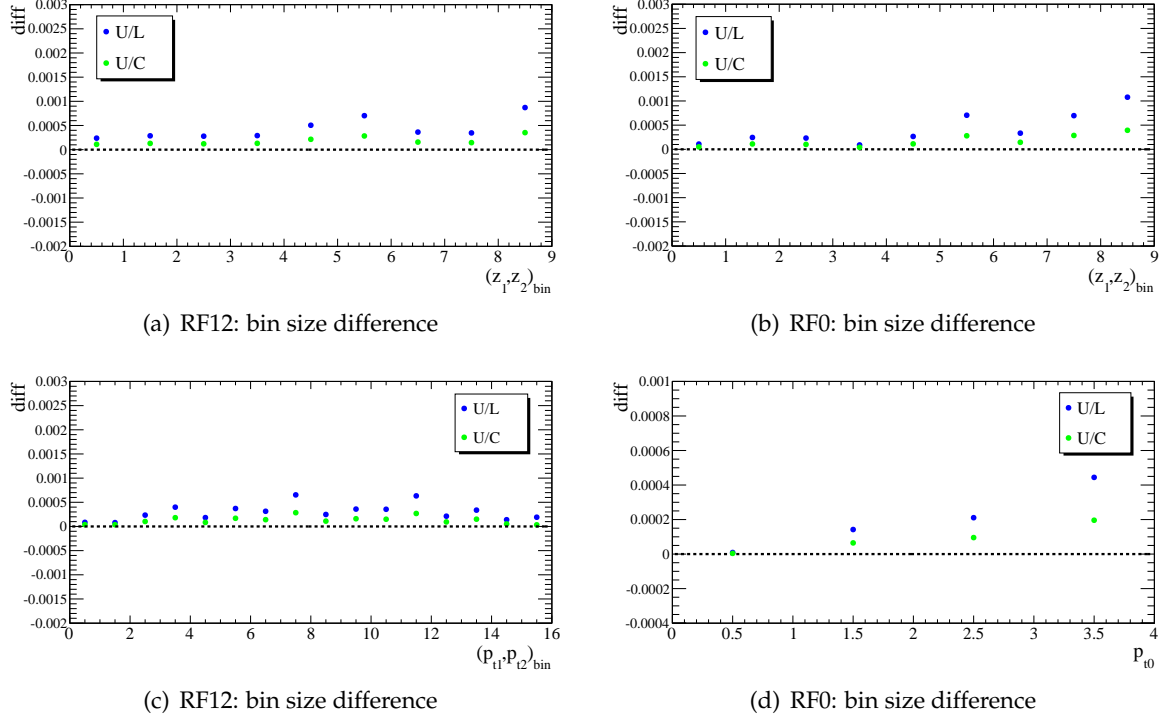


Figure 5.23: Absolute values of the difference between the asymmetries calculated for 100 bins subdivision of the azimuthal angles ( $\phi_{12}$  and  $2\phi_0$ ), and 10 bins subdivision. Plots (a) and (b) show the difference as a function of  $z$  bins for the  $\phi_{12}$  and  $2\phi_0$  azimuthal distribution respectively. Two adjacent bins of fractional energy are grouped together in order to reduce the statistical fluctuation. Plots (c) and (d) show the difference as a function of  $p_t$  bins. Blue and green circles refer to the U/L and U/C double ratio respectively.

## 5.6 Higher harmonic contributions

In order to test the robustness of the fit, we perform different fits including additional sine and cosine modulation of twice the argument as free parameters. The asymmetry results as a function of  $(z_1, z_2)$  are reported in Tab. 5.18, while in Tab. 5.19 are summarized the results as a function of  $p_t$ . The function  $f(x) = B_\alpha^{ij} + A_\alpha^{ij} \cdot \cos(\beta_\alpha)$  is the function used to fit the azimuthal distribution in this analysis (see Eq. 4.20). No significant changes are observed and, therefore, no systematic uncertainty is assigned.

## 5.7 $\pi^+\pi^+/\pi^-\pi^-$ Double Ratio test

Another possible source of systematic errors could be a charge dependence of the detector response, which may manifest itself in azimuthal asymmetries. We can test this effect by probing the double ratio of positively charged pion pairs over negatively charged pion pairs. In fact, the Collins effect and the radiative effects do not depend on the electric charge, so we expect this double ratio to be consistent with one. We performed this test using the off-peak data sample, and the results are shown in Fig. 5.24. No modulation is observed, and therefore no systematic error will be considered.

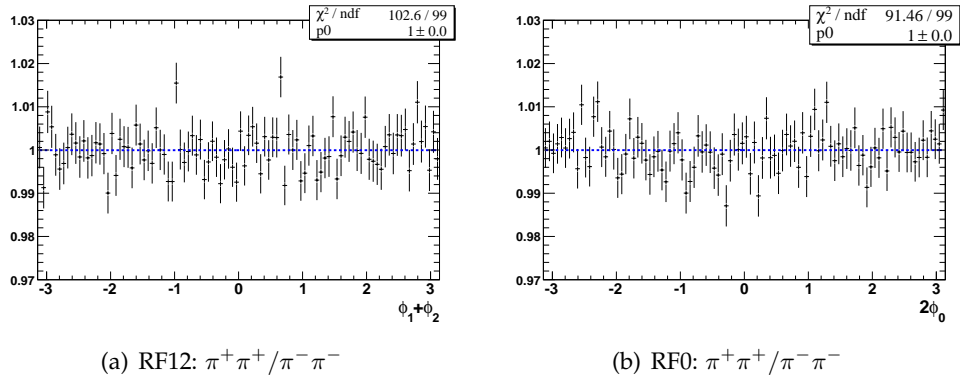


Figure 5.24:  $\pi^+\pi^+/\pi^-\pi^-$  double ratio test

## 5.8 Subtraction and Double Ratio methods

The method of building the double ratio (raw asymmetry for Unlike sign over raw asymmetry for Like or Charged sign pion pairs) cancels possible acceptance effects as well as radiative effects to leading order. However, higher orders in the expansion of radiative terms might still remain and could affect the results if they are large.

We can use a second method that we call Subtraction Method (Sub) in which, instead of the ratio, we take the difference between the U sign pion pairs and the L sign pion pairs. In this case the radiative effects cancel to all orders but not necessarily the acceptance effects. Subtracting the normalized yields as following:

$$\text{Sub}_\alpha^{ij} = \frac{N_\alpha^U(\beta_\alpha)}{\langle N_\alpha^U(\beta_\alpha) \rangle} - \frac{N_\alpha^{L(C)}(\beta_\alpha)}{\langle N_\alpha^{L(C)}(\beta_\alpha) \rangle}, \quad (5.10)$$

one is sensitive only to the Collins asymmetry and possible acceptance effects. Again, these yields are fitted with a cosine function:

$$\text{Sub}_\alpha^{ij} = P_{0,\alpha}^{ij} - P_{1,\alpha}^{ij} \cdot \cos(\beta_\alpha), \quad (5.11)$$

with  $i, j = U, L, C, \alpha = 12, 0$ , and the constant parameters now should be consistent with zero.

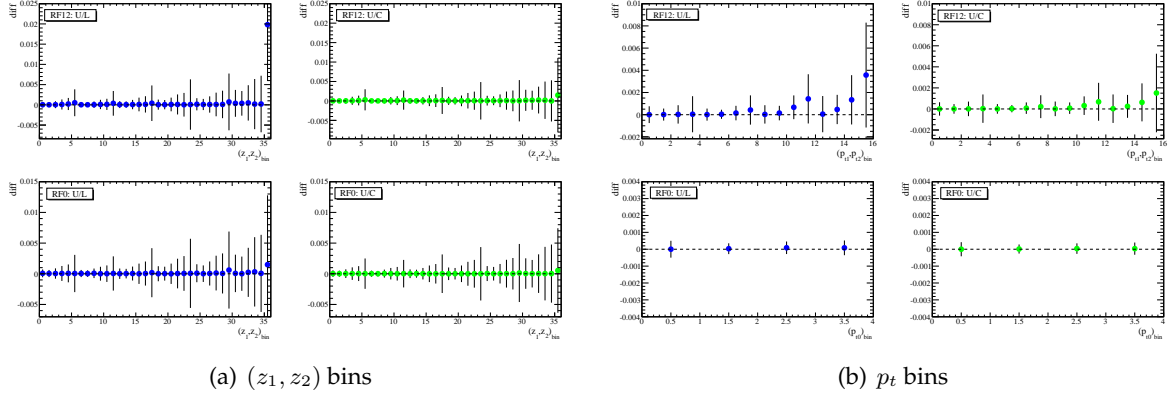


Figure 5.25: Difference between the asymmetry measured using the DR method and the Sub method, in the RF12 (upper plots) and RF0 (lower plots) frames. In (a) are summarized the results as a function of  $(z_1, z_2)$ , and in (b) as a function of  $p_t$ . The blue and green circles refer to the U/L and U/C pion pair combination.

Figure 5.25 shows the differences between the azimuthal asymmetry parameters obtained using the DR method and the asymmetry parameters obtained with the Sub method, evaluated for each bins of fractional energy and pion transverse momentum. Excluding the last  $z$  bin in the RF12 frame, these differences are very tiny and consistent with zero for all bins, and they can be neglected.

## 5.9 Beam Polarization studies

Another important study is the polarization of the electron and positron beams. Thus far we have assumed that no beam polarization is present. However, it is well known that charged particles circulating in a magnetic field become polarized transversely to the beam direction due to the emission of spin-flipping synchrotron radiation: the Sokolov-Ternov effect [106]. This effect can be significant for electrons and positrons due to their small mass. The transverse polarization for particles circulating in a uniform magnetic field would build up in time according to:

$$P(t) = \frac{8\sqrt{3}}{15} \left( 1 - \exp\left[-\frac{5\sqrt{3}}{8} \frac{e^2 h \gamma^5}{m^2 c^2 \rho^3}\right] \right) \quad (5.12)$$

where  $\gamma = E/m$  is the Lorentz factor of the particle and  $\rho$  is the bending radius of the orbit. The polarization has a strong dependence on the mass in the exponent: the lighter the particle, the faster it becomes polarized. The beam polarization can affect the angular distribution of produced hadrons in  $e^+e^- \rightarrow hX$  introducing a  $\cos(2\phi)$  asymmetry, where  $\phi$  is the angle defined with respect to the beam and the beam spin direction. This asymmetry has in common with

the Collins asymmetry that both are transverse single spin asymmetries: the former concerning lepton spins, the latter quark spins. The Collins effect does not contribute to the angular distribution of produced hadron in  $e^+e^- \rightarrow hX$ , but the transverse beam polarization may affect the angular distribution in  $e^+e^- \rightarrow h_1h_2X$ .

We can measure the beam polarization through the study of the reaction  $e^+e^- \rightarrow \mu^+\mu^-$ , whose cross section can be written as [107, 108]:

$$\frac{d\sigma(e^+e^- \rightarrow \mu^+\mu^-)}{d\Omega} \propto (1 + \cos^2(\theta) + P^2 \sin^2(\theta) \cos(2\phi)) \quad (5.13)$$

where  $P$  is the degree of transverse polarization of beams, and  $\theta$  and  $\phi$  are the polar and azimuthal angles of the produced muons in the  $e^+e^-$  center of mass system. We analyze the  $\cos(\theta)$  and  $\phi$  distributions of the muon pairs. In particular, the  $\cos(\theta)$  distribution is fitted with the function:  $a(1 + b \cdot x^2(\theta))$ , and the  $\phi$  distribution with the function:  $c(1 + d \cdot \cos(2\phi))$ . For unpolarized beams, we expect the  $d$  parameter of the latter fit, which contains the polarization information, to be consistent with zero, and the angular distribution in  $\theta$  to be consistent with  $1 + \cos^2(\theta)$ . For the event selection we used a skim of data (see Tab. 4.1), described in the *BABAR* note [109], for which the main cuts are the following:

1. muon background filter:
  - $P_1 > 4$  GeV/ $c$  and  $P_2 > 2$  GeV/ $c$ , where  $P_1$  and  $P_2$  correspond to the highest and second highest momentum charged tracks
  - $2.8 > \theta_1 + \theta_2 > 3.5$  rad.
  - $E_1 + E_2 < 2$  GeV, where  $E_1$  and  $E_2$  correspond to the highest and second highest energy neutral clusters.
2.  $\cos(\theta_{1,CM}) < 0.7485$  and  $\cos(\theta_{2,CM}) < 0.7485$ ;
3. Acolinearity in the center of mass frame  $< 0.17$ ;
4. Invariant mass of the muon pair  $> 7.5$  GeV/ $c^2$ ;
5.  $0 < (EMClab_{p1}, EMClab_{p2}) < 1$  GeV.

The cut on  $\cos(\theta)$  at 0.7485 in center of mass ensures that all tracks fall into the SVT coverage. The cut on acolinearity rejects cosmic rays, while the cut on the invariant mass rejects the  $\tau$  pairs. Finally, Bhabha events are rejected by requiring that the energy associated with the track be less than 1 GeV, measured in the laboratory frame.

Fig. 5.26 shows, as example, the  $\cos(\theta)$  and  $\phi$  distributions for the run 6, and in Tab. 5.17 are summarized the fit results for all runs. The  $\phi$  moments are consistent with zero in all runs which means that no polarization buildup is observed. Therefore, we can conclude that no significant beam polarization exists in this data sample and no systematic error is assigned.

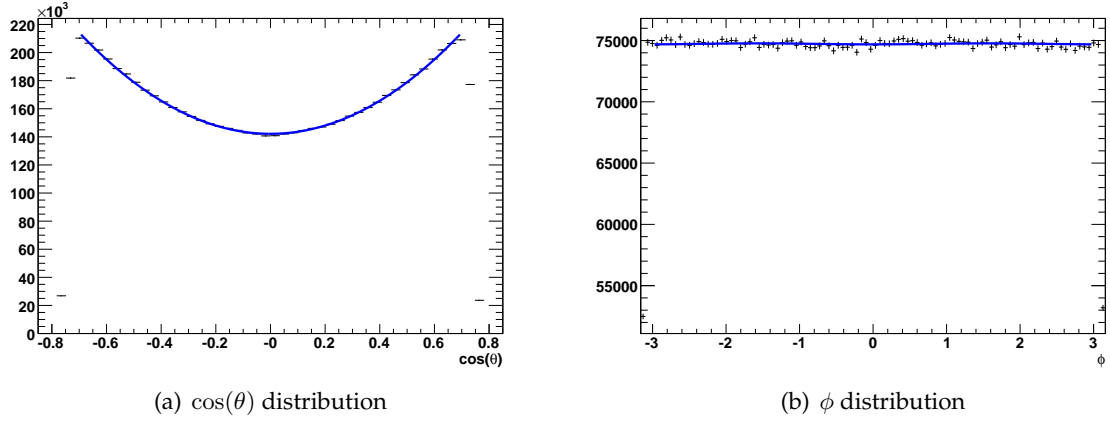


Figure 5.26: Angular distribution for  $\cos(\theta)$  (a) and  $\phi$  (b) for muon pairs in the center of mass frame. In the case of  $\cos(\theta)$  distribution, the fit is performed only in the range  $[-0.65, 0.65]$  since at large angles acceptance effects dominate. The  $\phi$  distribution is sensitive to the beam polarization. Any visible modulation in  $\phi$  is an index of polarization.

Fit function	$\cos(\theta)$ $a \cdot (1 + b \cdot x^2)$	$\phi$ $c \cdot (1 + d \cdot \cos(2x))$	$\phi$ constant function $b$
Run1	$b = 1.07 \pm 0.01$ $\chi^2/ndf = 102/90$	$d = -0.002 \pm 0.001$ $\chi^2/ndf = 91/98$	$0.9994 \pm 0.0006$ $\chi^2/ndf = 97/99$
Run2	$b = 1.06 \pm 0.01$ $\chi^2/ndf = 125/90$	$d = 0.002 \pm 0.001$ $\chi^2/ndf = 108/98$	$0.9994 \pm 0.0004$ $\chi^2/ndf = 120/99$
Run3	$b = 1.06 \pm 0.01$ $\chi^2/ndf = 109/90$	$d = 0.001 \pm 0.001$ $\chi^2/ndf = 97/98$	$0.9994 \pm 0.0006$ $\chi^2/ndf = 99/99$
Run4	$b = 1.06 \pm 0.01$ $\chi^2/ndf = 122/90$	$d = -0.001 \pm 0.001$ $\chi^2/ndf = 111/98$	$0.9994 \pm 0.0003$ $\chi^2/ndf = 119/99$
Run5	$b = 1.06 \pm 0.01$ $\chi^2/ndf = 128/90$	$d = -0.002 \pm 0.001$ $\chi^2/ndf = 166/98$	$0.9994 \pm 0.0003$ $\chi^2/ndf = 180/99$
Run6	$b = 1.06 \pm 0.01$ $\chi^2/ndf = 105/90$	$d = -0.0006 \pm 0.001$ $\chi^2/ndf = 90/98$	$0.9994 \pm 0.0004$ $\chi^2/ndf = 91/99$

Table 5.17: Beam polarization study: fit results for the  $\cos(\theta)$  and  $\phi$  distributions for the process  $e^+e^- \rightarrow \mu^+\mu^-$

## 5.10 Toy MC

A certain level of correlation among the entries of the double ratio distributions is expected because the same pion can be used to form different pion pairs, so that the statistical error returned by the fits could be underestimated. In order to check for effects of this kind and

to validate the fit procedure, a study based on the method of toy MC is performed. Toy MC studies test the self consistency of the fit model and how sensitive the fit parameters are with respect to the statistical fluctuations in the data sample. A toy MC consists of a series of pseudo-experiments, generating for each experiment, according to the fit model under consideration, a statistic sample equal to that selected by the analysis procedure. We generate a set of 30000 toy experiments. As an example, the results for the UL asymmetry measured in the RF12 frame are shown in Fig. 5.27.

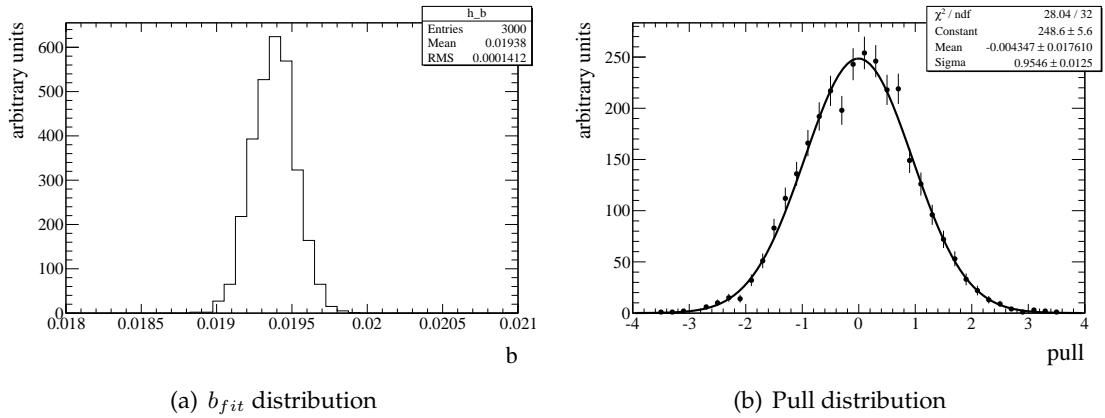


Figure 5.27: Toy MC results for the UL averaged asymmetry measured in the RF12 frame: (a) distribution of the asymmetry parameter returned by the fit ( $b_{fitted}$ ); (b) pull distribution calculated following Eq. 5.14. Similar results are obtained in the RF0 frame and for the UC asymmetries.

For a simple comparison of generated and fitted parameter, a pull is calculated as:

$$b_{pull} = \frac{b_{fit} - b_{generated}}{\sigma_{b,fit}}, \quad (5.14)$$

where  $b_{generated}$  is the value of the asymmetry parameter that is used to generate the data set,  $b_{fit}$  is the value of the same parameter returned by the fit, shown also in Fig. 5.27(a), and  $\sigma_{b,fit}$  is the error on that parameter returned by the fit.

If the fit model is unbiased, the pull follows a Gaussian distribution with mean zero and a unit variance, as shown in Fig. 5.27(b). This is the case for all tests performed, in particular the standard deviations of all pull distributions result consistent with unity or slightly less, as in the case shown in Fig. 5.27(b). Therefore, we conclude that the asymmetries are correctly described and that the statistical errors of the fit to the data samples are not underestimated.

## 5.11 Asymmetries versus thrust

In this section we study the Collins asymmetry as a function of the thrust variable, and the raw asymmetries behavior in different intervals of  $\theta_{th}$ , where  $\theta_{th}$  is the angle between the thrust

axis and the beam axis. The purpose of these studies is to identify possible effects due to the detector acceptances.

Using the same event selection with the exclusion of the thrust cut only for the off-resonance data sample, we calculated the asymmetries in different bins of the thrust value and for different thrust cuts, for both reference frames. Since  $\tau$  events are characterized by thrust values higher than 0.9, the asymmetry in the last two bins is visibly diluted, and for this reason we need to correct the measurements for the  $\tau$  contribution as follows:

$$A = \frac{A_{measured}}{1 - T}, \quad (5.15)$$

where  $T$  is the fraction of pion pairs from  $\tau^+\tau^-$  defined in Eq. 5.5. The results of the Collins asymmetry for the thrust studies are shown in Fig. 5.28.

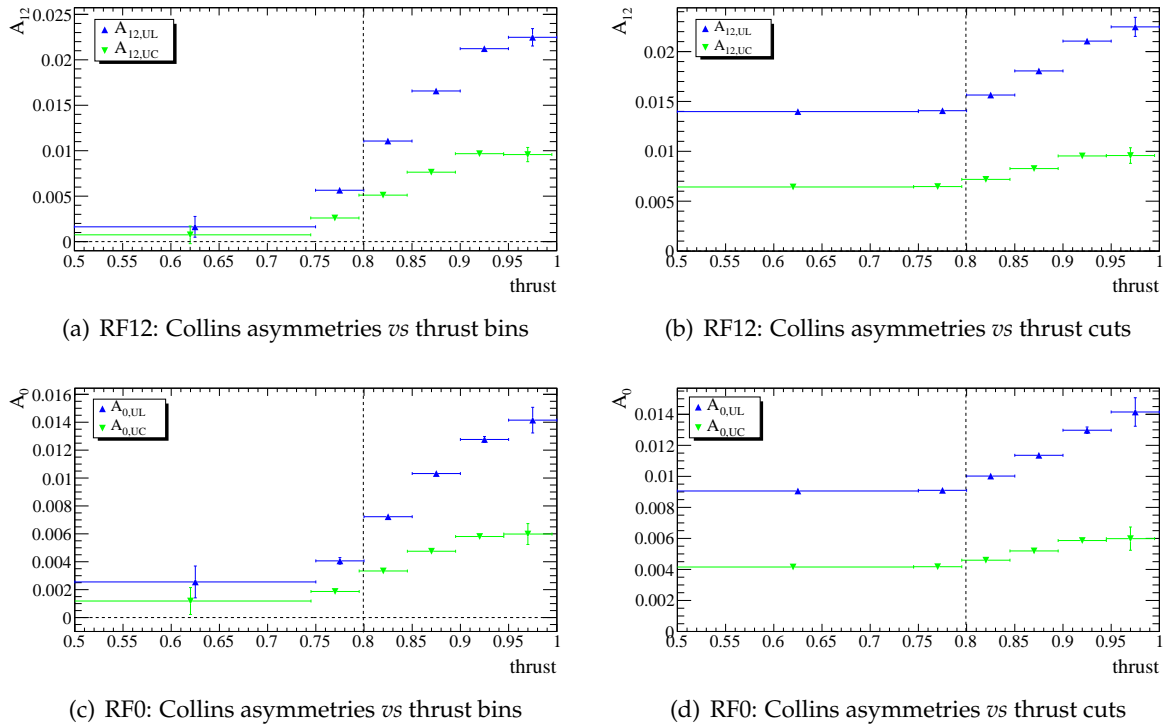


Figure 5.28: Study of the asymmetries for different thrust bins (a) and (c), and for different thrust cuts (b) and (d). The upper blue triangles represent the U/L double ratio, while the green down triangles the U/C ratio. The dashed line in each plot indicates the cuts applied in the analysis ( $thrust > 0.8$ ).

In particular, Figs 5.28(a) and 5.28(c) report the asymmetries as a function of six bins of the thrust value ( $[0.5 - 0.75]$ ,  $[0.75 - 0.8]$ ,  $[0.8 - 0.85]$ ,  $[0.85 - 0.9]$ ,  $[0.9 - 0.95]$ , and  $[0.95 - 1]$ ) for the two reference frames and double ratios. We see that the asymmetry calculated for lower thrust value is consistent with zero, and increase with it. This behavior may be due to two combined effects: first, for low thrust values, the assignment of the tracks to the right jet is more difficult,

and second, gluon emission spoils the  $q\bar{q}$  correlation. In both cases, we lost the correlation between the pions and the fragmenting  $q\bar{q}$  pair, and a dilution of the asymmetry is expected. The same conclusions can be reached from Fig. 5.28(b) and 5.28(d), which show the asymmetries as a function of cuts of the thrust value ( $thrust > 0.5, > 0.75, > 0.8, > 0.85, > 0.9, > 0.95$ ). Also in this case, we expect a dilution of the asymmetry for lower thrust. However, in order to select the jet topology and eliminate the bottom background, we integrated the asymmetry in the range  $thrust \geq 0.8$ .

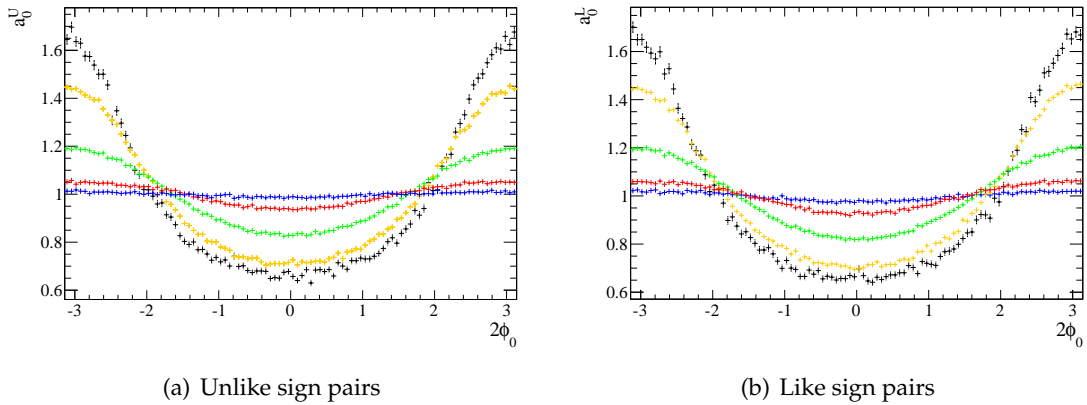


Figure 5.29: Raw asymmetries for different  $\cos(\theta_{th})$  bins measured in the RF0 frame, as example, for unlike (a) and like (b) sign pion pairs. Color legend: black (0.8,0.9), yellow (0.7,0.8), green (0.5,0.7), red (0.3,0.5), blue (0.,0.3).

In order to check the effects of the detector acceptances, we studied the behavior of the like and unlike raw asymmetry for different bins of  $\cos(\theta_{th})$ . As mentioned in section 4.4, the raw asymmetries are strongly influenced by the acceptance effects; this is clearly visible in Fig. 5.29, where are shown, as example, the like and unlike raw asymmetries in the RF0 frame and for which the color legend is as follow:

- black:  $0.8 < \cos(\theta_{th}) < 0.9$ ,
- yellow:  $0.7 < \cos(\theta_{th}) < 0.8$ ,
- green:  $0.5 < \cos(\theta_{th}) < 0.7$ ,
- red:  $0.3 < \cos(\theta_{th}) < 0.5$ ,
- blue:  $0. < \cos(\theta_{th}) < 0.3$ .

The effect is very strong for high  $\cos(\theta_{th})$ , becoming almost negligible at large angles. In fact, a small  $\theta_{th}$  angle means that the thrust axis is close to the beam axis, and in this region the acceptance effects are large since some tracks may fall out of the detector coverage introducing

modulations that do not compensate. However, the distortion of the azimuthal asymmetries is the same for unlike (Fig. 5.29(a)) and like (Fig. 5.29(b)) pion pairs. This consideration makes us confident that the double ratio (DR) effectively eliminates the detector influence.

## 5.12 Asymmetries measured in different data taking periods

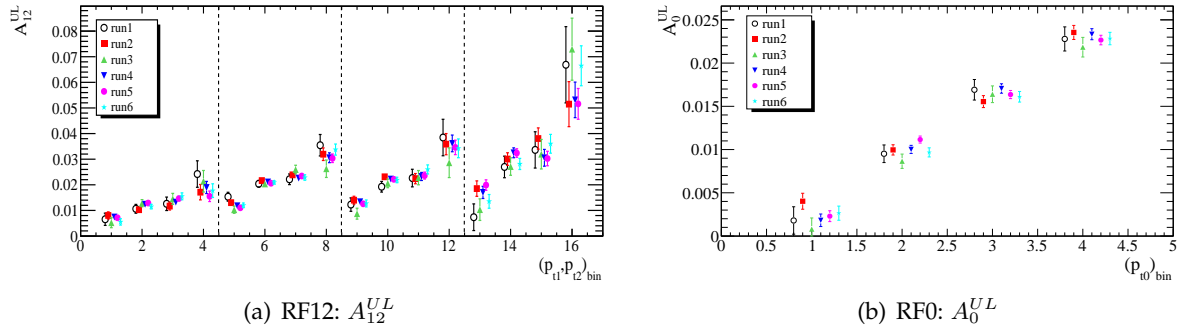


Figure 5.30: Comparison of UL double ratio parameters as a function of  $p_t$  measured for each data taking period (Run1 to Run6) in RF12 (a) and RF0 (b). The same behavior is observed for the UC double ratio, and for the the asymmetries as a function of  $(z_1, z_2)$ .

Since the *BABAR* data taking covers a period of about nine years, it is important to keep under control possible effects due to the changes of the experimental conditions, which can introduce a bias in the measurement of the asymmetries. As described in Chapter 3, a number of improvements has been made through the years, such as the implementation of *trickle injection* and the replacement of the RPCs of the muon detector with LSTs. In addition, also the efficiencies in the particle identification and the reconstruction technique differ for different Runs. We perform the analysis separately for each Run, and compare the results. As an example, Fig. 5.30 shows the asymmetries obtained for each Run fitting the UL double ratio as a function of the pion transverse momentum  $p_t$ , in both reference frames. No significant differences among the Runs are observed in any of the momentum ranges explored, assessing the stability of the measurements with time and with respect to the experimental conditions.

## 5.13 Handling of systematic errors

All the sizeable systematic errors which affect the measurement of Collins asymmetries are summarized in Tabs. 5.20 to 5.22. Each systematic uncertainty is evaluated for every bin of fractional energy  $z$  and pion transverse momentum  $p_t$ . In particular, the tables report the absolute contributions due to the particle identification (PID), different bin subdivision in the azimuthal angle (BIN), and the uncertainties on the correction factors for the dilution of the asymmetry due to the approximation of the  $q\bar{q}$  axis with the thrust axis (WEI). These three uncertainties

are calculated starting from their relative errors and multiplying them by the final values of the asymmetry. The small asymmetry observed analyzing the signal MC sample, instead is an offset, and the corresponding uncertainties (indicated with MC) do not scale with the value of the asymmetry. All these contributions are added in the quadrature, and the results summarized in the last column (TOT) of Tabs. 5.20 to 5.22.

The errors from the  $c\bar{c}$ ,  $B\bar{B}$ , and  $\tau^+\tau^-$  background events, and the difference between MC and data in the determination of the relative fraction  $F$  are propagated together with the statistical error of the measurements and included in it, as described Sec. 5.2.

The final Collins asymmetry results, with the statistical and systematic contributions calculated as summarized above, are reported and discussed in the next section.

$(z_1, z_2)$	$A_{12}^{UL}(\%)$			$A_0^{UL}(\%)$		
	$f(x)$	$f(x) + c \cos(2x)$	$f(x) + c \sin(2x)$	$f(x)$	$f(x) + c \cos(2x)$	$f(x) + c \sin(2x)$
1	1.323 ± 0.045	1.323 ± 0.045	1.323 ± 0.045	0.747 ± 0.045	0.745 ± 0.045	0.747 ± 0.045
2	1.598 ± 0.042	1.599 ± 0.042	1.598 ± 0.042	0.934 ± 0.041	0.935 ± 0.041	0.934 ± 0.041
3	1.672 ± 0.060	1.672 ± 0.060	1.672 ± 0.060	0.978 ± 0.060	0.977 ± 0.060	0.978 ± 0.060
4	1.875 ± 0.088	1.876 ± 0.088	1.875 ± 0.088	1.098 ± 0.087	1.097 ± 0.087	1.098 ± 0.087
5	2.375 ± 0.106	2.372 ± 0.106	2.375 ± 0.106	1.464 ± 0.103	1.465 ± 0.104	1.464 ± 0.103
6	2.755 ± 0.238	2.744 ± 0.238	2.755 ± 0.238	2.268 ± 0.216	2.277 ± 0.216	2.267 ± 0.216
7	1.596 ± 0.042	1.597 ± 0.042	1.596 ± 0.042	0.860 ± 0.041	0.860 ± 0.041	0.860 ± 0.041
8	1.825 ± 0.038	1.825 ± 0.038	1.825 ± 0.038	1.071 ± 0.038	1.073 ± 0.038	1.071 ± 0.038
9	2.072 ± 0.056	2.073 ± 0.056	2.072 ± 0.056	1.405 ± 0.055	1.403 ± 0.055	1.405 ± 0.055
10	2.315 ± 0.082	2.314 ± 0.082	2.315 ± 0.082	1.438 ± 0.080	1.440 ± 0.080	1.438 ± 0.080
11	2.900 ± 0.098	2.899 ± 0.098	2.900 ± 0.098	2.031 ± 0.095	2.037 ± 0.095	2.031 ± 0.095
12	3.508 ± 0.218	3.505 ± 0.218	3.509 ± 0.218	2.815 ± 0.198	2.841 ± 0.199	2.816 ± 0.198
13	1.657 ± 0.061	1.657 ± 0.061	1.657 ± 0.061	0.951 ± 0.060	0.954 ± 0.060	0.951 ± 0.060
14	1.966 ± 0.056	1.965 ± 0.056	1.966 ± 0.056	1.136 ± 0.055	1.136 ± 0.055	1.136 ± 0.055
15	2.365 ± 0.082	2.364 ± 0.082	2.365 ± 0.082	1.499 ± 0.081	1.501 ± 0.081	1.499 ± 0.081
16	2.184 ± 0.120	2.182 ± 0.120	2.184 ± 0.120	1.434 ± 0.117	1.439 ± 0.117	1.434 ± 0.117
17	3.087 ± 0.143	3.086 ± 0.143	3.087 ± 0.143	2.192 ± 0.139	2.198 ± 0.139	2.193 ± 0.139
18	3.850 ± 0.311	3.851 ± 0.311	3.851 ± 0.311	3.874 ± 0.283	3.877 ± 0.284	3.874 ± 0.283
19	1.860 ± 0.088	1.860 ± 0.088	1.860 ± 0.088	0.834 ± 0.087	0.839 ± 0.087	0.834 ± 0.087
20	2.177 ± 0.082	2.177 ± 0.082	2.177 ± 0.082	1.395 ± 0.080	1.397 ± 0.080	1.396 ± 0.080
21	2.244 ± 0.119	2.245 ± 0.119	2.244 ± 0.119	1.466 ± 0.117	1.467 ± 0.117	1.466 ± 0.117
22	2.483 ± 0.175	2.481 ± 0.175	2.483 ± 0.175	1.554 ± 0.171	1.555 ± 0.171	1.554 ± 0.171
23	3.386 ± 0.207	3.386 ± 0.207	3.386 ± 0.207	2.836 ± 0.200	2.843 ± 0.200	2.835 ± 0.200
24	4.588 ± 0.440	4.586 ± 0.440	4.588 ± 0.440	4.553 ± 0.399	4.555 ± 0.400	4.552 ± 0.399
25	2.312 ± 0.107	2.312 ± 0.107	2.312 ± 0.107	1.339 ± 0.104	1.337 ± 0.104	1.339 ± 0.104
26	2.726 ± 0.098	2.727 ± 0.098	2.726 ± 0.098	1.932 ± 0.095	1.934 ± 0.096	1.932 ± 0.095
27	3.123 ± 0.142	3.123 ± 0.142	3.122 ± 0.142	2.243 ± 0.139	2.249 ± 0.139	2.244 ± 0.139
28	3.882 ± 0.207	3.884 ± 0.207	3.883 ± 0.207	2.562 ± 0.201	2.572 ± 0.201	2.564 ± 0.201
29	5.535 ± 0.239	5.533 ± 0.239	5.535 ± 0.239	4.007 ± 0.231	4.015 ± 0.231	4.006 ± 0.231
30	8.523 ± 0.495	8.583 ± 0.496	8.520 ± 0.495	6.607 ± 0.444	6.644 ± 0.446	6.606 ± 0.445
31	2.745 ± 0.237	2.745 ± 0.237	2.743 ± 0.237	2.100 ± 0.216	2.100 ± 0.217	2.100 ± 0.216
32	3.457 ± 0.217	3.456 ± 0.217	3.456 ± 0.217	2.903 ± 0.198	2.912 ± 0.198	2.903 ± 0.198
33	4.075 ± 0.311	4.076 ± 0.311	4.076 ± 0.311	3.487 ± 0.283	3.502 ± 0.284	3.487 ± 0.283
34	4.846 ± 0.442	4.863 ± 0.442	4.851 ± 0.442	4.996 ± 0.401	5.026 ± 0.402	4.997 ± 0.401
35	8.802 ± 0.491	8.789 ± 0.491	8.801 ± 0.491	6.627 ± 0.441	6.557 ± 0.443	6.623 ± 0.441
36	19.652 ± 0.973	20.391 ± 0.992	19.651 ± 0.973	13.143 ± 0.793	12.991 ± 0.802	13.137 ± 0.794

$(z_1, z_2)$	$A_{12}^{UC}(\%)$			$A_0^{UC}(\%)$		
	$f(x)$	$f(x) + c \cos(2x)$	$f(x) + c \sin(2x)$	$f(x)$	$f(x) + c \cos(2x)$	$f(x) + c \sin(2x)$
1	0.620 ± 0.038	0.621 ± 0.038	0.620 ± 0.038	0.350 ± 0.038	0.349 ± 0.038	0.350 ± 0.038
2	0.743 ± 0.035	0.744 ± 0.035	0.743 ± 0.035	0.434 ± 0.035	0.434 ± 0.035	0.434 ± 0.035
3	0.765 ± 0.051	0.766 ± 0.051	0.765 ± 0.051	0.448 ± 0.050	0.447 ± 0.050	0.448 ± 0.050
4	0.846 ± 0.074	0.847 ± 0.074	0.846 ± 0.074	0.496 ± 0.072	0.495 ± 0.072	0.496 ± 0.072
5	1.064 ± 0.089	1.060 ± 0.089	1.064 ± 0.089	0.655 ± 0.086	0.655 ± 0.086	0.655 ± 0.086
6	1.169 ± 0.194	1.160 ± 0.194	1.169 ± 0.194	0.956 ± 0.176	0.958 ± 0.176	0.955 ± 0.176
7	0.741 ± 0.035	0.742 ± 0.035	0.741 ± 0.035	0.399 ± 0.035	0.399 ± 0.035	0.399 ± 0.035
8	0.837 ± 0.032	0.838 ± 0.032	0.837 ± 0.032	0.491 ± 0.032	0.492 ± 0.032	0.491 ± 0.032
9	0.929 ± 0.047	0.930 ± 0.047	0.929 ± 0.047	0.630 ± 0.046	0.629 ± 0.046	0.630 ± 0.046
10	1.019 ± 0.068	1.018 ± 0.068	1.019 ± 0.068	0.633 ± 0.066	0.634 ± 0.066	0.633 ± 0.066
11	1.261 ± 0.081	1.260 ± 0.081	1.261 ± 0.081	0.882 ± 0.079	0.884 ± 0.079	0.882 ± 0.079
12	1.434 ± 0.176	1.429 ± 0.176	1.434 ± 0.176	1.140 ± 0.159	1.145 ± 0.159	1.140 ± 0.159
13	0.758 ± 0.051	0.758 ± 0.051	0.758 ± 0.051	0.435 ± 0.050	0.436 ± 0.050	0.435 ± 0.050
14	0.881 ± 0.047	0.881 ± 0.047	0.881 ± 0.047	0.509 ± 0.046	0.509 ± 0.046	0.509 ± 0.046
15	1.027 ± 0.067	1.025 ± 0.067	1.027 ± 0.067	0.650 ± 0.066	0.650 ± 0.066	0.650 ± 0.066
16	0.923 ± 0.098	0.921 ± 0.098	0.923 ± 0.098	0.606 ± 0.096	0.607 ± 0.096	0.606 ± 0.096
17	1.283 ± 0.116	1.281 ± 0.116	1.283 ± 0.116	0.909 ± 0.112	0.910 ± 0.113	0.909 ± 0.112
18	1.480 ± 0.246	1.480 ± 0.246	1.480 ± 0.246	1.486 ± 0.222	1.486 ± 0.222	1.486 ± 0.222
19	0.841 ± 0.074	0.842 ± 0.074	0.841 ± 0.074	0.377 ± 0.073	0.379 ± 0.073	0.377 ± 0.073
20	0.959 ± 0.068	0.959 ± 0.068	0.959 ± 0.068	0.614 ± 0.066	0.615 ± 0.066	0.614 ± 0.066
21	0.946 ± 0.098	0.947 ± 0.098	0.946 ± 0.098	0.619 ± 0.096	0.619 ± 0.096	0.619 ± 0.096
22	1.017 ± 0.141	1.015 ± 0.141	1.017 ± 0.141	0.637 ± 0.138	0.638 ± 0.138	0.637 ± 0.138
23	1.353 ± 0.165	1.351 ± 0.165	1.353 ± 0.165	1.132 ± 0.160	1.133 ± 0.160	1.132 ± 0.160
24	1.689 ± 0.342	1.691 ± 0.342	1.689 ± 0.342	1.662 ± 0.308	1.661 ± 0.308	1.662 ± 0.308
25	1.035 ± 0.089	1.035 ± 0.089	1.035 ± 0.089	0.598 ± 0.087	0.598 ± 0.087	0.598 ± 0.087
26	1.186 ± 0.081	1.187 ± 0.081	1.186 ± 0.081	0.840 ± 0.079	0.840 ± 0.079	0.840 ± 0.079
27	1.297 ± 0.116	1.298 ± 0.116	1.297 ± 0.116	0.933 ± 0.112	0.933 ± 0.112	0.933 ± 0.112
28	1.551 ± 0.165	1.547 ± 0.165	1.551 ± 0.165	1.025 ± 0.160	1.026 ± 0.160	1.025 ± 0.160
29	2.115 ± 0.188	2.117 ± 0.188	2.115 ± 0.188	1.529 ± 0.181	1.529 ± 0.181	1.529 ± 0.181
30	2.973 ± 0.374	2.968 ± 0.374	2.973 ± 0.374	2.271 ± 0.334	2.274 ± 0.334	2.271 ± 0.334
31	1.160 ± 0.194	1.160 ± 0.194	1.160 ± 0.194	0.883 ± 0.176	0.882 ± 0.176	0.882 ± 0.176
32	1.410 ± 0.175	1.409 ± 0.175	1.410 ± 0.175	1.177 ± 0.159	1.179 ± 0.159	1.177 ± 0.159
33	1.571 ± 0.245	1.565 ± 0.245	1.571 ± 0.245	1.337 ± 0.222	1.339 ± 0.222	1.337 ± 0.222
34	1.789 ± 0.341	1.781 ± 0.341	1.789 ± 0.341	1.823 ± 0.308	1.826 ± 0.308	1.823 ± 0.308
35	3.072 ± 0.373	3.075 ± 0.373	3.072 ± 0.373	2.284 ± 0.334	2.278 ± 0.334	2.284 ± 0.334
36	5.801 ± 0.662	5.754 ± 0.663	5.801 ± 0.662	2.818 ± 0.488	2.820 ± 0.488	2.818 ± 0.488

Table 5.18: Asymmetry fit results for different fit function for the double ratio U/L (upper part) and U/C (lower part) in the two frames used in this analysis. The function  $f(x) = B_{\alpha}^{ij} + A_{\alpha}^{ij} \cdot \cos(\beta_{\alpha})$  is the function used to fit the Collins asymmetry. In particular, in this table is compared the the asymmetry parameter  $A_{\alpha}^{ij}$  obtained including additional cosine (third and sixth column) and sine (fourth and seventh column) modulation of twice the argument. No systematic uncertainty has been assumed.

$(p_{t1}, p_{t2})$	$A_{12}^{UL}(\%)$			$A_{12}^{UC}(\%)$		
	$f(x)$	$f(x) + c \cos(2x)$	$f(x) + c \sin(2x)$	$f(x)$	$f(x) + c \cos(2x)$	$f(x) + c \sin(2x)$
1	0.690 ± 0.053	0.690 ± 0.053	0.690 ± 0.053	0.690 ± 0.053	0.690 ± 0.053	0.690 ± 0.053
2	1.199 ± 0.038	1.199 ± 0.038	1.199 ± 0.038	1.199 ± 0.038	1.199 ± 0.038	1.199 ± 0.038
3	1.387 ± 0.059	1.388 ± 0.059	1.387 ± 0.059	1.387 ± 0.059	1.388 ± 0.059	1.387 ± 0.059
4	1.776 ± 0.115	1.776 ± 0.115	1.776 ± 0.115	1.776 ± 0.115	1.776 ± 0.115	1.776 ± 0.115
5	1.184 ± 0.038	1.184 ± 0.038	1.184 ± 0.038	1.184 ± 0.038	1.184 ± 0.038	1.184 ± 0.038
6	2.096 ± 0.029	2.097 ± 0.029	2.096 ± 0.029	2.096 ± 0.029	2.097 ± 0.029	2.096 ± 0.029
7	2.340 ± 0.046	2.342 ± 0.046	2.340 ± 0.046	2.340 ± 0.046	2.342 ± 0.046	2.340 ± 0.046
8	3.127 ± 0.093	3.128 ± 0.094	3.127 ± 0.093	3.127 ± 0.093	3.128 ± 0.094	3.127 ± 0.093
9	1.271 ± 0.059	1.271 ± 0.059	1.271 ± 0.059	1.271 ± 0.059	1.271 ± 0.059	1.271 ± 0.059
10	2.197 ± 0.046	2.199 ± 0.046	2.197 ± 0.046	2.197 ± 0.046	2.199 ± 0.046	2.197 ± 0.046
11	2.364 ± 0.076	2.353 ± 0.076	2.364 ± 0.076	2.364 ± 0.076	2.353 ± 0.076	2.364 ± 0.076
12	3.465 ± 0.159	3.446 ± 0.159	3.465 ± 0.159	3.465 ± 0.159	3.446 ± 0.159	3.465 ± 0.159
13	1.648 ± 0.115	1.650 ± 0.115	1.649 ± 0.115	1.648 ± 0.115	1.650 ± 0.115	1.649 ± 0.115
14	3.061 ± 0.094	3.058 ± 0.094	3.061 ± 0.094	3.061 ± 0.094	3.058 ± 0.094	3.061 ± 0.094
15	3.251 ± 0.159	3.237 ± 0.160	3.251 ± 0.159	3.251 ± 0.117	3.237 ± 0.154	3.251 ± 0.159
16	5.576 ± 0.337	5.553 ± 0.339	5.574 ± 0.337	5.576 ± 0.337	5.553 ± 0.339	5.574 ± 0.337

$p_{t0}$	$A_0^{UL}(\%)$			$A_0^{UC}(\%)$		
	$f(x)$	$f(x) + c \cos(2x)$	$f(x) + c \sin(2x)$	$f(x)$	$f(x) + c \cos(2x)$	$f(x) + c \sin(2x)$
1	0.241 ± 0.035	0.241 ± 0.035	0.241 ± 0.035	0.241 ± 0.035	0.241 ± 0.035	0.241 ± 0.035
2	1.019 ± 0.023	1.018 ± 0.023	1.019 ± 0.023	1.019 ± 0.023	1.018 ± 0.023	1.019 ± 0.023
3	1.642 ± 0.026	1.646 ± 0.026	1.642 ± 0.026	1.642 ± 0.026	1.646 ± 0.026	1.642 ± 0.026
4	2.293 ± 0.031	2.304 ± 0.031	2.293 ± 0.031	2.293 ± 0.031	2.304 ± 0.031	2.293 ± 0.031

Table 5.19: Asymmetry fit results for different fit function for the double ratio U/L (left columns) and U/C (right columns) in the two frames used in this analysis. The function  $f(x) = B_\alpha^{ij} + A_\alpha^{ij} \cdot \cos(\beta_\alpha)$  is the function used to fit the Collins asymmetry. In particular, in this table is compared the asymmetry parameter  $A_\alpha^{ij}$  obtained including additional cosine (third and sixth column) and sine (fourth and seventh column) modulation of twice the argument. No significant changes are observed and, therefore, no systematic uncertainty has been assumed.

$z_1$	$z_2$	$A_{12}^{UL}$ MC				$A_0^{UL}$ MC				$A_{12}^{UC}$ MC				$A_0^{UC}$ MC				
		PID	BIN	WEI	TOT	PID	BIN	WEI	TOT	PID	BIN	WEI	TOT	PID	BIN	WEI	TOT	
[0.15, 0.2]	[0.15, 0.2]	0.0007	0.0004	0.0014	0.0016	0.0001	0.0001	0.0008	0.0008	0.0003	0.0002	0.0001	0.0008	0.0000	0.0001	0.0004	0.0004	0.0004
[0.2, 0.3]	[0.2, 0.3]	0.0009	0.0005	0.0014	0.0017	0.0001	0.0001	0.0008	0.0008	0.0003	0.0002	0.0001	0.0008	0.0000	0.0001	0.0004	0.0000	0.0004
[0.15, 0.2]	[0.3, 0.4]	0.0010	0.0004	0.0019	0.0022	0.0000	0.0002	0.0020	0.0020	0.0004	0.0002	0.0001	0.0010	0.0000	0.0001	0.0009	0.0000	0.0009
[0.15, 0.2]	[0.4, 0.5]	0.0012	0.0005	0.0019	0.0023	0.0000	0.0003	0.0020	0.0020	0.0004	0.0002	0.0001	0.0010	0.0000	0.0001	0.0009	0.0000	0.0009
[0.15, 0.2]	[0.5, 0.7]	0.0007	0.0005	0.0034	0.0036	0.0001	0.0003	0.0019	0.0019	0.0002	0.0002	0.0001	0.0003	0.0000	0.0001	0.0008	0.0001	0.0008
[0.15, 0.2]	[0.7, 1]	0.0007	0.0005	0.0034	0.0036	0.0001	0.0003	0.0019	0.0019	0.0002	0.0002	0.0001	0.0003	0.0000	0.0001	0.0008	0.0001	0.0008
[0.2, 0.3]	[0.15, 0.2]	0.0008	0.0004	0.0014	0.0017	0.0001	0.0001	0.0008	0.0008	0.0003	0.0002	0.0001	0.0003	0.0000	0.0001	0.0004	0.0000	0.0004
[0.2, 0.3]	[0.2, 0.3]	0.0010	0.0005	0.0014	0.0018	0.0002	0.0002	0.0008	0.0008	0.0004	0.0002	0.0001	0.0008	0.0000	0.0001	0.0004	0.0000	0.0004
[0.2, 0.3]	[0.3, 0.4]	0.0014	0.0006	0.0019	0.0024	0.0000	0.0004	0.0020	0.0020	0.0005	0.0003	0.0001	0.0011	0.0000	0.0002	0.0009	0.0000	0.0009
[0.2, 0.3]	[0.4, 0.5]	0.0015	0.0006	0.0019	0.0025	0.0000	0.0004	0.0020	0.0020	0.0005	0.0003	0.0001	0.0011	0.0000	0.0002	0.0009	0.0000	0.0009
[0.2, 0.3]	[0.5, 0.7]	0.0008	0.0006	0.0034	0.0036	0.0001	0.0003	0.0019	0.0019	0.0002	0.0002	0.0001	0.0003	0.0000	0.0001	0.0008	0.0001	0.0008
[0.2, 0.3]	[0.7, 1]	0.0009	0.0007	0.0034	0.0037	0.0001	0.0004	0.0019	0.0019	0.0003	0.0003	0.0001	0.0004	0.0000	0.0001	0.0008	0.0001	0.0008
[0.3, 0.4]	[0.15, 0.2]	0.0011	0.0004	0.0014	0.0019	0.0001	0.0001	0.0008	0.0008	0.0005	0.0002	0.0001	0.0003	0.0000	0.0000	0.0009	0.0000	0.0009
[0.3, 0.4]	[0.2, 0.3]	0.0015	0.0005	0.0014	0.0021	0.0001	0.0001	0.0008	0.0008	0.0006	0.0002	0.0001	0.0009	0.0000	0.0001	0.0009	0.0000	0.0009
[0.3, 0.4]	[0.3, 0.4]	0.0015	0.0010	0.0019	0.0027	0.0004	0.0004	0.0036	0.0036	0.0005	0.0005	0.0002	0.0010	0.0003	0.0002	0.0016	0.0000	0.0016
[0.3, 0.4]	[0.4, 0.5]	0.0013	0.0009	0.0019	0.0025	0.0003	0.0004	0.0036	0.0036	0.0004	0.0004	0.0001	0.0010	0.0002	0.0001	0.0016	0.0000	0.0016
[0.3, 0.4]	[0.5, 0.7]	0.0020	0.0013	0.0058	0.0063	0.0008	0.0007	0.0054	0.0055	0.0007	0.0006	0.0004	0.0026	0.0002	0.0003	0.0023	0.0001	0.0023
[0.3, 0.4]	[0.7, 1]	0.0024	0.0015	0.0058	0.0066	0.0012	0.0011	0.0054	0.0056	0.0008	0.0006	0.0004	0.0026	0.0003	0.0004	0.0023	0.0001	0.0024
[0.4, 0.5]	[0.15, 0.2]	0.0013	0.0005	0.0014	0.0020	0.0001	0.0001	0.0008	0.0008	0.0005	0.0002	0.0001	0.0003	0.0000	0.0000	0.0009	0.0000	0.0009
[0.4, 0.5]	[0.2, 0.3]	0.0017	0.0006	0.0014	0.0023	0.0001	0.0001	0.0008	0.0008	0.0006	0.0003	0.0001	0.0009	0.0000	0.0001	0.0009	0.0000	0.0009
[0.4, 0.5]	[0.3, 0.4]	0.0014	0.0010	0.0019	0.0026	0.0004	0.0004	0.0036	0.0036	0.0004	0.0004	0.0001	0.0010	0.0002	0.0001	0.0016	0.0000	0.0016
[0.4, 0.5]	[0.4, 0.5]	0.0015	0.0011	0.0019	0.0027	0.0003	0.0004	0.0036	0.0036	0.0004	0.0004	0.0001	0.0010	0.0002	0.0001	0.0016	0.0000	0.0016
[0.4, 0.5]	[0.5, 0.7]	0.0022	0.0014	0.0058	0.0064	0.0009	0.0009	0.0054	0.0055	0.0008	0.0006	0.0004	0.0026	0.0003	0.0003	0.0023	0.0001	0.0023
[0.4, 0.5]	[0.7, 1]	0.0031	0.0019	0.0058	0.0070	0.0014	0.0013	0.0054	0.0056	0.0010	0.0007	0.0004	0.0027	0.0004	0.0005	0.0023	0.0001	0.0024
[0.5, 0.7]	[0.15, 0.2]	0.0013	0.0006	0.0035	0.0038	0.0002	0.0003	0.0018	0.0018	0.0005	0.0003	0.0001	0.0003	0.0000	0.0001	0.0008	0.0001	0.0008
[0.5, 0.7]	[0.2, 0.3]	0.0015	0.0008	0.0035	0.0040	0.0003	0.0004	0.0018	0.0018	0.0005	0.0003	0.0001	0.0003	0.0000	0.0001	0.0008	0.0001	0.0008
[0.5, 0.7]	[0.3, 0.4]	0.0012	0.0006	0.0035	0.0044	0.0002	0.0003	0.0018	0.0018	0.0004	0.0003	0.0001	0.0003	0.0000	0.0001	0.0008	0.0001	0.0008
[0.5, 0.7]	[0.4, 0.5]	0.0015	0.0008	0.0035	0.0046	0.0002	0.0003	0.0018	0.0018	0.0004	0.0003	0.0001	0.0003	0.0000	0.0001	0.0008	0.0001	0.0008
[0.5, 0.7]	[0.5, 0.7]	0.0025	0.0013	0.0078	0.0087	0.0008	0.0008	0.0047	0.0048	0.0004	0.0003	0.0001	0.0003	0.0000	0.0001	0.0008	0.0001	0.0008
[0.5, 0.7]	[0.7, 1]	0.0042	0.0022	0.0078	0.0102	0.0014	0.0016	0.0031	0.0031	0.0015	0.0009	0.0004	0.0034	0.0003	0.0003	0.0012	0.0002	0.0013
[0.7, 1]	[0.15, 0.2]	0.0014	0.0007	0.0035	0.0039	0.0003	0.0004	0.0018	0.0018	0.0005	0.0003	0.0001	0.0003	0.0000	0.0001	0.0008	0.0001	0.0008
[0.7, 1]	[0.2, 0.3]	0.0019	0.0009	0.0035	0.0042	0.0004	0.0006	0.0018	0.0018	0.0007	0.0004	0.0001	0.0003	0.0000	0.0001	0.0008	0.0001	0.0008
[0.7, 1]	[0.3, 0.4]	0.0015	0.0008	0.0035	0.0042	0.0002	0.0003	0.0018	0.0018	0.0004	0.0003	0.0001	0.0003	0.0000	0.0001	0.0008	0.0001	0.0008
[0.7, 1]	[0.4, 0.5]	0.0019	0.0010	0.0035	0.0044	0.0003	0.0003	0.0018	0.0018	0.0005	0.0004	0.0001	0.0003	0.0000	0.0001	0.0008	0.0001	0.0008
[0.7, 1]	[0.5, 0.7]	0.0044	0.0022	0.0078	0.0104	0.0014	0.0016	0.0031	0.0031	0.0015	0.0009	0.0004	0.0039	0.0005	0.0005	0.0012	0.0004	0.0014
[0.7, 1]	[0.7, 1]	0.0102	0.0052	0.0078	0.0178	0.0029	0.0032	0.0031	0.0032	0.0030	0.0018	0.0032	0.0057	0.0006	0.0007	0.0012	0.0005	0.0016

Table 5.20: Absolute contribution to the systematic error on the  $A_{\alpha}^{UL}$  and  $A_{\alpha}^{UC}$  results for the  $(z_1, z_2)$  bins (where  $\alpha = 12, 0$  indicates the reference frames). The different columns contain the systematic errors arising from uncertainties due to the particle identification (PID), different subdivision in the azimuthal angle (BIN), double ratio asymmetry from MC (MC), and uncertainties due to underestimation in re-weighted  $uds$  MC (WEI), as described in chapter 5. Finally, the results of the sum in quadrature of the systematic errors are shown in the last column (TOT).

$p_{t1}$		$p_{t2}$		$A_0^{UL}$		$A_0^{UL}$		$A_0^{UL}$		$A_0^{UL}$		$A_0^{UC}$		$A_0^{UC}$		$A_0^{UC}$		
				PID	BIN	MC	WEI	TOT	PID	BIN	MC	WEI	TOT	PID	BIN	MC	WEI	TOT
[0., 0.25]	[0., 0.25]	0.0007	0.0003	0.0005	0.0005	0.0005	0.0005	0.0010	0.0003	0.0001	0.0002	0.0002	0.0002	0.0004	0.0002	0.0001	0.0002	0.0004
[0., 0.25]	[0.25, 0.5]	0.0005	0.0002	0.0004	0.0003	0.0003	0.0003	0.0008	0.0002	0.0001	0.0002	0.0001	0.0003	0.0003	0.0001	0.0002	0.0001	0.0003
[0., 0.25]	[0.5, 0.75]	0.0004	0.0006	0.0009	0.0005	0.0005	0.0005	0.0013	0.0001	0.0003	0.0004	0.0004	0.0002	0.0004	0.0002	0.0002	0.0002	0.0005
[0., 0.25]	[> 0.75]	0.0002	0.0014	0.0012	0.0012	0.0012	0.0016	0.0025	0.0001	0.0006	0.0006	0.0007	0.0007	0.0011	0.0007	0.0007	0.0011	0.0011
[0.25, 0.5]	[0., 0.25]	0.0017	0.0006	0.0005	0.0005	0.0005	0.0005	0.0019	0.0007	0.0003	0.0002	0.0002	0.0002	0.0008	0.0001	0.0010	0.0001	0.0010
[0.25, 0.5]	[0.25, 0.5]	0.0006	0.0008	0.0007	0.0007	0.0007	0.0003	0.0012	0.0002	0.0004	0.0003	0.0003	0.0001	0.0005	0.0001	0.0010	0.0001	0.0005
[0.25, 0.5]	[0.5, 0.75]	0.0007	0.0005	0.0022	0.0022	0.0022	0.0003	0.0024	0.0002	0.0002	0.0009	0.0001	0.0010	0.0010	0.0001	0.0010	0.0001	0.0010
[0.25, 0.5]	[> 0.75]	0.0009	0.0013	0.0041	0.0008	0.0041	0.0003	0.0044	0.0001	0.0006	0.0019	0.0004	0.0020	0.0020	0.0001	0.0002	0.0006	0.0020
[0.5, 0.75]	[0., 0.25]	0.0012	0.0006	0.0007	0.0005	0.0007	0.0005	0.0016	0.0005	0.0003	0.0003	0.0003	0.0002	0.0006	0.0001	0.0002	0.0002	0.0006
[0.5, 0.75]	[0.25, 0.5]	0.0009	0.0007	0.0015	0.0003	0.0015	0.0003	0.0019	0.0003	0.0003	0.0007	0.0001	0.0008	0.0008	0.0001	0.0002	0.0001	0.0008
[0.5, 0.75]	[0.5, 0.75]	0.0008	0.0007	0.0042	0.0005	0.0042	0.0005	0.0044	0.0006	0.0003	0.0019	0.0002	0.0020	0.0020	0.0001	0.0002	0.0001	0.0020
[0.5, 0.75]	[> 0.75]	0.0026	0.0011	0.0075	0.0010	0.0075	0.0081	0.0081	0.0015	0.0005	0.0034	0.0012	0.0038	0.0038	0.0001	0.0002	0.0001	0.0038
[> 0.75]	[0., 0.25]	0.0006	0.0007	0.0027	0.0014	0.0027	0.0014	0.0032	0.0001	0.0003	0.0012	0.0006	0.0014	0.0014	0.0001	0.0002	0.0001	0.0014
[> 0.75]	[0.25, 0.5]	0.0005	0.0006	0.0023	0.0008	0.0023	0.0008	0.0026	0.0000	0.0003	0.0010	0.0003	0.0011	0.0011	0.0001	0.0003	0.0001	0.0011
[> 0.75]	[0.5, 0.75]	0.0006	0.0002	0.0079	0.0012	0.0079	0.0012	0.0080	0.0006	0.0001	0.0035	0.0004	0.0036	0.0036	0.0001	0.0002	0.0001	0.0036
[> 0.75]	[> 0.75]	0.0003	0.0002	0.0147	0.0019	0.0147	0.0019	0.0148	0.0007	0.0000	0.0064	0.0009	0.0065	0.0065	0.0001	0.0002	0.0001	0.0065

Table 5.21: Absolute contribution to the systematic error on the  $A_{\alpha}^{UL}$  and  $A_{\alpha}^{UC}$  results for the ( $p_{t1}$ ,  $p_{t2}$ ) bins, in the RF12 frame. The different columns contain the systematic errors arising from uncertainties due to the particle identification (PID), different subdivision in the azimuthal angle (BIN), double ratio asymmetry from MC (MC), and uncertainties due to underestimation in re-weighted  $uds$  MC (WEI), as described in chapter 5. Finally, the results of the sum in quadrature of the systematic errors are shown in the last column (TOT).

$p_{t0}$	$A_0^{UL}$				$A_0^{UC}$					
	PID	BIN	MC	WEI	TOT	PID	BIN	MC	WEI	TOT
[0., 0.25]	0.0000	0.0000	0.0001	0.0000	0.0001	0.0000	0.0000	0.0002	0.0000	0.0002
[0.25, 0.5]	0.0000	0.0002	0.0007	0.0001	0.0007	0.0000	0.0001	0.0003	0.0000	0.0003
[0.5, 0.75]	0.0002	0.0003	0.0034	0.0001	0.0034	0.0000	0.0001	0.0016	0.0000	0.0016
[> 0.75]	0.0001	0.0005	0.0070	0.0001	0.0070	0.0000	0.0002	0.0032	0.0000	0.0032

Table 5.22: Absolute contribution to the systematic error on the  $A_{\alpha}^{UL}$  and  $A_{\alpha}^{UC}$  results for the 4  $p_{t0}$  bins, in the RF0 frame. The different columns contain the systematic errors arising from uncertainties due to the particle identification (PID), different subdivision in the azimuthal angle (BIN), double ratio asymmetry from MC (MC), and uncertainties due to underestimation in re-weighted  $uds$  MC (WEI), as described in chapter 5. Finally, the results of the sum in quadrature of the systematic errors are shown in the last column (TOT).

# Chapter 6

## Results

### 6.1 Collins asymmetries $vs (z_1, z_2), (p_{t1}, p_{t2}),$ and $p_{t0}$ bins

The measurement of Collins asymmetries is obtained using the full *BABAR* data sample, which corresponds to an integrated luminosity  $\mathcal{L} = 468 \text{ fb}^{-1}$ , and it is performed in two different frames: the thrust reference frame (RF12), and the second hadron momentum frame (RF0). We measure the asymmetry taking the double ratio of raw distributions (U/L and U/C) as a function of the two pions fraction energies  $z$ , and transverse momentum  $p_t$ , following the bin subdivisions described in section 4.5.

Systematic effects which can influence the measurement of the asymmetry are discussed in chapter 5. These effects are, whenever possible, evaluated independently for each bin of fractional energy and pion transverse momentum.

In particular, we correct the asymmetries for a small bias observed when testing the procedure on simulated events. We then estimate the background contributions from  $c\bar{c}$ ,  $B\bar{B}$ , and  $\tau^+\tau^-$  event, and correct the measured asymmetry as described in section 5.2.

Because of the dilution due to the approximation of the  $q\bar{q}$  axis with the thrust axis, discussed in Sec. 5.3, we rescale the asymmetries measured in the RF12 frame by the factors obtained weighting the  $uds$  MC sample. No correction factors are needed for the asymmetries in RF0.

Tables 5.20-5.22 summarize all the sizable systematic effects as a function of  $z$  and  $p_t$  bins, evaluated for each frame and for each double ratio. All systematic uncertainties are added in quadrature.

The Collins asymmetries as a function of  $(z_1, z_2)$  bins, corrected for the background contributions summarized above, and including all systematic effects, are shown in Fig. 6.1 (for each plot  $z_1$  is fixed and  $z_2$  runs between 0.15 and 1, following the binning described in section 4.5). The up blue triangles refer to the U/L ratio, while the down green triangles to the U/C ratio. The blue and green dotted bands indicate the corresponding systematic errors. These results are summarized in Tab. 6.1 and 6.2, where we also report the mean values of  $z_1, z_2,$

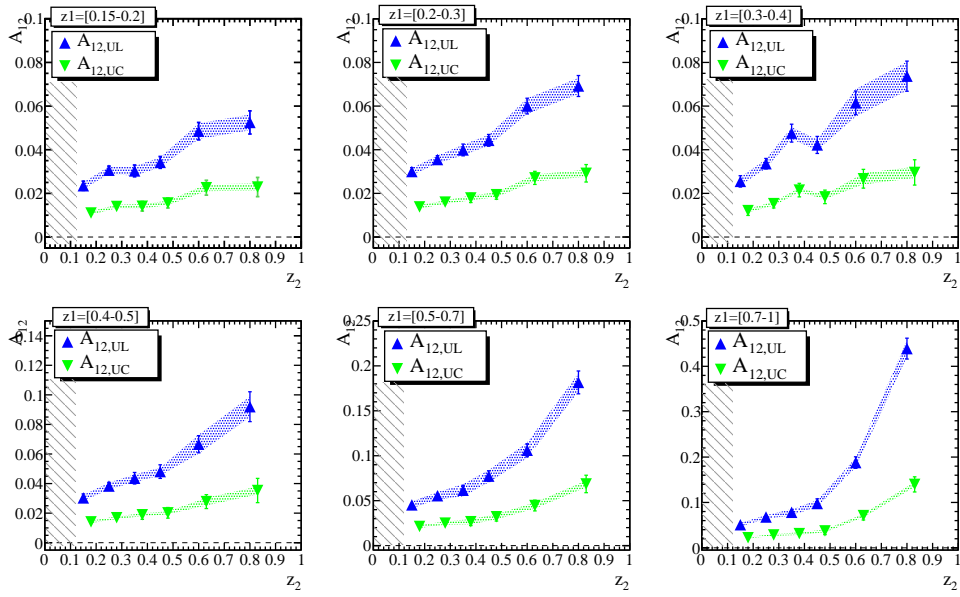
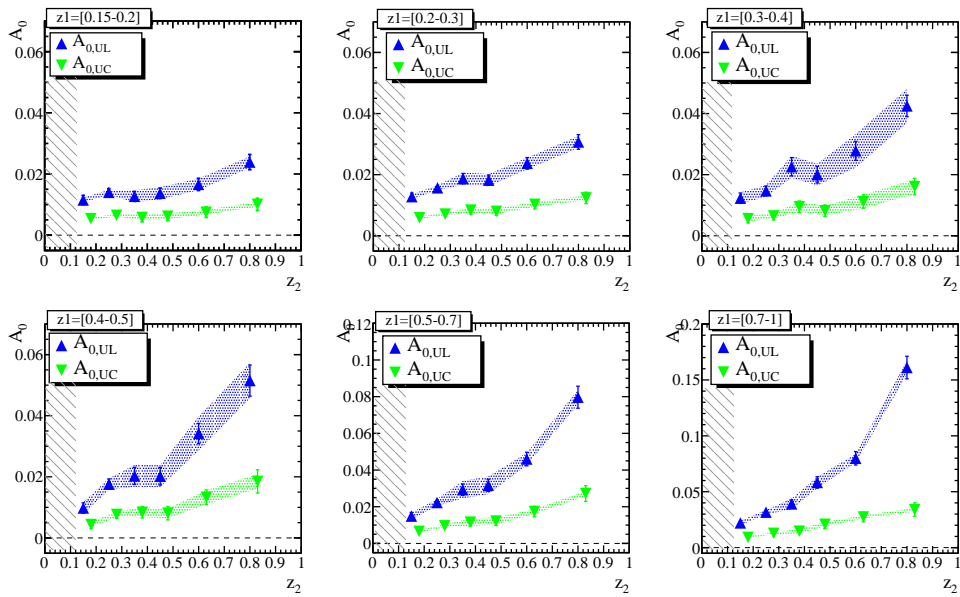
(a) RF12: Collins asymmetries  $vs (z_1, z_2)$ -bins(b) RF0: Collins asymmetries  $vs (z_1, z_2)$ -bins

Figure 6.1: Collins asymmetries for light quarks as a function of  $z_2$  for 6  $z_1$  bins. The UL data are represented by upper blue triangles and the systematic errors by the dotted blue band superimposed under the points. The UC data are described by the down green triangles, and their systematic uncertainties by the dotted green line. The upper plots (a) refer to the RF12 frame, while (b) to the RF0 frame.

$\frac{\sin^2 \theta_{th}}{1+\cos^2 \theta_{th}}$ , and  $\frac{\sin^2 \theta_2}{1+\cos^2 \theta_2}$ , that are needed in the global analysis fits in order to extract the Collins fragmentation function and transversity [16, 17].

We can clearly see the rising of the asymmetry in each plot as a function of the fractional energy, in agreement with theoretical predictions [35, 36, 110] and results from the Belle experiment [14, 15]. The UC asymmetries are significantly smaller than the UL asymmetries. Looking at Eqs. (4.18) and (4.19), one can observe that the U/C ratio introduces different combinations of favored and disfavored fragmentation functions. In particular, the smaller but not negligible value of the UC asymmetry suggests a large disfavored Collins fragmentation function with opposite sign of the favored one [96].

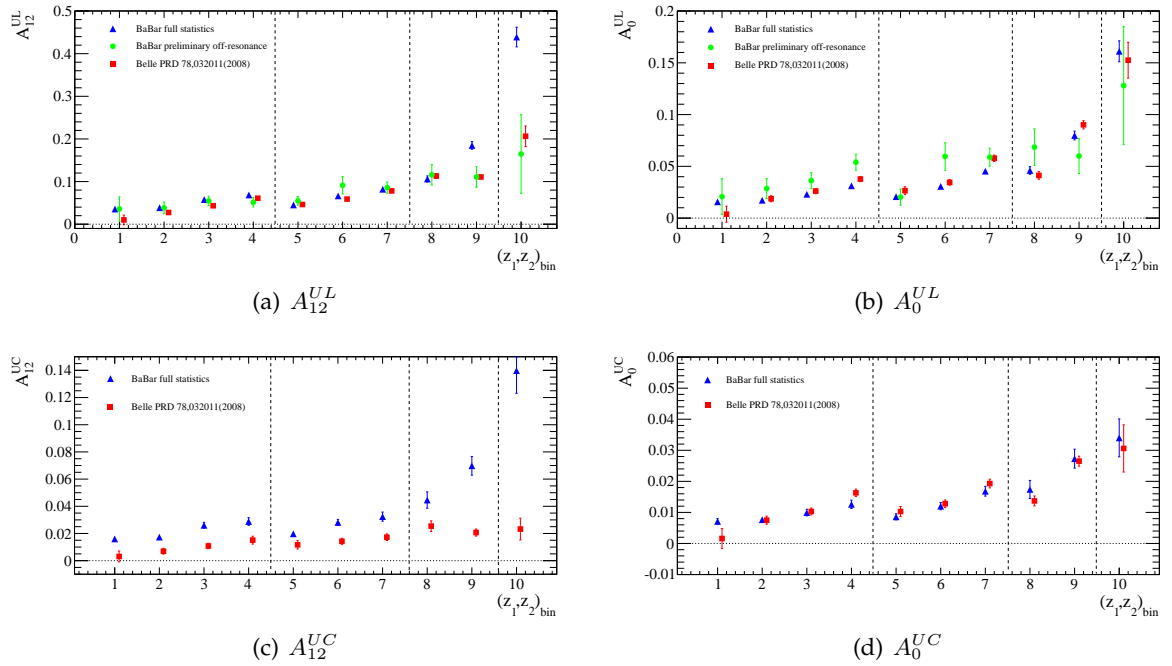


Figure 6.2: Comparison between our results (blue triangles) obtained using the full *BABAR* statistics, the *BABAR* preliminary off-resonance data (green circles, only for the UL double ratio), and the Belle results (red squares). In order to make the comparison, we averaged the results shown in Tab. 6.1 and 6.2 falling in symmetric  $(z_1, z_2)$  bins, as defined in the text. The same procedure is applied to the published Belle data [15]. The first four points are obtained by setting  $0.2 < z_1 < 0.3$  and ranging  $z_2$  between 0.2-1; the next three points by setting  $0.3 < z_1 < 0.5$  and ranging  $z_2$  between 0.3-1; the next two points by setting  $0.5 < z_1 < 0.7$  and ranging  $z_2$  between 0.5-1; the last point is the bin with  $0.7 < z_1, z_2 < 1$ . All bins are summarized in the text.

Figures 6.2(a) and 6.2(b) show the asymmetry results obtained in this analysis (blue triangles), the preliminary *BABAR* off-resonance data (green circles), and the Belle results [15] (red squares), for the RF12 and RF0 frame, respectively. For this comparison we used the same  $z$ -bin subdivisions as for the preliminary study, which consists of 10 symmetric bins of pion

fractional energy defined as follow:

1.  $z_1 = [0.2 - 0.3]$   $z_2 = [0.2 - 0.3]$ ,
2.  $z_1 = [0.2 - 0.3]$   $z_2 = [0.3 - 0.5]$  and  $z_1 = [0.3 - 0.5]$   $z_2 = [0.2 - 0.3]$ ,
3.  $z_1 = [0.2 - 0.3]$   $z_2 = [0.5 - 0.7]$  and  $z_1 = [0.5 - 0.7]$   $z_2 = [0.2 - 0.3]$ ,
4.  $z_1 = [0.2 - 0.3]$   $z_2 = [0.7 - 1]$  and  $z_1 = [0.7 - 0.1]$   $z_2 = [0.2 - 0.3]$ ,
5.  $z_1 = [0.3 - 0.5]$   $z_2 = [0.3 - 0.5]$ ,
6.  $z_1 = [0.3 - 0.5]$   $z_2 = [0.5 - 0.7]$  and  $z_1 = [0.5 - 0.7]$   $z_2 = [0.3 - 0.5]$ ,
7.  $z_1 = [0.3 - 0.5]$   $z_2 = [0.7 - 1]$  and  $z_1 = [0.7 - 1]$   $z_2 = [0.3 - 0.5]$ ,
8.  $z_1 = [0.5 - 0.7]$   $z_2 = [0.5 - 0.7]$ ,
9.  $z_1 = [0.5 - 0.7]$   $z_2 = [0.7 - 1]$  and  $z_1 = [0.7 - 1]$   $z_2 = [0.5 - 0.7]$ ,
10.  $z_1 = [0.7 - 1]$   $z_2 = [0.7 - 1]$ ,

and we take the average of the results which fall in the same symmetrized  $(z_1, z_2)$  bin (note that the lower bin ( $z < 0.2$ ) is excluded). We note that the  $A^{UL}$  asymmetries measured in the RF0 frame are in reasonable agreement each other (Fig. 6.2(b)), while a large difference is observed in the thrust reference frame for the last two bins of fractional energy (Fig. 6.2(a)). Part of this

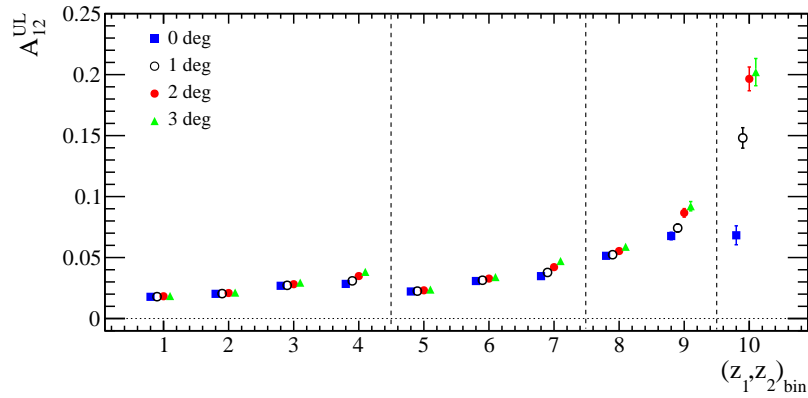


Figure 6.3:  $A^{UL}$  asymmetry in the RF12 frame calculated for different cuts on the opening angle between the pion momentum and the thrust axis: no cut (blue squares), 1 degree (open black circles), 2 degree (full red circles, which corresponds to the cut used in this analysis), and 3 degree (green triangles). The asymmetry is significantly diluted in the last two  $z$ -bins (higher values of fractional energy), since the momenta of both pions are very close to the thrust axis, and the uncertainties in the azimuthal angles become large.

discrepancy, up to 20%, is due to the correction factors which are estimated bin-by-bin (see

Fig. 5.19 and Tab. 5.14), instead of using the mean value as done in the *BABAR* preliminary and Belle results. However, the largest effect is due to the additional cut that removes those pions with an opening angle smaller than  $2^\circ$  around the thrust axis, not applied in the analysis for the preliminary results. The determination of the azimuthal angles for tracks very close to the thrust axis is affected by large uncertainties, with the effect that the azimuthal asymmetry in this kinematic conditions is strongly diluted. The fraction of tracks very close to the thrust axis is very small, but, by definition of the thrust axis, they are also the most energetic tracks in the event, and this explains why this effect is visible only in the bins with the highest  $z$  values, while the  $z$ -integrated asymmetries are almost unaffected. The dilution effect is clearly visible in Fig. 6.3, where the measured  $A_{12}^{UL}$  asymmetries, not corrected for the background contributions, is reported for different cuts on the opening angle between the thrust axis and the pion momenta. The red circles correspond to the asymmetries measured requiring a minimum opening angle of  $2^\circ$ , chosen for this analysis, and can be compared with the blue squares, for which the cut is not applied. It is clearly visible the dilution of the asymmetries for high  $z$  values, the last two bins, while for an opening angle of  $3^\circ$  the measured asymmetry seems to have stabilized. The same effect does not influence the  $p_t$  distributions since the dependence on  $z$  is integrated over.

Figures 6.2(c) and 6.2(d) compare our results for the UC double ratio (blue triangles) with the Belle asymmetry (red squares) as a function of the symmetric  $z$ -bins previously described. Also in this case the results in the RF0 frame are in good agreement, while our data is systematically above Belle data in the RF12 frame. The largest discrepancies for high fractional energy can be explained as above, while the deviation observed at smaller  $z$  has not yet been understood.

The asymmetries as a function of  $(p_{t1}, p_{t2})$ -bins (a) and  $p_{t0}$  (b) are shown Fig. 6.4. The UL results are represented by the upper blue triangles, and the UC by the down green one. Systematic errors are shown by the dotted blue and green bands superimposed to the respective points.

This is the first measurement ever of the Collins asymmetry dependence on the pion transverse momenta in  $e^+e^-$  annihilation. Data show a rising of the asymmetry as a function of  $p_t$ , with the UC asymmetry parameters smaller than UL, confirming an opposite sign of the favored and disfavored fragmentation functions. This new result is particularly important from a theoretical point of view since it allows to understand the behavior of the Collins fragmentation function, and its evolution.

## 6.2 Collins asymmetries vs polar angle $\sin^2 \theta / (1 + \cos^2 \theta)$

The transverse quark polarization of the original  $q\bar{q}$  pair created in  $e^+e^-$  annihilation, should lead to a  $\sin^2 \theta / (1 + \cos^2 \theta)$  dependence of the Collins asymmetry.

Experimentally, we cannot access the polar angle emission of the  $q\bar{q}$ , but a similar dependence

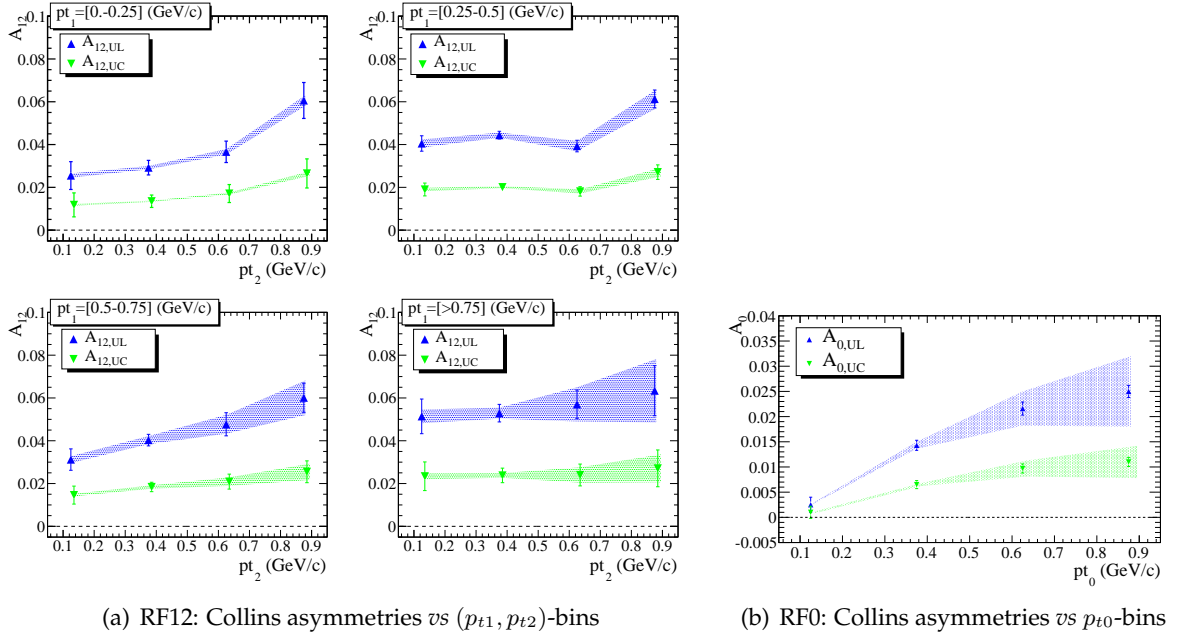


Figure 6.4: Light quark ( $uds$ ) Collins asymmetries as a function of  $p_{t2}$  for 4  $p_{t1}$  bins (a), and as a function of 4  $p_{t0}$  bins (b). The UL data are represented by upper blue triangles and the systematic errors by the dotted blue band superimposed under the points. The UC data are described by the down green triangles, and their systematic uncertainties by the dotted green line.

is obtained assuming as  $\theta$  respectively the polar angle of the thrust axis ( $\theta_{th}$ ), and the polar angle of the reference hadron ( $\theta_2$ ) in the two reference frames:

$$\begin{aligned} \frac{R_{12}^U}{R_{12}^L} &\propto 1 + \frac{\sin^2 \theta_{th}}{1 + \cos^2 \theta_{th}} \cos(\phi_1 + \phi_2) \{G^U - G^L\} \\ \frac{R_0^U}{R_0^L} &\propto 1 + \frac{\sin^2 \theta_2}{1 + \cos^2 \theta_2} \cos(2\phi_0) \{G^U - G^L\} \end{aligned} \quad (6.1)$$

where  $G^U$  and  $G^L$  are described in the Eq. (4.17). The same dependence is true for the UC double ratio, with the only difference that  $G^C$  contains different combinations of favored and disfavored fragmentation functions, as shown in Eq. (4.19). The behavior of the asymmetries  $A_{12}$  and  $A_0$  as a function of  $\sin^2 \theta / (1 + \cos^2 \theta)$ , with the proper polar angle, are shown in Fig. 6.5. For each bins, we corrected the asymmetries for the background contributions of  $c\bar{c}$ ,  $B\bar{B}$ , and  $\tau^+\tau^-$  events following the same procedure described in section 5.2. The  $A_{12}$  asymmetries are not rescaled by the correction factor  $\zeta_{12}$ , since we found that it is the same for all bins ( $\zeta_{12} = 1.559 \pm 0.003$ ), and thus changes only the slope of the distributions, but not the intercept with the vertical axis. As systematic uncertainties we assigned the average values of the significant contributions studied in Chapter 5, added in quadrature in Fig. 6.5 (dotted blue and green error bands).

The dotted lines in Fig. 6.5(a), which represent the results of linear fit to the two sets of point of RF12, approximatively intersect the origin consistently with the expectations. On the contrary, the fits clearly favor a non zero constant terms for  $A_0^{UL}$  and  $A_0^{UC}$  (Fig. 6.5(b)). This behavior is not completely unexpected given that  $\theta_2$  is much less correlated to the original  $q\bar{q}$  direction with respect to the thrust axis, which is in some way an average of the momenta of the fragmenting products.

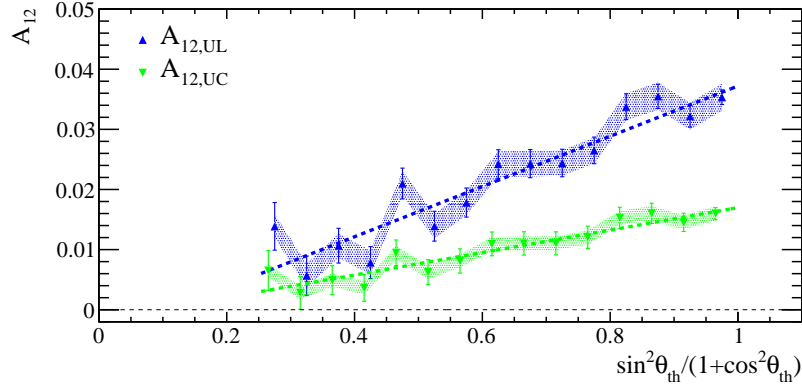
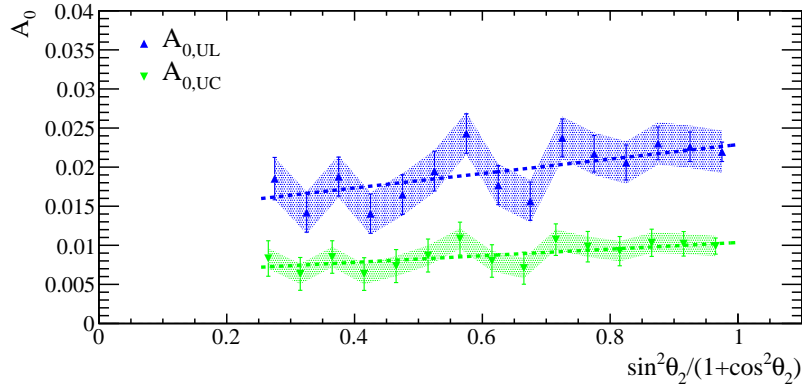
(a) RF12: Collins asymmetries vs  $\sin^2 \theta_{th} / (1 + \cos^2 \theta_{th})$ (b) RF0: Collins asymmetries vs  $\sin^2 \theta_2 / (1 + \cos^2 \theta_2)$ 

Figure 6.5: Light quark asymmetry parameters calculated in the RF12 frame (a) and in the RF0 frame (b), as a function of  $\sin^2 \theta / (1 + \cos^2 \theta)$ , where  $\theta \equiv \theta_{th}$  in plot (a) and  $\theta \equiv \theta_2$  in plot (b). The upper blue triangles refer to the UL asymmetry, while the down green triangles to the UC asymmetry. Systematic contributions are showed by dotted blue and green bars, respectively. The linear fits ( $p_0 + p_1 \cdot x$ ) is also displayed by a dashed lines for each double ratio, following the same color legend as described before. The fit results are:  $A_{12,UL} \rightarrow p_0 = (-0.005 \pm 0.002)$  and  $p_1 = (0.043 \pm 0.003)$ ;  $A_{12,UC} \rightarrow p_0 = (-0.002 \pm 0.002)$  and  $p_1 = (0.019 \pm 0.002)$ ;  $A_{0,UL} \rightarrow p_0 = (0.014 \pm 0.002)$  and  $p_1 = (0.009 \pm 0.003)$ ;  $A_{0,UC} \rightarrow p_0 = (0.006 \pm 0.001)$  and  $p_1 = (0.004 \pm 0.002)$ .

$z_1$	$\langle z_1 \rangle$	$z_2$	$\langle z_2 \rangle$	$\frac{\sin^2 \theta_{th}}{1+\cos^2 \theta_{th}}$	$\frac{\sin^2 \theta_2}{1+\cos^2 \theta_2}$	$A_{12}^{UL}$	$A_0^{UL}$
[0.15, 0.2]	0.174	[0.15, 0.2]	0.174	0.716	0.687	$0.0235 \pm 0.0021 \pm 0.0016$	$0.0115 \pm 0.0015 \pm 0.0008$
[0.15, 0.2]	0.174	[0.2, 0.3]	0.244	0.715	0.683	$0.0306 \pm 0.0019 \pm 0.0017$	$0.0140 \pm 0.0012 \pm 0.0008$
[0.15, 0.2]	0.174	[0.3, 0.4]	0.344	0.711	0.676	$0.0303 \pm 0.0027 \pm 0.0022$	$0.0127 \pm 0.0016 \pm 0.0020$
[0.15, 0.2]	0.174	[0.4, 0.5]	0.443	0.706	0.670	$0.0342 \pm 0.0027 \pm 0.0023$	$0.0137 \pm 0.0017 \pm 0.0020$
[0.15, 0.2]	0.174	[0.5, 0.7]	0.576	0.698	0.662	$0.0485 \pm 0.0040 \pm 0.0036$	$0.0166 \pm 0.0020 \pm 0.0019$
[0.15, 0.2]	0.174	[0.7, 1]	0.772	0.679	0.646	$0.0525 \pm 0.0053 \pm 0.0036$	$0.0239 \pm 0.0025 \pm 0.0019$
[0.2, 0.3]	0.244	[0.15, 0.2]	0.174	0.715	0.685	$0.0300 \pm 0.0018 \pm 0.0017$	$0.0128 \pm 0.0012 \pm 0.0008$
[0.2, 0.3]	0.244	[0.2, 0.3]	0.244	0.714	0.682	$0.0355 \pm 0.0018 \pm 0.0018$	$0.0157 \pm 0.0011 \pm 0.0008$
[0.2, 0.3]	0.244	[0.3, 0.4]	0.344	0.710	0.676	$0.0399 \pm 0.0027 \pm 0.0024$	$0.0187 \pm 0.0017 \pm 0.0020$
[0.2, 0.3]	0.244	[0.4, 0.5]	0.444	0.706	0.671	$0.0443 \pm 0.0027 \pm 0.0025$	$0.0182 \pm 0.0017 \pm 0.0020$
[0.2, 0.3]	0.244	[0.5, 0.7]	0.576	0.698	0.664	$0.0600 \pm 0.0036 \pm 0.0036$	$0.0237 \pm 0.0019 \pm 0.0019$
[0.2, 0.3]	0.244	[0.7, 1]	0.773	0.681	0.650	$0.0692 \pm 0.0048 \pm 0.0037$	$0.0307 \pm 0.0024 \pm 0.0020$
[0.3, 0.4]	0.344	[0.15, 0.2]	0.174	0.711	0.682	$0.0255 \pm 0.0026 \pm 0.0019$	$0.0123 \pm 0.0017 \pm 0.0019$
[0.3, 0.4]	0.344	[0.2, 0.3]	0.244	0.710	0.680	$0.0336 \pm 0.0024 \pm 0.0021$	$0.0147 \pm 0.0016 \pm 0.0019$
[0.3, 0.4]	0.344	[0.3, 0.4]	0.344	0.706	0.674	$0.0476 \pm 0.0041 \pm 0.0027$	$0.0226 \pm 0.0030 \pm 0.0036$
[0.3, 0.4]	0.344	[0.4, 0.5]	0.444	0.703	0.670	$0.0422 \pm 0.0039 \pm 0.0025$	$0.0200 \pm 0.0027 \pm 0.0036$
[0.3, 0.4]	0.344	[0.5, 0.7]	0.577	0.696	0.664	$0.0615 \pm 0.0054 \pm 0.0063$	$0.0278 \pm 0.0031 \pm 0.0055$
[0.3, 0.4]	0.344	[0.7, 1]	0.774	0.681	0.653	$0.0737 \pm 0.0069 \pm 0.0066$	$0.0425 \pm 0.0035 \pm 0.0056$
[0.4, 0.5]	0.443	[0.15, 0.2]	0.174	0.706	0.680	$0.0303 \pm 0.0027 \pm 0.0020$	$0.0098 \pm 0.0017 \pm 0.0019$
[0.4, 0.5]	0.444	[0.2, 0.3]	0.244	0.706	0.678	$0.0383 \pm 0.0025 \pm 0.0023$	$0.0176 \pm 0.0017 \pm 0.0019$
[0.4, 0.5]	0.444	[0.3, 0.4]	0.344	0.703	0.673	$0.0436 \pm 0.0039 \pm 0.0026$	$0.0203 \pm 0.0028 \pm 0.0036$
[0.4, 0.5]	0.444	[0.4, 0.5]	0.444	0.699	0.669	$0.0481 \pm 0.0046 \pm 0.0027$	$0.0202 \pm 0.0029 \pm 0.0036$
[0.4, 0.5]	0.444	[0.5, 0.7]	0.577	0.693	0.664	$0.0666 \pm 0.0058 \pm 0.0064$	$0.0342 \pm 0.0033 \pm 0.0056$
[0.4, 0.5]	0.445	[0.7, 1]	0.776	0.679	0.653	$0.0920 \pm 0.0101 \pm 0.0070$	$0.0515 \pm 0.0051 \pm 0.0058$
[0.5, 0.7]	0.576	[0.15, 0.2]	0.174	0.698	0.677	$0.0453 \pm 0.0039 \pm 0.0038$	$0.0149 \pm 0.0020 \pm 0.0018$
[0.5, 0.7]	0.577	[0.2, 0.3]	0.244	0.698	0.676	$0.0555 \pm 0.0036 \pm 0.0040$	$0.0223 \pm 0.0019 \pm 0.0019$
[0.5, 0.7]	0.577	[0.3, 0.4]	0.344	0.696	0.671	$0.0616 \pm 0.0055 \pm 0.0068$	$0.0293 \pm 0.0031 \pm 0.0048$
[0.5, 0.7]	0.577	[0.4, 0.5]	0.444	0.693	0.668	$0.0773 \pm 0.0059 \pm 0.0069$	$0.0317 \pm 0.0033 \pm 0.0048$
[0.5, 0.7]	0.578	[0.5, 0.7]	0.578	0.688	0.662	$0.1061 \pm 0.0072 \pm 0.0087$	$0.0460 \pm 0.0037 \pm 0.0034$
[0.5, 0.7]	0.580	[0.7, 1]	0.779	0.674	0.652	$0.1816 \pm 0.0127 \pm 0.0102$	$0.0797 \pm 0.0060 \pm 0.0040$
[0.7, 1]	0.772	[0.15, 0.2]	0.174	0.679	0.672	$0.0509 \pm 0.0051 \pm 0.0039$	$0.0221 \pm 0.0025 \pm 0.0019$
[0.7, 1]	0.773	[0.2, 0.3]	0.244	0.682	0.672	$0.0679 \pm 0.0048 \pm 0.0042$	$0.0317 \pm 0.0023 \pm 0.0020$
[0.7, 1]	0.775	[0.3, 0.4]	0.344	0.682	0.668	$0.0783 \pm 0.0070 \pm 0.0069$	$0.0391 \pm 0.0035 \pm 0.0048$
[0.7, 1]	0.777	[0.4, 0.5]	0.444	0.679	0.665	$0.0977 \pm 0.0103 \pm 0.0071$	$0.0583 \pm 0.0051 \pm 0.0050$
[0.7, 1]	0.779	[0.5, 0.7]	0.580	0.674	0.660	$0.1879 \pm 0.0127 \pm 0.0104$	$0.0799 \pm 0.0060 \pm 0.0040$
[0.7, 1]	0.788	[0.7, 1]	0.787	0.661	0.649	$0.4390 \pm 0.0230 \pm 0.0178$	$0.1611 \pm 0.0101 \pm 0.0060$

Table 6.1: Light quark ( $uds$ ) Collins asymmetries obtained fitting the UL double ratio as a function of  $(z_1, z_2)$ . In the first two columns, are reported the  $z$  bins and the respective mean value for the pions in one hemisphere; in the following two columns, are shown the same variables for the second pion; in the middle columns are summarized the mean value of  $\sin^2 \theta / (1 + \cos^2 \theta)$  calculated in the RF12 and RF0 frames, respectively; finally, in the last two columns are summarized the asymmetry results. The errors shown are statistical and systematic.

$z_1$	$\langle z_1 \rangle$	$z_2$	$\langle z_2 \rangle$	$\frac{\sin^2 \theta_{th}}{1 + \cos^2 \theta_{th}}$	$\frac{\sin^2 \theta_2}{1 + \cos^2 \theta_2}$	$A_{12}^{UC}$	$A_0^{UC}$
[0.15, 0.2]	0.174	[0.15, 0.2]	0.174	0.716	0.687	$0.0110 \pm 0.0016 \pm 0.0008$	$0.0054 \pm 0.0011 \pm 0.0004$
[0.15, 0.2]	0.174	[0.2, 0.3]	0.244	0.715	0.683	$0.0140 \pm 0.0015 \pm 0.0008$	$0.0065 \pm 0.0010 \pm 0.0004$
[0.15, 0.2]	0.174	[0.3, 0.4]	0.344	0.711	0.676	$0.0141 \pm 0.0022 \pm 0.0010$	$0.0058 \pm 0.0014 \pm 0.0009$
[0.15, 0.2]	0.174	[0.4, 0.5]	0.443	0.706	0.670	$0.0156 \pm 0.0023 \pm 0.0010$	$0.0062 \pm 0.0014 \pm 0.0009$
[0.15, 0.2]	0.174	[0.5, 0.7]	0.576	0.698	0.662	$0.0226 \pm 0.0034 \pm 0.0016$	$0.0075 \pm 0.0017 \pm 0.0008$
[0.15, 0.2]	0.174	[0.7, 1]	0.772	0.679	0.646	$0.0229 \pm 0.0044 \pm 0.0016$	$0.0101 \pm 0.0020 \pm 0.0008$
[0.2, 0.3]	0.244	[0.15, 0.2]	0.174	0.715	0.685	$0.0138 \pm 0.0015 \pm 0.0008$	$0.0059 \pm 0.0010 \pm 0.0004$
[0.2, 0.3]	0.244	[0.2, 0.3]	0.244	0.714	0.682	$0.0160 \pm 0.0014 \pm 0.0008$	$0.0071 \pm 0.0009 \pm 0.0004$
[0.2, 0.3]	0.244	[0.3, 0.4]	0.344	0.710	0.676	$0.0179 \pm 0.0021 \pm 0.0011$	$0.0084 \pm 0.0013 \pm 0.0009$
[0.2, 0.3]	0.244	[0.4, 0.5]	0.444	0.706	0.671	$0.0194 \pm 0.0021 \pm 0.0011$	$0.0080 \pm 0.0013 \pm 0.0009$
[0.2, 0.3]	0.244	[0.5, 0.7]	0.576	0.698	0.664	$0.0271 \pm 0.0030 \pm 0.0016$	$0.0103 \pm 0.0015 \pm 0.0008$
[0.2, 0.3]	0.244	[0.7, 1]	0.773	0.681	0.650	$0.0292 \pm 0.0040 \pm 0.0016$	$0.0124 \pm 0.0019 \pm 0.0008$
[0.3, 0.4]	0.344	[0.15, 0.2]	0.174	0.711	0.682	$0.0121 \pm 0.0022 \pm 0.0008$	$0.0056 \pm 0.0014 \pm 0.0009$
[0.3, 0.4]	0.344	[0.2, 0.3]	0.244	0.710	0.680	$0.0153 \pm 0.0020 \pm 0.0009$	$0.0065 \pm 0.0013 \pm 0.0009$
[0.3, 0.4]	0.344	[0.3, 0.4]	0.344	0.706	0.674	$0.0215 \pm 0.0031 \pm 0.0010$	$0.0095 \pm 0.0019 \pm 0.0016$
[0.3, 0.4]	0.344	[0.4, 0.5]	0.444	0.703	0.670	$0.0184 \pm 0.0031 \pm 0.0010$	$0.0082 \pm 0.0019 \pm 0.0016$
[0.3, 0.4]	0.344	[0.5, 0.7]	0.577	0.696	0.664	$0.0267 \pm 0.0043 \pm 0.0026$	$0.0112 \pm 0.0022 \pm 0.0023$
[0.3, 0.4]	0.344	[0.7, 1]	0.774	0.681	0.653	$0.0296 \pm 0.0058 \pm 0.0026$	$0.0161 \pm 0.0027 \pm 0.0024$
[0.4, 0.5]	0.344	[0.15, 0.2]	0.174	0.681	0.653	$0.0141 \pm 0.0023 \pm 0.0008$	$0.0044 \pm 0.0014 \pm 0.0009$
[0.4, 0.5]	0.344	[0.2, 0.3]	0.244	0.681	0.653	$0.0169 \pm 0.0021 \pm 0.0009$	$0.0077 \pm 0.0013 \pm 0.0009$
[0.4, 0.5]	0.344	[0.3, 0.4]	0.344	0.681	0.653	$0.0189 \pm 0.0031 \pm 0.0010$	$0.0084 \pm 0.0019 \pm 0.0016$
[0.4, 0.5]	0.344	[0.4, 0.5]	0.444	0.681	0.653	$0.0202 \pm 0.0036 \pm 0.0010$	$0.0081 \pm 0.0022 \pm 0.0016$
[0.4, 0.5]	0.344	[0.5, 0.7]	0.574	0.681	0.653	$0.0278 \pm 0.0047 \pm 0.0026$	$0.0133 \pm 0.0024 \pm 0.0023$
[0.4, 0.5]	0.344	[0.7, 1]	0.774	0.681	0.653	$0.0353 \pm 0.0082 \pm 0.0027$	$0.0185 \pm 0.0038 \pm 0.0024$
[0.5, 0.7]	0.443	[0.15, 0.2]	0.174	0.706	0.680	$0.0213 \pm 0.0033 \pm 0.0017$	$0.0066 \pm 0.0017 \pm 0.0008$
[0.5, 0.7]	0.444	[0.2, 0.3]	0.244	0.706	0.678	$0.0250 \pm 0.0030 \pm 0.0018$	$0.0096 \pm 0.0015 \pm 0.0008$
[0.5, 0.7]	0.444	[0.3, 0.4]	0.344	0.703	0.673	$0.0266 \pm 0.0043 \pm 0.0029$	$0.0116 \pm 0.0022 \pm 0.0020$
[0.5, 0.7]	0.444	[0.4, 0.5]	0.444	0.699	0.669	$0.0321 \pm 0.0048 \pm 0.0029$	$0.0122 \pm 0.0024 \pm 0.0020$
[0.5, 0.7]	0.444	[0.5, 0.7]	0.577	0.693	0.664	$0.0446 \pm 0.0060 \pm 0.0034$	$0.0174 \pm 0.0029 \pm 0.0013$
[0.5, 0.7]	0.445	[0.7, 1]	0.776	0.679	0.653	$0.0686 \pm 0.0097 \pm 0.0038$	$0.0272 \pm 0.0043 \pm 0.0014$
[0.7, 1]	0.576	[0.15, 0.2]	0.174	0.698	0.677	$0.0222 \pm 0.0044 \pm 0.0017$	$0.0092 \pm 0.0021 \pm 0.0008$
[0.7, 1]	0.577	[0.2, 0.3]	0.244	0.698	0.676	$0.0284 \pm 0.0040 \pm 0.0018$	$0.0128 \pm 0.0019 \pm 0.0008$
[0.7, 1]	0.577	[0.3, 0.4]	0.344	0.696	0.671	$0.0313 \pm 0.0058 \pm 0.0029$	$0.0147 \pm 0.0027 \pm 0.0020$
[0.7, 1]	0.577	[0.4, 0.5]	0.444	0.693	0.668	$0.0373 \pm 0.0082 \pm 0.0029$	$0.0209 \pm 0.0039 \pm 0.0021$
[0.7, 1]	0.578	[0.5, 0.7]	0.578	0.688	0.662	$0.0710 \pm 0.0097 \pm 0.0039$	$0.0274 \pm 0.0043 \pm 0.0014$
[0.7, 1]	0.580	[0.7, 1]	0.779	0.674	0.652	$0.1398 \pm 0.0167 \pm 0.0057$	$0.0340 \pm 0.0061 \pm 0.0016$

Table 6.2: Light quark (*uds*) Collins asymmetries obtained fitting the UC double ratio as a function of  $(z_1, z_2)$ . In the first two columns, are reported the  $z$  bins and the respective mean value for the pions in one hemisphere; in the following two columns, are shown the same variables for the second pion; in the middle columns are summarized the mean value of  $\sin^2 \theta / (1 + \cos^2 \theta)$  calculated in the RF12 and RF0 frames, respectively; finally, in the last two columns are summarized the asymmetry results. The errors shown are statistical and systematic.

$p_{t1}$	$\langle p_{t1} \rangle$	$\langle z_1 \rangle$	$p_{t2}$	$\langle p_{t2} \rangle$	$\langle z_2 \rangle$	$\frac{\sin^2 \theta_{th}}{1+\cos^2 \theta_{th}}$	$A_{12}^{UL}$	$A_{12}^{UC}$
[0., 0.25]	0.171	0.250	[0., 0.25]	0.171	0.249	0.691	$0.0255 \pm 0.0065 \pm 0.0010$	$0.0118 \pm 0.0056 \pm 0.0004$
[0., 0.25]	0.170	0.251	[0.25, 0.5]	0.370	0.263	0.700	$0.0292 \pm 0.0034 \pm 0.0008$	$0.0135 \pm 0.0029 \pm 0.0003$
[0., 0.25]	0.169	0.252	[0.5, 0.75]	0.596	0.309	0.708	$0.0366 \pm 0.0050 \pm 0.0013$	$0.0171 \pm 0.0042 \pm 0.0005$
[0., 0.25]	0.169	0.253	[> 0.75]	0.894	0.412	0.709	$0.0606 \pm 0.0084 \pm 0.0025$	$0.0265 \pm 0.0068 \pm 0.0011$
[0.25, 0.5]	0.370	0.263	[0., 0.25]	0.171	0.251	0.700	$0.0405 \pm 0.0036 \pm 0.0019$	$0.0190 \pm 0.0030 \pm 0.0008$
[0.25, 0.5]	0.367	0.271	[0.25, 0.5]	0.366	0.271	0.711	$0.0444 \pm 0.0018 \pm 0.0012$	$0.0201 \pm 0.0015 \pm 0.0005$
[0.25, 0.5]	0.365	0.275	[0.5, 0.75]	0.596	0.323	0.720	$0.0393 \pm 0.0027 \pm 0.0024$	$0.0181 \pm 0.0022 \pm 0.0010$
[0.25, 0.5]	0.363	0.279	[> 0.75]	0.890	0.424	0.720	$0.0613 \pm 0.0042 \pm 0.0044$	$0.0271 \pm 0.0034 \pm 0.0020$
[0.5, 0.75]	0.596	0.308	[0., 0.25]	0.169	0.252	0.708	$0.0312 \pm 0.0050 \pm 0.0016$	$0.0146 \pm 0.0042 \pm 0.0006$
[0.5, 0.75]	0.596	0.322	[0.25, 0.5]	0.365	0.276	0.720	$0.0403 \pm 0.0027 \pm 0.0019$	$0.0184 \pm 0.0022 \pm 0.0008$
[0.5, 0.75]	0.595	0.325	[0.5, 0.75]	0.595	0.326	0.731	$0.0477 \pm 0.0054 \pm 0.0044$	$0.0209 \pm 0.0035 \pm 0.0020$
[0.5, 0.75]	0.595	0.330	[> 0.75]	0.885	0.423	0.735	$0.0601 \pm 0.0068 \pm 0.0081$	$0.0255 \pm 0.0051 \pm 0.0038$
[> 0.75]	0.894	0.412	[0., 0.25]	0.169	0.253	0.709	$0.0514 \pm 0.0081 \pm 0.0032$	$0.0234 \pm 0.0067 \pm 0.0014$
[> 0.75]	0.890	0.423	[0.25, 0.5]	0.363	0.279	0.721	$0.0529 \pm 0.0041 \pm 0.0026$	$0.0238 \pm 0.0034 \pm 0.0011$
[> 0.75]	0.885	0.422	[0.5, 0.75]	0.595	0.332	0.735	$0.0570 \pm 0.0067 \pm 0.0080$	$0.0240 \pm 0.0051 \pm 0.0036$
[> 0.75]	0.882	0.427	[> 0.75]	0.882	0.428	0.742	$0.0634 \pm 0.0117 \pm 0.0148$	$0.0271 \pm 0.0086 \pm 0.0065$

$p_{t0}$	$\langle p_{t0} \rangle$	$\langle z_1 \rangle$	$\langle z_2 \rangle$	$\frac{\sin^2 \theta_2}{1+\cos^2 \theta_2}$	$A_0^{UL}$	$A_0^{UC}$
[0., 0.25]	0.171	0.227	0.299	0.683	$0.0025 \pm 0.0015 \pm 0.0001$	$0.0010 \pm 0.0012 \pm 0.0002$
[0.25, 0.5]	0.380	0.237	0.293	0.679	$0.0143 \pm 0.0010 \pm 0.0007$	$0.0065 \pm 0.0008 \pm 0.0003$
[0.5, 0.75]	0.607	0.276	0.280	0.677	$0.0216 \pm 0.0013 \pm 0.0034$	$0.0097 \pm 0.0009 \pm 0.0016$
[> 0.75]	1.054	0.424	0.261	0.677	$0.0250 \pm 0.0012 \pm 0.0070$	$0.0110 \pm 0.0009 \pm 0.0032$

Table 6.3: Light quark ( $uds$ ) Collins asymmetries obtained fitting the UL and UC double ratios as a function of  $p_t$ . In particular, the first part of the table summarizes the results in the RF12 frame (as a function of  $(p_{t1}, p_{t2})$  bins), while in the lower part are shown the results obtained in the RF0 frame (as a function of  $p_{t0}$ ). In the first three columns, are reported the quantities which refer to the first pion, followed by the same variables for the second pion. In the seventh column are summarized the mean value of  $\sin^2 \theta / (1 + \cos^2 \theta)$ , with  $\theta \equiv \theta_{th}$  in RF12 and  $\theta \equiv \theta_2$  in RF0. Finally, in the last two columns are reported the asymmetry results. The errors shown are statistical and systematic.

# Conclusions and outlook

In this thesis we presented the measurement of the Collins asymmetries in inclusive production of pion pairs with the *BABAR* experiment data. The results obtained in these studies can be compared with the Belle asymmetries [15], which first performed the extraction of the Collins asymmetry with high precision in  $e^+e^-$  annihilation. Our results are competitive with Belle measurement, and, in addition, we also studied the behavior of the asymmetries not only as a function of fractional pion energy  $z$ , but also as a function of transverse momentum  $p_t$ , which had never been done so far in  $e^+e^-$  annihilation.

This analysis is based on a data sample of  $468 \text{ fb}^{-1}$  collected by the *BABAR* detector at the PEP-II storage ring from 1999 to 2008. Despite the *BABAR* experiment was initially designed for studying CP violation in  $B$  mesons, it has been demonstrated to be one of the most suitable environment for inclusive hadrons analysis. The tracking system and the excellent particle identification of *BABAR* allow to measure these small asymmetries with high precision and small systematic uncertainties.

In particular, the measurement of Collins asymmetries is performed in two reference frames: the RF12 frame (or thrust RF), and the RF0 frame (or second hadron momentum RF). Detector acceptance and higher order radiative effects are removed performing the double ratio of raw asymmetries, for example the raw asymmetry of unlike (U) sign pion pairs over that for like (L) sign pion pairs. In addition to these double ratios (UL), we performed the ratio of unlike over any charged (C) pion pairs, called also UC double ratio. In this way, we can access the information of the sign and relative amplitude of the favored and disfavored fragmentation processes [96].

Figures 6.1 and 6.4 show the results as a function of  $(z_1, z_2)$ ,  $(p_{t1}, p_{t2})$ , and  $p_{t0}$  bins, respectively. The UL double ratio results as a function of  $(z_1, z_2)$  are summarized in Tab. 6.1, while Tab. 6.2 reports the results of the UC double ratio. Finally, the  $p_t$  dependence of the Collins asymmetries for the UL and UC ratio are shown in Tab. 6.3. The measured asymmetries are corrected by the charm, bottom and tau background contributions, and all the sizable systematic effects are included.

We also studied the Collins asymmetry in different bins of  $\sin^2 \theta / (1 + \cos^2 \theta)$ , where  $\theta \equiv \theta_{th}$  in the RF12 frame, and  $\theta \equiv \theta_2$  in the RF0 frame. Also in these case the final asymmetry is

corrected by the background contributions (charm, bottom, and tau as before), and all the systematic effects are evaluated. Figure 6.5 shows the behavior as a function of  $\sin^2 \theta / (1 + \cos^2 \theta)$ .

We also compare the measured asymmetry as a function of the fractional energies with our preliminary results [111] and Belle results [15]. Because of the different binning in the three analysis, we combine opportunely the various bins in order to have the asymmetries evaluated in 10 symmetrized bins of fractional energies, as described in Sec. 6.1. We find a good agreement of the asymmetry measured in the RF0 frame, for both UL and UC double ratio. Nevertheless, significant discrepancies are clearly visible for the asymmetries measured in the thrust reference frame. For the UL double ratio, shown in Fig. 6.2(a), the discrepancies are observable in the last two  $z$ -bins (pion pairs with higher fractional energy), and are due to the additional cut which discarded tracks with an opening angle with respect to the thrust axis less than  $2^\circ$ . This requirement, that was not used in the previous analysis, is indeed necessary because the measurement of the azimuthal angles for the rejected tracks is unreliable, with a result of a dilution of the measured asymmetries, in particular for high  $z$  values. Instead, the discrepancy observed for the UC double ratio is not yet understood.

The measurement of the Collins asymmetries in the pions system is completed and a journal paper summarizing the results is in preparation. These data can be used for the extraction of the transversity PDF, as just done by the authors of Ref. [16, 17], and will be helpful to increase the precision of the present fits. The same analysis procedure can be used to study the asymmetries in the kaons system, for which no data in  $e^+e^-$  annihilation are still present. In this case, the pions contamination is the most significant background source, and a very accurate description of it is needed in order to perform the measurement. These results are eagerly awaited, since they bring information about the role of the strange quark. However, a lot of other measurements will be performed, as measuring the asymmetries for different combinations of hadron pairs or the measurement of Interference FF. In this scenario, the measurement of Collins asymmetries for pion pairs is only the first step of an entirely new and reach program of measurements that can be performed with the high quality *BABAR* data.

# Appendix A

## Light-Cone Quantization

In this appendix, we reported a review of some basic features of Light-Cone (LC) quantization [20, 112, 113, 114], since the discussion of hard processes is particularly simple in this context. We use the following component notation

$$a^\mu = [a^+, a^-, \mathbf{a}_\perp] \quad (\text{A.1})$$

for any four vector  $a^\mu$ , with the light-cone components  $a^\pm = (a^0 \pm a^3)/\sqrt{2}$  and the two-dimensional transverse part  $\mathbf{a}_\perp = (a^1, a^2)$ .

With the non-diagonal metric tensor ( $\mu, \nu = +, -, 1, 2$ )

$$g^{\mu\nu} = \begin{bmatrix} 0 & 1 & 0 & 0 \\ 1 & 0 & 0 & 0 \\ 0 & 0 & -1 & 0 \\ 0 & 0 & 0 & -1 \end{bmatrix} \quad (\text{A.2})$$

the scalar product of two four-vectors is given as

$$a \cdot b = a^\mu \cdot b_\mu = g^{\mu\nu} a_\mu b_\nu = a^+ b^- + a^- b^+ - \mathbf{a}_\perp \cdot \mathbf{b}_\perp. \quad (\text{A.3})$$

Notice that the non-zero off-diagonal entries in the metric tensor make the conversion of contravariant and covariant vectors somewhat confusing, resulting for instance in  $a^\pm = a_\mp$ , and  $\partial^\pm \equiv \partial/\partial z_\pm = \partial/\partial z^\mp$ . Frequently, in the formalism used in this report, we used the two light-like unit vectors  $n_\pm$

$$n_+ \equiv [1, 0, \mathbf{0}_\perp] \quad n_- \equiv [0, 1, \mathbf{0}_\perp] \quad (\text{A.4})$$

satisfying  $n_+^2 = n_-^2 = 0$  and  $n_+ \cdot n_- = 1$ . With the help of  $n_\pm$  LC components can be projected out by

$$a^+ = n_- \cdot a \quad a^- = n_+ \cdot a. \quad (\text{A.5})$$

What are the motivations for defining such coordinates, which evidently depend on a particular choice of the  $z$  axis? One is that these coordinates transform very simply under boost along the  $z$ -axis. Another is that when a vector is highly boosted along the  $z$ -axis, LC coordinates show what are the large and small components of momentum.

### Longitudinal and Transverse boost

A Lorentz transformation which boost coordinates from the rest frame of a particle to a frame where the particle moves with velocity  $v$  along the  $z$ -axis, changes the ordinary components according to

$$\tilde{x}^0 = \frac{x^0 + vx^3}{\sqrt{1-v^2}}, \quad \tilde{x}^3 = \frac{x^3 + vx^0}{\sqrt{1-v^2}}, \quad \tilde{x}^1 = x^1, \quad \tilde{x}^2 = x^2. \quad (\text{A.6})$$

The same relation written in LC components take the form

$$\tilde{x}^+ = x^+ e^\psi, \quad \tilde{x}^- = x^- e^{-\psi}, \quad \tilde{\mathbf{x}}_\perp = \mathbf{x}_\perp \quad (\text{A.7})$$

where the hyperbolic angle  $\psi$  is  $\ln((1+v)/(1-v))/2$ , so that  $v = \tanh \psi$  [115]. The momentum of a particle with mass  $m$  obtained by a boost with  $\psi$  from the rest frame is

$$\tilde{p}^\mu = \left[ p^+, \frac{m^2}{2p^+}, \mathbf{0}_\perp \right] = \left[ \frac{m}{\sqrt{2}} e^\psi, \frac{m}{\sqrt{2}} e^{-\psi}, \mathbf{0}_\perp \right] \quad (\text{A.8})$$

A particularly useful Lorentz transformation is a *transverse boost* which leave the *plus* (or minus) component of any momentum vector  $a$  unchanged, and which involves a parameter  $b^+$  and transverse vector  $\mathbf{b}_\perp$ :

$$a^\mu = [a^+, a^-, \mathbf{a}_\perp] \quad (\text{A.9})$$

$$\rightarrow \tilde{a}^\mu = \left[ a^+, a^- - \frac{\mathbf{a}_\perp \cdot \mathbf{b}_\perp}{b^+} + \frac{a^+ \mathbf{b}_\perp^2}{2(b^+)^2}, \mathbf{a}_\perp - \frac{a^+}{b^+} \mathbf{b}_\perp \right] \quad (\text{A.10})$$

with  $\tilde{a}^2 = 2a^+a^- - \mathbf{a}_\perp^2 = a^2$ .

Note the distinction of a transverse boost from a rotation. There is always a rotation in coordinate space which has the same effect on the transverse momentum components. But a rotation leaves the energy component unchanged and thus changes the plus (minus) LC component. Rotations and transverse boosts in general do not commute.

### Equations of motion

It turns out useful to define projectors

$$P_\pm = \frac{1}{2} \gamma^\mp \gamma^\pm \quad (\text{A.11})$$

with

$$P_+ + P_- = 1 \quad P_+ P_- = P_- P_+ = 0 \quad P_\pm^2 = P_\pm. \quad (\text{A.12})$$

The LC projections of the Dirac field,  $\psi_+ \equiv P_+ \psi$  and  $\psi_- \equiv P_- \psi$  are known as the *good* and *bad* LC component of  $\psi$  respectively. To save on subscripts we shall replace  $\psi_\pm$  as follow:

$$\psi_+ \Rightarrow \phi \quad \psi_- \Rightarrow \chi$$

The importance of  $P_{\pm}$ , and the following different role of *good* and *bad* components of the quark fields, becomes clear when they are used to project the Dirac equation of motion down to the two-component equations,

$$i\gamma^+ D^- \phi = i\vec{\gamma}_{\perp} \cdot \mathbf{D}_{\perp} \chi + m\chi \quad (\text{A.13})$$

$$i\gamma^- D^+ \chi = i\vec{\gamma}_{\perp} \cdot \mathbf{D}_{\perp} \phi + m\phi, \quad (\text{A.14})$$

where  $D^{\pm} = \partial/\partial z^{\mp} + igA^{\pm}$ . In the LC gauge  $A^+ = 0$ , for example,  $z^+$  is the evolution ('time') parameter. The equation (A.14) only involves  $\partial/\partial z^-$  (the LC-time  $z^+$  does not occur at all), so it appears that  $\chi$  is not an independent dynamical field. Instead the Dirac equation constrains  $\chi$  in terms of  $\phi$  and  $\mathbf{A}_{\perp}$  at fixed  $z^+$ , which therefore should be regarded as composite  $\chi = F[\phi, \mathbf{A}_{\perp}]$ .

Although the complete quantization of QCD requires much more work, the implication of the Dirac field is already clear: the *good* components should be regarded as independent propagating degrees of freedom; the *bad* components are dependent field (actually quark-gluon composites).

### General bilocal quark field operator

We want to find a general form for a bilocal quark field operator with an arbitrary  $4 \times 4$  matrix  $A$ , such as  $\bar{\psi}(z_1)A\psi(z_2) = \psi^{\dagger}(z_1)\gamma^0 A\psi(z_2)$ . In the chiral representation (Weyl representation) defined by

$$\gamma^0 = \begin{pmatrix} 0 & \mathbb{1} \\ \mathbb{1} & 0 \end{pmatrix}; \quad \vec{\gamma} = \begin{pmatrix} 0 & -\vec{\sigma} \\ \vec{\sigma} & 0 \end{pmatrix}; \quad \gamma_5 = \begin{pmatrix} \mathbb{1} & 0 \\ 0 & -\mathbb{1} \end{pmatrix} \quad (\text{A.15})$$

where  $\sigma$  are the usual Pauli matrices, the projectors to *good* and *bad* components take the explicit form

$$P_+ = \begin{pmatrix} 1 & 0 & 0 & 0 \\ 0 & 0 & 0 & 0 \\ 0 & 0 & 0 & 0 \\ 0 & 0 & 0 & 1 \end{pmatrix}, \quad P_- = \begin{pmatrix} 0 & 0 & 0 & 0 \\ 0 & 1 & 0 & 0 \\ 0 & 0 & 1 & 0 \\ 0 & 0 & 0 & 0 \end{pmatrix}, \quad (\text{A.16})$$

such that

$$P_+ \begin{pmatrix} a \\ b \\ c \\ d \end{pmatrix} = \begin{pmatrix} a \\ 0 \\ 0 \\ d \end{pmatrix}, \quad P_- \begin{pmatrix} a \\ b \\ c \\ d \end{pmatrix} = \begin{pmatrix} 0 \\ b \\ c \\ 0 \end{pmatrix}, \quad (\text{A.17})$$

i.e., the 1st and 4th components of a four-spinor in the Weyl representation represent the *good* components of the fields, whereas the 2nd and 3rd represent the *bad* ones.

The chiral structure of the operator can easily be included by defining chiral projectors

$$P_{R,L} = \frac{1}{2}(\mathbb{1} \pm \gamma_5) \quad (\text{A.18})$$

which, in the Weyl representation, have the simple form

$$P_R = \begin{pmatrix} 1 & 0 & 0 & 0 \\ 0 & 1 & 0 & 0 \\ 0 & 0 & 0 & 0 \\ 0 & 0 & 0 & 0 \end{pmatrix}, \quad P_L = \begin{pmatrix} 0 & 0 & 0 & 0 \\ 0 & 0 & 0 & 0 \\ 0 & 0 & 1 & 0 \\ 0 & 0 & 0 & 1 \end{pmatrix}, \quad (\text{A.19})$$

such that

$$P_R \begin{pmatrix} a \\ b \\ c \\ d \end{pmatrix} = \begin{pmatrix} a \\ b \\ 0 \\ 0 \end{pmatrix}, \quad P_L \begin{pmatrix} a \\ b \\ c \\ d \end{pmatrix} = \begin{pmatrix} 0 \\ 0 \\ c \\ d \end{pmatrix}. \quad (\text{A.20})$$

In other words the upper two components of a four-spinor represent the right-handed part of the field, whereas the lower components represent the left-handed one. Combining equations (A.17) and (A.20) a four-spinor in Weyl representation can be written generically

$$\psi = \begin{pmatrix} \phi_R \\ \chi_R \\ \chi_L \\ \phi_L \end{pmatrix} \quad (\text{A.21})$$

and a matrix has the general structure

$$\begin{pmatrix} \phi_R^\dagger \phi_R & \chi_R^\dagger \phi_R & \chi_L^\dagger \phi_R & \phi_L^\dagger \phi_R \\ \phi_R^\dagger \chi_R & \chi_R^\dagger \chi_R & \chi_L^\dagger \chi_R & \phi_L^\dagger \chi_R \\ \phi_R^\dagger \chi_L & \chi_R^\dagger \chi_L & \chi_L^\dagger \chi_L & \phi_L^\dagger \chi_L \\ \phi_R^\dagger \phi_L & \chi_R^\dagger \phi_L & \chi_L^\dagger \phi_L & \phi_L^\dagger \phi_L \end{pmatrix} \quad (\text{A.22})$$

where the generic notation indicates that a matrix element labelled for instance by  $\phi_L^\dagger \chi_R$  relates a left-handed *good* component of a quark field with a right-handed *bad* one, and so on.

Equipped with these tools one can read off the proprieties of the operator combination  $\psi^\dagger(z_1)(\gamma^0 A)\psi(z_2)$  from its explicit form in Weyl representation. For instance, with  $A = \gamma^+$  a comparison of

$$\gamma^0 \gamma^+ = \sqrt{2} \begin{pmatrix} 1 & 0 & 0 & 0 \\ 0 & 0 & 0 & 0 \\ 0 & 0 & 0 & 0 \\ 0 & 0 & 0 & 1 \end{pmatrix} \quad (\text{A.23})$$

with (A.22) results in the observation that  $\bar{\psi}(z_1)\gamma^+\psi(z_2)$  counts the sum of right and left left-handed *good* quarks components:

$$\bar{\psi}(z_1)\gamma^+\psi(z_2) = \sqrt{2}(\phi_R^\dagger(z_1)\phi_R(z_2) + \phi_L^\dagger(z_1)\phi_L(z_2)). \quad (\text{A.24})$$

In Appendix C is reported a list of appropriate  $4 \times 4$  matrices  $M_i$  ( $i = 1, \dots, 16$ ) in Weyl representation which by simple comparison with the generic pattern given in (A.22) reveals its chiral structure in terms of *good* and *bad* quark field components.

## Appendix B

# Transverse momenta in (semi-)inclusive reactions

### B.1 The concept of Parton Distribution Function (PDF) and Parton Fragmentation Function (PFF)

The deep inelastic scattering of leptons on nucleons (DIS) has led to the discovery of partons, and is certainly the archetype of all hard reactions involving the concept of parton distribution functions.

When a high-energetic lepton beam is scattered on a nucleon target, the electroweak interaction is mediated by the exchange of a highly virtual gauge boson: a photon,  $Z$  or  $W$ -boson. The kinematics of the reaction is characterized by a Lorentz invariants which can be build from the momenta of the lepton before and after the scattering,  $l$  and  $l'$ , and from the momentum of the nucleon  $P$ . Conventionally one chooses as independent invariants the square of the centre mass energy

$$s = (P + l)^2, \quad (\text{B.1})$$

the virtuality of the gauge boson

$$q^2 = (l' - l)^2 \equiv -Q^2 \quad (\text{B.2})$$

and

$$\nu = \frac{P \cdot q}{M} \quad (\text{B.3})$$

where  $M$  is the nucleon mass. In the rest frame of the nucleon,  $\nu$  has the interpretation of transferred energy.

Two crucial steps have led to the discovery of partons and the formulation of parton model:

1. The observation of the *Bjorken scaling* and its interpretation. At very large  $Q^2$ , the differential cross section for elastic scattering processes is

$$\frac{d\sigma}{d\Omega dE'} = \frac{4\alpha_{CM}E'^2}{Q^4} \left\{ 2 \sin^2 \frac{\Theta}{2} W_1(\nu, Q^2) + \cos^2 \frac{\Theta}{2} W_2(\nu, Q^2) \right\}, \quad (\text{B.4})$$

where  $E'$  is the energy,  $\Omega$  the solid angle of the outgoing lepton, and  $\Theta$  the scattering angle in the nucleon rest frame. In the limit of  $Q^2 \rightarrow \infty$ , the so called Bjorken limit, the structure functions  $F_1$  and  $F_2$ , defined from  $W_1$  and  $W_2$ , depend to a good approximation only on a certain combination of  $Q^2$  and  $\nu$

$$x_{Bj} = \frac{Q^2}{2P \cdot q} = \frac{Q^2}{2M\nu} \quad (\text{B.5})$$

and not on both invariants independently:

$$\begin{aligned} 2MW_1(\nu, Q^2) &= F_1(\nu, Q^2) \rightarrow F_1(x_{Bj}), \\ \nu W_2(\nu, Q^2) &= F_2(\nu, Q^2) \rightarrow F_2(x_{Bj}). \end{aligned} \quad (\text{B.6})$$

The fact that the dimensionless structure functions  $F_1$  and  $F_2$  depend on the dimensionless combination of invariants indicates that the elastic scattering takes place on point-like particles (otherwise dimensional form factors would show up).

2. A natural interpretation of the phenomenon arises in *Feynmans parton model* the basic idea of which can be summarized in two simple rules:

- a rapidly moving hadron is treated as a jet of quasi-free partons moving almost collinear;
- the cross section of the hadronic process is calculated as a convolution of partonic cross section and parton distribution functions (PDFs) summed incoherently over all partons.

The contribution to the cross section of DIS is given by the famous 'handbag' diagram shown in Fig. B.1, where also the factorization in soft and hard parts is indicated. The non-perturbative information is encoded as quark-quark correlation function which in a light-cone gauge takes the form [69]

$$\Phi_{ij}(p, P, S) = \int \frac{d^4\xi}{(2\pi)^4} e^{-ip \cdot \xi} \langle P, S | \bar{\psi}_j(\xi) \psi_i(0) | P, S \rangle \quad (\text{B.7})$$

depending on the quark momentum  $p$ , the target nucleon momentum  $P$ , and possibility on the spin of the nucleon ( $S$ ). The link operator normally needed to render the definition gauge-invariant does not appear because we choose the gauge  $A^+ = 0$  (it is in this picture that field theory has the closest connection with the parton model [113, 116]), and in this gauge  $\mathcal{G} = 1$ ,

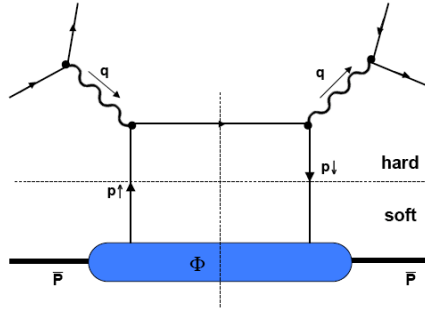


Figure B.1: DIS: the “handbag” diagram leading to the dominant contribution to the cross section.

where  $\mathcal{G}$  is a path-ordered exponential of the gluon field that appear in the definition of the parton model.

In the totally inclusive DIS process the quark-quark correlation function (B.7) occurs traced with certain Dirac matrices, and integrated over three of the four quark momentum components:

$$\Phi^{[\Gamma]}(x) = \frac{1}{2} \int dp^- d^2 \mathbf{p}_T \text{Tr}(\Phi \Gamma) |_{p^+ = x P^+} \quad (\text{B.8})$$

where  $\Gamma$  is a  $4 \times 4$  Dirac matrix (see Appendix C), and  $x$  is the light-cone momentum fraction.

Whenever hadrons in the final state are observed in a hard (semi-)inclusive process, another bit of non-perturbative information is needed to describe the reaction: the hadronisation process of a parton. The most simple process involving hadronisation is the  $e^+e^-$  annihilation into hadrons:  $e^+e^- \rightarrow hX$ . The dominant contribution to the differential cross section of this process involves the annihilation of electron and positron into a highly virtual photon (or  $Z$  boson), and the creation of a quark-antiquark pair, as reported in Fig. B.2. The hadronisation of one member of the pair, say the final state hadron is observed in the quark jet, is of non-perturbative nature and described by another quark-quark correlation function defined as Fourier transformation of a hadronix matrix element of a bilocal quark field operator:

$$\Delta_{ij}(k, P_h, S_h) = \sum_{X'} \frac{1}{(2\pi)^4} \int d^4 \xi e^{ik \cdot \xi} \cdot \langle 0 | \psi_i(\xi) | P_h, S_h; X' \rangle \langle P_h, S_h; X' | \bar{\psi}_j(0) | 0 \rangle \quad (\text{B.9})$$

depending on the momentum  $k$  of the fragmenting quark, the momentum of the observed hadron  $P_h$ , and possibly its spin  $S_h$ . In this definition,  $X'$  denotes all other hadrons produced.

Again, the link operator normally needed to render the definition gauge-invariant is not shown adopting a light-cone gauge ( $A^- = 0$ ) and a suitable choice of the integration path. The PFF are defined from  $\Delta$  by tracing the quark-quark correlation function with certain Dirac

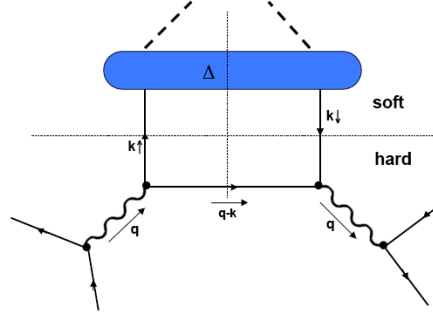


Figure B.2: Dominant contribution to the differential cross section of  $e^+e^-$  annihilation with one observed hadron in the final state.

matrices, and integrating over three of the four momentum components of the fragmenting quark:

$$\Delta^{[\Gamma]}(z) \equiv \frac{1}{4z} \int dk^+ d^2\mathbf{k}_T \text{Tr}(\Delta\Gamma) \Big|_{k^- = P_h^-/z} \quad (\text{B.10})$$

where  $z$  is the fraction of the momentum in the minus direction carried by the hadron  $h$  originating from the fragmentation of the quark. Note that we assume initial state hadrons to move from left to right with a large plus component, and hadrons in the final state moving from right to left with a large minus component.

PDFs and PFFs occur together in the description of SIDIS ( $lH \rightarrow l'hX$ ), and the product of two PFFs in the process  $e^+e^- \rightarrow h_1h_2X$  (described in this analysis).

The sensitivity to the quark transverse momenta arises, in general, for any hard process involving two or more soft hadronic matrix elements like two hadron inclusive  $e^+e^-$  annihilation, the Drell-Yan process, or SIDIS. For the description of totally inclusive DIS, for example, one can always choose a reference frame where the target momentum  $P$  and the photon momenta  $q$  are collinear. If one hadron in the final state is measured, there is no frame where all the relevant four vectors are collinear; one of them will unavoidably have transverse momentum components. Observable which are unintegrated in this external transverse momentum component will have a sensitivity to the transverse momentum components which quarks can have relative to their parents momenta (this sensitivity is due to the momentum conservation). In Fig. B.3 is illustrated how the transverse momentum dependent PDFs and PFFs are related to the integrated ones, where  $f_1(x)$  and  $D_1(z)$  are the spin-independent PDF and PFF occurring at leading order respectively.

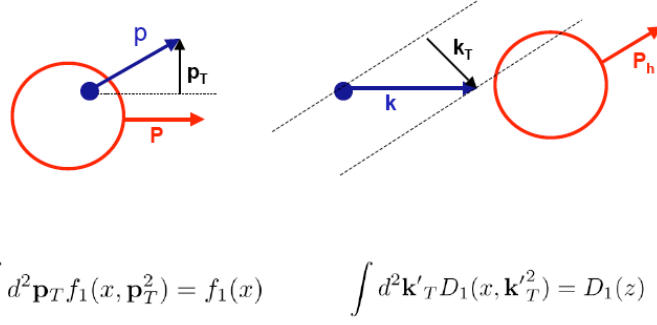


Figure B.3: Illustration of transverse momentum components quarks can have relative to their parent hadron momenta, and transverse momentum dependent PDFs and PFFs.  $\mathbf{P}$  and  $\mathbf{p}$  are defined in Fig. B.1;  $\mathbf{k}$  in Fig. B.2.

## B.2 PFFs

Starting from equation (B.9), two constraints arising from the hermiticity proprieties of the field and invariance under parity:

$$\Delta^\dagger(k, P_h, S_h) = \gamma_0 \Delta(k, P_h, S_h) \gamma_0 \quad [Hermiticity] \quad (\text{B.11})$$

$$\Delta(k, P_h, S_h) = \gamma_0 \Delta(\bar{k}, \bar{P}_h, -\bar{S}_h) \gamma_0 \quad [Parity] \quad (\text{B.12})$$

with the shorthand notation  $\bar{P} \equiv (P^0, -P^i)$  for four vectors with reversed sign in their spatial components. Recalling that  $\Delta_{ij}$  is a  $4 \times 4$  matrix in Dirac space, the most general expression for  $\Delta$  consistent with the constraints from hermiticity and parity is:

$$\begin{aligned} \Delta(k, P, S) = & MA_1 + A_2 \not{P} + A_3 \not{k} + (A_4/M) \sigma^{\mu\nu} P_\mu k_\nu + iA_5 (k \cdot S) \gamma_5 \\ & + MA_6 \not{S} \gamma_5 + (A_7/M) (k \cdot S) \not{P} \gamma_5 + (A_8/M) (k \cdot S) \not{k} \gamma_5 + \\ & + iA_9 \sigma^{\mu\nu} \gamma_5 \delta_{\mu\nu} P_\nu + iA_{10} \sigma^{\mu\nu} \gamma_5 S_\mu k_\nu + i(A_{11}/M^2) (k \cdot S) \sigma^{\mu\nu} \gamma_5 k_\mu P_\nu \\ & + (A_{12}/M) \epsilon_{\mu\nu\rho\sigma} \gamma^\mu P^\nu k^\rho S^\sigma \end{aligned} \quad (\text{B.13})$$

where we use the shorthand notation  $P = P_h$ ,  $S = S_h$ , and the amplitude  $A_i = A_i(\sigma_h, \tau_h)$  depend on the invariants  $\sigma \equiv 2k \cdot P_h$  and  $\tau_h \equiv k^2$ .

Hermiticity requires all amplitude  $A_i$  to be real. The corresponding expression for spin-0 hadrons (or for the description of hadrons with averaged polarization) is obtained by keeping the terms with amplitude  $A_1$ ,  $A_2$ ,  $A_3$ , and  $A_4$ , and discarding the spin dependent ones. Note that the constraint for time reversal invariance (needed for the PDFs) would require the amplitudes  $A_4$ ,  $A_5$ , and  $A_{12}$  to be purely imaginary and hence to vanish, since it is in contradiction with the requirements from hermiticity. For the PFFs this constraint is not applicable and those terms are conventionally, albeit quite misleading, called (*naive*) *time-reversal odd*.

Choosing the gauge  $A^- = 0$ , in hard processes one encounters the quantities:

$$\Delta^{[\Gamma]}(z) \equiv \frac{1}{4z} \int dk^+ d^2\mathbf{k}_T \text{Tr}(\Delta\Gamma) \Big|_{k^- = P_h^-/z} = \int [d\sigma_h d\tau_h \theta()] \frac{\text{Tr}(\Delta\Gamma)}{8zP_h^-}, \quad (\text{B.14})$$

with the short hand notation

$$[d\sigma_h d\tau_h \theta()] = d\sigma_h d\tau_h \theta \left( \frac{\sigma_h}{z} - \frac{M_h^2}{z^2} - \tau_h \right) \quad (\text{B.15})$$

A convenient parameterization of the momentum of the produced hadron, with mass  $M_h$ , in the hadron frame<sup>1</sup> is:

$$P_h = \frac{M_h^2}{2P_h^-} n_+ + P_h^- n_- = \frac{M_h^2}{z_h Q \sqrt{2}} n_+ + \frac{z_h Q}{\sqrt{2}} n_-. \quad (\text{B.16})$$

A Sudakov decomposition of the quark momentum and the spin vector can be written as

$$k = \frac{z(k^2 + \mathbf{k}_T^2)}{z_h Q \sqrt{2}} n_+ + \frac{z_h Q}{z \sqrt{2}} n_- + \mathbf{k}_T, \quad (\text{B.17})$$

$$S_h = -\frac{\lambda_h M_h}{z_h Q \sqrt{2}} n_+ + \frac{\lambda_h z_h Q}{M_h \sqrt{2}} n_- + \mathbf{S}_{hT} \quad (\text{B.18})$$

where  $z$  is the fraction of the momentum in the minus direction carried by the hadron originating from the fragmentation of the quark. The spin vector satisfied  $P_h \cdot S_h = 0$  and for a pure state  $\lambda_h^2 + \mathbf{S}_{hT}^2 = 1$ .

The projections of  $\Delta$  on different Dirac structures define PFF<sup>2</sup>. The projections

$$\Delta^{[\gamma^-]}(z) = D_1(z) \quad (\text{B.19})$$

$$\Delta^{[\gamma^- \gamma_5]}(z) = \lambda_h G_1(z) \quad (\text{B.20})$$

$$\Delta^{[i\sigma^{i-} \gamma_5]}(z) = S_{hT}^i H_1(z) \quad (\text{B.21})$$

are leading in  $1/Q$  and the probabilistic interpretation is shown in Fig. B.4

The following projections occur with a pre-factor  $M_h/P_h^-$ , which signals the subleading (or

<sup>1</sup>The hadron frame is the frame in which the hadron momentum  $P$  has no transverse components:  $(P^+, P^-, \mathbf{0}_T)$ .

<sup>2</sup>A complete list of independent  $4 \times 4$  Dirac matrices together with their explicit form in the chiral (Weyl) representation is given in Appendix C.

$D_1(z) = \left[ \bullet \rightarrow \text{red} \right]$	$D_1(z, \mathbf{k}_T^2) = \left[ \bullet \rightarrow \text{red} \right]$ $D_{1T}^\perp(z, \mathbf{k}_T^2) = \left[ \bullet \rightarrow \text{blue} \right]$
$G_1(z) = \left[ \bullet \rightarrow \text{red} \right] - \left[ \bullet \leftarrow \text{red} \right]$	$G_{1L}(z, \mathbf{k}_T^2) = \left[ \bullet \rightarrow \text{red} \right] - \left[ \bullet \leftarrow \text{red} \right]$ $G_{1T}(z, \mathbf{k}_T^2) = \left[ \bullet \rightarrow \text{green} \right] - \left[ \bullet \leftarrow \text{green} \right]$
$H_1(z) = \left[ \uparrow \bullet \rightarrow \text{red} \right] - \left[ \downarrow \bullet \rightarrow \text{red} \right]$	$H_{1T}(z, \mathbf{k}_T^2) = \left[ \uparrow \bullet \rightarrow \text{red} \right] - \left[ \downarrow \bullet \rightarrow \text{red} \right]$ $H_{1L}^\perp(z, \mathbf{k}_T^2) = \left[ \uparrow \bullet \rightarrow \text{green} \right] - \left[ \downarrow \bullet \rightarrow \text{green} \right]$ $H_{1T}^\perp(z, \mathbf{k}_T^2) = \left[ \uparrow \bullet \rightarrow \text{green} \right] - \left[ \downarrow \bullet \rightarrow \text{green} \right]$ $H_1^\perp(z, \mathbf{k}_T^2) = \left[ \uparrow \bullet \rightarrow \text{blue} \right] - \left[ \downarrow \bullet \rightarrow \text{blue} \right]$

Figure B.4: Probability interpretation of leading order integrated PFFs in the first columns and Transverse Momentum Dependent PFFs in the second column. The quark is assumed to move from left to right, which defines the longitudinal direction. Green arrows symbolize the hadron spin, blue arrows the spin state of the quark. For the transverse momentum dependent PFFs, there are two additional time-reversal odd functions ( $D_{1T}^\perp$  and  $H_1^\perp$ , indicated with the blue shaded hadrons), and three additional function ( $G_{1T}$ ,  $H_{1L}^\perp$ ,  $H_{1T}^\perp$ , indicated with the green shaded hadrons) which correlated quark and hadron spin orientation in different directions.

higher twist) nature of the corresponding fragmentation functions:

$$\Delta^{[1]}(z) = \frac{M_h}{P_h^-} E(z), \quad (\text{B.22})$$

$$\Delta^{[i\gamma_5]}(z) = \frac{M_h}{P_h^-} \lambda_h E_L(z), \quad (\text{B.23})$$

$$\Delta^{[\gamma^i]}(z) = \frac{M_h}{P_h^-} \epsilon_T^{ij} S_{hTj} D_T(z), \quad (\text{B.24})$$

$$\Delta^{[\gamma^i \gamma_5]}(z) = \frac{M_h}{P_h^-} S_{hT}^i G_T(z), \quad (\text{B.25})$$

$$\Delta^{[i\sigma^{ij} \gamma_5]}(z) = \frac{M_h}{P_h^-} \epsilon_T^{ij} H(z), \quad (\text{B.26})$$

$$\Delta^{[i\sigma^{+-} \gamma_5]}(z) = \frac{M_h}{P_h^-} \lambda_h H_L(z). \quad (\text{B.27})$$

Each factor  $M_h/P_h^-$  leads to a suppression with a power of  $M_h/Q$  in the cross section and we

will refer to the function multiplying a power  $(M_h/P_h^-)^{t-2}$  as 'twist'  $t$ .

In observable differential in transverse momenta there occur also the associated unintegrated quantities:

$$\Delta^{[\Gamma]}(z, \mathbf{k}_T) = \frac{1}{4z} \int dk^+ \text{Tr}(\Delta\Gamma) \Big|_{k^- = P_h^-/z, \mathbf{k}_T} = \int [d\sigma_h d\tau_h \delta()] \frac{\text{Tr}(\Delta\Gamma)}{8zP_h^-}, \quad (\text{B.28})$$

with the shorthand notation

$$[d\sigma_h d\tau_h \delta()] = d\sigma_h d\tau_h \delta\left(\tau_h - \frac{\sigma_h}{z} + \frac{M_h^2}{z^2} + \mathbf{k}_T^2\right), \quad (\text{B.29})$$

which lead to the definition of Transverse Momentum Dependent PFFs (also called TMD). The projections

$$\Delta^{[\gamma^-]}(z, \mathbf{k}_T) = D_1(z, \mathbf{k}_T^{\prime 2}) + \frac{\epsilon_T^{ij} k_{Tj} S_{hTj}}{M_h} D_{1T}^\perp(z, \mathbf{k}_T^{\prime 2}), \quad (\text{B.30})$$

$$\Delta^{[\gamma^- \gamma_5]}(z, \mathbf{k}_T) = \lambda_h G_{1L}(z, \mathbf{k}_T^{\prime 2}) + \frac{\mathbf{k}_T \cdot \mathbf{S}_{hT}}{M_h} G_{1T}^\perp(z, \mathbf{k}_T^{\prime 2}), \quad (\text{B.31})$$

$$\begin{aligned} \Delta^{[i\sigma^{i-} \gamma_5]}(z, \mathbf{k}_T) &= S_{hT}^i H_{1T}(z, \mathbf{k}_T^{\prime 2}) + \frac{\epsilon_T^{ij} k_{Tj}}{M_h} H_1^\perp(z, \mathbf{k}_T^{\prime 2}) + \\ &+ \frac{k_T^i}{M_h} \left( \lambda_h H_{1L}^\perp(z, \mathbf{k}_T^{\prime 2}) + \frac{\mathbf{k}_T \cdot \mathbf{S}_{hT}}{M_h} H_{1T}^\perp(z, \mathbf{k}_T^{\prime 2}) \right) \end{aligned} \quad (\text{B.32})$$

are leading order in  $1/Q$  and their partonic interpretation is depicted in Fig. B.4.

The choice of the arguments  $z$  and  $\mathbf{k}'_T$  in the fragmentation function is worth a comment. In the expansion of  $k$  in Eq. (B.17) the quantities  $1/z$  and  $\mathbf{k}_T$  appear in a natural way. However, one wants to express the fragmentation functions in terms of the hadron momentum. In order to switch from quark to hadron transverse momentum, a Lorentz transformation that leaves the minus components (and hence the definition of  $z = P_h^-/k^-$ ) unchanged needs to be performed, and one find that  $\mathbf{k}'_T \equiv -z\mathbf{k}_T$  is the transverse component of the hadron in a frame where the quark has no transverse momentum.

The function  $D_{1T}^\perp$  and  $H_1^\perp$  are example of what are generally called *time-reversal odd* functions. This terminology refers to the behavior of the functions under the so-called *naive* time-reversal operation  $T_N$ , which acts as follows on the correlation function:

$$\Delta(P_h, S_h; k) \xrightarrow{T_N} (\gamma_5 C \Delta(\bar{P}_h, \bar{S}_h; \bar{k}) C^\dagger \gamma_5)^* \quad (\text{B.33})$$

where  $\bar{k} = (k^0, -\mathbf{k})$ , etc. If  $T_N$  invariance would apply, the FF would be purely imaginary. On the other hand, hermiticity requires the functions to be real, so these functions should then vanish.

The operation  $T_N$  differs from the usual time-reversal operation  $T$  in that the former does not transform *in* into *out*-state, and vice versa. Due to the final state interaction, the *out*-state  $|P_h, S_h; X \rangle$  in the correlation matrix is not a plane wave state and thus, is not simply related

to an *in*-state. Therefore, one has  $T_N \neq T$  and since  $T$  itself does not pose any constraints on the functions, they need not vanish.

In the analogous case of distribution functions, which are derived from matrix elements with plane wave states,  $T_N = T$  and therefore it was generally believed there are no 'time-reversal odd' distribution functions [37].

The following projections occur with a pre-factor  $M_h/P_h^-$ :

$$\Delta^{[1]}(z, \mathbf{k}_T) = \frac{M_h}{P_h^-} E(z, \mathbf{k}_T^{\prime 2}), \quad (\text{B.34})$$

$$\begin{aligned} \Delta^{[\gamma^i]}(z, \mathbf{k}_T) &= \frac{k_T^i}{P_h^-} D^\perp(z, \mathbf{k}_T^{\prime 2}) + \lambda_h \frac{\epsilon_T^{ij} k_{Tj}}{P_h^-} D_L^\perp(z, \mathbf{k}_T^{\prime 2}) + \\ &+ \frac{M_h}{P_h^-} \epsilon_T^{ij} S_{hTj} D_T(z, \mathbf{k}_T^{\prime 2}), \end{aligned} \quad (\text{B.35})$$

$$\Delta^{[i\gamma_5]}(z, \mathbf{k}_T) = \frac{M_h}{P_h^-} \left( \lambda_h E_L(z, \mathbf{k}_T^{\prime 2}) + \frac{\mathbf{k}_T \cdot \mathbf{S}_{hT}}{M_h} E_T(z, \mathbf{k}_T^{\prime 2}) \right), \quad (\text{B.36})$$

$$\begin{aligned} \Delta^{[\gamma^i \gamma_5]}(z, \mathbf{k}_T) &= \frac{M_h}{P_h^-} S_{hT}^i G_T'(z, \mathbf{k}_T^{\prime 2}) + \\ &+ \frac{k_T^i}{M_h} \left( \lambda_h G_L^\perp(z, \mathbf{k}_T^{\prime 2}) + \frac{\mathbf{k}_T \cdot \mathbf{S}_{hT}}{M_h} G_T^\perp(z, \mathbf{k}_T^{\prime 2}) \right) \end{aligned} \quad (\text{B.37})$$

$$\Delta^{[i\sigma^{ij} \gamma_5]}(z, \mathbf{k}_T) = \frac{M_h}{P_h^-} \frac{S_{hT}^i k_T^j - S_{hT}^j k_T^i}{M_h} H_T^\perp(z, \mathbf{k}_T^{\prime 2}) + \frac{M_h}{P_h^-} \epsilon^{ij} H(z, \mathbf{k}_T^{\prime 2}), \quad (\text{B.38})$$

$$\Delta^{[i\sigma^{+-} \gamma_5]}(z, \mathbf{k}_T) = \frac{M_h}{P_h^-} \left( \lambda_h H_L(z, \mathbf{k}_T^{\prime 2}) + \frac{\mathbf{k}_T \cdot \mathbf{S}_{hT}}{M_h} H_T(z, \mathbf{k}_T^{\prime 2}) \right) \quad (\text{B.39})$$

where  $G_T = G_T' + (\mathbf{k}_T^2/2M_h^2)G_T^\perp$ .

## The naming scheme

At first glance, the names of PFFs (or PDFs) look complicated with all their sub and superscripts, but they publicly announce the physical situation to be considered, in which these quantities can be accessed.

The naming scheme can be summarized with the following set of five rules:

1. The Dirac projection of the correlation function, i.e. the matrix  $\Gamma$ , determines the letter of the resulting PFFs (PDFs):

Dirac projection with $\Gamma$		PFF	PDF
vector	$\gamma^+, \gamma^i, \gamma^-$	D	f
axial vector	$\gamma^+ \gamma_5, \gamma^i \gamma_5, \gamma^- \gamma_5$	G	g
tensor	$\sigma^{+i} \gamma_5, \sigma^{ij} \gamma_5, \sigma^{-i} \gamma_5$	H	h
(pseudo) scalar	$\mathbf{1}, \gamma_5$	E	e

2. The first subscript indicate the *effective twist* of the function:

effective twist	first subscript
twist 2	1
twist 3	2 (or none)
twist 4	3

3. The second subscript indicate the polarization of the hadron:

hadron polarization	second subscript
unpolarized	none
longitudinal	L
transverse	T

4. non-contracted transverse index of a quark momentum  $\rightarrow$  superscript  $\perp$ ;  
 5. higher  $k_T^2$ -moments  $\rightarrow$  superscript  $(n)$ .

## Appendix C

# Dirac matrices in chiral (Weyl) representation

**Dirac matrices** (Weyl or chiral representation): One writes the representation of Dirac matrices compactly in the *bispinor* notation [20]. If  $(\sigma^1, \sigma^2, \sigma^3)$  and  $(\rho^1, \rho^2, \rho^3)$  are two copies of the standard  $2 \times 2$  Pauli matrices, any  $4 \times 4$  Dirac matrices can be represented as  $\rho^i \otimes \sigma^j$ .

The chiral (Weyl) representation is defined by

$$\begin{aligned}\gamma^0 &= \rho^1 \otimes \mathbb{1} = \begin{pmatrix} 0 & \mathbb{1} \\ \mathbb{1} & 0 \end{pmatrix} \\ \vec{\gamma} &= -i\rho^2 \otimes \vec{\sigma} = \begin{pmatrix} 0 & -\vec{\sigma} \\ \vec{\sigma} & 0 \end{pmatrix} \\ \gamma_5 &= \rho^3 \otimes \mathbb{1} = i\gamma^0\gamma^1\gamma^2\gamma^3 = \begin{pmatrix} \mathbb{1} & 0 \\ 0 & -\mathbb{1} \end{pmatrix}\end{aligned}\tag{C.1}$$

A commonly used basis for the space of all  $4 \times 4$  matrices are the 16 independent matrices

$$\mathbb{1}, \gamma_5, \gamma^\mu, \gamma^\mu\gamma_5, \sigma^{\mu\nu}$$

in terms of which any matrix  $M$  can be decomposed as <sup>1</sup>

$$\begin{aligned}M &= \frac{\text{Tr}[M\mathbb{1}]}{4}\mathbb{1} + \frac{\text{Tr}[M\gamma_5]}{4}\gamma_5 + \frac{\text{Tr}[M\gamma^\mu]}{4}\gamma^\mu - \\ &- \frac{\text{Tr}[M\gamma_5\gamma^\mu]}{4}\gamma_5\gamma^\mu + \frac{\text{Tr}[M\sigma^{\mu\nu}]}{2 * 4}\sigma^{\mu\nu}\end{aligned}\tag{C.2}$$

Instead one can use the alternative basis

$$\begin{aligned}\gamma^+, \gamma^+\gamma_5, i\sigma^{i+}\gamma_5, \\ \mathbb{1}, \gamma^i, i\gamma_5, \gamma^i\gamma_5, i\sigma^{ij}\gamma_5, i\sigma^{+-}\gamma_5, \\ \gamma^-, \gamma^-\gamma_5, i\sigma^{i-}\gamma_5\end{aligned}\tag{C.3}$$

---

<sup>1</sup>note the minus sign of the 4th term and the extra factor 1/2 in the last term to avoid double counting in the summation over  $\mu$  and  $\nu$ .

where  $i, j$  are purely transverse indices ( $i, j \in \{1, 2\}$ ), and  $\gamma^\pm = 1/\sqrt{2}(\gamma^0 \pm \gamma^3)$ . In this basis, any matrix can be decomposed as

$$\begin{aligned}
M = & \frac{\text{Tr}[M\gamma^+]}{4}\gamma^- - \frac{\text{Tr}[M\gamma^+\gamma_5]}{4}\gamma^-\gamma_5 + \frac{\text{Tr}[Mi\sigma^{1+}\gamma_5]}{4}i\sigma^{1-}\gamma_5 + \\
& + \frac{\text{Tr}[M\mathbb{1}]}{4}\mathbb{1} - \frac{\text{Tr}[M\gamma^i]}{4}\gamma^i - \frac{\text{Tr}[Mi\gamma_5]}{4}i\gamma_5 + \frac{\text{Tr}[M\gamma^i\gamma_5]}{4}\gamma^i\gamma_5 - \\
& - \frac{\text{Tr}[Mi\sigma^{ij}\gamma_5]}{2 \cdot 4}i\sigma^{ij}\gamma_5 - \frac{\text{Tr}[Mi\sigma^{+-}\gamma_5]}{4}i\sigma^{-+}\gamma_5 + \\
& + \frac{\text{Tr}[M\gamma^-]}{4}\gamma^+ - \frac{\text{Tr}[M\gamma^-\gamma_5]}{4}\gamma^+\gamma_5 + \frac{\text{Tr}[Mi\sigma^{i-}\gamma_5]}{4}i\sigma^{i+}\gamma_5
\end{aligned} \tag{C.4}$$

Below I list all matrices of the basis (C.3) multiplied from the left by  $\gamma^0$ , since this is the form relevant for a classification of bilocal quark field operators  $\bar{\psi}(z_1)A\psi(z_2)$ . The *effective twist* and chirality of  $\bar{\psi}(z_1)A\psi(z_2)$  with  $A \in$  basis (C.3) is indicated, as well.

*Effective twist 2:*

$$(\gamma^0\gamma^+) = \sqrt{2} \begin{pmatrix} 1 & 0 & 0 & 0 \\ 0 & 0 & 0 & 0 \\ 0 & 0 & 0 & 0 \\ 0 & 0 & 0 & 1 \end{pmatrix} \quad \phi_R^\dagger\phi_R + \phi_L^\dagger\phi_L \text{ (chiral even)} \tag{C.5}$$

$$(\gamma^0\gamma^+\gamma_5) = \sqrt{2} \begin{pmatrix} 1 & 0 & 0 & 0 \\ 0 & 0 & 0 & 0 \\ 0 & 0 & 0 & 0 \\ 0 & 0 & 0 & -1 \end{pmatrix} \quad \phi_R^\dagger\phi_R - \phi_L^\dagger\phi_L \text{ (chiral even)} \tag{C.6}$$

$$(\gamma^0i\sigma^{1+}\gamma_5) = \sqrt{2} \begin{pmatrix} 0 & 0 & 0 & 1 \\ 0 & 0 & 0 & 0 \\ 0 & 0 & 0 & 0 \\ 1 & 0 & 0 & 0 \end{pmatrix} \quad \phi_L^\dagger\phi_R + \phi_R^\dagger\phi_L \text{ (chiral odd)} \tag{C.7}$$

$$(\gamma^0i\sigma^{2+}\gamma_5) = i\sqrt{2} \begin{pmatrix} 0 & 0 & 0 & -1 \\ 0 & 0 & 0 & 0 \\ 0 & 0 & 0 & 0 \\ 1 & 0 & 0 & 0 \end{pmatrix} \quad -\phi_L^\dagger\phi_R + \phi_R^\dagger\phi_L \text{ (chiral odd)} \tag{C.8}$$

Effective twist 3:

$$(\gamma^0 \mathbb{1}) = \begin{pmatrix} 0 & 0 & 1 & 0 \\ 0 & 0 & 0 & 1 \\ 1 & 0 & 0 & 0 \\ 0 & 1 & 0 & 0 \end{pmatrix} \quad \chi_L^\dagger \phi_R + \phi_L^\dagger \chi_R + \phi_R^\dagger \chi_L + \chi_R^\dagger \phi_L \text{ (chiral odd)} \quad (\text{C.9})$$

$$(\gamma^0 \gamma^1) = \begin{pmatrix} 0 & 1 & 0 & 0 \\ 1 & 0 & 0 & 0 \\ 0 & 0 & 0 & -1 \\ 0 & 0 & -1 & 0 \end{pmatrix} \quad \chi_R^\dagger \phi_R + \phi_R^\dagger \chi_R - \phi_L^\dagger \chi_L - \chi_L^\dagger \phi_L \text{ (chiral even)} \quad (\text{C.10})$$

$$(\gamma^0 \gamma^2) = i \begin{pmatrix} 0 & -1 & 0 & 0 \\ 1 & 0 & 0 & 0 \\ 0 & 0 & 0 & 1 \\ 0 & 0 & -1 & 0 \end{pmatrix} \quad -\chi_R^\dagger \phi_R + \phi_R^\dagger \chi_R + \phi_L^\dagger \chi_L - \chi_L^\dagger \phi_L \text{ (chiral even)} \quad (\text{C.11})$$

$$(\gamma^0 i \gamma_5) = i \begin{pmatrix} 0 & 0 & -1 & 0 \\ 0 & 0 & 0 & -1 \\ 1 & 0 & 0 & 0 \\ 0 & 1 & 0 & 0 \end{pmatrix} \quad -\chi_L^\dagger \phi_R - \phi_L^\dagger \chi_R + \phi_R^\dagger \chi_L + \chi_R^\dagger \phi_L \text{ (chiral odd)} \quad (\text{C.12})$$

$$(\gamma^0 \gamma^1 \gamma_5) = \begin{pmatrix} 0 & 1 & 0 & 0 \\ 1 & 0 & 0 & 0 \\ 0 & 0 & 0 & 1 \\ 0 & 0 & 1 & 0 \end{pmatrix} \quad \chi_R^\dagger \phi_R + \phi_R^\dagger \chi_R + \phi_L^\dagger \chi_L + \chi_L^\dagger \phi_L \text{ (chiral even)} \quad (\text{C.13})$$

$$(\gamma^0 \gamma^2 \gamma_5) = i \begin{pmatrix} 0 & -1 & 0 & 0 \\ 1 & 0 & 0 & 0 \\ 0 & 0 & 0 & -1 \\ 0 & 0 & 1 & 0 \end{pmatrix} \quad -\chi_R^\dagger \phi_R + \phi_R^\dagger \chi_R + \phi_L^\dagger \chi_L + \chi_L^\dagger \phi_L \text{ (chiral even)} \quad (\text{C.14})$$

$$(\gamma^0 i \sigma^{12} \gamma_5) = i \begin{pmatrix} 0 & 0 & -1 & 0 \\ 0 & 0 & 0 & 1 \\ 1 & 0 & 0 & 0 \\ 0 & -1 & 0 & 0 \end{pmatrix} \quad -\chi_L^\dagger \phi_R + \phi_L^\dagger \chi_R + \phi_R^\dagger \chi_L - \chi_R^\dagger \phi_L \text{ (chiral odd)} \quad (\text{C.15})$$

$$(\gamma^0 i \sigma^{+-} \gamma_5) = \begin{pmatrix} 0 & 0 & 1 & 0 \\ 0 & 0 & 0 & -1 \\ 1 & 0 & 0 & 0 \\ 0 & -1 & 0 & 0 \end{pmatrix} \quad \chi_L^\dagger \phi_R - \phi_L^\dagger \chi_R + \phi_R^\dagger \chi_L - \chi_R^\dagger \phi_L \text{ (chiral odd)} \quad (\text{C.16})$$

Effective twist 4:

$$(\gamma^0 \gamma^-) = \sqrt{2} \begin{pmatrix} 0 & 0 & 0 & 0 \\ 0 & 1 & 0 & 0 \\ 0 & 0 & 1 & 0 \\ 0 & 0 & 0 & 0 \end{pmatrix} \quad \chi_R^\dagger \chi_R + \chi_L^\dagger \chi_L \text{ (chiral even)} \quad (\text{C.17})$$

$$(\gamma^0 \gamma^- \gamma_5) = \sqrt{2} \begin{pmatrix} 0 & 0 & 0 & 0 \\ 0 & 1 & 0 & 0 \\ 0 & 0 & -1 & 0 \\ 0 & 0 & 0 & 0 \end{pmatrix} \quad \chi_R^\dagger \chi_R - \chi_L^\dagger \chi_L \text{ (chiral even)} \quad (\text{C.18})$$

$$(\gamma^0 i \sigma_1 - \gamma_5) = \sqrt{2} \begin{pmatrix} 0 & 0 & 0 & 0 \\ 0 & 0 & 1 & 0 \\ 0 & 1 & 0 & 0 \\ 0 & 0 & 0 & 0 \end{pmatrix} \quad \chi_L^\dagger \chi_R + \chi_R^\dagger \chi_L \text{ (chiral odd)} \quad (\text{C.19})$$

$$(\gamma^0 i \sigma_2 - \gamma_5) = i\sqrt{2} \begin{pmatrix} 0 & 0 & 0 & 0 \\ 0 & 0 & 1 & 0 \\ 0 & -1 & 0 & 0 \\ 0 & 0 & 0 & 0 \end{pmatrix} \quad \chi_L^\dagger \chi_R - \chi_R^\dagger \chi_L \text{ (chiral odd)} \quad (\text{C.20})$$

# Bibliography

- [1] J.M. Gell-Mann, Phys. Lett. **8**, 214 (1964).
- [2] G. Zweig, CERN preprints **TH-401**, **TH-412** (1964).
- [3] J. Ashman *et al.*, Nucl. Phys. **B328**, 161 (1989).
- [4] A. Airapetian *et al.* [HERMES Collaboration], Phys. Rev. **D75**, 012007 (2007).
- [5] V. Alexakhin *et al.*, Phys. Lett. **B647**, 8 (2007).
- [6] E.S. Ageev *et al.* (COMPASS Collaboration), Phys. Lett. **B633**:25-32 (2006) [arXiv:hep-ex/0511028].
- [7] A. Airapetian *et al.* [HERMES Collaboration], JHEP **1008**, 130 (2010) [arXiv:hep-ex/1002.3921].
- [8] A. Adore *et al.* (PHENIX Collaboration), Phys. Rev. Lett. **103**, 012003 (2009).
- [9] J.C. Collins, Nucl. Phys. **B396**, 161 (1993).
- [10] A. Airapetian *et al.* [HERMES Collaboration], Phys. Rev. Lett. **94**, 012002 (2005).
- [11] E.S. Ageev *et al.* [COMPASS Collaboration], Nucl. Phys. **B765**, 31 (2007).
- [12] A.V. Efremov, O.G. Smirnova and L.G. Tkatchev, Nucl. Phys. **B** (Proc. Suppl.) **74**, 49 (1999) [arXiv:hep-ph/9812522].
- [13] W. Bonivento *et al.*, Internal Note DELPHI-95-81 PHYS 516, Contribution eps0549 to the "EPS-HEP 95" Conference, Brussels (1995), unpublished.
- [14] K. Abe *et al.* [BELLE Collaboration], Phys. Rev. Lett. **96**, 232002 (2006).
- [15] R. Seidl *et al.* [BELLE Collaboration], Phys. Rev. **D78**, 032011 (2008).
- [16] M. Anselmino *et al.*, Phys. Rev. **D75**, 054032 (2007).
- [17] M. Anselmino *et al.*, Nucl.Phys.Proc.Suppl. **191**:98-107 (2009) [arXiv:0812.4366v1 (2008)].

- [18] J.C. Collins, D.E. Soper, Nucl. Phys. **B193**, 381 (1981).
- [19] J.C. Collins, D.E. Soper, Nucl. Phys. **B194**, 445 (1982).
- [20] R.L. Jaffe, Lectures on QCD, Erice 1995, hep-ph/9602236.
- [21] M. Anselmino *et al.*, Phys. Rev. **D73**, 014020 (2006).
- [22] D.W. Sivers, Phys. Rev. **D41**, 83 (1990).
- [23] D. Boer and P.J. Mulders, Phys. Rev. **D57**, 5780 (1998).
- [24] S. Albino, B.A. Kniehl, and G. Kramer, Nucl. Phys. **B803**, 42 (2008).
- [25] S. Kretzer, Phys. Rev. **D62**, 054001 (2000).
- [26] D. de Florian, R. Sassot, and M. Stratmann, Nucl. Phys. **D75**, 114010 (2007).
- [27] A. Bacchetta *et al.*, JHEP **02**, 093 (2007) [arXiv:hep-ph/0707.3372].
- [28] M. Anselmino *et al.*, Phys. Rev. **D83**, 114019 (2011).
- [29] O. Martin *et al.*, Phys. Rev. **D60**, 117502 (1999) [arXiv:hep-ph/9902250].
- [30] P. Lenisa, F. Rathmann *et al.* [PAX Collaboration], arXiv:hep-ex/0505054 (2005).
- [31] A. Airapetian *et al.* [HERMES Collaboration], Phys. Rev. Lett. **103**, 152002 (2009).
- [32] M. Alekseev *et al.* [COMPASS Collaboration], Phys. Lett. **B673**, 127 (2009).
- [33] M. Alekseev *et al.* [COMPASS Collaboration], Phys. Lett. **B692**, 240 (2010).
- [34] X. Artru, J. Czyzewski, and H. Yabuki, Z. Phys. **C73**, 527 (1997).
- [35] A. Bacchetta, R. Kundu, A. Metz, and P.J. Mulders, Phys. Lett. **B506**, 155 (2001).
- [36] A. Bacchetta, R. Kundu, A. Metz, and P.J. Mulders, Phys. Rev. **D64**, 094021 (2002).
- [37] D. Boer, R. Jakob, and P.J. Mulders, Nucl. Phys. **B504**, 345 (1997).
- [38] J. Soffer, Phys. Rev. Lett. **74**, 1292 (1995).
- [39] A. Majumder, and X.N. Wang, Phys. Rev. **D70**, 014007 (2004).
- [40] F.A. Ceccopieri, M. Radici, and A. Bacchetta, Phys. Lett. **B650**, 81 (2007).
- [41] D. Boer, R. Jakob and M. Radici, Phys. Rev. **D67**, 094003 (2003).
- [42] A. Bacchetta, F.A. Ceccopieri, A. Mukherjee, and M. Radici, Phys. Rev. **D79**, 034029 (2009).

- [43] A. Airapetian *et al.* [HERMES Collaboration], JHEP **0806**, 017 (2008) [arXiv:0803.2367].
- [44] F. Massmann (on behalf of the COMPASS Collaboration), Eur. Phys. J. Special Topics **162**, 85 (2008).
- [45] H. Wollny *et al.* [COMPASS Collaboration], arXiv:0907.0961 (2009).
- [46] A. Vossen *et al.* [BELLE Collaboration], Phys. Rev. Lett. **107**, 072004 (2011) [arXiv:1104.2425].
- [47] G. Altarelli, Phys. Reports **81**, 1 (1982).
- [48] G. Altarelli and G. Parisi, Nucl. Phys. **B126**, 298 (1977).
- [49] V.N. Gribov and L.N. Lipatov, Sov. J. Nucl. Phys. **15**, 438 (1972).
- [50] Y.L. Dokshitzer, Sov. Phys. JEPT **46**, 641 (1977).
- [51] K. Nakamura *et al.* (Particle Data Group), J. Phys. **G37**, 075021 (2010).
- [52] H.F. Jones, Nuovo Cimento **40A**, 1018 (1965);  
K.H. Streng *et al.*, Z. Phys. **C2**, 237 (1979).
- [53] J.F. Patric *et al.* [MARK II Collaboration], Phys. Rev. Lett. **49**, 1232 (1982).
- [54] R.D. Field and R.P. Feynman, Nucl. Phys. **B136**, 1 (1978).
- [55] T. Meyer, Z. Phys. **C12**, 77 (1982).
- [56] B. Andersson *et al.*, Phys. Rep. **97**, 31 (1983).
- [57] T. Sjöstrand and M. Bengtsson, Comp. Phys. Comm. **43**, 367 (1987).
- [58] T. Sjöstrand, M.Mrenna, and P. Skands, JHEP **0605**, 026 (2006);  
T. Sjöstrand, M.Mrenna, and P. Skands, Comp. Phys. Comm. **178**, 852 (2008).
- [59] S. Chun and C. Buchanan, Phys. Reports **292**, 239 (1998).
- [60] B. Andersson *et al.*, Z. Phys. **C20**, 317 (1983).
- [61] G. Corcella *et al.*, JHEP **0101**, 010 (2001) [arXiv:peh-ph/0011363v3];  
M. Bähr *et al.*, Eur. Phys. J. **C58**, 639 (2008).
- [62] T. Gleisberg *et al.*, JHEP **0902**, 007 (2009).
- [63] D. Amati and G. Veneziano, Phys. Lett. **B83**, 87 (1979).
- [64] D. Boer, Nucl. Phys. **B806**, 23 (2009).

- [65] C. S. Lam and W. K. Tung, Phys. Rev. **D18**, 2447 (1978).
- [66] C. S. Lam and W. K. Tung, Phys. Rev. **D21**, 2712(1980).
- [67] J. C. Collins, Phys. Rev. Lett. **42**, 291 (1979).
- [68] E.N. Argyres and C.S. Lam, Phys. Rev. **D26**, 114 (1982).
- [69] R. Jakob, P.J. Mulders, and J. Rodrigues, Nucl. Phys. **A626**, 937 (1997).
- [70] J. Levelt and P. J. Mulders, Phys. Lett. **B338**, 357 (1994).
- [71] J. Levelt and P. J. Mulders, Phys. Rev. **D49**, 96 (1994).
- [72] D. Boer, P. J. Mulders and F. Pijlman , Nucl. Phys. **B667**, 201 (2003).
- [73] J. C. Collins, Phys. Lett. **B536**, 43 (2002).
- [74] A. V. Belitsky, X. Ji and F. Yuan , Nucl. Phys. **B656**, 165 (2007).
- [75] A. Metz, Phys. Lett. **B549**, 139 (2002).
- [76] J. C. Collins and A. Metz , Phys. Rev. Lett. **93**, 252001 (2004).
- [77] D. Boer, Z.B. Kang, W. Vogelsang, and F. Yuan, Phys. Rev. Lett. **105**, 202001 (2010).
- [78] F. Yuan, Phys. Rev. Lett. **100**, 032003 (2008).
- [79] B. Aubert et al. (*BABAR* Collaboration), “The *BABAR* Detector”, *Nucl. Instrum. Meth.*, **A479**:1-116 (2002) [arXiv:hep-ex/0105044].
- [80] “PEP-II: An Asymmetric B Factory. Conceptual Design Report”. June 1993, 1993. SLAC-418, LBL-PUB-5379.
- [81] “The *BABAR* Physics Book. Physics at an Asymmetric B Factory” (*BABAR* Collaboration), ed. P.F. Harrison and H.R. Quinn, SLAC-R-504 (1998).
- [82] J. Seeman *et al.* (*BABAR* Collaboration), “A luminosity of  $10^{34}$  cm<sup>-2</sup>s<sup>-1</sup> in the PEP-II B-factory”, SLAC-PUB-12023.
- [83] C. Bozzi *et al.* (*BABAR* Collaboration), “The *BABAR* silicon vertex tracker”, *Nucl. Instrum. Meth.*, **A435**:25-33 (1999).
- [84] V. Re *et al.* (*BABAR* Collaboration), “Performance of the *BABAR* silicon vertex detector”, *Nucl. Instrum. Meth.*, **A501**:14-21 (2003).
- [85] G. Sciola *et al.* (*BABAR* Collaboration), “The *BABAR* drift chamber”, *Nucl. Instrum. Meth.*, **A419**:310-314 (1998).

- [86] M.H. Kelsey *et al.* (*BABAR* Collaboration), “Performance and aging of the *BABAR* Drift Chamber”, Nucl. Instrum. Meth., **A536**,206 (2004).
- [87] I. Adam *et al.* (*BABAR* Collaboration), “DIRC, the internally reflecting ring imaging Čerenkov detector for *BABAR*”, IEEE Trans. Nucl. Sci., **45**:657-664 (1998) [arXiv:hep-ex/9712001].
- [88] B. Lewandowski, “The *BABAR* electromagnetic calorimeter”, Nucl. Instrum. Meth., **A494**:303-307 (2002);
- [89] R. Santonico, R. Cardarelli, Nucl. Instrum. Meth., **A187**, 377 (1981);
- [90] F. Anulli *et al.* (*BABAR* Collaboration), “The muon and neutral hadron detector for *BABAR*”, Nucl. Instrum. Meth., **A409**:542-546 (1998);
- [91] W. Menges *et al.* (*BABAR* Collaboration), “The *BABAR* muon system upgrade”, IEEE Nucl. Sci. Symp. Conf. Rec., **5**:1470-1474 (2006) [arXiv:physics/0609039];
- [92] G. Battistoni, E. Iarocci, M.M. Massai, G. Nicoletti, and L. Trasatti, “Operation of Limited Streamer Tubes”, Nucl. Instr. Meth., **164**, 57-66 (1979);
- [93] F. Anulli *et al.* (*BABAR* Collaboration), “*BABAR* forward endcap upgrade”, Nucl. Instrum. Meth., **A539**:155-171 (2005);
- [94] A. Bacchetta, U. D’Alessio, M. Diehl and C. A. Miller, Phys. Rev. **D70**, 117504 (2004).
- [95] A. Bacchetta, M. Boglione, A. Henneman and P. J. Mulders, Phys. Rev. Lett. **85**,712 (2000).
- [96] A. Efremov, K. Goetze and P. Schweitzer, Phys. Rev. **D73**,094025 (2006).
- [97] D.J. Lange, Nucl. Instrum. Meth. Phys. Res., **A462**,152 (2001);
- [98] B.F. Ward, S. Jadach, and Z. Was, Nucl. Phys. Proc. Suppl., **116**,73 (2003);
- [99] S. Jadach, Z. Was, R. Decker, and J.H. Kuhn, Comput. Phys. Commun., **76**,361 (1993);
- [100] P. Billoir, Nucl. Instrum. Meth., **A225**:352-366 (1984);
- [101] G.C. Fox and S. Wolfram, Nucl. Phys. **B149**,413 (1979).
- [102] BaBar Analysis Document number 2199, version 2 (2009).
- [103] “Third International Workshop on Transverse Polarization Phenomena in Hard Scattering”, <http://ecsac.ictp.it/transversity2011>.
- [104] I. Garzia (for the *BABAR* Collaboration), arXiv:1201.4678 (2012).

- [105] S. Agostinelli et al. (GEANT4 Collaboration), Nucl. Instrum. Meth. **A506**, 250 (2003).
- [106] A. A. Sokolov and I. M. Ternov, Sov. Phys. Dokl. **8**, 1203 (1964).
- [107] R. F. Schwitters, SLAC-PUB-2258 (1979).
- [108] J. G. Learner, L. K. Resvanis, and C. M. Spenser, Phys. Rev. Lett. **35**, 25 (1975).
- [109] BaBar Analysis Document number 30, version 5 (2000).
- [110] A. Bacchetta, L.P. Gamberg, G.R. Goldstein, A. Mukherjee, Phys. Lett. **B659**, 234-243 (2008).
- [111] I. Garzia and F. Anulli, BaBar Analysis Document number 2424, version 7 (2011).
- [112] P.A. Dirac, Rev. Mod. Phys. **21**, 392 (1949).
- [113] J.B. Kogut and D.E. Soper, Phys. Rev. **D1**, 2901 (1970).
- [114] Z. Dziembowski, Phys. Rev. **D37**, 768 (1988).
- [115] J.C. Collins, *Light-Cone variables, Rapidity and All That* [arXiv:hep-ph/9705393].
- [116] J.D. Bjorken, J.Kogut and D.E. Soper, Phys. Rev. **D3**, 1382 (1971).